Quantum many body physics in single and bilayer graphene

by

Rahul Nandkishore

Submitted to the Department of Physics
in partial fulfillment of the requirements for the degree of

Doctor of Philosophy

at the

MASSACHUSETTS INSTITUTE OF TECHNOLOGY

September 2012

Author .....
Department of Physics
July 27, 2012

Certified by .....
Leonid S. Levitov
Professor of Physics
Thesis Supervisor

Accepted by .....
John Belcher
Associate Department Head for Education

Quantum many body physics in single and bilayer graphene

by

Rahul Nandkishore

Submitted to the Department of Physics
on July 27, 2012, in partial fulfillment of the
requirements for the degree of
Doctor of Philosophy

Abstract

Two dimensional electron systems (2DES) provide a uniquely promising avenue for investigation of many body physics. Graphene constitutes a new and unusual 2DES, which may give rise to unexpected collective phenomena. However, the vanishing density of states in charge neutral single layer graphene suppresses many body effects, and one has to alter the system to observe strongly ordered states. We consider three ways of accessing quantum many body physics using graphene.

First, we consider doping single layer graphene to a Van Hove singularity in the density of states. We show that there are strong instabilities to several strongly ordered states, with the leading instability being to a d-wave superconducting state. The superconducting state realizes chiral superconductivity, an exotic form of superconductivity wherein the phase of the order parameter winds by 4π as we go around the Fermi surface. We also discuss the nature of the spin density wave state which is the principal competitor to superconductivity in doped graphene.

Next, we study bilayer graphene (BLG), which has a non-vanishing density of states even at charge neutrality. We show that Coulomb interactions give rise to a zero bias anomaly in the tunneling density of states for BLG, which manifests itself at high energy scales. We also show that the quadratic band crossing in BLG is unstable to arbitrarily weak interactions, and estimate the energy scale for formation of strongly ordered states. We show that gapped states in BLG have topological properties, and we classify the various possible gapped and gapless states in terms of symmetries. We study the competition between various ordered states, and discuss how the nature of the ground state may be deduced experimentally. We also discuss recent experimental observations of strongly ordered states in bilayer graphene.

Finally, we study bilayer graphene in a transverse magnetic field, focusing on the properties of the quantum Hall ferromagnet (QHF) state. We resolve an apparent discrepancy between the experimentally observed energetics and theory. We close with a discussion of the exotic topological defects that form above the QHF state.

Thesis Supervisor: Leonid S. Levitov
Title: Professor of Physics

Acknowledgments

Firstly I thank my advisor, Leonid Levitov, without whom this thesis would not have been possible. With his keen eye for an interesting problem and his thorough command of theoretical physics, Leonid was an ideal supervisor. Equally important, Leonid had an intuitive feel for when I needed guidance, and when I could be left to work independently, which greatly helped me develop as a physicist. I was very lucky to be Leonid's student, and he remains a source of inspiration to me.

I thank Andrey Chubukov and T. Senthil, with both of whom I collaborated extensively. With his impressive calculational abilities, his enthusiasm, and his willingness to discuss calculations at any time, Andrey was a fantastic collaborator. Meanwhile, Senthil's profound intuition and infectious enthusiasm have frequently clarified my thinking, and have inspired me to think deeply.

Other physicists with whom I have collaborated include Gia Wei Chern and Rafael Fernandes, with whom I collaborated in my work on spin density waves in doped graphene, and Arjun Nandkishore, who performed the numerical calculations reported in the chapter on ε expansion RG for bilayer graphene.

My research has been strongly motivated and inspired by ongoing experiments. I thank Amir Yacoby, Ben Feldman, Thomas Weitz, Jens Martin, Monica Allen, Pablo Jarillo-Herrero, Leonardo Campos, Javier Sanchez-Yamagishi, Andrea Young and C.N.Lau for sharing unpublished experimental data with me.

I thank the various members of the MIT CMT group with whom I have frequently discussed physics. Patrick Lee, Liang Fu, Andrew Potter, David Mross, Justin Song, Karen Michaeli, Brian Swingle and Nan Gu have frequently served as my sounding boards for physics ideas, and I thank them for their insightful comments.

I thank my undergraduate advisors, in particular David Khmelnitski, Ben Simons and Peter Littlewood, for inspiring me to do condensed matter physics, and my high school physics teacher, Phil Pyburn, for inspiring me to become a physicist. I also thank my father for instilling in me a love of science from an early age.

Important as my professional mentors and collaborators have been, an equally

important role has been played by Meagan, my family, and by my friends. Thank you for making my life better, and for allowing me to devote so much of my energy to physics.

Contents

List of Figures

Chapter 1

Introduction

The idea that 'more is different' [1], and that large collections of interacting particles can display emergent behavior qualitatively different to the behavior of a few particles, is the inspiration for condensed matter physics. While the fundamental laws governing ordinary matter, namely electromagnetism and quantum mechanics, are well known, the behavior of material systems is endlessly varied, and continues to surprise us. Superconductivity [2], the quantum Hall effects [3], and the recent discovery of topological phases of matter [4] are only a few examples of the way that new physics can emerge in material systems.

Electronic systems provide a particularly interesting playground for exploration of collective phenomena. Whereas the behavior of systems of non-interacting electrons is well understood in terms of band theory [5], there is no exhaustive theory for the behavior of interacting electron systems. Interactions between electrons can lead to formation of ground states that spontaneously break symmetries of the microscopic Hamiltonian [6], exhibit topological order [7], or otherwise display properties that are markedly different to those exhibited by non-interacting electron systems. The study of many body physics in electronic systems is thus a centerpiece of modern condensed matter physics.

The dimensionality of the physical system has important consequences for the many body physics. Interaction effects are stronger in low dimensional systems. Thus, two dimensional systems are generically more sensitive to interactions than three di-

mensional systems, and one dimensional systems are more sensitive still. However, in one dimension, the very low dimensionality reduces the complexity of the problem, and the behavior of one dimensional systems is largely understood [8]. Two dimensional electron systems are thus ideal for the study of many body physics - the low dimensionality enhances the effect of interactions, but the dimensionality is still high enough for unexpected behavior to arise. Many of the most dramatic recent discoveries in condensed matter, including high temperature superconductivity [9] and the fractional quantum Hall effect [3, 7] have occurred in two dimensional or quasi-two dimensional systems.

Recently, an entirely new family of two dimensional electron systems has become available, which are based on graphene. Graphene, a single, atomically thin sheet of carbon atoms, was discovered in 2004 [10], and rapidly became one of the most popular systems for experimental and theoretical condensed matter research. For an exhaustive review of work done on graphene, see [11, 12].

The popularity of graphene is motivated partly because of its potential for technological applications: it is a two dimensional electron system (2DES) with high mobility, where the carrier density can be tuned by gating, and it can be tuned to exhibit either electron-like or hole-like (ambipolar) behavior. These properties make graphene a promising material for building devices and for technological applications. At the same time, graphene is interesting for physicists because it represents an entirely new 2DES with unique features (for example, the low energy excitations are governed by a Dirac equation), and as a result qualitatively new physics can arise. New physics observed in graphene include Klein tunneling and an anomalous 'half integer' quantum Hall effect [11].

However, at the time that this thesis was started, the existing work on graphene had almost entirely neglected many body effects. The reason for this neglect was that almost all the observed properties of single layer graphene near charge neutrality appear fully consistent with a model of non-interacting electrons. The recent observation of a logarithmic dependence of the Fermi velocity on doping level [13], represents the first truly many body effect to be observed in single layer graphene,

and even this can be understood within a 'marginal Fermi liquid' description that is adiabatically connected to the non-interacting description [14]. The apparent weakness of many body effects is surprising, given our earlier identification of 2DES as being ideal for investigation of many body physics. It turns out that the lack of any striking departures from non-interacting behavior can be attributed to the vanishing low energy density of states in charge neutral graphene, which suppresses the effect of interactions. The search for new quantum many body physics in graphene was the principal objective of this thesis.

How can one sidestep the vanishing density of states, to realize truly new many body physics in graphene? There are three potential avenues of attack. One possibility is to dope graphene to alter the low energy density of states. A second is to study bilayer graphene, where the density of states is non-vanishing. Finally, one can also apply a transverse magnetic field to alter the electronic spectrum and produce a non-vanishing density of states. I discuss each of these approaches in turn.

First, I discuss doping single layer graphene. Upon doping, the density of states becomes non-vanishing, and at a critical doping level the density of states actually diverges. At this doping level, exotic strongly correlated states are highly likely, and the behavior at this doping level will be the focus of Chapters 2 and 3. Prior to the work described in Chapters 2 and 3, a large number of possible states had been proposed for single layer graphene, but there was little understanding of which states were actually likely. This is the question I set out to address, using a weak coupling renormalization group technique which allowed for an unbiased analysis of the competition between various orders.

In Chapter 2, I will argue that the most likely many body ground state at this doping level is a superconducting state of a form that has not been hitherto observed. The other (less likely) candidate state is an unusual spin density wave (SDW) state, the properties of which I will discuss in Chapter 3. Both possible states, the superconductor and the spin density wave, have highly unusual features which were not appreciated prior to our work. The superconducting state provides a realization of chiral superconductivity, wherein the phase of the superconducting order parameter

winds by 4π as one goes around the Fermi surface, breaking time reversal symmetry. This phase winding also endows the superconducting state with a host of topological properties, such a thermal Hall effect, protected edge states, and zero modes in vortex cores, which are desirable for nano-science applications. Meanwhile, the SDW state possesses gapless charged excitations in one spin branch only, and therefore allows for electrical control of spin currents, which is also desirable for nanoscience applications.

Doped single layer graphene could thus allow realization of one of two highly exotic and long sought after quantum states, neither of which has been previously seen in experiments, and either of which could be extremely useful technologically. Since our work on doped graphene appeared, there has been a flurry of theoretical papers dealing with superconducting and spin density wave phases in doped graphene. Meanwhile, experiments are under way to dope graphene to this level, and may soon be able to directly test the theoretical predictions for doped graphene.

An alternative approach to interesting many body physics involves studying bilayer graphene (BLG). Bilayer graphene (BLG) consists of two graphene sheets chemically bonded together, and shares many of the properties of single layer graphene, except that the density of states is non-vanishing even at zero doping. As a result, non-trivial many body states can arise, and there is strong experimental evidence suggesting that the ground state of undoped BLG is distinct from the non-interacting ground state (for a review, see [18], or Chapter 8).

In Chapter 4, I will discuss the behavior of BLG in the presence of dynamically screened Coulomb interactions. I will predict the existence of a zero bias anomaly in the tunneling density of states that manifests itself at energy scales as high as 100 meV (a feature that has been observed experimentally, although not widely appreciated, see e.g. [19]). In Chapter 5, I will discuss the possibility that Coulomb interactions might trigger spontaneous gap opening in bilayer graphene - something that has been observed in experiments [20, 21, 22]. I also point out that because of the non-vanishing Berry phase in BLG, the gapped states have interesting topological properties.

Our prediction of unusual gapped phases with topological properties helped trigger an explosion of interest in bilayer graphene. A large theoretical literature has

appeared dealing with strong correlation physics in BLG [23, 24, 25, 26, 27, 28, 29, 30, 31, 32, 33, 34]. It has been conclusively established [25] that for short range repulsive interactions, the leading instability in BLG is to a gapless nematic state, and not a gapped topological state. The situation for long range interactions is less clear. If long range (Coulomb) interactions are treated within an RPA screening approximation, as is done in Chapter 7, and also in [26, 27], then it appears that the leading weak coupling instability is to a nematic state, just as for the case of short range interactions only. However, a rigorous treatment of the problem with long range interactions, which does not privilege the RPA diagrams, has not yet been performed.

Meanwhile, a large number of experimental studies of BLG have also appeared [38, 36, 20, 21, 22, 37], which all seem to observe non-trivial strongly ordered states in BLG. Intriguingly, the experiments on BLG appear to be at odds with the theoretical expectations. With the exception of [37], all of the other experiments appear to observe gapped states, whereas the most sophisticated theoretical calculations [25, 26], discussed in Chapter 7, seem to predict that the ground state should be gapless. This conflict between theory and experiment suggests that new developments in many body theory may be necessary to fully explain BLG. Meanwhile, the different experiments also appear to disagree with each other, and I discuss in Chapter 8 what experiments may be done to yield insight into the nature of the ground state of BLG.

The third and final way to produce a non-vanishing density of states (and hence to access new many body physics) is to apply a magnetic field perpendicular to the graphene plane. The resulting quantum Hall physics will be discussed briefly in Chapter 9.

The rest of this introduction is structured as follows: first I provide a brief overview of the Hamiltonian and the electronic properties of single layer graphene. Then, I review the Hamiltonian and electronic properties of bilayer graphene, and the symmetries of bilayer graphene. I conclude by providing a brief summary of the main results of this thesis.

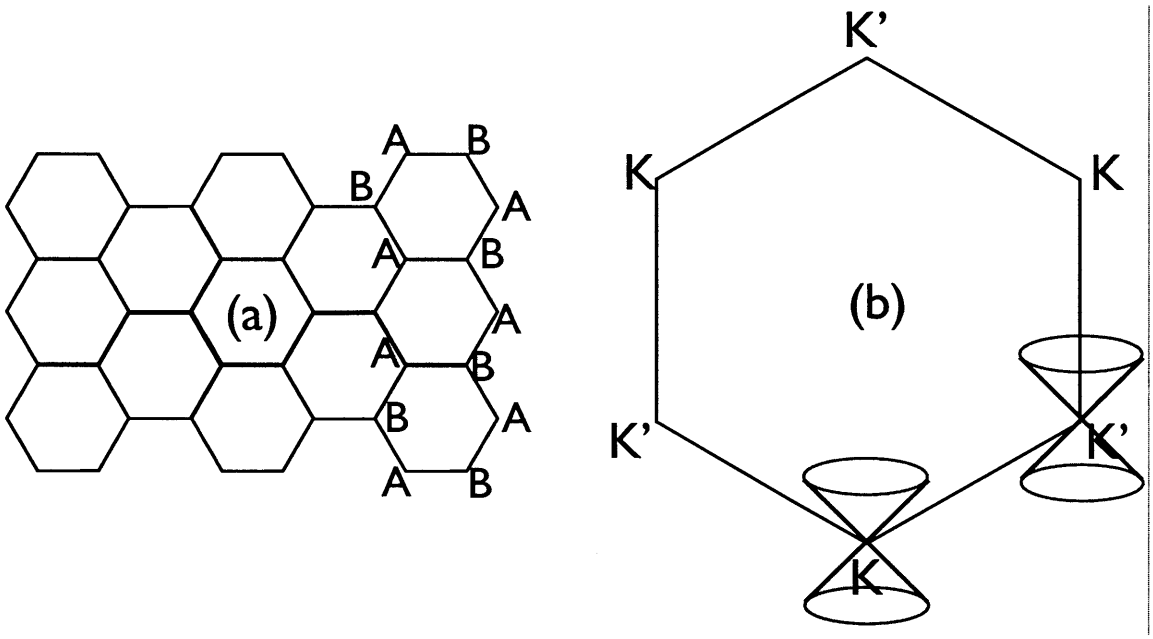

Figure 1-1: (a) Graphene consists of a honeycomb lattice of carbon atoms. The honeycomb lattice can be thought of as two interpenetrating triangular sublattices, labelled A and B. The A and B sublattice labels have been indicated on part of the honeycomb lattice. (b) Momentum space for graphene can be represented on a plane as a hexagon with opposite edges identified (momentum is only well defined up to a reciprocal lattice vector). The region inside the hexagon is known as the first Brillouin zone. The Brillouin zone has two inequivalent corners, conventionally labelled K and K'. At half filling, there are gapless states at the points K and K' only. The spectrum close to these 'Dirac points' is linear, with energy $\varepsilon \approx vk$, where v is the Fermi velocity and k is the distance to the nearest Dirac point. This spectrum takes the form of the famous 'Dirac cone,' drawn above in blue.

1.1 Graphene: structure and electronic properties

Graphene consists of a two dimensional array of carbon atoms arranged in a honeycomb lattice. The discovery of graphene [10] came as a surprise to the condensed matter community, since there is a theorem in statistical mechanics which states that two dimensional crystals cannot exist at non-zero temperature [6]. This is because the Debye-Waller factor (which measures the disordering effect of thermal fluctuations) is logarithmically divergent in two dimensions [6]. However, the statistical mechanical theorem strictly only applied to samples that are infinitely large. For a crystal of finite size, the logarithmic divergence in the Debye-Waller factor is cut off by the finite system size, and micron sized samples of graphene can therefore exist, and can be measured in the laboratory.

I now make some brief comments on carbon chemistry in graphene (for details, see [35, 39]). The carbon atoms in graphene are sp_2 hybridised, with the s, p_x and p_y orbitals lying in the graphene plane, and the p_z orbitals normal to the graphene plane. Carbon has four valence electrons per atom, three of which go into the sp_2 hybridised system, with the fourth going into the p_z system. The electrons that go into the sp_2 orbital system form strong σ bonds. These control the structural properties of graphene, but are irrelevant for the low energy electronic properties. The low energy electronic properties are controlled by π bonding in the p_z orbital system.

If I neglect electron-electron interactions, then the low energy electronic physics consists of electrons hopping from site to site through the p_z orbital system. This is most straightforwardly described in a tight binding model

$$H_0 = \sum_{ij} t_{ij} \psi_i^\dagger \psi_j \tag{1.1}$$

where ψ_i annihilates an electron on site i, and t_{ij} is the amplitude to hop from site i to site j. It is sufficient to restrict our attention to nearest neighbor hopping only, since further neighbor hopping is much weaker than nearest neighbor hopping. The nearest neighbor tight binding Hamiltonian is diagonal in momentum space. For electrons

moving in a periodic potential, momentum is only well defined up to reciprocal lattice vectors, where the reciprocal lattice vectors $\mathbf{P}_{1,2,3}$ are

$$\mathbf{P}_2 = (0, 4\pi/\sqrt{3a}), \quad \mathbf{P}_{1,3} = (\pm 2\pi/(3a), -2\pi/\sqrt{3a}). \tag{1.2}$$

where a is the carbon-carbon spacing. Momentum space is thus a two dimensional surface with a complicated topology, which can be represented on the plane as a regular hexagon with opposite edges identified. The area inside the hexagon is known as the (first) Brillouin zone, and it is sufficient to diagonalize the Hamiltonian within the Brillouin zone.

The unit cell for the honeycomb lattice contains two sites, conventionally labelled A and B. The tight binding Hamiltonian in momentum space thus takes the form of a 2×2 matrix, $H = \sum_{\mathbf{p}} \psi^\dagger_{\mathbf{p}} H_0(\mathbf{p}) \psi_{\mathbf{p}}$, where $\mathbf{p}$ is a wavenumber and $\psi_{\mathbf{p}}$ is a two component spinor $\psi_{\mathbf{p}} = (c^A_{\mathbf{p}}, c^B_{\mathbf{p}})$, where $c^\alpha_{\mathbf{p}}$ annihilates a particle on the α sublattice with wavenumber $\mathbf{p}$. The Hamilonian $H_0(\mathbf{p})$ is defined by

$$H_0(\mathbf{p}) = \begin{pmatrix} 0 & t_{\mathbf{p}} \\ t^*_{\mathbf{p}} & 0 \end{pmatrix}; \qquad t_{\mathbf{p}} = t_1 \Big[e^{ip_x a} + 2e^{-ip_x a/2} \cos\Big(\frac{\sqrt{3} p_y a}{2}\Big)\Big] \tag{1.3}$$

where, $t_1 \approx 3eV$ is the nearest neighbor hopping amplitude (sometimes denoted simply as t) and $a = 0.142nm$ is the carbon-carbon spacing in graphene [12]. Henceforth, I set $a = 1$ for simplicity. The above Hamiltonian can be straightforwardly diagonalized, and has eigenvalues $\varepsilon(\mathbf{p}) = \pm|t_{\mathbf{p}}|$, where [12]

$$|t_{\mathbf{p}}| = t_1 \sqrt{1 + 4\cos\frac{p_y\sqrt{3}}{2}\cos\frac{3p_x}{2} + 4\cos^2\frac{p_y\sqrt{3}}{2}} \tag{1.4}$$

Note that the spectrum is particle-hole symmetric about $\varepsilon = 0$.

Now when graphene is undoped, each carbon atom contributes one electron to the p_z orbital system, which is sufficient to fill exactly half the states. Since the spectrum is symmetric about $\varepsilon = 0$, it follows that for undoped graphene, the chemical potential μ must lie at zero energy, with all negative energy states being filled, and all positive

energy states unfilled. The dispersion relation (1.4) has zero energy solutions only at two in-equivalent points (conventionally labelled $\mathbf{K}$ and $\mathbf{K}'$), which are the two in-equivalent corners of the hexagonal Brillouin zone (Fig. 1-1) (corners that are connected by a reciprocal lattice vector represent the same point). In the vicinity of the Brillouin zone corners, $t_{\mathbf{p}}$ behaves as $t_{\mathbf{p}\approx\mathbf{K}} = \hbar v[(p_x - K_x) + i(p_y - K_y)] + O(|\mathbf{p}-\mathbf{K}|^2)$ and $t_{\mathbf{p}\approx\mathbf{K}'} = -\hbar v[(p_x - K'_x) - i(p_y - K'_y)] + O(|\mathbf{p}-\mathbf{K}'|^2)$, with $v \approx 10^6 ms^{-1}$ being the Fermi velocity for graphene [11]. Henceforth, I set $\hbar = 1$ and define $\mathbf{k} = \mathbf{p} - \mathbf{K}$, $\mathbf{k}' = \mathbf{p} - \mathbf{K}'$. Thus, in the vicinity of the $\mathbf{K}$ and $\mathbf{K}'$ points, the Hamiltonian takes the form

$$H_0(\mathbf{p} \approx \mathbf{K}) = \begin{pmatrix} 0 & v(k_x + ik_y) \\ v(k_x - ik_y) & 0 \end{pmatrix};$$
$$H_0(\mathbf{p} \approx \mathbf{K}') = \begin{pmatrix} 0 & -v(k'_x - ik'_y) \\ -v(k'_x + ik'_y) & 0 \end{pmatrix} \tag{1.5}$$

where $\mathbf{k}$ and $\mathbf{k}'$ are the displacements from the $\mathbf{K}$ and $\mathbf{K}'$ points respectively. The low energy spectrum is linear and isotropic, $\varepsilon_{\mathbf{k}} = \pm v|\mathbf{k}|$ and $\varepsilon_{\mathbf{k}'} = \pm v|\mathbf{k}'|$, and looks like two double-cones in momentum space (Fig. 2-1). The equation (1.5) is the Dirac Hamiltonian which appears to govern all the low energy properties of graphene. It is so called because the low energy Hamiltonian parallels the Dirac equation, with $v \approx 10^6 ms^{-1}$ replacing the speed of light, and with a sublattice pseudospin playing the role of real spin.

This non-interacting Hamiltonian should be supplemented by electron-electron interactions. The electron-electron interactions are most conveniently expressed in real space, and include both short range (contact) four fermion interactions, and also long range ($1/r$) Coulomb interactions. It has been established in theoretical calculations [40, 11] that contact interactions do not qualitatively alter the low energy physics of graphene if they are weaker than a critical value, although they can open a gap in the spectrum if they exceed a critical interaction strength. Experimentally, no gap is observed, so the contact interactions are assumed to be subcritical [11].

Meanwhile, the strength of Coulomb interactions is controlled by a dimensionless

constant $\alpha' = e^2/\hbar v$, which is analogous to the fine structure constant, but with the Fermi velocity replacing the speed of light. This graphene fine structure constant $\alpha' \approx 2$, thus it is not clear if the non-interacting approach is appropriate to describe graphene. However, it has been established [11] that for sufficiently weak α', the low energy properties of graphene are qualitatively unaltered from the non-interacting model, save for a logarithmic renormalization of the Fermi velocity (which grows bigger at low energies). Whether the physical value $\alpha' \approx 2$ is small enough for this 'weak coupling' description to hold is not clear. However, no significant departure from the weak coupling description has been observed experimentally (despite an enormous experimental effort), and thus it has been widely accepted that single layer graphene is weakly coupled. The reason why interaction effects are so weak in single layer graphene can be traced back to the low density of states $N(\varepsilon)$, which vanishes as $N(\varepsilon) \sim \varepsilon$ at low energies.

To access strong coupling physics in graphene, it is therefore necessary to get around the vanishing density of states. One way to sidestep the vanishing density of states is to dope graphene. At small doping levels, graphene is well described by the 'Dirac Hamiltonian' (1.5), and the Fermi surface of the non-interacting theory consists of two small circles centered on the $\mathbf{K}$ and $\mathbf{K}'$ points (the Fermi surface is the surface in momentum space which separates occupied and unoccupied states). However, at very large levels of doping, when the π band system is nearly empty (full), the system is analogous to a two dimensional electron gas (hole gas), and has a Fermi surface that consists of a single circle centered at zero momentum. At some intermediate doping level, there must be a topological transition from a one piece Fermi surface to a two piece Fermi surface, and at such a topological transition, the density of states must diverge [5]. The strong coupling physics that arises in the vicinity of this divergent density of states will be addressed in the first chapters of this thesis. An alternative way to get around the vanishing density of states is to change the system that is studied, and to study instead bilayer graphene. This system will be discussed in the next section.

1.2 Bilayer graphene

Bilayer graphene (BLG) consists of two graphene layers chemically bonded together. The BLG lattice has a four site unit cell - one site each from the A and B sublattices on the upper and lower layer, which I refer to as the $A1$, $B1$, $A2$ and $B2$ sublattices respectively. The $A1$ and $B2$ sites lie on top of each other in the Bernal stacking, and are chemically bonded, whereas the $A2$ and $B1$ sites do not lie on top of each other, and are not bonded. For undoped BLG the chemical potential also lies at zero energy, and there are zero energy states at two in-equivalent points (the $\mathbf{K}$ and $\mathbf{K}'$ points), just like in single layer graphene (SLG). However, the band crossing at these points is quadratic and not linear (i.e. the low energy dispersion is $\varepsilon = \pm k^2/2m$, where $m \approx 0.05 m_e$ is the band mass and m_e is the free electron mass). This quadratic band crossing is unstable to arbitrarily weak electron-electron interactions, unlike the linear band crossing in SLG.

One way to understand the instability of the quadratic band crossing is as follows. Consider promoting a single electron from the valence band to the conduction band, thus forming a particle-hole pair. Since the particle and hole are oppositely charged there will be an attractive interaction between them. If the low energy dispersion is quadratic, then this particle-hole pair can be approximately described by a two-dimensional two particle Schrodinger equation, which is known to have bound states for arbitrarily weak attractive interactions. It thus follows that the system can lower its energy by promoting particles from the valence band to the conduction band, which means that the filled Fermi sea is manifestly unstable. (Whether the leading instability is to particle-hole pair production or in some other channel cannot be deduced from this argument). I thus conclude on very general grounds that a spontaneously ordered nontrivial ground state must arise in BLG.

I now present the Hamiltonian for bilayer graphene, and discuss the relative importance of the various terms. The general Hamiltonian in the absence of any external

electric and magnetic fields can be written as a sum over lattice sites i and j

$$H = \sum_{ij} \psi_i^\dagger t_{ij} \psi_j + \frac{1}{2} V_{ij} n_i n_j \tag{1.6}$$

where t_{ij} represents the tight-binding hopping matrix element between sites i and j, and V_{ij} represents a general 'density-density' interaction $V(\mathbf{r}_i - \mathbf{r}_j)$, which has a long range Coulomb component in addition to short range lattice scale components. Further theoretical progress depends crucially on the relative importance of the tight binding and interaction terms. A non-interacting model that sets $V_{ij} = 0$ adequately describes the observed transport physics in bilayer graphene on energy scales greater than a few meV (and at all doping levels other than charge neutrality) [11, 12]. Since the characteristic scale for the tight binding Hamiltonian is $\approx 3eV$, and the scale at which departures from non-interacting behavior become significant is $\approx 3meV$, most theoretical analyses assume that interactions are weak, and treat them perturbatively. I will adopt this weak coupling perspective in this thesis, commenting on possible weaknesses of the approach as and when necessary.

In the spirit of the weak coupling approach, I first discuss the non-interacting Hamiltonian, before moving on to discuss the interactions. Upon going to momentum space, the tight binding Hamiltonian becomes a four-by-four matrix in the space of Bloch functions $(\psi_1, \psi_2, \psi_3, \psi_4)$ which are localized on the $A1$, $B1$, $A2$ and $B2$ sublattices respectively. This non-interacting Hamiltonian takes the form :

$$H_0(\mathbf{p}) = \begin{bmatrix} 0 & t_{\mathbf{p}} & 0 & t_3(\mathbf{p}) \\ t_{\mathbf{p}}^* & 0 & E_0 & 0 \\ 0 & E_0 & 0 & t_{\mathbf{p}} \\ t_3^*(\mathbf{p}) & 0 & t_{\mathbf{p}}^* & 0 \end{bmatrix}, \quad E_0 \approx 0.4\,\mathrm{eV}, \tag{1.7}$$

where $t_{\mathbf{p}}$ was defined in Eq.(1.3). Note that $t_{\mathbf{p}}$ vanishes at the K and K' points, behaving as vp_+ near point K and as $-vp_-$ near point K', where $p_\pm = p_x \pm ip_y$ and $v \approx 10^6 ms^{-1}$ is the Fermi velocity for graphene [11]. Meanwhile, the term $E_0 \approx 300meV$ reflects dimerization of the $|A1\rangle$ and $|B2\rangle$ sites (which are directly

on top of each other), and the term $t_3(\mathbf{p})$ reflects the 'trigonal warping' arising from direct hopping between $|B1\rangle$ and $|A2\rangle$ sites. It also vanishes at the K and K' points, behaving as $v_3 p_-$ near point K and as $v_3 p_+$ near the point K'. Note that $v_3/v \approx 0.1$, [41], so trigonal warping represents only a small perturbation to the tight binding Hamiltonian.

The specrum of the Hamiltonian (8.23) features four bands. If we set the small perturbation $t_3 = 0$, then we find that the band energies are given by

$$\varepsilon^2(\mathbf{p}) = |t_\mathbf{p}|^2 + \frac{1}{2}E_0^2 \pm \frac{1}{2}E_0^2\sqrt{1 + 4|t_\mathbf{p}|^2/E_0^2}. \tag{1.8}$$

Near the points K and K', this gives two massless Dirac bands $\varepsilon_{1,2}(\mathbf{p})$ that cross at zero energy, and two high-energy bands $\varepsilon_{3,4}(\mathbf{p}) \approx \pm E_0$. This spectrum acquires small corrections from the t_3 term, which we will discuss below.

The low energy physics near charge neutrality is dominated by the low energy states. One can therefore restrict oneself to the regions in momentum space near the K and K' points, where there are gapless states. Moreover, one can project out the high energy bands $\varepsilon_{3,4}$ to obtain an effective two band Hamiltonian [12] for each valley K and K', which takes the form

$$H_{0,K} = \begin{pmatrix} 0 & \frac{p_+^2}{2m} + v_3 p_- \\ \frac{p_-^2}{2m} + v_3 p_+ & 0 \end{pmatrix}, H_{0,K'}(\mathbf{p}) = H_{0,K}^*(-\mathbf{p}), \tag{1.9}$$

where $m \approx 0.05 m_e$ and m_e is the free electron mass. This Hamiltonian provides a good description for BLG on energy scales less than $\approx 200meV$ - above this energy scale the higher bands must also be taken into account. The Hamiltonian is independent of spin. Moreover, the low energy bands that constitute the Hilbert space of this effective Hamiltonian have weight on the $|B1\rangle$ and $|A2\rangle$ sites only.

The effective two band Hamiltonian (1.9), diagonalized in the absence of trigonal warping ($v_3 = 0$) gives rise to energy bands with quadratic dispersion $E = \pm\frac{p^2}{2m}$. The inclusion of trigonal warping causes the quadratic band crossing to split into four linear band crossings - however this effect only manifests itself on energy scales

smaller than $1meV$ [12], whereas the non-interacting description already fails at energy scales smaller than a few meV. For this reason, the trigonal warping term is usually neglected in theoretical analyses, and an effective quadratic model consisting of Eq.(1.9) with $v_3 = 0$ is used.

The non-interacting Hamiltonian above is supplemented by electron-electron interactions.

$$H = H_0 + H_C + H_1, \tag{1.10}$$

where H_0 is defined by (1.9), H_C represents the Coulomb interactions, and H_1 represents lattice scale interactions. I have separated out the Coulomb interactions because they are long range, and thus require a different and more careful treatment.

The Coulomb interactions can be described by a many-body Hamiltonian written in terms of $\rho_{\mathbf{q}} = \sum_{\mathbf{p}} \psi^\dagger_{\mathbf{p}} \psi_{\mathbf{p+q}}$ (the density summed over layers) and $\lambda_{\mathbf{q}} = \sum_{\mathbf{p}} \psi^\dagger_{\mathbf{p}} \tau_3 \psi_{\mathbf{p+q}}$ (the density difference between layers). Here, $\psi_{\mathbf{p}}$ is an eight component spinor, with spin, valley and sublattice indices which have been suppressed for clarity. The matrix τ_3 acts in the sublattice space. Meanwhile, the resulting Coulomb Hamiltonian H_c, which incorporates a difference between interlayer and intralayer interaction [42], can be written in second quantized notation as

$$H_C = \frac{1}{2} \sum_{\mathbf{q}} V_+(q) \rho_{\mathbf{q}} \rho_{-\mathbf{q}} + V_- \lambda_{\mathbf{q}} \lambda_{-\mathbf{q}}, \tag{1.11}$$

where $V_+(q) = 2\pi e^2/\kappa q$ is the Coulomb interaction, and $V_- = \pi e^2 d/\kappa$ accounts for the layer polarization energy (here $d = 3.5\mathring{A}$ is the BLG layer separation and κ reflects dielectric screening in the substrate). For the purposes of a perturbative treatment, the densities ρ and λ should be projected onto the low energy bands (i.e. one should take into account only the densities on the $A2$ and $B1$ sublattices). Henceforth whenever I speak of densities I will implicitly be referring to the projected densities, unless specified otherwise.

Note that the long range nature of the interaction V_+ creates considerable technical difficulties. One way around these difficulties is to ignore the long range nature of the interactions entirely, and to assume all interactions are short range. Such a neglect

can be justified by appealing to metallic screening, and this approach has been used in [25, 31, 32]. A more careful approach is to take into account the RPA screening of the interaction, and then perform calculations with the RPA screened interaction [23, 24, 26, 27]. In this approach, dynamical screening effects that give the interaction a frequency and momentum dependence are important, and are responsible for the Green function acquiring an anomalous dimension, as discussed in Chapter 4. Finally, the long range nature of the interaction can be handled on a computer in a functional RG treatment, as done in [30]. These issues will be discussed further in Section 8.4.1.

Having dealt with the long range Coulomb interactions, I now consider the short range, lattice scale interactions contained in H_1. These are most naturally expressed in real space, as an onsite Hubbard interaction, a nearest neighbor interaction, etc. However, for a perturbative treatment of interactions what is needed are the interaction matrix elements in the low energy Hilbert space. This means the short range interactions must also be expressed in momentum space.

The low energy single particle states are Bloch states near one of the band crossing points, which can be denoted as $|\varphi_{\mathbf{k},l}\rangle$, where $l = 1...8$ is a super-index that tracks the spin, valley, and sublattice, and $\mathbf{k}$ is the momentum relative to the band crossing point. Since short range interactions are dispersionless in momentum space, I drop the momentum labels, and simply denote the low energy states as $|\varphi_l\rangle$. It is convenient to define the operator $\hat{\psi}$, which acts on the vacuum as $\hat{\psi}^\dagger|0\rangle = \sum_l |\varphi_l\rangle$. The short range interaction Hamiltonian may then be written as

$$H_1 = \sum_{\alpha\beta} g_{\alpha\beta} H'_{\alpha\beta} \tag{1.12}$$

where $g_{\alpha\beta}$ are coupling constants, and

$$H'_{\alpha\beta} = (\hat{\psi}^\dagger M_\alpha \hat{\psi})(\hat{\psi}^\dagger M_\beta \psi). \tag{1.13}$$

In this expression, the $M_{\alpha(\beta)}$ are matrices in the eight dimensional spin-valley-sublattice space.

The allowed couplings $g_{\alpha\beta}$ are restricted by lattice symmetries, and by the requirements that spin and valley index must be conserved (spin conservation follows from spin rotation invariance of the Hamiltonian, and valley conservation follows from momentum conservation). After using exact symmetries and Fierz identities to restrict and organize the interactions, it emerges [25] that there are nine distinct independent short range coupling constants in the low energy Hilbert space. The full interacting Hamiltonian is thus given by (1.10), where H_1 is given by (1.12), and the sum goes over the nine independent coupling constants.

All theoretical approaches agree that the quadratic band crossing (with $v_3 = 0$) is unstable even to arbitrarily weak interactions, and at sufficiently low energy scales the spectrum undergoes a dramatic reconstruction that spontaneously breaks one or more symmetries of the Hamiltonian. The origin of this instability is rooted in the existence of bound states for arbitrarily weak attractive interactions. It has been established [25] that the leading weak coupling instability for purely short range repulsive interactions is to a gapless nematic state. A fully rigorous analysis for long range interactions has not yet been conducted, although one attempt to analyse the problem with long range interactions is presented in Chapter 7. Meanwhile, experimentally there is now overwhelming evidence for a spontaneously ordered ground state (Chapter 8). However, the precise nature of the ground state is at present unclear - the different candidate states will be discussed in Chapter 8. In Chapter 8 I will also discuss how the nature of the ground state may be determined experimentally.

I close this section by commenting on the effect of external electric and magnetic fields. An external electric field E applied perpendicular to the two layers enters by making the chemical potential on the two layers different - it adds a term $\frac{1}{2}eEd\tau_3$ to the non-interacting Hamiltonian (1.9), where τ_3 is a Pauli matrix in sublattice space, e is the electronic charge, and d is the interlayer spacing. This opens a gap eEd in the spectrum. Meanwhile, an external magnetic field applied perpendicular to the BLG enters the Hamiltonian in multiple ways. Firstly, it couples to the orbital degrees of freedom - the orbital effect of magnetic fields can be incorporated through minimal substitution $\mathbf{p} \rightarrow \mathbf{p} - e\mathbf{A}$. The magnetic field also introduces a Zeeman splitting

between the two spin species, $\mu_B B\sigma_3$, where σ_3 is the appropriate Pauli matrix in spin space. Finally, a magnetic field can also introduce a 'valley Zeeman splitting' - such a term lies beyond the minimal substitution approach, and requires a full tight binding analysis [46]. However, the spin and valley Zeeman splittings are inversely proportional to the free electron mass, whereas the orbital coupling energy is set by the cyclotron frequency, which is inversely proportional to the band mass. Since the band mass is much lower than the free electron mass, $m_e/m \approx 20$, it follows that the dominant effect of magnetic field is on the orbital physics.

1.3 Symmetries in bilayer graphene

An understanding of the symmetry structure of BLG enables the classification of interaction matrix elements, making a theoretical analysis possible. It also allows a classification of the various possible broken symmetry states, and facilitates understanding of the experimental signatures. Therefore, I now survey the various symmetries exhibited by the Hamiltonian of BLG. Some of the symmetries are exact, such as time reversal symmetry, and a three-fold rotation symmetry, whereas other higher symmetries emerge from a low energy approximation.

I first discuss the symmetries of the non-interacting Hamiltonian, and then discuss the symmetries of the interaction. This is appropriate since interactions are being treated perturbatively. Moreover, I concentrate on the effective two band non-interacting Hamiltonian that is obtained by projecting out the high energy states (1.9). It is useful to define the Pauli matrices τ, η and σ, acting in the sublattice, valley and spin spaces respectively. The non-interacting Hamiltonian may then be written as $H_0 = \mathrm{diag}(H_{K\uparrow}, H_{K\downarrow}, H_{K'\uparrow}, H_{K'\downarrow})$, where

$$H_{K\uparrow} = H_{K\downarrow} = (\frac{p_+^2}{2m} + v_3 p_-)\tau_+ + (\frac{p_-^2}{2m} + v_3 p_+)\tau_-. \tag{1.14}$$

The Hamiltonian in the K' valley may be obtained by applying $H_{K'}(\mathbf{p}) = H_K^*(-\mathbf{p})$ (Eq.1.9). Here $\tau_\pm = \tau_1 \pm i\tau_2$, and τ_+ takes an electron from the B2 sublattice to the

A1 sublattice, and τ_- takes an electron from the A1 sublattice to the B2 sublattice.

Bilayer graphene displays a number of **exact symmetries**, which are symmetries of the interaction terms as well as of the non-interacting Hamiltonian. In particular the full Hamiltonian is invariant under time reversal (T) and under parity inversion (P). Time reversal involves complex conjugation, taking $\mathbf{p} \rightarrow -\mathbf{p}$, and swapping spins and valleys, $|\uparrow\rangle \rightarrow |\downarrow\rangle$ and $|K\rangle \rightarrow |K'\rangle$. In the spin space $T^2 = -1$, whereas in the valley space $T^2 = 1$. Parity inversion involves taking $\mathbf{p} \rightarrow -\mathbf{p}$, and also exchanging sublattices and valleys, $|K\rangle \rightarrow |K'\rangle$ and $A1 \rightarrow B2$. The BLG is also invariant under mirror reflection (M) in the three high-symmetry directions. Mirror reflection changes the sign of one of the two components of the momentum $(p_x, p_y) \rightarrow (p_x, -p_y)$, and also swaps sublattices $A1 \rightarrow B2$, but leaves the valley and spin degrees of freedom untouched.

Additionally, BLG exhibits an exact symmetry under a threefold lattice rotation, that will henceforth be referred to as C_3. The generator of the C_3 symmetry is $R(\theta = 2\pi/3)$, where

$$R(\theta) = \exp\left(i\theta(L_z - \tau_3\eta_3)\right) \tag{1.15}$$

with $L_z = \partial/\partial_\varphi$ the generator of spatial rotations in the plane. Thus, the C_3 symmetry involves rotating the vector $\mathbf{p}$ by $\theta = 2\pi/3$, while the sublattice pseudospin 1/2 is rotated by $-2\theta = -4\pi/3$ in the K valley, and by $2\theta = 4\pi/3$ in the K' valley. Under such a transformation, in the K valley, a term of the form $p_+^2\tau_+$ is invariant, whereas a term of the form $p_-\tau_+$ picks up a factor of $e^{-2\pi i} = 1$, and is thus also left invariant. Invariance in the K' valley follows similarly, and the full Hamiltonian is thus seen to be unchanged under $2\pi/3$ rotation. Finally, BLG is invariant under $SU(2)$ spin rotations, and also under $U(1)$ valley rotations (i.e. giving a relative phase to states in the two valleys).

It is useful to introduce, in additon to exact symmetries, the notion of **approximate symmetries**. While Eq.1.9 is the full non-interacting Hamiltonian for BLG, not all terms in this Hamiltonian are of equal importance. As discussed previously, the trigonal warping term is weak, manifesting itself only on energy scales lower than

the energy scales for spontaneous symmetry breaking, and thus can be neglected in a first approximation. When trigonal warping is neglected, the exact threefold spatial rotation symmetry (1.15) gets promoted to a continuous rotation symmetry, with the Hamiltonian (7.1) invariant under rotation (1.15) by any θ, not just $\theta = \pm 2\pi/3$. This continuous rotation symmetry is respected also by the interaction terms in (1.10). Additionally, the SU(2) spin rotation symmetry, and the U(1) valley rotation symmetries of the non-interacting Hamiltonian become part of a larger approximate SU(4) symmetry, discussed in detail in [34]. To manifest this SU(4) symmetry, I make a basis transformation that interchanges sublattices in the valley K'. After this basis transformation, the non-interacting Hamiltonian (setting $v_3 = 0$), becomes

$$H_0 = \left(\frac{p_+^2}{2m}\tilde{\tau}_+ + \frac{p_-^2}{2m}\tilde{\tau}_-\right) \otimes \mathcal{I}_4. \tag{1.16}$$

where $\mathcal{I}_4$ is the identity matrix in the twisted spin-valley space and the Pauli matrices $\tilde{\tau}_i$ act on the twisted sublattice space (sublattices interchanged for the K' valley only). The SU(4) invariance under rotations in the twisted spin valley space is now manifest. This enlarged SU(4) symmetry is also respected by the Coulomb interaction V_+ in (1.10), although not by the 'capacitance energy' interaction V_-. Furthermore, only three out of the nine independent couplings in (1.12) respect this SU(4) symmetry. Thus, if the six $SU(4)$ non-invariant bare couplings in (1.12) and the interaction V_- are initially set to zero, then they are not generated at any order in perturbation theory. This trick was exploited to simplify the theoretical analysis in [24, 31], and it provides a useful toy model for BLG, although a detailed understanding of the phase structure requires consideration of the full set of interactions, including $SU(4)$ non-invariant couplings.

1.4 Main results of this thesis

In this section I provide an overview of the main results from this thesis.

1.4.1 Chiral superconductivity from repulsive interactions in strongly doped single layer graphene

In Chapter 2, I consider graphene doped to a Van Hove singularity in the density of states. The divergent density of states guarantees the emergence of non-trivial ordered states, even for infinitesimally weak bare interactions. I show using a renormalization group method that superconductivity dominates over all competing orders for any choice of weak repulsive interactions. Thus, I predict that at this doping level, graphene should superconduct. Superconductivity develops in a doubly degenerate, spin singlet channel, and a mean field calculation indicates that the superconductivity is of a chiral $d + id$ type. Chiral superconductivity involves a pairing gap that winds in phase around the Fermi surface, breaking time reversal symmetry. Chiral superconductors have a rich phenomenology which is highly desirable for nanoscience applications, but there are as yet no experimentally known examples of chiral d-wave superconductivity. In this chapter, I predict that doped graphene can provide experimental realization of d-wave chiral superconductivity.

This work was published in [15]. Experiments are underway to dope graphene to this level, and it may soon be possible to test the theoretical prediction of chiral d-wave superconductivity.

1.4.2 Spin density wave physics in strongly doped single layer graphene

While superconductivity is the leading instability when graphene is doped to the Van Hove point, a spin density wave (SDW) instability is a close second. When graphene is doped close to (but not exactly to) the Van Hove point, the SDW instability can even become dominant. In chapter 3, I consider the nature of the SDW state.

First, I argue that the preferred finite temperature SDW phase (within a saddle point calculation) is a uniaxial SDW phase whose ordering pattern breaks $O(3) \times Z_4$ symmetry and corresponds to an eight site unit cell with non-uniform spin moments on different sites. This state is a half-metal – it preserves the full original Fermi

surface, but has gapless charged excitations in one spin branch only. It allows for electrical control of spin currents, which is desirable for nano-science applications.

The second part of Chapter 3 is motivated by the observation that it is not possible to break $O(3)$ symmetry at finite temperature in two dimensions. Thus the broken $O(3)$ symmetry associated with the uniaxial SDW phase must be restored when thermal fluctuations are taken into account. However, the uniaxial SDW phase also breaks a discrete Z_4 symmetry, and it is possible to break discrete symmetries at finite temperature in two dimensions. One might therefore suspect that the 'true' finite temperature state of the system is a SDW state that breaks Z_4 symmetry but not $O(3)$ symmetry. I show that this is indeed what happens, and a Z_4 breaking paramagnetic state results. Unlike other emergent paramagnetic phases in itinerant and localized-spin systems, this state preserves the rotational symmetry of the lattice but breaks its translational symmetry, giving rise to a super-lattice structure that can be detected by STM. I show that spin fluctuations are also enhanced in this emergent phase, leaving distinctive signatures in the magnetic spectrum that can be probed experimentally.

This work was reported in [16] and in [17]. Experimental efforts to dope graphene to the vicinity of the Van Hove point are currently underway, and it may soon be possible to experimentally look for this SDW state.

1.4.3 Electron Interactions in Bilayer Graphene: Marginal Fermi Liquid Behavior and Zero-Bias Anomaly

In Chapter 4, I turn my attention to bilayer graphene. I analyze the many-body properties of bilayer graphene (BLG) at charge neutrality, taking into account long range interactions between electrons. The long range Coulomb interaction is treated in a random phase approximation, taking into account dynamical screening effects. Crucially, the dynamically screened interaction retains some long range character, resulting in enhanced ($\log^2$) renormalization of key quantities.

I treat the $\ln^2$ renormalizations arising from dynamically screened interactions

in a perturbative renormalization group formalism. I carry out the perturbative renormalization group calculations to one loop order, and find that BLG behaves to leading order as a marginal Fermi liquid. Interactions produce a log squared renormalization of the quasiparticle residue and the interaction vertex function, while all other quantities renormalize only logarithmically. The cancellation of higher log divergences is explained in terms of symmetries.

I solve the RG flow equations for the Green function with logarithmic accuracy, and find that the quasiparticle residue flows to zero under RG. At the same time, the gauge-invariant quantities, such as the compressibility, remain finite to $\log^2$ order, with subleading logarithmic corrections. The key experimental signature of this marginal Fermi liquid behavior is a strong suppression of the tunneling density of states, which manifests itself as a zero bias anomaly in tunneling experiments in a regime where the compressibility is essentially unchanged from the non-interacting value.

The central prediction of this Chapter is that there should be a zero bias anomaly in the tunneling density of states which manifests itself on a characteristic scale of $\approx 10 - 100meV$, whereas the more striking departures from non-interacting behavior occur only on scales $\approx 1meV$. This zero bias anomaly at high energy scales has been observed in experiments [19], although the significance of these results has not yet been widely appreciated in the experimental community. The work reported in this chapter was published in [43]

1.4.4 Spontaneous gap opening in bilayer graphene

In this chapter, I consider the nature of the strongly ordered state that should arise at the lowest energies in BLG. In Section 1, I consider the possibility that dynamically screened Coulomb interactions may cause the spectrum to develop a band gap. I work within a mean field approximation, taking into account self energy effects, and I show that spontaneous gap opening lowers the free energy. Minimization of the free energy allows us to estimate the size of the gap. In this manner, I obtain a characteristic gap scale of a few meV, which is in good agreement with experiments. This work

was reported in [23]

1.4.5 Quantum anomalous Hall state in bilayer graphene

In this chapter, I show that due to the non-trivial Berry phase in BLG, any gapped states must have interesting topological properties. I also consider the competition between the various possible gapped states. I show that whereas all the gapped states are degenerate at a mean field level, the inclusion of thermal and quantum fluctuations lifts the degeneracy. Working within a 'saddle point plus quadratic fluctuations' approximation, I show that thermal fluctuations favor a state that breaks $SU(4)$ spin valley symmetry, such as a Quantum Spin Hall (QSH) or antiferromagnetic state. Meanwhile, quantum zero point fluctuations appear to favor a state that preserves $SU(4)$ symmetry but breaks time reversal symmetry - this is a Quantum Anomalous Hall (QAH) state, which exhibits a spontaneous quantum Hall effect. I argue based on this analysis that if the ground state of BLG is a gapped state, then it should be a QAH state. This work was reported in [34].

1.4.6 Weak coupling renormalization group and nematic states in bilayer graphene

In this chapter I outline a perturbative renormalization group calculation that allows for an unbiased determination of the leading instability in bilayer graphene, assuming interactions are sufficiently weak. This chapter is based on unpublished work (which is similar in spirit to [25, 26]), and indicates that the leading weak coupling instability in graphene is to a gapless 'nematic' state that breaks rotation symmetry.

1.4.7 Spontaneously ordered states in bilayer graphene: summary and outlook

I begin this chapter by listing the various possible broken symmetry states that compete to be the ground state for BLG, including gapless states as well as gapped states,

and by highlighting their experimental signatures. Next, I review the experiments on bilayer graphene, and compare the experimental observations with existing theories. I point out that none of the existing theories are consistent with all the experiments (and moreover the experiments also seem to be inconsistent with each other). I comment on what experiments are needed to bring clarity to the field. I also comment on what theoretical developments are necessary to complete our understanding of BLG. Parts of this section were published in [44] and [18].

1.4.8 Quantum Hall Ferromagnetism in bilayer graphene

In this chapter, I discuss what happens when a perpendicular magnetic field is applied to BLG. The spectrum splits into Landau levels, and at particular filling factors, the partially filled Landau levels spontaneously polarise in spin and valley to gain exchange energy. I explain the essential properties of this quantum Hall ferromagnet state, and I also highlight the unusual nature of the topological defects of this state. This work was published in [33] and [45].

Bibliography

[1] P.W.Anderson, *Science.* Vol. 177, No. 4047. (Aug. 4, 1972), pp. 393-396.

[2] M. Tinkham, *Introduction to Superconductivity*, Dover Books, (2004)

[3] *Perspectives in Quantum Hall effects: novel quantum liquids in low dimensional semiconductor structures*, edited by S. Das Sarma and A. Pinczuk, John Wiley and Sons, (1997)

[4] M.L.Hasan and C.K.Kane, Topological insulators. *Rev. Mod. Phys.* **82**, 3045 (2010)

[5] N. W. Ashcroft and N. D. Mermin, *Solid State Physics*, Holt, Rinehart and Winston (1976)

[6] L.D. Landau and E.M. Lifshitz, Statistical Physics. Vol. 5 (3rd ed.). Butterworth-Heinemann (1951).

[7] X.G.Wen, *Quantum Field Theory of Many-body Systems: From the Origin of Sound to an Origin of Light and Electrons*, Oxford Graduate Texts, Oxford, 2007.

[8] T. Giamarchi, *Quantum Physics in One Dimension*, Clarendon Press (2005).

[9] J. G. Bednorz, K. A. Mueller. "Possible high TC superconductivity in the Ba-La-Cu-O system". Zeitschrift fr Physik B 64 (2): 189193. (1986)

[10] Novoselov, K. S.; Geim, A. K.; Morozov, S. V.; Jiang, D.; Zhang, Y.; Dubonos, S. V.; Grigorieva, I. V.; Firsov, A. A. "Electric Field Effect in Atomically Thin Carbon Films". Science 306 (5696): 666669. (2004).

[11] Castro Neto, A.H., Guinea, F., Peres, N.M.R., Novoselov, K.S. and Geim, A.K. The electronic properties of graphene. *Rev. Mod. Phys.* **81**, 109-162 (2009)

[12] DasSarma, S., Adam, S., Hwang, E.H. and Rossi, E. Electronic transport in two dimensional graphene. *Rev. Mod. Phys.* **83**, 407-470 (2011)

[13] D. C. Elias, et al, "Dirac cones reshaped by interaction effects in suspended graphene. " Nature Physics 7, 701704 (2011)

[14] J. Gonzalez, F. Guinea and M. A. H. Vozmediano, "Marginal-Fermi-liquid behavior from two-dimensional Coulomb interaction." Phys. Rev. B 59, R2474-R2477 (1999)

[15] R. Nandkishore, L. Levitov and A.V.Chubukov, *Nature Physics* **8** 158 (2012)

[16] R. Nandkishore, G.W.Chern and A.V. Chubukov, Phys. Rev. Lett. 108, 227204 (2012)

[17] G.W.Chern, R. Fernandes, R. Nandkishore and A.V.Chubukov, http://arxiv.org/abs/1203.5776 (2012)

[18] R. Nandkishore and L. Levitov, "Many body effects in bilayer graphene." Annual Reviews of Condensed Matter Physics. to be published (2012)

[19] G.M.Rutter *et al*, http://arxiv.org/abs/1103.2164 (2011) (unpublished)

[20] B. Feldman, J. Martin and A. Yacoby, Nature Physics 5, 889 (2009).

[21] J. Velasco et al, Nature Nanotechnology, 7, 156 (2012)

[22] F.Freitag et al, Phys. Rev. Lett. 108, 076602 (2012)

[23] R. Nandkishore and L. Levitov, Phys. Rev. Lett. 104, 156803 (2010)

[24] R. Nandkishore and L. Levitov, Phys. Rev. B 82, 115431 (2010)

[25] O. Vafek, Phys.Rev. B 82, 205106 (2010)

[26] Y. Lemonik, I.L Aleiner, C. Toke and V. I Falko, Phys. Rev. B 82, 201408 (2010)

[27] Y. Lemonik, I. L. Aleiner, V. I. Fal'ko, Phys. Rev. B 85, 245451 (2012)

[28] J. Jung, F. Zhang and A.H.MacDonald, Phys. Rev. B 83, 115408 (2011)

[29] H. Min, G. Borghi, M. Polini and A.H. MacDonald, Phys. Rev. B 77, 041407(R) (2008). Phys. Rev. B 81, 041402(R) (2010).

[30] R. Throckmorton and O. Vafek, arXiv: 1111.2076 (2011)

[31] O. Vafek and K. Yang, Phys. Rev. B 81, 041401(R) (2010).

[32] F. Zhang, H. Min, M. Polini, and A. H. MacDonald Phys. Rev. B 81, 041402(R) (2010).

[33] R. Nandkishore and L. Levitov, Phys. Scr. T 146, 014011 (2012).

[34] R. Nandkishore and L. Levitov, Phys. Rev. B 82, 115124 (2010)

[35] P. R. Wallace, Phys. Rev. **71**, 622-634 (1947).

[36] J. Martin, B.E.Feldman, R.T.Weitz, M.T.Allen and A.Yacoby, Phys. Rev. Lett. 105, 256806 (2010)

[37] A.S.Mayorov et al, Science 333(6044) pp. 860-863 (2011)

[38] R.T.Weitz, M.T.Allen, B.E.Feldman, J. Martin and A. Yacoby, Science Vol. 330 no. 6005 pp. 812-816 (2010)

[39] D.Abanin, 'Charge, Spin and Pseudospin in Graphene.' PhD. Thesis, Massachusetts Institute of Technology, (2008) and references contained therein

[40] D.V. Khveshchenko, Phys. Rev. Lett., 87, 246802 (2001)

[41] J. Cserti, A. Csordas, G. David, *Phys. Rev. Lett.* 99, 066802 (2007)

[42] J. Nilsson, A.H.Castro Neto, N. Peres and F. Guinea, Phys. Rev. B 73, 214418 (2006).

[43] R. Nandkishore and L. Levitov, Phys. Rev. B 82, 115431 (2010)

[44] R. Nandkishore and L. Levitov, Phys. Rev. Lett. 107, 097402 (2011)

[45] R. Nandkishore and L. Levitov, to be published (2012)

[46] I.A.Luk'yanchuk and A.M.Bratkovsky, Phys. Rev. Lett. 100, 176404 (2008)

Chapter 2

Chiral superconductivity from repulsive interactions in strongly doped single layer graphene

We identify graphene as a system where chiral superconductivity can be realized. Chiral superconductivity involves a pairing gap that winds in phase around the Fermi surface, breaking time reversal symmetry. We consider a unique situation arising in graphene at a specific level of doping, where the density of states is singular, strongly enhancing the critical temperature T_c. At this doping level, the Fermi surface is nested, allowing superconductivity to emerge from repulsive electron-electron interactions. We show using a renormalization group method that superconductivity dominates over all competing orders for any choice of weak repulsive interactions. Superconductivity develops in a doubly degenerate, spin singlet channel, and a mean field calculation indicates that the superconductivity is of a chiral $d + id$ type. We therefore predict that doped graphene can provide experimental realization of spin-singlet chiral superconductivity.

This work was published in R. Nandkishore, L. Levitov and A. V. Chubukov, Nature Physics **8** *158 (2012).*

Chiral superconductors feature pairing gaps that wind in phase around the Fermi surface (FS) by multiples of 2π, breaking time-reversal symmetry (TRS) and parity and exhibiting a wealth of fascinating properties [1, 2, 3]. The search for experimental realizations of chiral superconductivity greatly intensified in the last few years with the advent of topological superconductivity [4, 5, 6]. Here we show that chiral superconductivity with a $d_{x^2-y^2} \pm id_{xy}$ $(d + id)$ gap structure can be realized in graphene monolayer, a system of choice of modern nanoscience [7, 8]. We demonstrate that when graphene is doped to the vicinity of a Van Hove singularity in the density of states (DOS), repulsive electron-electron interactions induce d-wave superconductivity. Our renormalization group analysis indicates that superconductivity dominates over competing density wave orders, and also indicates that interactions select the chiral $d + id$ state over TRS-preseving d-wave states. The nontrivial topology of the $d + id$ state [1] manifests itself in exceptionally rich phenomenology, including a quantized spin and thermal Hall conductance [9].

The search for chiral superconductivity has a long history. Spin-triplet p-wave chiral superconductivity ($p_x \pm ip_y$ state) has likely been found in Sr_2RuO_4 [10], which represents a solid state analog of superfluid ^{3}He [1], but the *spin-singlet* $d + id$ state has not yet been observed experimentally. Such a state was once proposed as a candidate state for high T_c cuprate superconductors [9, 11], but later gave way to a more-conventional TRS-preserving $d-$wave state. The key difficulty in realizing a $d + id$ state is that the interactions that favor a d-wave state usually have strong momentum dependence and hence distinguish between $d_{x^2-y^2}$ and d_{xy} pairing. However, in graphene the $d_{x^2-y^2}$ and d_{xy} pairing channels are degenerate by symmetry [12, 13], opening the door to formation of a $d + id$ superconducting state.

How can superconductivity be induced in graphene? Existing proposals for superconductivity in undoped graphene rely on the conventional phonon mediated BCS mechanism [14], which leads to an $s-$wave superconductivity with low T_c values for realistic carrier densities due to the vanishing density of states of relativistic particles. However, there is an alternative route to superconductivity, wherein repulsive microscopic interactions give rise to attraction in a d-wave channel [15]. This alternative

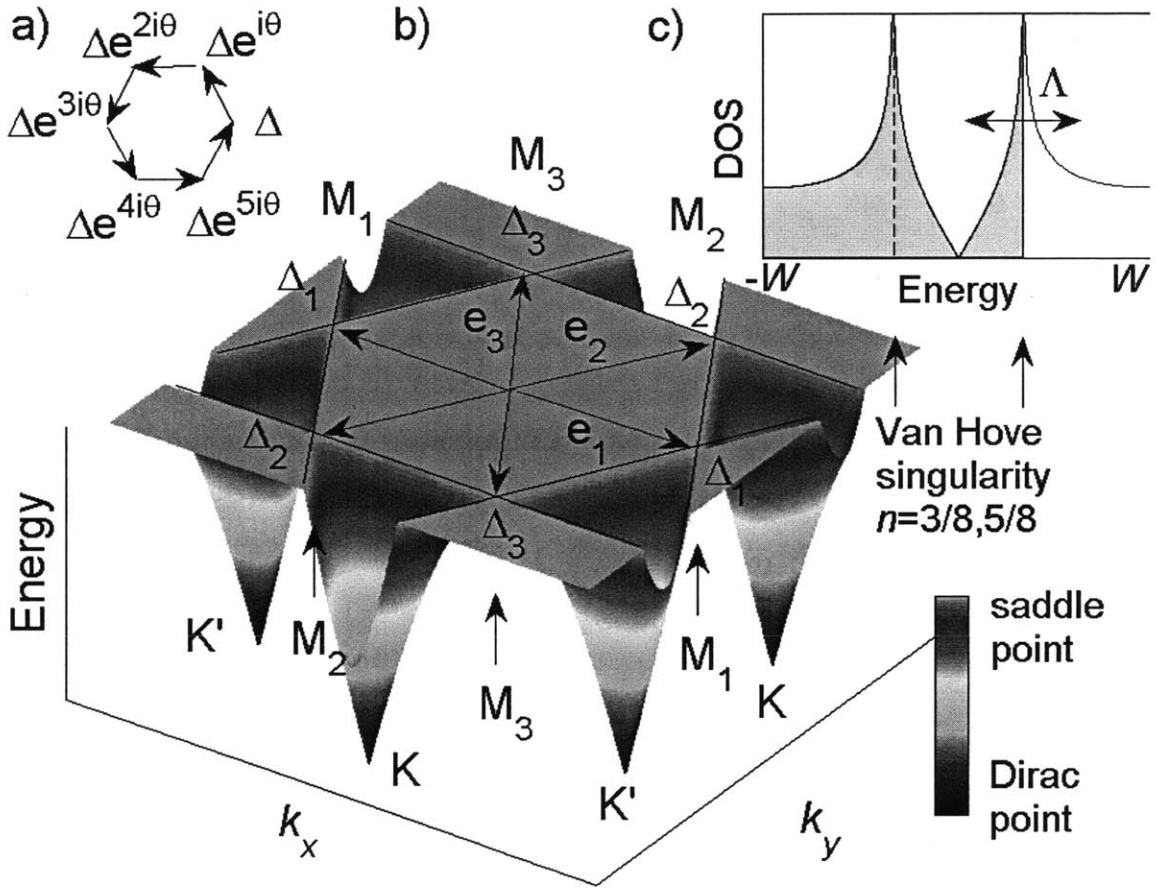

Figure 2-1: Chiral superconductivity arises when graphene is doped to the Van Hove singularity at the saddle point (M points of the Brillouin zone). a) $d + id$ pairing exhibiting phase winding around the hexagonal FS, which breaks TRS and parity ($\theta = 2\pi/3$). b) Conduction band for monolayer graphene [7]. At 5/8 filling of the π band, the FS is hexagonal, and the DOS is logarithmically divergent (c) at three inequivalent saddle points of the dispersion M_i (i=1,2,3). Their location is given by $\pm\mathbf{e}_i$, where $2\mathbf{e}_i$ is a reciprocal lattice vector. The singular DOS strongly enhances the effect of interactions, driving the system into a chiral superconducting state (a). Since the FS is nested, superconductivity competes with density wave instabilities, and a full RG treatment is required to establish the dominance of superconductivity.

route becomes viable when graphene is doped to the M point of the Brillouin zone corresponding to 3/8 or 5/8 filling of the π band (pristine graphene corresponds to 1/2 filling). At this filling factor, a logarithmic Van Hove singularity originates from three inequivalent saddle points, and the FS also displays a high degree of nesting, forming a perfect hexagon when third and higher neighbor hopping effects are neglected [7, 12] (Fig.2-1). The combination of a singular DOS and a near-nested FS strongly enhances the effect of interactions [20, 18, 19], allowing non-trivial phases to emerge at relatively high temperatures, even if interactions are weak compared to the fermionic bandwidth W. Relevant doping levels were recently achieved experimentally using calcium and potassium dopants [16]. Also, the new technique [17] which employs ionic liquids as gate dielectrics allows high levels of doping to be reached without introducing chemical disorder.

Competing orders: In systems with near-nested FS, superconductivity (SC) has to compete with charge density wave (CDW) and spin density wave (SDW) instabilities [21]. At the first glance, it may seem that a system with repulsive interactions should develop a density-wave order rather than become a superconductor. However, to analyze this properly, one needs to know the susceptibilities to the various orders at a relatively small energy, E_0, at which the order actually develops. The couplings at E_0 generally differ from their bare values because of renormalizations by fermions with energies between E_0 and W. At weak coupling, these renormalizations are well captured by the renormalization group (RG) technique.

Interacting fermions with a nested FS and logarithmically divergent DOS have previously been studied on the square lattice using the RG methods[20, 18, 19, 21], where spin fluctuations were argued to stimulate superconciductivity. However, analysis also revealed near degeneracy between SC and SDW orders. The competition between these orders is decided by subtle interplay between deviations from perfect nesting, which favor SC, and subleading terms in the RG flow, which favor SDW. In contrast, the RG procedure on the honeycomb lattice unambiguously selects SC at leading order, allowing us to safely neglect subleading terms. The difference arises because the honeycomb lattice contains three saddle points, whereas the square lat-

tice has only two, and the extra saddle point tips the delicate balance seen on the square lattice between magnetism and SC decisively in favor of superconductivity. A similar tipping of a balance between SC and SDW in favor of SC has been found in RG studies of some Fe-pnictide superconductors [22, 23].

In previous works on graphene at the M point, various instabilities were analyzed using the random-phase approximation (RPA) and mean field theory. In [12], the instability to d-wave SC was studied, whereas [24] considered a charge 'Pomeranchuk' instability to a metallic phase breaking lattice rotation symmetry, and [25, 26] considered a spin density wave (SDW) instability to an insulating phase. Within the framework of mean field theory, utilized in the above works, all of these phases are legitimate potential instabilities of the system. However, clearly graphene at the M point cannot be simultaneously superconducting, metallic and insulating. The RG analysis treats all competing orders on an equal footing, and predicts that the *dominant* weak coupling instability is to superconductivity, for any choice of repulsive interactions, even for perfect nesting. Further, the Ginzburg-Landau theory constructed near the RG fixed point favors the $d+id$ state.

The model: We follow the procedure developed for the square lattice [21] and construct a patch RG that considers only fermions near three saddle points, which dominate the DOS. There are four distinct interactions in the low energy theory, involving two-particle scattering between different patches, as shown in Fig.2-2.

The system is described by the low energy theory

$$\begin{aligned}\mathcal{L} &= \sum_{\alpha=1}^{3}\sum_{\sigma}\psi^{\dagger}_{\alpha,\sigma}(\partial_\tau - \varepsilon_{\mathbf{k}} + \mu)\psi_{\alpha,\sigma} - \sum_{\alpha=1}^{3}\sum_{\sigma,\delta}\frac{1}{2}g_4\psi^{\dagger}_{\alpha\sigma}\psi^{\dagger}_{\alpha\delta}\psi_{\alpha\delta}\psi_{\alpha\sigma} \\ &\quad - \sum_{\alpha\neq\beta}\sum_{\sigma\delta}\frac{1}{2}[g_1\psi^{\dagger}_{\alpha\sigma}\psi^{\dagger}_{\beta\delta}\psi_{\alpha\delta}\psi_{\beta\sigma} + g_2\psi^{\dagger}_{\alpha\sigma}\psi^{\dagger}_{\beta\delta}\psi_{\beta\delta}\psi_{\alpha\sigma} + g_3\psi^{\dagger}_{\alpha\sigma}\psi^{\dagger}_{\alpha\delta}\psi_{\beta\delta}\psi_{\beta\sigma}], \quad (2.1)\end{aligned}$$

where summation is over patch labels $\alpha, \beta = M_1, M_2, M_3$ and over spin labels σ, δ. Here $\varepsilon_{\mathbf{k}}$ is the tight binding dispersion, expanded up to quadratic terms about each saddle point. For example, near point M_1, the tight-binding model [27] predicts dispersion $\varepsilon_{\mathbf{k}} = 2\pi^2 a^2 t((\delta k_x)^2 - \sqrt{3}\delta k_x \delta k_y + O((\delta k)^4))$, where t is the nearest neighbor

hopping, and a is the lattice constant, and $\delta\mathbf{k} = \mathbf{k} - \mathbf{k}_{M_1}$. The chemical potential value $\mu = 0$ describes system doped exactly to the saddle point. We note that while the existence of saddle points is a topological property of the FS and is robust to arbitrarily long range hopping, the FS nesting is spoilt by third and higher neighbor hopping effects [7, 12]. Inequivalent saddle points are connected by a nesting vector $Q_{\alpha\beta} = \mathbf{e}_\alpha - \mathbf{e}_\beta$ (Fig.2-1). A spin sum is implicit in the above expression, and the interactions are assumed to be spin independent. The short-range interaction model, used in our analysis, is expected to provide a good approximation under the conditions of metallic screening arising due to the states near the FS. We further assume that screening is insensitive to the level of doping relative to the M point. While these assumptions introduce a large uncertainty into the bare values for the interactions, we will show that precise knowledge of these bare values is not required for determining the final state.

The patch structure of the interactions is restricted by momentum conservation, which allows only the four interactions in (2.1). The Umklapp interaction g_3 is allowed, because it conserves momentum modulo a reciprocal lattice vector. All four interactions in (2.1) are marginal at tree level, but acquire logarithmic corrections in perturbation theory, which come from energy scales $E < \Lambda$, where $\Lambda \approx t$ is the energy scale at which higher order corrections to the dispersion become important.

Logarithmic divergences in perturbation theory analysis indicate that the problem is well suited to study using RG. The building blocks of the RG are the susceptibilities in the particle-particle and particle-hole channels, $\Pi_{\rm pp}$ and $\Pi_{\rm ph}$, evaluated respectively at momentum transfer zero and at momentum transfer $Q_{\alpha\neq\beta}$ (Fig.2-1). Similarly to [21], we have

$$\Pi_{\rm pp}(0) = \frac{\nu_0}{4} \ln \frac{\Lambda}{\max(T,\mu)} \ln \frac{\Lambda}{T}, \quad \Pi_{\rm ph}(Q_{\alpha\neq\beta}) = \frac{\nu_0}{4} \ln \frac{\Lambda}{\max(T,\mu)} \ln \frac{\Lambda}{\max(T,\mu,t_3)}, \tag{2.2}$$

and $\Pi_{\rm ph}(0), \Pi_{\rm pp}(Q_{\alpha\neq\beta}) = \nu_0 \ln \frac{\Lambda}{\max(T,\mu)}$, where Λ is our UV cutoff (Fig.2-1) and T is the temperature. The single spin density of states at a saddle point is $\nu_0 \ln \frac{\Lambda}{\max(T,\mu)}$. The additional log factor in $\Pi_{\rm pp}(0)$ (Cooper channel) arises because $\varepsilon_{\mathbf{k}} = \varepsilon_{-\mathbf{k}}$, generic

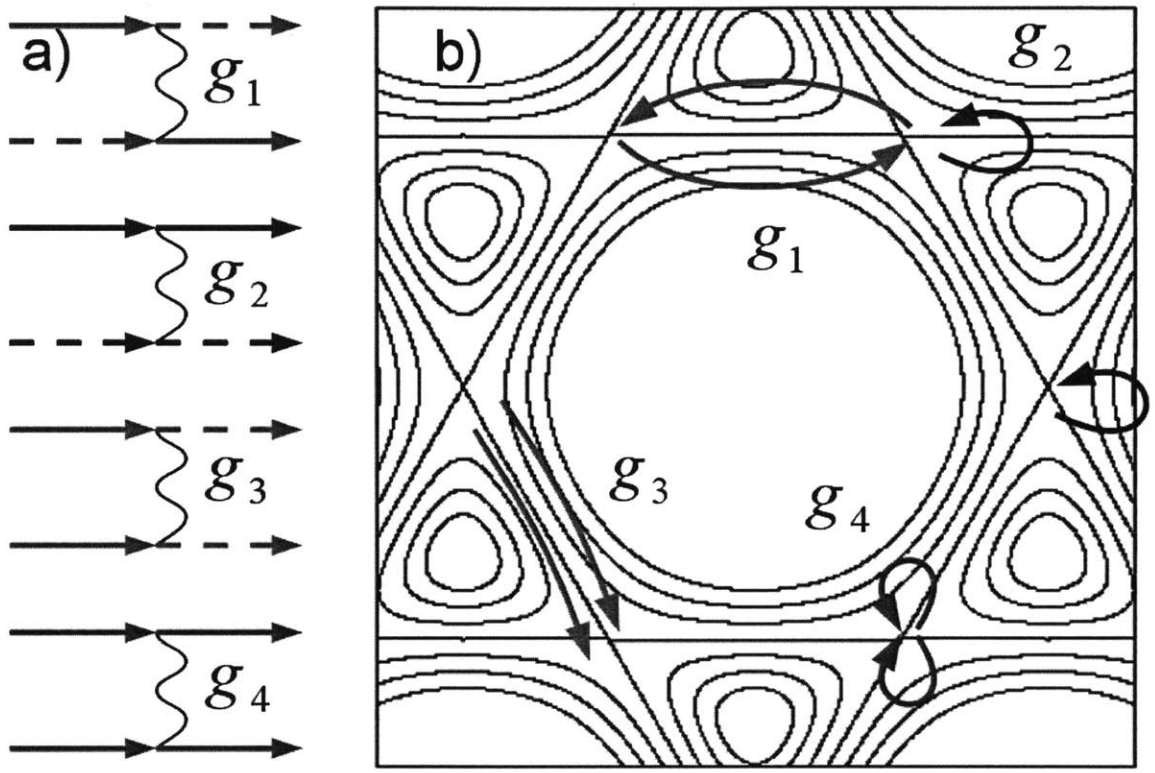

Figure 2-2: Possible interactions in the patch model. (a) Feynman diagrams representing allowed two-particle scattering processes among different patches, Eq.2.1. Solid and dashed lines represent fermions on different patches, whereas wavy lines represent interactions. (b) Pictorial representation of these scattering processes, superimposed on a contour plot of the energy dispersion. Each scattering process comes in three flavors, according to the patches involved. However, it follows by symmetry that the scattering amplitudes are independent of the patches involved, and therefore we suppress the flavor labels.

for any system with time reversal or inversion symmetry. In contrast, the additional log factor in $\Pi_{\rm ph}(Q_{\alpha\neq\beta})$ arises from nesting of the FS, and is cut in the IR by any term that spoils the nesting, such as third neighbor hopping t_3 or doping μ [12]. We assume $\max(t_3,\mu) \ll \Lambda$, so $\Pi_{\rm ph}(Q_{\alpha\neq\beta})$ and $\Pi_{\rm pp}(0)$ are of the same order under RG.

RG equations: The RG equations are obtained by extending the approach developed for the square lattice problem [20] to the number of patches $n > 2$. The number of patches matters only in diagrams with zero net momentum in fermion loops, since it is only there that we get summation over fermion flavors inside the loop. The only zero-momentum loop with a $\log^2$ divergence is in the Cooper channel. Moreover, only the g_3 interaction changes the patch label of a Cooper pair, therefore, the number of patches affects only diagrams where two g_3 interactions are combined in the Cooper channel. With logarithmic accuracy, using $y = \Pi_{\rm pp}(\mathbf{k}=0,E) = \frac{\nu_0}{4}\ln^2\frac{\Lambda}{E}$ as the RG time, we obtain the β functions

$$\begin{aligned} \frac{dg_1}{dy} &= 2d_1 g_1(g_2-g_1), & \frac{dg_2}{dy} &= d_1(g_2^2+g_3^2), \\ \frac{dg_3}{dy} &= -(n-2)g_3^2 - 2g_3g_4 + 2d_1g_3(2g_2-g_1), & \frac{dg_4}{dy} &= -(n-1)g_3^2 - g_4^2. \end{aligned} \quad (2.3)$$

Here $d_1(y) = d\Pi_{\rm ph}(Q)/dy \approx \Pi_{\rm ph}(Q)/\Pi_{\rm pp}(0)$ is the 'nesting parameter' [20, 21]. This quantity equals one in the perfectly nested limit. For non-perfect nesting, $d_1(y)$ has the asymptotic forms $d_1(y=0)=1$, $d_1(y\gg 1) = \ln|\Lambda/t_3|/\sqrt{y}$, and interpolates smoothly in between. Since the RG equations flow to strong coupling at a finite scale y_c, we treat $0 < d_1(y_c) < 1$ as a parameter in our analysis.

The β-functions, Eq.(2.3), reproduce the two-patch RG from [20] when we take $n = 2$, and neglect subleading $O(\log)$ divergent terms ($d_{2,3}(y)$ from [20]), and also reproduce for $n = 2$ the RG equations for the Fe-pnictides [22]. Graphene near the Van Hove singularity however is described by $n = 3$.

We note from inspection of (2.3) that g_1, g_2 and g_3 must stay positive (repulsive) if they start out positive. This follows because the β function for g_2 is positive definite, and the β functions for g_1 and g_3 vanish as the respective couplings go to zero. However, g_4 decreases under RG and eventually changes sign and becomes

negative. As we will see, $g_3 - g_4$ becomes large and positive under RG, driving an instability to a superconducting phase. However, the positive g_3 coupling penalizes s-wave superconductivity, so pairing occurs in a higher angular momentum (d-wave) channel.

We integrate our RG equations with $n = 3$ from starting from $g_i = g_0 = 0.1$ and modeling d_1 as $d_1(y) = 1/\sqrt{1+y}$. The results are plotted in Fig.2-3. Similar results are obtained if we just treat d_1 as a constant. The couplings diverge at a scale $y_c \approx 1/g_0$, corresponding to a critical temperature and ordering energy scale

$$T_c,\, E_0 \sim \Lambda \exp(-A/\sqrt{g_0 \nu_0}). \tag{2.4}$$

Here A is a non-universal number that depends on how we model $d_1(y)$. For $d_1 = 1$ (perfect nesting, corresponding to zero third neighbor hopping t_3), we obtain $A = 1.5$. An RPA-type estimate of g_0 is outlined in the online supplementary material. While T_c and E_0 are exponentially sensitive to g_0, thus introducing a considerable uncertainty to our estimate, a strong enhancement of characteristic energy scales relative to the BCS result is evident from Eq.(2.4).

A similar $\sqrt{g_0}$ dependence arises in the treatment of color superconductivity [28] and in the analysis of the pairing near quantum-critical points in 3D [29]. It results in a T_c that is strongly enhanced compared to the standard BCS result $T_c \sim \exp(-A'/g_0\nu_0)$. It should be noted that the enhancement of T_c in (2.4) arises from weak coupling physics. It is distinct from the high T_c superconductivity that could arise if the microscopic interactions were strong Refs.[30, 13, 31, 32].

Returning to our RG analysis, we note that near the instability threshold, $g_1, g_2, g_3 \to \infty$ and $g_4 \to -\infty$, with $-g_4 > g_3 > g_2 > g_1$. This observation may be made precise by noting that close to y_c, the interactions scale as

$$g_i(y) \approx \frac{G_i}{y_c - y} \tag{2.5}$$

Substituting into Eq.2.3, we obtain a set of polynomial equations, which may be solved for the co-efficients G_i as a function of $d_1(y_c)$. The solution is plotted in the

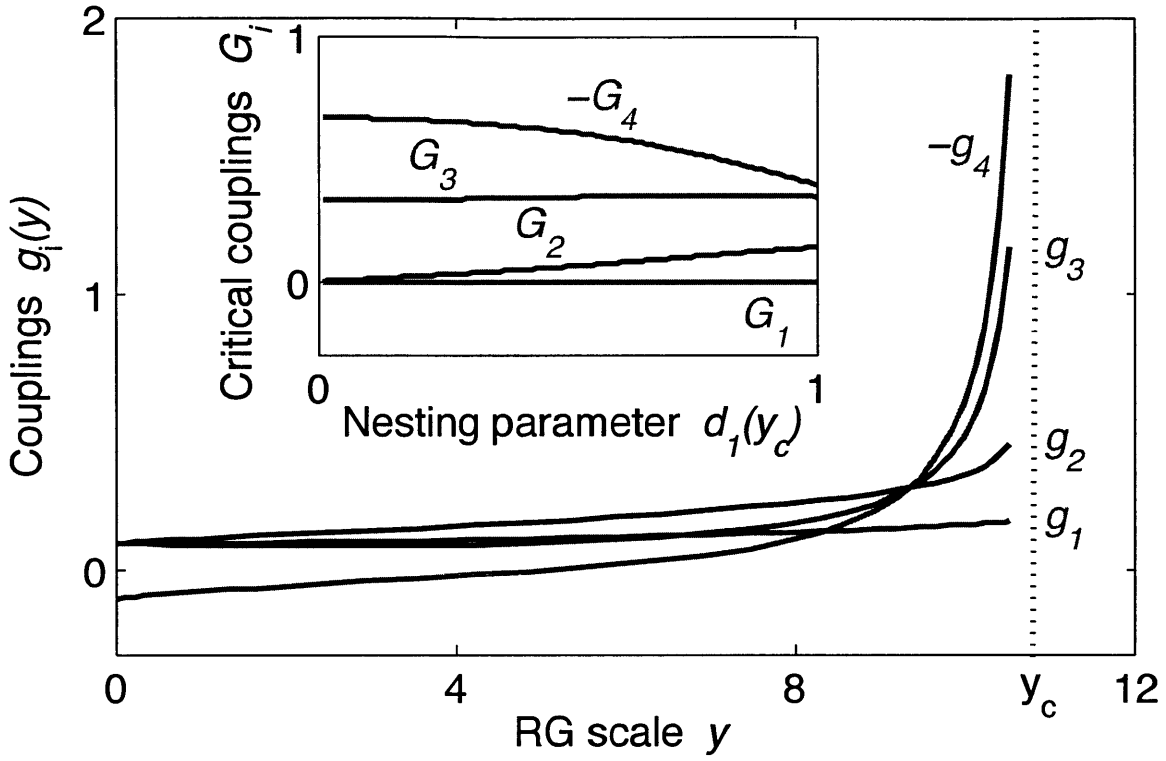

Figure 2-3: Flow of couplings with RG scale y, starting from repulsive interactions. Note that the coupling g_4 changes sign and becomes attractive, leading to a (superconducting) instability at the energy scale y_c (Eq.2.4). Inset: Critical couplings G_i (2.5) near y_c as a function of the nesting parameter at the ordering energy scale, $d_1(y_c)$. The dominance of superconductivity over spin density wave order arises because $-G_4 > G_2$ for all values of $d_1(y_c)$. *Initial conditions:* The RG flow is obtained by numerical integration of (2.3) with initial conditions $g_i(0) = 0.1$, and modeling the nesting parameter as $d_1(y) = 1/\sqrt{1+y}$. The qualitative features of the flow are insensitive to initial conditions, and to how we model d_1. The critical couplings (inset) are universal, and independent of initial conditions.

inset of Fig.2-3. Note that $-G_4 > G_3 > G_2 > G_1$ for all values of $d_1(y_c)$ satisfying $0 \leq d_1(y_c) \leq 1$. We have verified that any choice of repulsive bare couplings leads to the same limiting trajectory (see online supplementary material).

Susceptibilities: We now investigate the instabilities of the system by evaluating the susceptibilities χ for various types of order. To analyze the superconducting instability, we introduce infinitesimal test vertices corresponding to particle-particle pairing into the action, $\mathcal{L} = \mathcal{L}_0 + \delta\mathcal{L}$, where $\mathcal{L}_0$ is given by (2.1) and

$$\delta\mathcal{L} = \sum_{\alpha=1}^{3} \tilde{\Delta}_\alpha \psi^\dagger_{\alpha,\uparrow} \psi^\dagger_{\alpha,\downarrow} + \tilde{\Delta}^*_\alpha \psi_{\alpha,\uparrow} \psi_{\alpha,\downarrow}, \tag{2.6}$$

one test vertex for each patch. The renormalisation of the test vertices is governed by the equation [20]

$$\frac{\partial}{\partial y} \begin{bmatrix} \tilde{\Delta}_1 \\ \tilde{\Delta}_2 \\ \tilde{\Delta}_3 \end{bmatrix} = -2 \begin{bmatrix} g_4 & g_3 & g_3 \\ g_3 & g_4 & g_3 \\ g_3 & g_3 & g_4 \end{bmatrix} \begin{bmatrix} \tilde{\Delta}_1 \\ \tilde{\Delta}_2 \\ \tilde{\Delta}_3 \end{bmatrix} \tag{2.7}$$

which can be diagonalized by transforming to the eigenvector basis

$$\tilde{\Delta}_a = \frac{\tilde{\Delta}}{\sqrt{2}}(0, 1, -1), \quad \tilde{\Delta}_b = \sqrt{\frac{2}{3}}\tilde{\Delta}\left(1, -\frac{1}{2}, -\frac{1}{2}\right) \tag{2.8}$$

$$\tilde{\Delta}_c = \frac{\tilde{\Delta}}{\sqrt{3}}(1, 1, 1). \tag{2.9}$$

Here $\tilde{\Delta}_c$ is an s-wave order, whereas $\tilde{\Delta}_a$ and $\tilde{\Delta}_b$ correspond to order parameters that vary around the Fermi surface as $\tilde{\Delta}\cos(2\varphi)$ and $\tilde{\Delta}\sin(2\varphi)$, where φ is the angle to the x axis (see Fig 2-4). Such dependence describes d-wave superconducting orders (SCd), since the gap changes sign four times along the FS. In 2D notation, the two order parameters $\tilde{\Delta}_a$ and $\tilde{\Delta}_b$ correspond to d_{xy} and $d_{x^2-y^2}$ superconducting orders respectively.

Notably, we find the s-wave vertex $\tilde{\Delta}_c$, Eq.(2.9), has a negative eigenvalue and is suppressed under RG flow (2.7). This is to be expected given that we started

out with repulsive microscopic interactions. At the same time, the d-wave orders $\tilde{\Delta}_a$ and $\tilde{\Delta}_b$ have (identical) eigenvalue $g_3 - g_4$, which may be negative at the bare level but definitely becomes *positive* under RG, indicating an instability in the d-wave channel. We solve (2.7) for the d-wave orders by substituting the scaling form of the interactions (2.5), and find that the d-wave susceptibility diverges near y_c as

$$\chi_{SCd}(y) = \frac{\tilde{\Delta}_{a,b}(y)}{\tilde{\Delta}_{a,b}(0)} \sim (y_c - y)^{2(G_4 - G_3)}, \tag{2.10}$$

where, we remind, $G_3 - G_4 > 0$.

The divergence of the SCd susceptibility indicates an instability to d wave superconductivity under RG, with the $\tilde{\Delta}\cos(2\varphi)$ and $\tilde{\Delta}\sin(2\varphi)$ order parameters having *identical* susceptibility. The degeneracy of the two d-wave orders is guaranteed, since the $d_{x^2-y^2}$ and d_{xy} functions belong to the same two dimensional irreducible representation of the lattice point group [12, 13]. However, this does not guarantee that d-wave superconductivity will develop, since the SCd instability must compete against the tendency for density wave formation.

To investigate density wave formation, we introduce test vertices representing pairing of particles with holes on a different patch. The particles and holes may pair in the charge channel, forming CDW, or in the spin channel, forming SDW. We compute the renormalization of the pairing vertices under RG, and find that the CDW vertex is suppressed by interactions, but the SDW vertex $\tilde{\Delta}_{SDW}$ is enhanced, similar to [20]. The SDW susceptibility χ_{SDW} diverges near y_c as

$$\chi_{SDW} = \frac{\tilde{\Delta}_{SDW}(y)}{\tilde{\Delta}_{SDW}(0)} \sim (y_c - y)^{-2(G_3+G_2)d_1(y_c)}. \tag{2.11}$$

This describes a potential instability towards SDW formation, which will compete with the SCd instability. The SDW instability arises provided there is at least partial nesting i.e. the nesting parameter $d_1(y_c) \neq 0$. However, since $-G_4 > G_2$ for all $0 \leq d_1(y_c) \leq 1$ (Fig.2-3 inset), it follows from comparison of Eq.2.11 and Eq.2.10 that the SCd susceptibility diverges faster than the SDW susceptibility, for all values of

nesting. At perfect nesting ($d_1 = 1$), the SCd susceptibility diverges as $(y_c - y)^{-1.5}$, whereas the SDW susceptibility diverges only as $(y_c - y)^{-1}$. As we move away from perfect nesting, the SCd susceptibility diverges faster, and the SDW susceptibility diverges more slowly, so that SCd is the leading instability for all values of nesting, within validity of the RG. This is in contrast to the square lattice [20], where at perfect nesting the SDW and SCd instabilities have the same exponent under RG, with subleading terms lifting the degeneracy in favor of SDW, which is in turn overtaken by SCd at some $d_1 < 1$.

We also considered the possibility of ordering in a channel exhibiting only a $\log^1$ divergence e.g. the Pomeranchuk ordering. However, we found that such orders cannot compete with superconductivity (see online supplementary material). Finally, the phonon-mediated attraction in the pairing channel could induce s-wave superconductivity provided that it overwhelms the electronic repulsion in the s-wave channel at the Debye frequency scale, $\omega_D < \Lambda$. However, the s-wave coupling $(2g(3) + g(4))$ remains positive and grows ever more repulsive under our $\log^2$ RG. Thus, as long as the nesting parameter is not too small ($2G_3 > -G_4$ for $d_1 > 0.05$), the s-wave pairing appears to be unlikely to win.

Competition of d-wave orders below T_c: We now investigate the competition of the $d_{x^2-y^2}$ and d_{xy} superconducting orders (2.8) below T_c. In this regime, the system may either develop one of these two orders, or a linear combination of the two. The ordered state that minimizes the free energy wins. The hexagonal lattice point group symmetry dictates that the free energy below T_c must take the form [33]

$$F = \alpha(T - T_c)(|\Delta_a|^2 + |\Delta_b|^2) + K_1(|\Delta_a|^2 + |\Delta_b|^2)^2 + K_2|\Delta_a^2 + \Delta_b^2|^2 + O(\Delta^6) \quad (2.12)$$

with $K_1 > 0$. This free energy allows for two possible superconducting phases. If $K_2 < 0$ then a $d_{x^2-y^2}$ or a d_{xy} superconducting state would arise, whereas if if $K_2 > 0$ then the $d_{x^2-y^2}$ and d_{xy} orders can co-exist [33]. We now calculate K_2 microscopically (an alternative but equivalent microscopic treatment is provided in the online supplementary material).

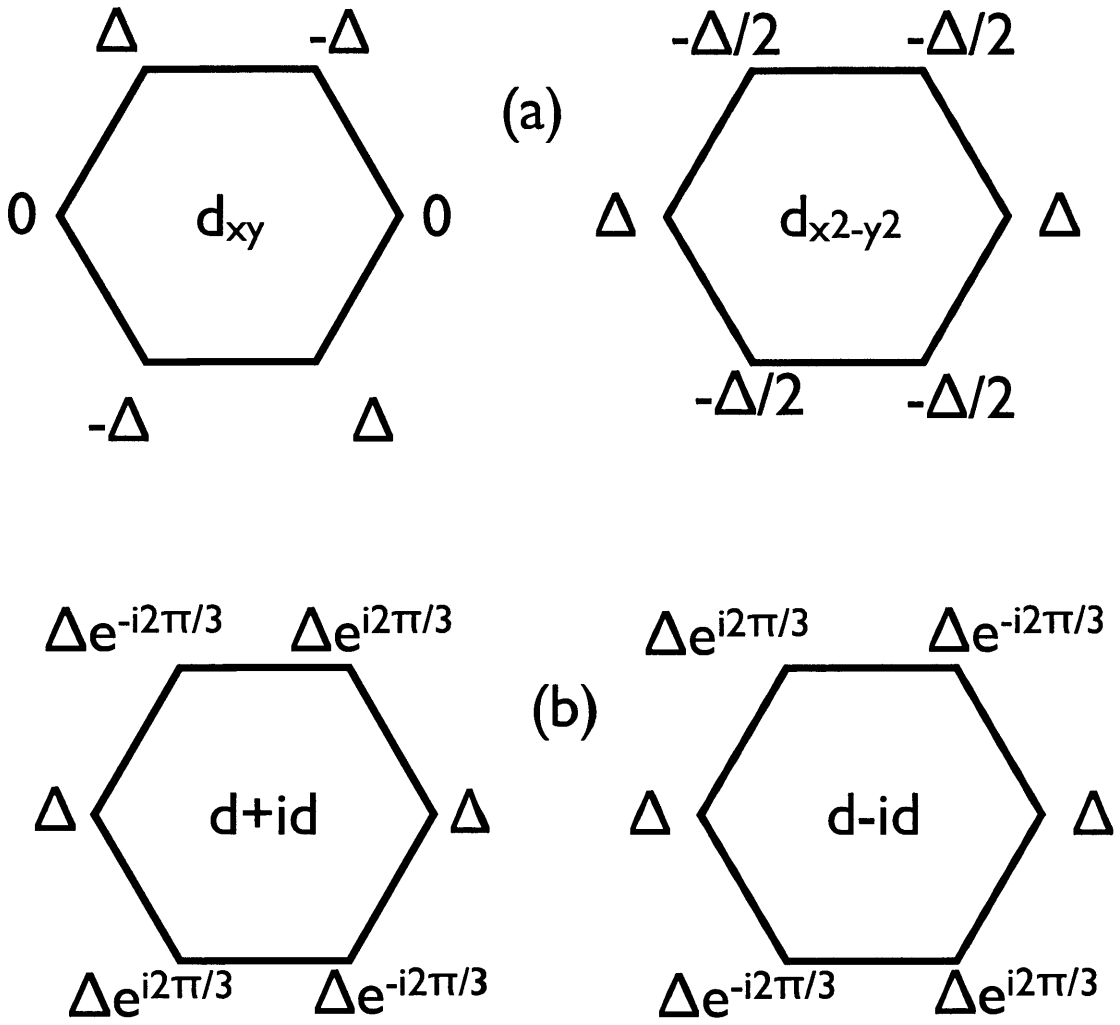

Figure 2-4: Possible superconducting orders that could develop at the M point. (a) A $d_{x^2-y^2}$ or d_{xy} state would be realised if $K_2 < 0$ in the Landau expression for the free energy, Eq.2.12 (b) The $d_{x^2-y^2}$ and d_{xy} orders can co-exist if $K_2 > 0$ in Eq.2.12. A microscopic calculation indicates that the states (b) have lower free energy.

We begin by writing the free energy as the sum of the free energy on three patches,

$$F = F(\Delta_1) + F(\Delta_2) + F(\Delta_3), \tag{2.13}$$

where the free energy on a patch is given by the standard Landau expansion

$$F(\Delta_i) = \alpha'(T - T_c)|\Delta_i|^2 + K|\Delta_i|^4, \quad K > 0 \tag{2.14}$$

In this expression, it is essential to realize that Δ_1, Δ_2, and Δ_3 are not independent, but must be expressed in terms of the two parameters Δ_a and Δ_b, Eq.(2.8). Rewriting (2.13) and (2.14) in terms of the two *independent* variables $\Delta_{a,b}$, we obtain Eq.(2.12) with $K_1 = \frac{1}{3}K > 0$ and $K_2 = \frac{1}{6}K > 0$. This implies the co-existence of $d_{x^2-y^2}$ and d_{xy} orders. Minimization of the free energy (2.12) with $K_2 > 0$ leads to $|\Delta_a| = |\Delta_b|$ and $\mathrm{Arg}(\Delta_a/\Delta_b) = \pi/2$. This order parameter can be rewritten as a three component vector in the patch basis, which takes the form

$$\Delta_a \pm i\Delta_b = \Delta(1, e^{\pm 2\pi i/3}, e^{\mp 2\pi i/3}). \tag{2.15}$$

This corresponds to a superconducting gap that varies around the FS as $\Delta \exp(\pm 2i\varphi)$. Such an order parameter corresponds to $d+id$ (or $d-id$) superconductivity (Fig.2-4), and is a spin singlet analog of the $p+ip$ state that has been predicted for Sr_2RuO_4.

Conclusions: The robustness of $d + id$ superconductivity in the weak coupling limit, demonstrated by the above analysis, leads us to believe that the graphene based chiral superconductivity can be realized experimentally. While our analysis is controlled for the weak short-range interaction model, several questions pertaining to the behavior of realistic systems should be clarified by future work. Determination of the phase structure for interactions of moderate strength and of long-range character remains an open problem, as does an accurate estimate of T_c and the role of disorder, against which d-wave superconductivity is not protected. The graphene based $d + id$ superconductivity, if realized in experiment, will play a vital role in the development of technology designed to exploit topological superconductivity.

Bibliography

[1] Volovik, G.E. Quantized Hall Effect in Superfluid Helium-3 Film. *Phys. Lett.* **A 128**, 277-279 (1988)

[2] Sigrist, M. and Ueda, K. Phenomenological theory of unconventional superconductivity. *Rev. Mod. Phys.* **63**, 239-311 (1991).

[3] Vojta M., Zhang Y., Sachdev S. Quantum phase transitions in d-wave superconductors. *Phys. Rev. Lett.* **85**, 4940-4943 (2000).

[4] Fu, L. and Kane, C.L. Superconducting Proximity Effect and Majorana Fermions at the Surface of a Topological Insulator. *Phys. Rev. Lett.* **100**, 096407 (2008)

[5] Qi X.L., Hughes T., Raghu S., and Zhang S-C, Time-Reversal-Invariant Topological Superconductors and Superfluids in Two and Three Dimensions *Phys. Rev. Lett.* **102**, 187001 (2009)

[6] Cheng, M. Sun, K. Galitski, V. and Das Sarma, S. Stable topological superconductivity in a family of two-dimensional fermion models. *Phys. Rev. B* 81, 024504 (2010)

[7] Castro Neto, A.H., Guinea, F., Peres, N.M.R., Novoselov, K.S. and Geim, A.K. The electronic properties of graphene. *Rev. Mod. Phys.* **81**, 109-162 (2009)

[8] DasSarma, S., Adam, S., Hwang, E.H. and Rossi, E. Electronic transport in two dimensional graphene. *Rev. Mod. Phys.* **83**, 407-470 (2011)

[9] Senthil, T. Marston, J.B. and Fisher, M.P.A. Spin quantum Hall effect in unconventional superconductors. *Phys. Rev. B* **60**, 4245-4254 (1999)

[10] Mackenzie, A.P. and Maeno, Y., The superconductivity of Sr2RuO4 and the physics of spin-triplet pairing. *Rev. Mod. Phys.*, **75**, 657-712 (2003).

[11] Laughlin, R.B. Magnetic Induction of $d_{x^2-y^2} + id_{xy}$ Order in High-T_c Superconductors. *Phys. Rev. Lett.* **80**, 5188-5191 (1998)

[12] Gonzalez, J. Kohn Luttinger superconductivity in Graphene. *Phys. Rev. B* **78**, 205431 (2008)

[13] Black-Schaffer, A.M. and Doniach, S. Resonating valence bonds and mean-field d-wave superconductivity in graphite. *Phys. Rev. B* **75**, 134512 (2007)

[14] Uchoa B. and Castro Neto, A.H. Superconducting States of Pure and Doped Graphene. *Phys. Rev. Lett.* **98**, 146801 (2007)

[15] Kohn, W. and Luttinger, J.M. New Mechanism for Superconductivity. *Phys. Rev. Lett.* **15**, 524-526 (1965)

[16] McChesney, J.L., Bostwick, A., Ohta, T., Seyller, T., Horn, K., Gonzalez, J. and Rotenberg, E. Extended van Hove Singularity and Superconducting Instability in Doped Graphene. *Phys. Rev. Lett.* **104**, 136803 (2010)

[17] Ye, J. T., Inoue, S., Kobayashi, K., Kasahara, Y., Yuan, H.T., Shimotani, H. and Y. Iwasa, Y. Liquid-gated interface superconductivity on an atomically flat film. *Nature Mater.* **9**, 125-128 (2010).

[18] Schulz, H.J. Superconductivity and Antiferromagnetism in the Two-Dimensional Hubbard Model: Scaling Theory. *Europhys. Lett.* **4**, 609-615 (1987)

[19] Dzyaloshinskii, I.E. Maximal inrease of the superconducting transition temperature due to the presence of van Hove singularities. *Sov. Phys. JETP* **66(4)**, 848-854 (1987)

[20] Furukawa, N., Rice, T.M. and Salmhofer, M. Truncation of a Two-Dimensional Fermi Surface due to Quasiparticle Gap formation at the Saddle Points. *Phys. Rev. Lett.* **81**, 3195-3198 (1998)

[21] LeHur, K. and Rice, T.M. Superconductivity close to the Mott state: From condensed-matter systems to superfluidity in optical lattices. *Annals of Physics* **324** 1452-1515 (2009)

[22] Maiti, S. and Chubukov, A.V. Renormalization group flow, competing phases and the structure of superconducting gap in multiband models of iron-based superconductors. *Phys. Rev. B* **82**, 214515 (2010)

[23] Thomale, R., Platt, C., Hanke, W. and Bernevig, B.A. Mechanism for Explaining Differences in the Order Parameters of $FeAs$-Based and FeP-Based Pnictide Superconductors. *Phys. Rev. Lett.* **106**, 187003 (2011)

[24] Valenzuela B. and Vozmediano, M.AH. Pomeranchuk instability in doped graphene. *New. J. Phys.* **10** 113009 (2008)

[25] Li,T. Spontaneous quantum Hall effect in quarter doped Hubbard model on honeycomb lattice and its possible realization in quarter doped graphene system. http://arxiv.org/abs/1103.2420 (2011) (unpublished)

[26] Makogon, D., van Gelderen, R., Roldan, R. and Morais Smith, C. Spin-density-wave instability in graphene doped near the van Hove singularity. Phys. Rev. B 84, 125404 (2011)

[27] Wallace, P.R. The Band Theory of Graphite. *Phys. Rev.* **71**, 622-634 (1947)

[28] Son, D.T. Superconductivity by long-range color magnetic interaction in high-density quark matter. *Phys. Rev. D* **59**, 094019 (1999)

[29] see e.g., Moon, E.G. and Chubukov, A.V. Quantum-critical pairing with varying exponents. *J. Low Temperature Physics*, **161**, Numbers 1-2, 263-281 (2010) and references therein.

[30] Pathak, S., Shenoy, V.B. and Baskaran, G. Possibility of High T_c Superconductivity in doped Graphene. http://arxiv.org/abs/0809.0244 (2008) (unpublished)

[31] Honerkamp, C., Density Waves and Cooper Pairing on the Honeycomb Lattice. *Phys. Rev. Lett.* **100**, 146404 (2008)

[32] Roy, B. and Herbut, I.F. Unconventional superconductivity on honeycomb lattice: Theory of Kekule order parameter. *Phys. Rev. B* **82**, 035429 (2010)

[33] Mineev, V.P. and Samokhin, K.V. Introduction to Unconventional Superconductivity, *Gordon and Breach Science Publishers*, (1998), p69

Chapter 3

Properties of the spin density wave state in strongly doped graphene

Section 1: We consider electrons on a honeycomb or triangular lattice doped to the saddle point of the bandstructure. We assume system parameters are such that spin density wave (SDW) order emerges below a temperature T_N and investigate the nature of the SDW phase. We argue that at $T \leq T_N$ the system develops a uniaxial SDW phase whose ordering pattern breaks $O(3) \times Z_4$ symmetry and corresponds to an eight site unit cell with non-uniform spin moments on different sites. This state is a half-metal – it preserves full original Fermi surface, but has gapless charged excitations in one spin branch only. It allows for electrical control of spin currents and is desirable for nano-science.

This work was reported in R. Nandkishore, G.W.Chern and A.V. Chubukov, Phys. Rev. Lett. 108, 227204 (2012)

Section 2: We show that the spin-density wave state near the $3/8$ or $5/8$-filling of the honeycomb lattice is preempted by a paramagnetic phase that breaks an emergent Z_4 symmetry of the system, associated with the four different arrangements of spins in the unit cell. Unlike other emergent paramagnetic phases in itinerant and localized-spin systems, this state preserves the rotational symmetry of the lattice but breaks its translational symmetry, giving rise to a super-lattice structure that can be detected by STM. We show that spin fluctuations are also enhanced in this emergent phase, leaving distinctive signatures in the magnetic spectrum that can be probed experimentally.

This work was reported in G.W.Chern, R. Fernandes, R. Nandkishore and A.V.Chubukov, http://arxiv.org/abs/1203.5776 (2012).

3.1 Spin density wave physics without thermal fluctuations

Introduction: The electronic properties of single layer graphene have been the subject of considerable experimental and theoretical interest [1]. Near half-filling, a description in terms of non-interacting Dirac electrons captures the essential physics, since interactions effects are suppressed by the low density of states (DOS). A sharply different behavior arises when graphene is strongly doped to 3/8 or 5/8 filling [2]. At this filling, a divergent density of states and nested Fermi surface (FS) conspire to produce weak coupling instabilities to an extensive buffet of ordered states, including spin density waves (SDW) [3, 4, 7], Pomeranchuk metals [8], and d wave superconductors (SC) [9, 5, 6]. A similar situation arises on a triangular lattice at 3/4 filling [10, 25].

It has recently been established using renormalization group (RG) methods [5] that the two most relevant instabilities at weak coupling are towards SDW and a d-wave SC. Other potential instabilities, like a charge-density wave have much smaller susceptibilities. The SDW vertex is the largest at intermediate RG scales, but superconducting vertex eventually overshoots it, making d-wave superconductivity the leading weak coupling instability at the Van Hove filling. The SC state has a $d + id$ gap structure and breaks time-reversal symmetry [5]. Upon doping away from Van-Hove filling, the Cooper and SDW channels decouple at a scale set by doping, and the RG flow is altered. In this situation, the SDW, which is the largest at intermediate RG scales, may become the dominant instability, and numerical functional RG studies found [6] that SDW is indeed the leading instability in substantially wide doping range away from 3/8 or 5/8. Previous work on SDW order argued that the SDW state is non-coplanar and has non-zero spin chirality [3, 7, 10]. Such a state gaps out the entire Fermi surface (FS).

We argue that the situation is more complex than originally thought, and the chiral SDW state is present only at the lowest temperatures. Over a wide intermediate range of temperatures, a different SDW state emerges in which SDW order develops simultaneously at three inequivalent wavevectors $\mathbf{Q}_i$, but the three vector order pa-

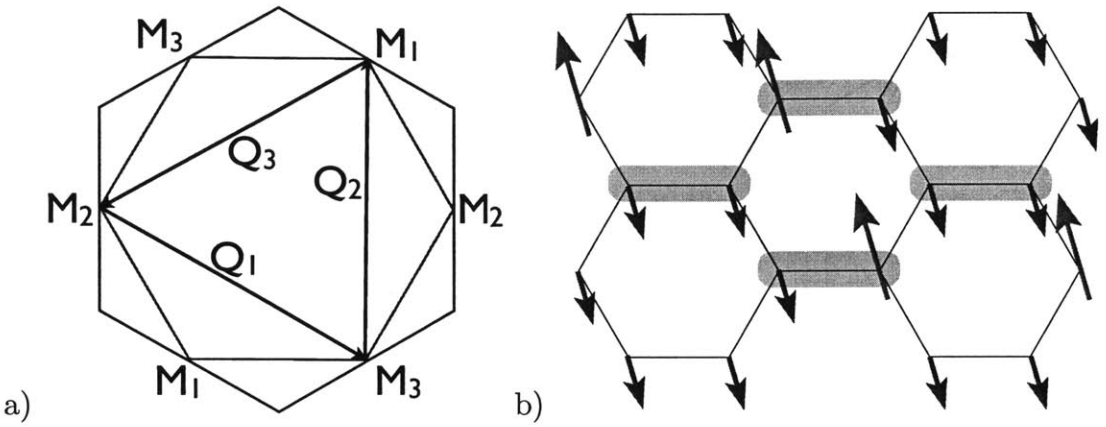

Figure 3-1: (Color online) a) The Fermi surface at the doping level of interest is a hexagon inscribed within a hexagonal Brillouin zone (BZ), for both honeycomb and triangular lattices. The FS has three inequivalent corners, which are saddle points of the dispersion, marked by a vanishing Fermi velocity and a divergent density of states. The three inequivalent saddle points M_i are connected by three inequivalent nesting vectors $\mathbf{Q}_i$, each of which is equal to half a reciprocal lattice vector, such that $\mathbf{Q}_i = -\mathbf{Q}_i$. b) Spin structure for the uniaxial SDW state. The SDW order quadruples the unit cell to a unit cell with eight sites (shaded). The enlarged unit cell has a large spin moment 3Δ on two sites and a small spin moment $-\Delta$ on the other six. The total spin on each unit cell is zero.

rameters are all aligned along the same axis. This state has an eight site unit cell with non-uniform spin moments and zero net magnetization (Fig. 3-1b). Such a state cannot be accessed starting from a spin Hamiltonian for local moments with a fixed length, and can only be accessed starting from a model of itinerant fermions. We show that in this state, unlike in any other known SDW state, the chemical potential shifts proportionally to the SDW order parameter preserving the original Fermi surface for one spin branch and gapping out the other spin branch. The uniaxial SDW state is therefore a 'half-metal' that allows for electrical control of spin currents. Such a state is highly desirable for nano-science applications.

The model: For definiteness we focus on doped graphene at 3/8 filling. Our point of departure is the tight binding model [12], with the nearest-neighbor dispersion

$$\varepsilon_{\mathbf{k}} = -t_1 \sqrt{1 + 4\cos\frac{k_y\sqrt{3}}{2}\cos\frac{3k_x}{2} + 4\cos^2\frac{k_y\sqrt{3}}{2}} - \mu \tag{3.1}$$

where $\mu = -t_1$ at 3/8 filling. The FS then forms a perfect hexagon inscribed within

a hexagonal BZ (Fig. 3-1a). The perfect nesting of the FS in doped graphene is quite robust – it is broken only by third and higher neighbor hoppings, which are generally quite small. The Fermi velocity vanishes near the hexagon corners $\mathbf{M}_1 = (\pi/3, \pi/\sqrt{3})$, $\mathbf{M}_2 = (2\pi/3, 0)$, $\mathbf{M}_3 = (\pi/3, -\pi/\sqrt{3})$, which are saddle points of the dispersion:

$$\varepsilon_{\mathbf{M}_2+\mathbf{k}} \approx \frac{3t_1}{4}(k_y^2 - 3k_x^2), \quad \varepsilon_{\mathbf{M}_{1,3}+\mathbf{k}} \approx -\frac{3t_1}{4} 2k_y(k_y \mp \sqrt{3}k_x), \tag{3.2}$$

where each time $\mathbf{k}$ denotes the deviation from a saddle point. Saddle points give rise to a logarithmic singularity in the DOS and control the SDW instability at weak coupling. There are three in-equivalent nesting vectors connecting in-equivalent pairs of saddle points (see Fig. 3-1a):

$$\mathbf{Q}_2 = (0, 2\pi/\sqrt{3}), \quad \mathbf{Q}_{1,3} = (\pm\pi/3, -\pi/\sqrt{3}). \tag{3.3}$$

Each $\mathbf{Q}_i$ is equivalent to $-\mathbf{Q}_i$ modulo a reciprocal lattice vector.

For the interactions we use the low energy model from [5], which provides an exact description of the system in the weak coupling limit. This model contains four interactions – density-density, exchange, pair-hopping and forward scattering, labeled g_1, g_2, g_3, g_4, respectively. Of these, the interactions g_4 and g_1 do not couple to spin density waves [5] and may be safely ignored [16]. The SDW physics is controlled by the density-density interaction g_2 ($|\mathbf{k}, \mathbf{k}+\mathbf{Q}_i\rangle \to |\mathbf{k}, \mathbf{k}+\mathbf{Q}_i\rangle$), and the umklapp pair-hopping interaction g_3 ($|\mathbf{k}, \mathbf{k}'\rangle \to |\mathbf{k}+\mathbf{Q}_i, \mathbf{k}'+\mathbf{Q}_i\rangle$). The partition function in the SDW sector can be written as $Z = \int D[\psi^\dagger, \psi] \exp(-S[\psi^\dagger, \psi])$, where $S = \int_0^{1/T} \mathcal{L}(\mathbf{k}, \tau)$ and

$$\begin{aligned} \mathcal{L} &= \sum_\alpha \psi^\dagger_{a,\alpha}(\partial_\tau - \varepsilon_\mathbf{k} + \mu)\psi_{a,\alpha} \\ &- \sum_{\alpha\neq\beta} g_3 \psi^\dagger_{a,\alpha}\psi^\dagger_{a,\beta}\psi_{b,\beta}\psi_{b,\alpha} - g_2 \psi^\dagger_{a,\alpha}\psi^\dagger_{b,\beta}\psi_{b,\beta}\psi_{a,\alpha}, \end{aligned} \tag{3.4}$$

where the action is written in terms of electron operators, a, b are patch labels, and

α and β are spin components.

Each nesting vector $\mathbf{Q}_i$ has associated with it an SDW order parameter $\mathbf{\Delta}_i = \mathbf{\Delta}_{a,b} = \frac{g_2+g_3}{3}\sum_k \langle \psi^\dagger_{a,\alpha} \boldsymbol{\sigma}_{\alpha\beta} \psi_{b,\beta} \rangle$. The condition for the emergence of each $\mathbf{\Delta}_i$ is the same: $((g_2+g_3)/t_1)\log^2 t_1/T_N = O(1)$ [5], leaving a large number of SDW states as potential candidates. We study the selection of the SDW order within Ginzburg-Landau theory and by comparing different SDW solutions in the mean-field approximation for Eq. (3.4) at arbitrary $T < T_N$.

Ginzburg-Landau theory: To construct the Ginzburg-Landau theory, we decouple the quartic interaction terms by restricting the interaction to the spin channel and a Hubbard Stratonovich transformation to collective spin variables $\mathbf{\Delta}_i$. Note that the Hubbard Stratanovich transformation is exact and does not introduce any approximation. We integrate out the fermions in the Matsubara frequency representation and obtain an action in terms of $\mathbf{\Delta}_i$ in the form

$$\begin{aligned} \mathcal{L} &= T\sum_{n=-\infty}^{\infty}\int \frac{d^2k}{(2\pi)^2}\Big[\frac{2}{g_2+g_3}\sum_i (\mathbf{\Delta}_i)^2 \\ &+ \mathrm{Tr}\ln\Big(i\omega_n - \varepsilon_{\mathbf{k}} - \sum_i \mathbf{\Delta}_i\cdot\boldsymbol{\sigma}\Big)\Big]. \end{aligned} \tag{3.5}$$

For $T \approx T_N$, we can expand (3.5) in small $\mathbf{\Delta}_i/T_N$. It is useful to define the expansion coefficients

$$Z_i = T\sum_{\omega_n}\int \frac{d^2k}{(2\pi)^2}\xi_i \tag{3.6}$$

where the integrands ξ_i are expressed in terms of fermionic Green functions $G = (i\omega_n - \varepsilon_{\mathbf{k}} - \mu)^{-1}$, $G_i = (i\omega_n - \varepsilon_{\mathbf{k}+\mathbf{Q}_i} - \mu)^{-1}$, and $G_{i+j} = (i\omega_n - \varepsilon_{\mathbf{k}+\mathbf{Q}_i+\mathbf{Q}_j} - \mu)^{-1}$ as

$$\begin{aligned} \xi_1 &= G^2G_3^2, & \xi_2 &= G^2G_3G_1, \\ \xi_3 &= GG_3G_1G_{1+3}, & \xi_4 &= G^2G_3^2G_1^2. \end{aligned} \tag{3.7}$$

Diagrammatically, Z_1 $-Z_3$ are given by 'square' diagrams with four fermionic propagators and $\boldsymbol{\sigma}_{\alpha\beta}$ in the vertices, and Z_4 is given by a 'hexagonal' diagram with six fermionic propagators, (see Fig. 3-2). The free energy evaluated at $T \approx T_N$ can be

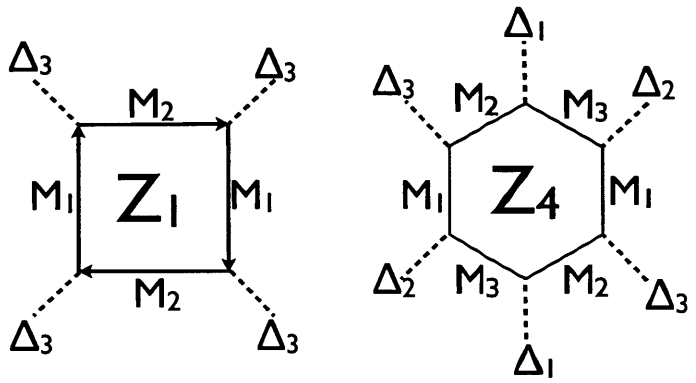

Figure 3-2: (Color online) The terms quartic in Δ are produced by processes represented diagrammatically by square diagrams. The diagrams for Z_2 and Z_3 correspond to patterns $\Delta_3, \Delta_3, \Delta_1, \Delta_1$ and $\Delta_3, \Delta_1, \Delta_3, \Delta_1$, respectively. The sixth order chirality sensitive term is produced by 'hexagonal diagrams.' Sample square and hexagonal diagrams are shown above. The integrals are dominated by momenta that bring all the fermion propagators to the vicinity of one of the saddle points of the dispersion.

expressed in terms of these coefficients as

$$\begin{aligned}\mathcal{L} \;\propto\; & \alpha(T-T_N)\sum_i \Delta_i^2 + Z_1(\Delta_1^2+\Delta_2^2+\Delta_3^2)^2 + 2(Z_2-Z_1-Z_3)(\Delta_1^2\Delta_2^2+\Delta_2^2\Delta_3^2+\Delta_3^2\Delta_1^2) \\ & + \; 4Z_3((\Delta_1\cdot\Delta_2)^2+(\Delta_2\cdot\Delta_3)^2+(\Delta_3\cdot\Delta_1)^2) - 4Z_4(\Delta_1\cdot\Delta_2\times\Delta_3)^2+\cdots \qquad (3.8)\end{aligned}$$

where α is an inessential positive constant.

The quadratic term and the first quartic term in (3.8) set the overall magnitude of $\Delta_{\rm tot}^2 = \sum_i \Delta_i^2$, but do not differentiate between different SDW states. The second quartic term in (3.8) determines whether SDW order develops only at one nesting vector, or at all three (depending on the sign of $Z_2 - Z_1 - Z_3$). Finally, the third quartic term and sixth order term control the relative orientation of the vector order parameters, if SDW order develops at multiple wavevectors. Close to T_N the expansion to order Δ_i^4 is generally sufficient, but we include the sixth order term because Z_3 is suppressed by an extra factor of T_N/t_1, which is exponentially small in the weak coupling limit. The relative smallness of Z_3 arises because in the integrals for Z_1, Z_2, and Z_4, all fermions can be simultaneously brought to the saddle points, whereas in the integral for Z_3, three fermions can be brought simultaneously to saddle points,

but the remaining fermion stays far away from the saddle point and the FS.

We evaluate the coefficients $Z_1 - Z_4$ to leading order in small T_N/t_1 and obtain [16]

$$Z_1 = \frac{0.20 \log \frac{t_1}{T_N}}{\pi^4 T_c^2 t_1}, \quad Z_2 = \frac{0.58}{\pi^4 T_N^2 t_1},$$
$$Z_3 = -\frac{0.08}{\pi^2 T_N^2 t_1} \frac{T_N}{t_1}, \quad Z_4 = -\frac{0.1}{T_N^4 t_1} \tag{3.9}$$

The positivity of Z_1 guarantees a second order phase transition, with the type of SDW order depending on the signs and relative magnitudes of Z_2, Z_3, and Z_4. Since Z_3 is smaller by T_N/t_1 than $Z_{1,2}$, and Z_2 is smaller by $\log \frac{t_1}{T_N}$ than Z_1, it follows that $Z_2 - Z_1 - Z_3 < 0$, so the system forms SDW order simultaneously at all three nesting vectors (the $3Q$ state). Meanwhile, the relative orientation of the three SDW order parameters is controlled by the sign of Z_3 at the smallest $\mathbf{\Delta}_i$, and by the sign of Z_4 at somewhat larger $\mathbf{\Delta}_i$. Both Z_3 and Z_4 are negative and favor the non-chiral SDW order with the three $\mathbf{\Delta}_i$ all aligned along the same axis.

An order parameter of the form $\mathbf{\Delta}(e^{i\mathbf{Q}_3\cdot\mathbf{r}} + e^{i\mathbf{Q}_1\cdot\mathbf{r}} \pm e^{i\mathbf{Q}_2\cdot\mathbf{r}})$ leads to spin moments on the lattice of the form shown in Fig. 3-1. A quarter of lattice sites have spin moment 3Δ, the other three quarters have moment $-\Delta$. Such an order cannot be obtained from any spin Hamiltonian for local moments of constant magnitude on every site. Our result differs from earlier mean-field analysis [25] which found non-coplanar insulating SDW order at weak coupling. We note, however, the $3Q$ state that we found, with non-equal spin length on different sites, was not considered in that work and other earlier considerations of SDW order. We found analogous results for fermions on a triangular lattice at Van Hove filling, which are described by an identical low energy theory provided we neglect further neighbor hopping.

Properties of a uniaxial SDW: Is the uniaxial SDW state a metal or an insulator? To address this issue we need to compute the fermionic spectrum. Without loss of generality, we take the SDW to be uniaxial along the z axis, so that S^z is a good quantum number, and spin-up and spin-down fermions decouple. Consider the state with $\mathbf{\Delta}_1 = \mathbf{\Delta}_2 = \mathbf{\Delta}_3 = \Delta\hat{\mathbf{z}}\,\sigma_3$. Up spins near the three Van Hove points are described

by a simple Hamiltonian

$$H = \begin{pmatrix} \varepsilon_{1,\mathbf{k}} - \delta\mu & \Delta & \Delta \\ \Delta & \varepsilon_{2,\mathbf{k}} - \delta\mu & \Delta \\ \Delta & \Delta & \varepsilon_{3,\mathbf{k}} - \delta\mu \end{pmatrix} \tag{3.10}$$

where $\varepsilon_1, \varepsilon_2, \varepsilon_3$ are the dispersions near the Van Hove points, Eq. (3.18), and $\delta\mu$ is the SDW-induced shift of the chemical potential. The 3×3 Hamiltonian describing the spin down branch is obtained by taking $\Delta \to -\Delta$. At $\mathbf{k} = 0$ (i.e., at Van Hove points) the energies of spin-up excitations $E_{\mathbf{k}} - \delta\mu$ are $-\Delta, -\Delta$, and 2Δ, and the energies of spin-down excitations are Δ, Δ, and -2Δ. In conventional SDW states (e.g., SDW on a 2D square lattice) $\delta\mu/\Delta \propto T_N/E_F$ is negligibly small and can be safely neglected. We find that in our case $\delta\mu = -\Delta$, so that gapless excitations arise in the spin-down spectrum.

To see the unexpected shift of the chemical potential, we diagonalize Eq. (3.10) and the corresponding equation for down spins and inspect six branches of excitations. We find that fixing $\delta\mu = -\Delta$ ensures that both in the paramagnetic and in the $3Q$ uniaxial SDW state there are four bands with $E_{\mathbf{k}} \leq \mu$ and two bands with $E_{\mathbf{k}} \geq \mu$ for all momenta in the reduced BZ (see Fig. 3-3). Since the chemical potential is fixed by the constraint that the total number of electrons (equal to the number of states below the chemical potential) must not change between $\Delta = 0$ and $\Delta \neq 0$ [13], it follows that we must set $\delta\mu = -\Delta$. For verification, we computed the thermodynamic potential $\Omega(\Delta, \mu)$ from (3.5), numerically solved the simultaneous equations $\partial\Omega/\partial\Delta = 0$ and $\partial\Omega/\partial\mu = -N$, and confirmed that $\delta\mu = -\Delta$ to a high accuracy.

Having determined that $\delta\mu = -\Delta$, we find from (3.10) that gapless excitations emerge when $\varepsilon_{1,\mathbf{k}}\, \varepsilon_{2,\mathbf{k}}\, \varepsilon_{3,\mathbf{k}} = 0$, which has solutions along three lines passing through each Van Hove point. Two of then coincide with the original FS, the third is directed towards the center of the BZ. The $3Q$ uniaxial SDW state is then obviously a metal. We emphasize, however, that gapless states exist only for the electrons with spin projection opposite to $\mathbf{\Delta}$. The electrons with spin projection along $\mathbf{\Delta}$ are fully gapped. Since a Fermi surface exists for one spin projection only, we dub this state a

'half metal.' We found an analogous 'half-metal' spectrum for the $3Q$ uniaxial SDW phase on the triangular lattice.

The half-metallic nature of the SDW should manifest itself in numerous experiments. For example, in tunneling experiments conducted with electrons spin polarized along the z axis, a hard gap will be seen for down spins, but a Fermi surface will be seen for up spins. Furthermore, since the low energy charged excitations involve up spins only, any charge currents will necessarily also be spin currents. Thus, the half metal state allows for electrical control of spin currents, which may be beneficial for nanoscience applications.

Order parameter manifold: The uniaxial SDW order obviously breaks $O(3)$ spin-rotational symmetry. It also breaks Z_4 discrete symmetry associated with either parallel or antiparallel ordering of $\mathbf{\Delta}_i$, i.e., in addition to the (Δ, Δ, Δ) state which we considered above, there are also $(\Delta, -\Delta, -\Delta)$, $(-\Delta, \Delta, -\Delta)$, and $(-\Delta, -\Delta, \Delta)$ states. These states have an identical structure of fermionic excitations, and correspond to the four in-equivalent ways to choose which two of the eight sites of the SDW unit cell carry large spins (see Fig. 3-1(b)). Equivalently, the three other states from the Z_4 manifold are obtained from the (Δ, Δ, Δ) state by shifting the origin of coordinates to the center of one of three neighboring hexagons. An interesting possibility, which deserves further study, is that Z_4 symmetry can be broken before $O(3)$ symmetry, leading to a nematic-like state [22].

The phase diagram: Thus far we have constructed the Ginzburg-Landau expansion in small Δ/T_N. This expansion becomes less justified as we move towards zero temperature. To investigate the behavior at arbitrary T we calculate numerically the full Free energies of the various SDW states from (3.5). Upon doing this, we find that the $3Q$ uniaxial state has the lowest Free energy over a wide range of intermediate temperatures, roughly between $T_N/2$ and T_N, but undergoes a first order transition at a lower temperature to the insulating chiral SDW state discussed in earlier works [3, 7, 10]. We show the Free energy profile in Fig. 3-3b. We found this behavior both for graphene and for fermions on a triangular lattice. Intuitively, the chiral SDW state wins at the lowest T because it has spin-degenerate excitations and

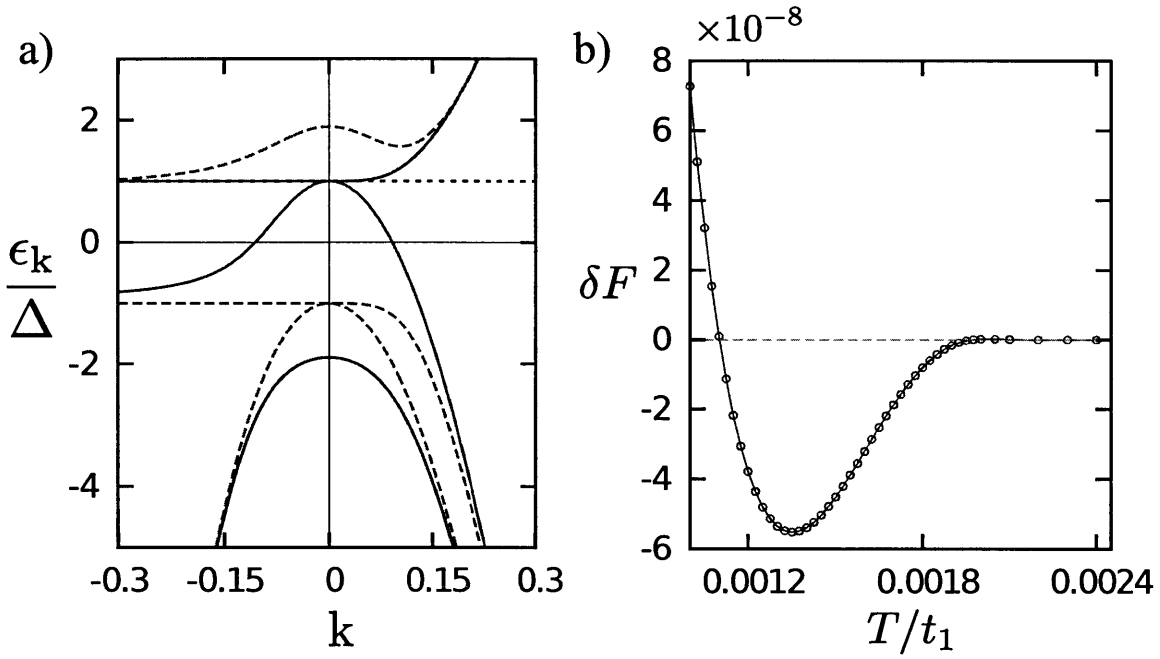

Figure 3-3: (Color online) a) Excitation spectrum $\varepsilon_k = E_k - \delta\mu$ of the $3Q$ uniaxial state. Negative k are along the FS, positive k are along the BZ boundary in the original BZ (along k_x in the reduced zone). Placing the chemical potential at $\delta\mu = -\Delta$ ensures that four bands lie below the chemical potential (horizontal dotted line) and two lie above for all $\mathbf{k}$, irrespective of the value of Δ. Thus the choice $\mu = -\Delta$ conserves electron number. Excitations with spin projection opposite to $\mathbf{\Delta}$ are in blue (solid), along $\mathbf{\Delta}$ are in red (dashed) lines. Note that gapless excitations arise in the spin-down branch only. b) Free energy difference $\delta F = F_{\text{uniaxial}} - F_{\text{chiral}}$ between the $3Q$ uniaxial SDW state and the chiral state, evaluated in the mean field approximation for the honeycomb lattice Hubbard model with $g_2 = g_3 = U = 1.7t_1$ ($T_N \sim 0.002t_1$). The $3Q$ uniaxial state has lower Free energy over a wide range of intermediate temperatures, but at the smallest T the non-coplanar, chiral state, studied in earlier works [3, 7, 10], has lower Free energy.

opens a full spectral gap, unlike the half-metal state.

The Free energy profile in Fig. 3-3b is for weak/moderate coupling, when $T_N/t_1 \ll 1$. At $T_N \sim t_1$, the phase diagram is more complex. For completeness, we discuss the forms of Z_i and the phase diagram at $T_N \sim t_1$ in the supplementary material [16]. The ordering temperature T_N depends sensitively on the strength of the microscopic interactions. For graphene doped near the saddle point we estimate $T_N \approx 3 - 30K$, whereas $t_1 \approx 3eV$ [15]. Thus, at least for doped graphene, we should be decisively in the limit $T_N/t_1 \ll 1$, where our calculations apply.

Conclusion: We considered in this work the SDW instability on the honeycomb and triangular lattices, when doped to the saddle points of the dispersion. The SDW instability is subleading to a $d-$wave superconducting instability at weak coupling, but becomes the leading instability if superconductivity is suppressed. We found that if the SDW ordering temperature T_N is much smaller than the fermionic bandwidth, then a uniaxial SDW order develops simultaneously at three inequivalent nesting vectors. This has an order parameter manifold $O(3) \times Z_4$ and corresponds to the ordering pattern shown in Fig.3-1. Such a state can only be obtained from an model of itinerant electrons with interactions, and not from a spin model of local moments. We found that such SDW state is a half-metal in which gapless excitations exist in one spin branch only. Such a state may be beneficial for nanoscience applications particularly because charge currents will necessarily also be spin currents, which allows for electrical control of the latter.

3.2 Spin density wave physics taking into account thermal fluctuations

Magnetic phases without long-range spin order exhibit unusual elementary excitations and thermodynamic properties. Unlike the common paramagnetic phase, they break a symmetry related to emergent degrees of freedom arising from the collective magnetic behavior of the system. These phases usually appear in frustrated systems

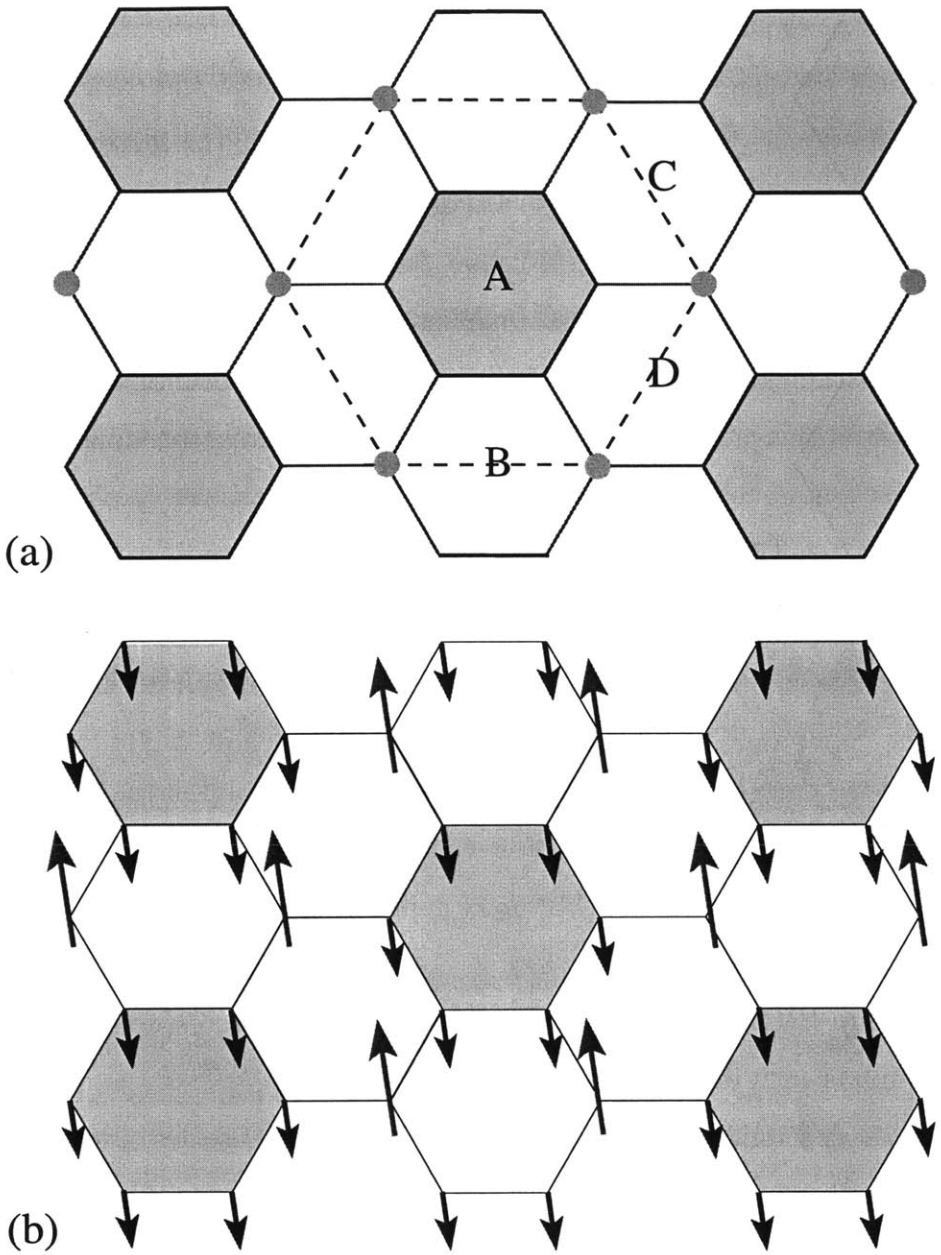

Figure 3-4: (Color online) (a) Schematic representation of the emergent Z_4 symmetry-breaking paramagnetic phase. The blue links are ferromagnetic bonds, while the red links denote antiferromagnetic bonds. The system still has hexagonal symmetry, i.e. the C_3 rotational symmetry is preserved, but the unit cell now contains 8 sites, i.e. the translational symmetry is broken. There is no long-range spin order, and the Z_4 symmetry corresponds to the four inequivalent choices for the center of the quadrupled unit cell (points A, B, C, and D). (b) The uniaxial SDW state. Among the eigth sites of the enlarged unit cell, two have large spin moment $3\mathbf{\Delta}$ (red arrows) and six have small moment $-\mathbf{\Delta}$ (blue arrows in the shaded hexagons). The total spin on each unit cell is zero. The only additional symmetry broken with respect to the state in panel (a) is the $O(3)$ spin-rotational symmetry.

with localized spins, as a result of the interplay between frustrated interactions and fluctuations. Canonical examples include the Ising-nematic phase of the extended Heisenberg model on the square lattice [17], the spin-nematic phase of the Heisenberg model on the kagome lattice [18], and the magnetic-charge ordered phase in kagome spin ice [19].

Itinerant magnetic systems - where the electronic interactions are at most moderate - can also display paramagnetic phases with unusual broken symmetries. This is believed to be the case in the ruthenates [20] and in the iron-based superconductors [21, 22, 23]. In these systems the emergent paramagnetic phase breaks the rotational symmetry of the lattice, while the spin-rotational symmetry remains preserved.

In this section, we present an unusual itinerant paramagnetic phase, which breaks the translational symmetry without changing the point-group symmetry of the lattice. This magnetic phase arises in doped triangular and honeycomb lattices and could potentially be realized in single-layer graphene doped to the saddle point of the band-structure (3/8 or 5/8 filling) [1, 2]. The divergent density of states at 3/8 or 5/8 filling combined with a near-nested Fermi surface (FS) make doped graphene a fertile ground for exploring nontrivial many-body states [5, 3, 4, 7, 8, 6, 9]. It has been established by renormalization-group (RG) analysis that the chiral d-wave superconductivity is the leading weak-coupling instability at exactly 3/8 or 5/8 filling [5], but the spin-density wave (SDW) susceptibility is the largest at intermediate RG scales, winning over superconductivity slightly away from 3/8 or 5/8 filling [6].

The SDW order immediately below the instability is uniaxial [24], and the magnetic unit cell contains eight sites with non-uniform magnetic moments - six sites have moment $-\mathbf{\Delta}$ while two sites have moment $3\mathbf{\Delta}$, see Fig. 3-4(b). This state breaks not only the $O(3)$ spin-rotational symmetry, but also a discrete Z_4 symmetry related to the four inequivalent choices for the position of the large $3\mathbf{\Delta}$ spin moments in the quadrupled unit cell. These four inequivalent spin configurations transform into each other upon translation of the origin of coordinates to neighboring hexagons - the points A, B, C, and D in Fig. 3-4(a). Thus, breaking the Z_4 symmetry corresponds to breaking the translational symmetry of the lattice.

Here we show that at finite temperatures the uniaxial SDW order can be preempted by a phase transition to an emergent paramagnetic phase that breaks *only* the Z_4 part of the order parameter manifold. The Z_4 symmetry breaking transition falls into the universality class of the four-state Potts model in two dimensions. In the Z_4-ordered phase, one quarter of the hexagons contain only ferromagnetic bonds and form an enlarged triangular lattice (see Fig. 3-4). Consequently, the phase preserves the lattice rotational symmetry but breaks the lattice translational symmetry, even though $\langle \mathbf{S}_i \rangle = 0$. Experimentally, these real-space modulations can be readily probed by scanning tunneling microscopy (STM). Furthermore, due to its magnetic origin, this phase also has stronger spin fluctuations than the paramagnetric phase, which can probed by neutron scattering or nuclear magnetic resonance (NMR).

The uniaxial SDW order. The FS of graphene near 3/8 or 5/8 filling contains three saddle points with nearly vanishing Fermi velocity (the M points in Fig. 3-5(a)). The density of states near these points is strongly enhanced, giving rise to an SDW instability already at weak coupling. Pairs of inequivalent M points are connected by three commensurate nesting vectors $\mathbf{Q}_1 = (0, 2\pi/\sqrt{3})$ and $\mathbf{Q}_{2,3} = (\mp\pi/3, -\pi/\sqrt{3})$. The collective magnetic degrees of freedom associated with SDW ordering at these nesting vectors are described by three bosonic vector fields [24]: $\mathbf{\Delta}_i = \mathbf{\Delta}_{a,b} = \gamma \sum_{\mathbf{k}} \langle c^\dagger_{a,\alpha} \boldsymbol{\sigma}_{\alpha\beta} c_{b,\beta} \rangle$, where γ is the SDW coupling and $c^\dagger_{a,\alpha}$ creates electrons with spin α around saddle point M_a.

In the uniaxial state, which minimizes the free energy in a wide T range below the SDW transition, all $\mathbf{\Delta}_i$ are directed along the same axis and have equal magnitude [24]. The uniaxial state with $(\mathbf{\Delta}_1, \mathbf{\Delta}_2, \mathbf{\Delta}_3) = (\Delta, \Delta, \Delta)\,\hat{\mathbf{n}}$ is shown in Fig. 3-4. There exists, however, three other states with the same energy, $(\Delta, -\Delta, -\Delta)\hat{\mathbf{n}}$, $(-\Delta, \Delta, -\Delta)\hat{\mathbf{n}}$, and $(-\Delta, -\Delta, \Delta)\hat{\mathbf{n}}$. These states can *not* be obtained from the one shown in Fig. 3-4(b) by a global spin rotation. Instead, these four degenerate states are related by a translational Z_4 symmetry. The uniaxial state (Fig.1b) chooses a particular direction of $\hat{\mathbf{n}}$ and also one of the four states, such that the total broken symmetry is $O(3) \times Z_4$.

Order parameters of the preemptive Z_4 phase. To investigate the potential pre-

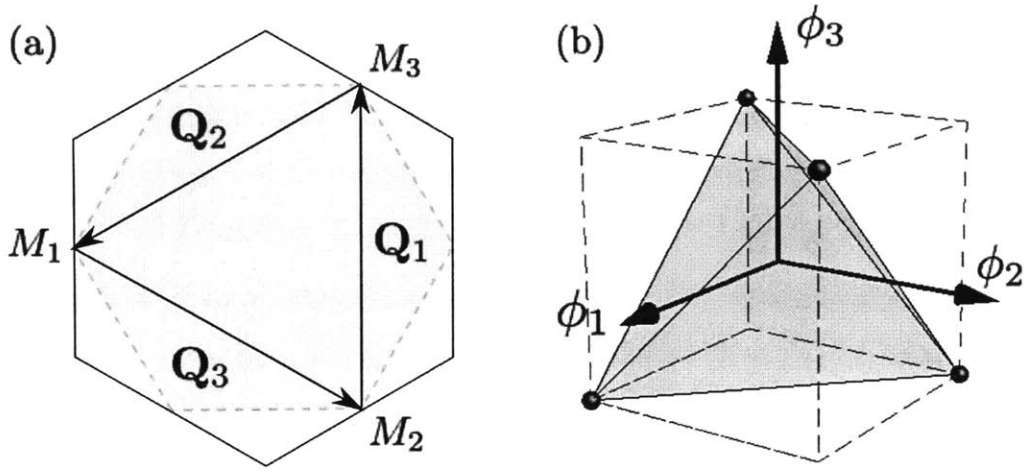

Figure 3-5: (Color online) (a) The Fermi surface at the doping level of interest is a hexagon inscribed within the hexagonal Brillouin zone (BZ), for both honeycomb and triangular lattices. The FS has three saddle points M_a located at the corners of the hexagon. Pairs of inequivalent saddle points are connected by three inequivalent nesting vectors $\mathbf{Q}_1 = (0, 2\pi/\sqrt{3})$, and $\mathbf{Q}_{2,3} = (\mp\pi/3, -\pi/\sqrt{3})$. (b) Order-parameter space of the preemptive Z_4 phase. In the ordered phase the vector order parameter $\boldsymbol{\varphi} = (\varphi_1, \varphi_2, \varphi_3)$ points toward one of the four corners of a regular tetrahedron.

emptive phase which breaks only the Z_4 symmetry, we start with the effective action for the $\boldsymbol{\Delta}_i$ fields. Quite generally, the expansion involves irreducible representations of $\boldsymbol{\Delta} = (\boldsymbol{\Delta}_1, \boldsymbol{\Delta}_2, \boldsymbol{\Delta}_3)$ and has the form

$$\begin{aligned} S[\boldsymbol{\Delta}_i] = r_0 \sum_i \int_x |\boldsymbol{\Delta}_i|^2 + \frac{u}{2} \int_x \left(|\boldsymbol{\Delta}_1|^2 + |\boldsymbol{\Delta}_2|^2 + |\boldsymbol{\Delta}_3|^2\right)^2 \\ + \frac{v}{2} \int_x \Big[\left(|\boldsymbol{\Delta}_1|^2 + |\boldsymbol{\Delta}_2|^2 - 2|\boldsymbol{\Delta}_3|^2\right)^2 + 3\left(|\boldsymbol{\Delta}_1|^2 - |\boldsymbol{\Delta}_2|^2\right)^2 \Big] \\ - \frac{g}{2} \int_x \Big[(\boldsymbol{\Delta}_1 \cdot \boldsymbol{\Delta}_2)^2 + (\boldsymbol{\Delta}_2 \cdot \boldsymbol{\Delta}_3)^2 + (\boldsymbol{\Delta}_3 \cdot \boldsymbol{\Delta}_1)^2 \Big] + \cdots \end{aligned} \tag{3.11}$$

where $r_0 \propto (T - T_N)$, and T_N is the mean-field SDW transition temperature. The coefficients u, v, g were calculated in Ref. [24] and found to be positive, with $v/u = 1/\log(W/T_N) \ll 1$ and $g/u = (T_N/W)/\log(W/T_N) \ll 1$, where W is the bandwidth. Minimizing $S[\boldsymbol{\Delta}_i]$ with respect to $\boldsymbol{\Delta}_i$ and neglecting momentarily the fluctuations of the $\boldsymbol{\Delta}_i$ fields, we see that $v > 0$ implies that the magnitudes of $\boldsymbol{\Delta}_i$ are equal, while $g > 0$ makes all $\boldsymbol{\Delta}_i$ collinear. As a result, we obtain one of the four uniaxial

SDW states described above.

The phase in which Z_4 is broken but $O(3)$ is preserved corresponds to $\langle \mathbf{\Delta}_i \cdot \mathbf{\Delta}_j \rangle \neq 0$ and $\langle \mathbf{\Delta}_i \rangle = 0$. A proper order parameter for this phase is thus the triplet $\boldsymbol{\varphi} = (\varphi_1, \varphi_2, \varphi_3)$, where $\varphi_i = g\,(\mathbf{\Delta}_j \cdot \mathbf{\Delta}_k)$ and (ijk) are cyclic permutation of (123). A preemptive phase for the uniaxial SDW order have $\langle \varphi_i \rangle = \pm\varphi$, with the constraint $\varphi_1\varphi_2\varphi_3 > 0$. To investigate whether such state emerges we go beyond the mean-field approximation for $S[\mathbf{\Delta}_i]$ by including fluctuations of the $\mathbf{\Delta}_i$ fields, and re-express the action in terms of the collective variables φ_i. We analyze this action assuming that fluctuations of φ_i are weak and check whether a non-zero $\langle \varphi_i \rangle$ emerges above the actual T_N.

Effective action in terms of $\boldsymbol{\varphi}$. To obtain the action in terms of φ_i we employ the standard Hubbard-Stratonovich transformation [22] and introduce six auxiliary fields, one for each quartic term. We verified that the only fields with non-zero mean value at finite T are the three fields $\varphi_i \propto \mathbf{\Delta}_j \cdot \mathbf{\Delta}_k$ associated with the Z_4 symmetry breaking and the field $\psi \propto \mathbf{\Delta}_1^2 + \mathbf{\Delta}_2^2 + \mathbf{\Delta}_3^2$ associated with the Gaussian fluctuations of the $\mathbf{\Delta}_i$ fields. With the aid of these auxiliary fields, action (3.11) becomes quadratic in the fields $\mathbf{\Delta}_i$, which can then be integrated out. Because we allow the $\mathbf{\Delta}_i$ fields to fluctuate, we include non-uniform space/time configurations, replacing $\mathbf{\Delta} \rightarrow \mathbf{\Delta}_{q,\omega}$ and $r_0 \rightarrow r_0 + q^2 + \gamma|\omega_m|$ in Eq. (3.11), with $\omega_m = 2m\pi T$. Since near finite temperature phase transitions the thermal fluctuations are the most relevant, we restrict our analysis to the $\omega_m = 0$ component. The new action now depends only on the ψ and $\boldsymbol{\varphi}$ fields:

$$S[\psi, \boldsymbol{\varphi}] = \int_x \left(\frac{|\boldsymbol{\varphi}|^2}{2g} - \frac{\psi^2}{2u} \right) + \frac{3}{2} \int_q \log\left(\det \mathcal{X}\right). \tag{3.12}$$

where $|\boldsymbol{\varphi}|^2 = \sum_i \varphi_i^2$, $\int_q = \frac{T}{4\pi^2} \int d^2q$, and the matrix $\mathcal{X}$ is

$$\mathcal{X} = \begin{pmatrix} \tilde{\chi}_q^{-1} & -\varphi_3 & -\varphi_2 \\ -\varphi_3 & \tilde{\chi}_q^{-1} & -\varphi_1 \\ -\varphi_2 & -\varphi_1 & \tilde{\chi}_q^{-1} \end{pmatrix}, \tag{3.13}$$

with renormalized $\tilde{\chi}_q^{-1} = r_0 + \psi + q^2 \equiv r + q^2$. In the absence of Z_4 symmetry-breaking, long-range SDW order sets in at $r = 0$, hence an intermediate phase exists if Z_4 symmetry is broken at some $r > 0$.

We assume that fluctuations of the fields ψ and φ_i are weak and treat $S[\psi, \boldsymbol{\varphi}] = S[r, \boldsymbol{\varphi}]$ in the saddle point approximation. This strategy can be rigorously justified if we extend the number of components of the $\boldsymbol{\Delta}_i$ fields from $N = 3$ to arbitrary N, rescale the coupling constants to $g \to g/N$ and $u \to u/N$, and take the limit $N \to \infty$. In this case, N appears as an overall factor in the action, justifying the saddle-point approximation.

The four possible realizations for the Z_4 symmetry breaking correspond to $\varphi_i = \pm\varphi$ subject to the constraint $\varphi_1\varphi_2\varphi_3 > 0$. Substituting this in Eq. (3.12), integrating over d^2q, and absorbing the factor T into the couplings, we obtain:

$$\begin{aligned} \frac{S[r,\varphi]}{NV} &= -\frac{(r-r_0)^2}{2u} + \frac{3\varphi^2}{2g} + \frac{3r}{8\pi} \\ &+ \frac{1}{8\pi}\left[(r-2\varphi)\log\frac{\Lambda^2}{r-2\varphi} + 2(r+\varphi)\log\frac{\Lambda^2}{r+\varphi}\right], \end{aligned} \tag{3.14}$$

where V is the volume of the system and Λ is the upper cutoff. Differentiating Eq. (3.14) with respect to r and φ yields the coupled saddle-point equations:

$$r = r_0 + \frac{\bar{u}}{2}\log\frac{\Lambda^6}{(r-2\varphi)(r+\varphi)^2}, \tag{3.15}$$

$$\varphi = \bar{g}\log\left(\frac{r+\varphi}{r-2\varphi}\right), \tag{3.16}$$

where the rescaled parameters are $\bar{u} = u/4\pi$ and $\bar{g} = g/12\pi$. For $\varphi = 0$ (i.e., when Z_4 is unbroken), Eq. (3.15) becomes the familiar equation $r + 3\bar{u}/(2\log\Lambda/r) = r_0$ whose solution $r = \tilde{r}$ is positive for arbitrary r_0, i.e. for any non-zero T. This is an obvious consequence of the Mermin-Wagner theorem, which prohibits $O(3)$ symmetry breaking in two dimensions at finite T. However, the discrete Z_4 symmetry can be broken at finite T.

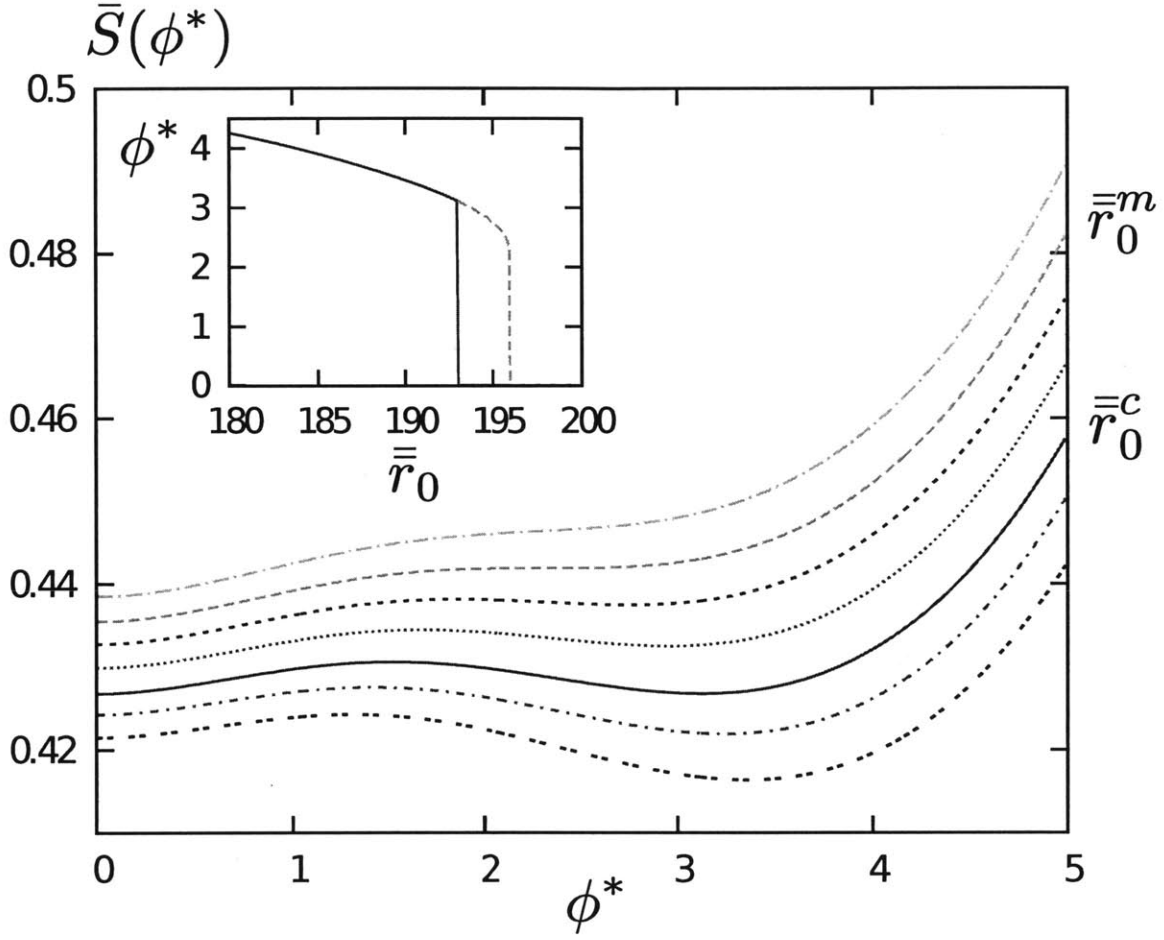

Figure 3-6: (Color online) (a) The effective action $\bar{S}(\tilde{\varphi}) = S[r, \tilde{\varphi}]/NV\bar{g}$ as a function of $\tilde{\varphi}$ for $\alpha = 100$ and various $\bar{r}_0$. The different curves correspond to $\bar{r}_0 = 197$, 195.94 ($\bar{r}_0^m$), 195, 194, 192.9 ($\bar{r}_0^c$), 192, and 191 (from top to bottom). (b) The (red) solid curve shows the order parameter $\tilde{\varphi}$ as a function $\Delta\bar{r}_0 = \bar{r}_0 - \bar{r}_0^c$. The (green) dashed curve shows the expectation value $\tilde{\varphi}$ of the metastable phase for $\bar{r}_0 < \bar{r}_0^m$. (c) The inverse susceptibility $1/\chi_s = r - 2\varphi$ of the singlet mode as a function of $\Delta\bar{r}_0$.

Assuming that φ is non-zero and eliminating r from Eqs. (3.16) and (3.15), we obtain the self-consistent equation for the rescaled order parameter $\tilde{\varphi} = \varphi/\bar{g}$:

$$\tilde{\varphi}\left(\frac{2e^{\tilde{\varphi}}+1}{e^{\tilde{\varphi}}-1}\right) + \frac{\bar{u}}{\bar{g}}\left[\tilde{\varphi} + \frac{3}{2}\log\left(\frac{3\tilde{\varphi}}{e^{\tilde{\varphi}}-1}\right)\right] = \bar{r}_0, \tag{3.17}$$

where $\bar{r}_0 = r_0/\bar{g} + (3\bar{u}/2\bar{g})\log\Lambda^2 \propto (T - \bar{T}_N)$, and $\bar{T}_N$ is the rescaled mean-field T_N. The ratio $\lambda = \bar{u}/\bar{g}$ is large, of the order of W/T_N The analysis of Eq. (3.17) for $\lambda \gg 1$ shows that the first non-zero solution appears below a particular $\bar{r}_0^m \approx \frac{3}{2}\lambda \ln 3$ at $\tilde{\varphi} \approx 2.15 + 14.2/\lambda$, indicating that the transition is first order.

At the temperature corresponding to $\bar{r}_0^m$, the effective action first develops a local minimum which over some range of $\bar{r}_0 < \bar{r}_0^m$ is a metastable state. To find when the actual transition occurs, we solve Eq. (3.15) for $r(\varphi)$, substitute the result into (3.14) and obtain the effective action $S(\tilde{\varphi})$ for which $\bar{r}_0$ is a parameter and Eq. (3.16) is the saddle-point solution. The behavior of $S(\tilde{\varphi})$ for various $\bar{r}_0$ is shown in Fig. 3-6(a): at sufficiently large $\bar{r}_0$, it increases monotonically with $\tilde{\varphi}$ and its only minimum is at $\tilde{\varphi} = 0$, implying that Z_4 is unbroken. As $\bar{r}_0$ is reduced to $\bar{r}_0^m$, the function $S(\tilde{\varphi})$ develops an inflection point, which at smaller $\bar{r}_0$ splits into a maximum and a minimum. Upon further decreasing T, the value of $S(\tilde{\varphi})$ at this minimum becomes equal to $S(0)$ at some $\bar{r}_0 = \bar{r}_0^c$. For $\bar{r}_0$ smaller than $\bar{r}_0^c$, the minimum of the free energy jumps to a finite $\tilde{\varphi} \neq 0$. Once this happens, the system spontaneously chooses one out of four states with the same $\tilde{\varphi}$, and the Z_4 symmetry is broken. We plot the minimum $\tilde{\varphi}$ versus $\bar{r}_0$ in Fig. 3-6(b).

That the breaking of the translational symmetry occurs in the saddle-point approximation via a first-order transition can also be seen by expanding the effective action $S(\tilde{\varphi})$ in powers of $\tilde{\varphi}$. For $\lambda \gg 1$, we obtain

$$\frac{S(\tilde{\varphi})}{\lambda} = \left(\frac{r_0}{u} + \frac{3}{2}\ln\frac{\Lambda^2}{3}\right)\tilde{\varphi}^2 - \frac{1}{12}\tilde{\varphi}^3 + \frac{1}{16}\tilde{\varphi}^4 + \cdots, \tag{3.18}$$

Clearly, the presence of the $\tilde{\varphi}^3$ term implies that the transition is first order. We note that $\tilde{\varphi}^3$ is the only odd-power term in $S(\tilde{\varphi})$, as all higher-order terms have even powers.

To analyze whether the discontinuous Z_4 transition triggers a first-order SDW transition, we obtain the eigenvalues of the spin susceptibility matrix $\hat{\chi}$ in (3.13), which correspond to a singlet and a doublet mode:

$$\chi_s = \frac{1}{r - 2\varphi}, \qquad \chi_d = \frac{1}{r + \varphi}. \tag{3.19}$$

If either $r - 2\varphi$ or $r + \varphi$ jumped to a negative value at the Z_4 transition, then the breaking of Z_4 would induce a simultaneous breaking of the $O(3)$ symmetry [22]. However, it follows from (3.16) that both χ_s and χ_d remain positive when φ jumps to a finite value, i.e. breaking the Z_4 symmetry does not induce SDW order (see Fig. 3-6(c)). We verified that this holds also in $d = 2 + \varepsilon$ dimensions by a calculation similar to that in [22].

Beyond mean-field, 4-state Potts model. At a finite N, the effective action (3.18) for our Z_4 transition has the same form as the action of the four-state Potts model [27], implying that both transitions belong to the same universality class. We can use this to go beyond the saddle-point solution and understand how the Z_4 transition is affected by fluctuations. The four-state Potts model in 2D does exhibit a transition, i.e. the preemptive Z_4 ordering is not destroyed by fluctuations [27]. Interestingly, however, fluctuations transform the first-order transition into a second-order transition, although with a rather small critical exponent $\beta = 1/12$ for $\varphi \sim (T_c - T)^\beta$ (Ref. [27]). A small β implies that the order parameter sharply increases below the critical temperature, and in practice this behavior is almost undistinguishable from that in the first-order transition.

Experimental manifestations. As spin rotational symmetry is preserved in the preemptive Z_4 phase, no magnetic Bragg peaks are to be observed in neutron scattering experiments. On the other hand, since the charge density $\rho(\mathbf{r})$ and the Casimir operator $\mathbf{S}^2(\mathbf{r})$ have the same symmetry, a spatial modulation of the latter induces a modulation in the charge density. Given the 2D character of graphene, such a superlattice structure can be directly probed by STM. The additional Bragg peaks due to the quadrupled unit cell should also be detectable by scattering measurements. Local

probes such as NMR can measure the different on-site fluctuating magnetic moments of the Z_4 phase, since the size of the local moment controls the linewidth of the NMR signal. We thus expect to see two different linewidths coming from the 3Δ and the Δ sites.

The order parameter φ can also be inferred by measuring the static magnetic susceptibility χ at any of the three nesting vectors. In the absence of $O(3)$ breaking, we have $\chi(\bar{r}_0) = (2\chi_d + \chi_s)/3$, where $\chi_{s,d}$ are given by (3.19). Once the order parameter φ jumps to a finite value below the transition, so does the susceptibility:

$$\chi(\bar{r}_0) = \frac{1}{\tilde{r}}\left[1 + \left(\frac{\varphi}{\tilde{r}}\right)^2 + \cdots\right]$$

where $\tilde{r}$ is the value of r at $\varphi = 0$. This provides a direct method for detecting the order parameter φ. The jump of the static susceptibility (i.e. of the spin correlation length) also affects the electronic spectrum. For larger correlation length the system can develop precursors to the SDW order, which in turn give rise to a pseudogap in the electronic spectral function, at the energy where the gap develops in the SDW state. This pseudogap can be probed in photoemission experiments in the same way as it was proposed in the Fe-pnictides [22].

Conclusion. We discussed in this work the intriguing possibility of an emergent paramagnetic phase with spontaneously broken translational symmetry for properly doped fermions on triangular and hexagonal lattices. This unique state emerges from a preemptive phase transition which breaks only a discrete translational Z_4 lattice symmetry but preserves $O(3)$ spin-rotational invariance. We demonstrated that this phase exists in 2D systems and by continuity should exist in anisotropic 3D systems. We argued that such a phase should be observed in STM, NMR, neutron scattering, and photoemission experiments.

Bibliography

[1] A. H. Castro Neto, F. Guinea, N. M. R. Peres, K. S. Novoselov and A. K. Geim, Rev. Mod. Phys. **81**, 109-162 (2009).

[2] J. L. McChesney, A. Bostwick, T. Ohta, T. Seyller, K. Horn, J. Gonzalez and E. Rotenberg, Phys. Rev. Lett. **104**, 136803 (2010).

[3] T. Li, cond-mat: 1103.2420 (2011).

[4] D. Makogon, R. van Gelderen, R. Roldan and C. M. Smith, Phys. Rev. B 84, 125404 (2011)

[5] R. Nandkishore, L. Levitov and A. Chubukov, Nature Physics 8, 158-163 (2012)

[6] M. Kiesel *et al.*, arXiv: 1109.2953 (2011).

[7] W. S. Wang *et al.*, Phys. Rev. B 85, 035414 (2012)

[8] B. Valenzuela and M. A. H. Vozmediano, New. J. Phys. **10** 113009 (2008).

[9] J. Gonzalez, Phys. Rev. B **78**, 205431 (2008).

[10] I. Martin and C. D. Batista, Phys. Rev. Lett. **101**, 156402 (2008).

[11] T. Li, arXiv: 1001.0620 (2010).

[12] P. R. Wallace, Phys. Rev. **71**, 622-634 (1947).

[13] B. Altshuler, A. V. Chubukov, A. Dashevskii, A. Finkelstein and D. Morr, Europhys. Lett. **41**, 401 (1998).

[14] see e.g., R. M. Fernandes, A. V. Chubukov, J. Knolle, I. Eremin, and J. Schmalian Phys. Rev. B **85**, 024534 (2012) and references therein.

[15] In infinite 2D samples, $T_N = 0$, since $O(3)$ symmetry is restored by thermal fluctuations at any non-zero temperature in two dimensions. However, in a sample of finite size L, $T_N \approx T_{MF}/\log L/a$, where T_{MF} is the transition temperature neglecting thermal fluctuation effects, and a is the lattice scale. For samples of micron size, $\ln L/a \approx 7$, whereas T_{MF} was estimated in the supplement to Ref. [5] as $20 - 200K$. Thus, we arrive at our estimate $T_N \approx 3 - 30K$.

[16] The details are relegated to appendix C

[17] P. Chandra, P. Coleman, and A. I. Larkin, Phys. Rev. Lett. **64**, 88 (1990).

[18] J. T. Chalker, P. C. W. Holdsworth, and E. F. Shender, Phys. Rev. Lett. **68**, 855 (1992).

[19] G. Mller and R. Moessner, Phys. Rev. B **80**, 140409(R) (2009); G.-W. Chern, P. Mellado, and O. Tchernyshyov, Phys. Rev. Lett. **106**, 207202 (2011).

[20] R. A. Borzi, S. A. Grigera, J. Farrell, R. S. Perry, S. J. S. Lister, S. L. Lee, D. A. Tennant, Y. Maeno and A. P. Mackenzie, Science **315**, 214 (2007).

[21] J.-H. Chu, J. G. Analytis, K. De Greve, P. L. McMahon, Z. Islam, Y. Yamamoto, and I. R. Fisher, Science **329**, 824 (2010).

[22] R. M. Fernandes, A. V. Chubukov, J. Knolle, I. Eremin, and J. Schmalian, Phys. Rev. B **85**, 024534 (2012) and references therein.

[23] I. Eremin and A. V. Chubukov, Phys. Rev. B **81**, 024511 (2010).

[24] R. Nandkishore, G.-W. Chern, and A. V. Chubukov, Phys. Rev. Lett. 108, 227204 (2012)

[25] T. Li, arXiv: 1001.0620 (2010).

[26] R. K. P. Zia and D. J. Wallace, J. Phys. A **8**, 1495 (1975).

[27] F. Y. Wu, Rev. Mod. Phys. **54**, 235 (1982).

Chapter 4

Electron Interactions in Bilayer Graphene: Marginal Fermi Liquid Behavior and Zero-Bias Anomaly

We analyze the many-body properties of bilayer graphene (BLG) at charge neutrality, governed by long range interactions between electrons. Perturbation theory in a large number of flavors is used in which the interactions are described within a random phase approximation, taking account of dynamical screening effect. Crucially, the dynamically screened interaction retains some long range character, resulting in $\log^2$ *renormalization of key quantities. We carry out the perturbative renormalization group calculations to one loop order, and find that BLG behaves to leading order as a marginal Fermi liquid. Interactions produce a log squared renormalization of the quasiparticle residue and the interaction vertex function, while all other quantities renormalize only logarithmically. We solve the RG flow equations for the Green function with logarithmic accuracy, and find that the quasiparticle residue flows to zero under RG. At the same time, the gauge-invariant quantities, such as the compressibility, remain finite to* $\log^2$ *order, with subleading logarithmic corrections. The key experimental signature of this marginal Fermi liquid behavior is a strong suppression of the tunneling density of states, which manifests itself as a zero bias anomaly in tunneling experiments in a regime where the compressibility is essentially unchanged from the non-interacting value.*

4.1 Introduction

Bilayer graphene (BLG), due to its unique electronic structure of a two dimensional gapless semiconductor with quadratic dispersion [1], offers an entirely new setting for investigating many body phenomena. In sharp contrast to single layer graphene, the density of states in BLG does not vanish at charge neutrality, and thus even arbitrarily weak interactions can trigger phase transitions. Theory predicts instabilities to numerous strongly correlated gapped and gapless states in BLG [2, 3, 4, 6, 5]. These instabilities have been analyzed in models with unscreened long-range interactions [2], dynamically screened long-range interactions [3] and in models where the interactions are treated as short range [6, 4, 5]. Irrespective of the form of the interaction, the instability develops only logarithmically with the energy scale. However, dynamically screened Coulomb interactions have been shown to produce $\log^2$ renormalization of the self energy[9] and vertex function [3]. Such strong renormalization can result in significant departures from non-interacting behavior on energy scales much greater than those characteristic for the onset of gapped states. However, there is as yet no systematic treatment of the $\log^2$ divergences. In this paper, we provide a systematic treatment of the effects of dynamically screened Coulomb interactions, focusing on the renormalisation of the Green function, and using the framework of the perturbative renormalization group (RG).

We analyze the RG flow perturbatively in the number of flavors, given by $N = 4$ in BLG. We use perturbation theory developed about the non-interacting fixed point, and calculate the renormalization of the fermion Green function and of the Coulomb interactions. We demonstrate that the quasiparticle residue and the Coulomb vertex function undergo $\log^2$ renormalization, while all other quantities renormalize only logarithmically. The quasiparticle residue and the Coulomb vertex function, moreover, are not independent, but are related by a Ward identity which stems from gauge invariance symmetry. Therefore, at $\log^2$ order, BLG behaves as a marginal Fermi liquid.

We solve the RG flow equations with logarithmic accuracy, finding that the quasi-

particle residue flows to zero under RG. This behavior manifests itself in a zero bias anomaly in the tunneling density of states (TDOS). We conclude by extracting the sub-leading (single log) renormalization of the electron mass, as a correction to the log square RG. This calculation allows us to predict the interaction renormalization of the electronic compressibility in BLG, a quantity which is interesting both because it is directly experimentally measurable, and because it allows us to contrast the slow single log renormalization of the compressibility with the fast $\log^2$ renormalization of the TDOS.

The structure of the perturbative RG for BLG has strong similarities to the perturbative RG treatment of the one dimensional Luttinger liquids [4, 11, 12, 13]. We recall that in the Luttinger liquids, the Green function acquires an anomalous scaling dimension, which manifests itself in a power law behaviour of a quasiparticle residue that vanishes on shell. In addition, the electronic compressibility in the Luttinger liquids remains finite even as the quasiparticle residue flows to zero. Finally, in the Luttinger liquids, there are logarithmic divergences in Feynman diagrams describing scattering in the particle-particle and particle hole channels, corresponding to mean field instabilities to both Cooper pairing and charge density wave ordering. However, when both instabilities are taken into account simultaneously within the framework of the RG, they cancel each other out, so that there is no instability to any long range ordered phase at low energies [11].

Exactly the same behavior follows from our RG analysis of BLG, including the cancellation of the vertices responsible for the pairing and charge density ordering. However, the diagrams in this instance are $\log^2$ divergent, and even after the leading $\log^2$ divergences are canceled out, there remains a subleading single log instability. Nevertheless, this single log instability manifests itself on much lower energy scales than the $\log^2$ RG flow. Therefore, over a large range of energies, bilayer graphene can be viewed as a two dimensional analogue of the one dimensional Luttinger liquids.

Our treatment of the $\log^2$ renormalization in BLG is somewhat reminiscent of the situation arising in two-dimensional disordered metals[14]. In the latter, the $\log^2$ divergences of the Green function and of the vertex function stem from the properties

of dynamically screened Coulomb interactions, which exhibit "unscreening" for the transferred frequencies and momenta such that ω/q^2 is large compared to the diffusion coefficient. Furthermore, the divergent corrections to the Fermi-liquid parameters, as well as conductivity, compressibility and other two-particle quantities in these systems, are only logarithmic. This allows to describe the RG flow of the Green function due to the $\log^2$ divergences by a single RG equation [15] of the form

$$\partial G/\partial \xi = -\frac{\xi}{4\pi^2 g} G, \tag{4.1}$$

where g is the dimensionless conductance. The suppression of the quasiparticle residue, described by this equation, manifests itself in a zero-bias anomaly in the tunneling density of states, readily observable by tunneling measurements.

4.2 Dynamically screened interaction

We begin by reviewing some basic facts about BLG. BLG consists of two AB stacked graphene sheets (Bernal stacking). The low-energy Hamiltonian can be described in a 'two band' approximation, neglecting the higher bands that are separated from the Dirac point by an energy gap $W \sim 0.4$ eV [1]. There is four-fold spin/valley degeneracy. The wavefunction of the low energy electron states resides on the A sublattice of one layer and the B sublattice of the other layer. The non-interacting spectrum consists of quadratically dispersing quasiparticle bands $E_\pm = \pm p^2/2m$ with band mass $m \approx 0.054 m_e$. We work throughout at charge neutrality, when the Fermi surface consists of Fermi points. The discrete point-like nature of the Fermi surface is responsible for most of the similarities to the Luttinger liquids.

Although the canonical Hamiltonian has opposite chirality in the two valleys, a suitable unitary transformation on the spin-valley-sublatttice space brings the Hamiltonian to a form where there are four flavors of fermions, each governed by the same 2×2 quadratic Dirac-type Hamiltonian [7]. We introduce the Pauli matrices that act on the sublattice space τ_i, and define $\tau_\pm = \tau_1 \pm i\tau_2$, and $p_\pm = p_x \pm i p_y$, and hence

write[1]

$$H = H_0 + \frac{e^2}{2\kappa}\sum_{\mathbf{x},\mathbf{x}'}\frac{n(\mathbf{x})n(\mathbf{x}')}{|\mathbf{x}-\mathbf{x}'|}, \tag{4.2}$$

$$H_0 = \sum_{\mathbf{p},\sigma}\psi^\dagger_{\mathbf{p},\sigma}\left(\frac{p_+^2}{2m}\tau_+ + \frac{p_-^2}{2m}\tau_-\right)\psi_{\mathbf{p},\sigma}. \tag{4.3}$$

Here $\sigma = 1,2,3,4$ is a flavour index, $n(\mathbf{x}) = \sum_\sigma n_\sigma(\mathbf{x})$ is the electron density, summed over spins, valleys and sublattices, while the dielectric constant κ incorporates the effect of polarization of the substrate. Note that the single-particle Hamiltonian H_0 takes the same form for each of the four fermion flavors, and is thus $SU(4)$ invariant under unitary rotations in the flavor space.

The Coulomb interaction sets a characteristic length scale and a characteristic energy scale ("Bohr radius and Rydberg energy")[3]:

$$a_0 = \frac{\hbar^2\kappa}{me^2} \approx 10\kappa\,\text{Å}, \qquad E_0 = \frac{e^2}{\kappa a_0} \approx \frac{1.47}{\kappa^2}\,\text{eV}. \tag{4.4}$$

In Eq.(4.2), we have approximated by assuming that the interlayer and intra-layer interaction are equal. This approximation may be justified by noting that the interlayer spacing $d \approx 3\,\text{Å}$ is much less than the characteristic lengthscale a_0, Eq.(4.4). Within this approximation, the Hamiltonian (4.2) is invariant under $SU(4)$ flavour rotations [7].

We note that for $\kappa \sim 1$ the energy E_0 value is comparable to the energy gap parameter $W \sim 0.4\,\text{eV}$ of the higher BLG bands (see Ref.[[8]] for a discussion of four band model of BLG). This suggests that there is some interaction induced mixing with the higher bands of BLG. However, since a four band analysis is exceedingly tedious, here we focus on the weak coupling limit $E_0 \ll W$, where the two band approximation, Eq.(4.2), is rigorously accurate. We perform all our calculations in this weak coupling regime, and then extrapolate the result to $E_0 \approx 1.47\,\text{eV}\kappa^{-2}$. Since

[1]We have performed a unitary transformation on the Hamiltonian, as outlined in Ref.[[7]], to clearly manifest the symmetries. As a consequence, our 'valley' and 'sublattice' variables are not the physical valley and sublattice variables, but are linear combinations thereof.

the low energy properties should be independent of the higher bands, we believe this approximation correctly captures, at least qualitatively, the essential physics in BLG. Meanwhile, since W is the maximum energy scale up to which the two band Hamiltonian, Eq.(4.2), is valid, we use W as the initial UV cutoff for our RG analysis.

We wish to obtain a RG flow for the problem (4.2) by systematically integrating out the high energy modes. However, the implementation of this strategy is complicated by the long range nature of the unscreened Coulomb interaction. Within perturbation theory, the long range interaction gives contributions which are relevant at tree level, making it difficult to come up with a meaningful perturbative RG scheme. Therefore, it is technically convenient to perform a two-step calculation, where we first take into account screening within the random-phase approximation (RPA), and then carry out an RG calculation with the RPA screened effective interaction. We emphasize that it is necessary to consider the full *dynamic* RPA screening of the Coulomb interaction, since a static screening approximation does not capture the effects we discuss below.

The dynamically screened interaction may be calculated by summing over the RPA series of bubble diagrams, to obtain a screened interaction. The RPA approach to screening may be justified by invoking the large number $N = 4$ of fermion species in BLG. The screened interaction takes the form

$$U(\omega, \mathbf{q}) = \frac{2\pi e^2}{\kappa|\mathbf{q}| - 2\pi e^2 \Pi(\omega, \mathbf{q})}. \tag{4.5}$$

Here $\Pi(\omega, \mathbf{q})$ is the non-interacting polarization function, which can be evaluated analytically[21, 3]. Here we will need an expression for $\Pi(\omega, \mathbf{q})$ in terms of Matsubara frequencies ω, derived in Ref.[[3]], where it was shown that the quantity $\Pi(\omega, \mathbf{q})$ depends on a single parameter $2m\omega/q^2$, and is well described by the approximate form

$$\Pi(\omega, \mathbf{q}) = -\frac{Nm}{2\pi} \frac{\ln 4 \frac{\mathbf{q}^2}{2m}}{\sqrt{(\frac{\mathbf{q}^2}{2m})^2 + u\omega^2}}, \quad u = \frac{4 \ln^2 4}{\pi^2}, \tag{4.6}$$

where $N = 4$ is the number of fermion species. The dependence (4.6) reproduces $\Pi(\omega, \mathbf{q})$ exactly in the limits $\omega \ll \mathbf{q}^2/2m$ and $\omega \gg \mathbf{q}^2/2m$, and interpolates accurately in between. We discover upon substituting Eq.(4.6) in Eq.(4.5) that the dynamically screened interaction is retarded in time, but crucially is only marginal at tree level. It therefore becomes possible to develop the RG analysis perturbatively in weak coupling strength, by taking the limit of $N \gg 1$.

Since the quantity $\Pi(\omega, \mathbf{q})$ vanishes when $q \to 0$, the RPA screened interaction (4.5) retains some long range character, exhibiting "unscreening" for $\omega \gg \mathbf{q}^2/2m$. This will lead to divergences in Feynman diagrams of a $\log^2$ character.

4.3 Setting up the RG

To calculate the RG flow of the Hamiltonian, Eq.(4.2), in the weak coupling regime, we begin by writing the zero-temperature partition function Φ as an imaginary-time functional field integral. We have

$$\Phi = \int D\psi^\dagger D\psi \exp\left(-S_0[\psi^\dagger, \psi] - S_1[\psi^\dagger, \psi]\right), \tag{4.7}$$

$$S_0 = \sum_\sigma \int \frac{d\omega d^2p}{(2\pi)^3} \psi^\dagger_{\sigma,\omega,\mathbf{p}} \left(\frac{-i\omega + H_0^\sigma(\mathbf{p})}{Z}\right) \psi_{\sigma,\omega,\mathbf{p}}, \tag{4.8}$$

$$S_1 = \frac{1}{2} \int \frac{d\omega d^2q}{(2\pi)^3} \Gamma^2 U(\omega, \mathbf{q}) n_{\omega,\mathbf{q}} n_{-\omega,-\mathbf{q}} + S_2. \tag{4.9}$$

Here the ψ fields are Grassman valued (fermionic) fields with flavour (spin-valley) index σ, while ω is a fermionic Matsubara frequency, Γ is a vertex renormalization parameter, Z is the quasiparticle residue, and $n_{\omega,\mathbf{q}}$ is the Fourier transform of the electron density, summed over spins, valleys and sublattices. The effective interaction $U(\omega, \mathbf{q})$ is given by Eq.(4.5). The term S_2 is included tentatively to represent more complicated interactions that may be generated under RG. In the bare theory, $\Gamma = 1$, $Z = 1$ and $S_2 = 0$. The theory is defined with the initial UV cutoff Λ_0. Since the two band model, Eq.4.2, is only justified on energy scales less than the gap $W \approx 0.4eV$ to the higher bands in BLG, we conservatively identify $\Lambda_0 = W$. Our main results

will be independent of Λ_0.

As we shall see, the RG flow will inherit the symmetries of the Hamiltonian, Eq.(4.2), strongly constraining the possible terms S_2. The relevant symmetries are particle-hole symmetry, time reversal symmetry, SU(4) flavour symmetry [7], and the symmetry of the Hamiltonian under the transformation $e^{i\theta\tau_3}R(\theta/2)$, where $R(\theta)$ generates spatial rotations, $R(\theta)p_\pm = e^{\pm i\theta}p_\pm$.

We will employ an RG scheme which treats frequency ω on the same footing as $p^2/2m$, in order to preserve the form of the free action Eq.(4.8) under RG. Thus, we integrate out the shell of highest energy fermion modes

$$\Lambda' < \sqrt{\omega^2 + \left(\frac{\mathbf{p}^2}{2m}\right)^2} < \Lambda, \tag{4.10}$$

and subsequently rescale $\omega \to \omega(\Lambda/\Lambda')$, $p \to p(\Lambda/\Lambda')^{1/z}$, where z is the dynamical critical exponent [12], which takes value $z = 2$ at tree level. Because the value $z = 2$ is not protected by any symmetry, it may acquire renormalization corrections. However, it will follow from our analysis that the quasiparticle spectrum does not renormalize at leading $\log^2$ order, so that the exponent z does not flow at leading order. We therefore use $z = 2$ for the rest of the paper, which corresponds to scaling dimensions $[\omega] = 1$ and $[p^2] = 1$. Under such an RG transformation, the Lagrangian density in momentum space has scaling dimension $[\mathcal{L}] = 2$, and we have tree level scaling dimensions $[\psi] = 1/2$ and $[\Gamma] = [Z] = 0$ respectively.

Given these tree level scaling dimension values, it can be seen that all potentially relevant terms arising as part of S_2 must involve four fermion fields. Indeed, any term involving more than four ψ fields will be irrelevant at tree level under RG, and may be neglected. The terms with odd numbers of ψ fields are forbidden by charge conservation, while the quadratic terms $\Delta_{ij}\psi_i^\dagger\psi_j$ cannot be generated under perturbative RG, since they break the symmetries of the Hamiltonian listed above[2]. Thus, the only potentially relevant terms that could arise under perturbative RG

[2]The symmetry of the Hamiltonian may be spontaneously broken. However, the energy scale for spontaneous symmetry breaking is set by the subleading single log flows [3] and is lower than the energy scale for the phenomena discussed in this paper.

take the form of a four point interaction which may be written as

$$S_2 = \frac{1}{2}\int d^3x d^3x' \Upsilon^{\sigma\sigma'}_{ijkl} \psi^\dagger_{\sigma,i}(x)\psi_{\sigma,j}(x)\psi^\dagger_{\sigma',k}(x')\psi_{\sigma',l}(x'), \tag{4.11}$$

where $x = (\mathbf{r}, t)$, $x' = (\mathbf{r}', t')$, Here Υ is an effective four particle vertex, which is marginal at tree level, the indices σ, σ' refer to the flavour (spin-valley) of the interacting particles, and i, j, k, l are sublattice indices.

The symmetries of the Hamiltonian, Eq.(4.2), impose strong constraints on the spin-valley-sublattice structure of the four point vertex Υ. Since the Coulomb interaction does not change fermion flavour (spin or valley), and the electron Green function is diagonal in flavour space, the vertex Υ cannot change fermion flavour. Moreover, the $SU(4)$ flavour symmetry of the Hamiltonian implies that Υ does not depend on the flavour index of the interacting particles, and we may therefore drop the indices σ, σ' in Eq.(4.11). Finally, the bare Hamiltonian (4.2) is invariant under combined pseudospin/spatial rotations through $e^{i\theta\tau_3}R(\theta/2)$. This symmetry further restricts the form of four point vertices in Eq.(4.11) to have sublattice structure Υ_{iijj} or Υ_{ijji} only [3]. That is, the allowed scattering processes are restricted to $(AA) \to (AA)$, $(AB) \to (AB)$ and $(AB) \to (BA)$. We note that the processes $(AB) \to (AB)$ and $(AB) \to (BA)$ are distinct, since the particles have flavour, and the interaction (4.5) is not short range.

Below we obtain the RG flow for bilayer graphene, working in the manner of Ref.[[12]]. We consider the partition function, Eq.(4.7), where the interaction is given by Eq.(4.5). Starting from this action, supplied with ultraviolet (UV) cutoff Λ_0, we systematically integrate out the shell of highest energy fermion modes, Eq.(4.10). We perform the integrals perturbatively in the interaction, Eq.(4.5). This corresponds to a perturbation theory in small $\Gamma^2 Z^2/N$. We carry out our calculations to one loop order, and examine the renormalization, in turn, of the electron Green function (Sec.4.4), the vertex function Γ (Sec.4.5) and the four point vertex Υ (Sec.4.6).

[3] In that, we ignore vertices of the form $\Upsilon_{AAAB}\partial_+^2$, $\Upsilon_{AABA}\partial_-^2$, and other similar terms, which are allowed by symmetries, but are irrelevant in the RG sense.

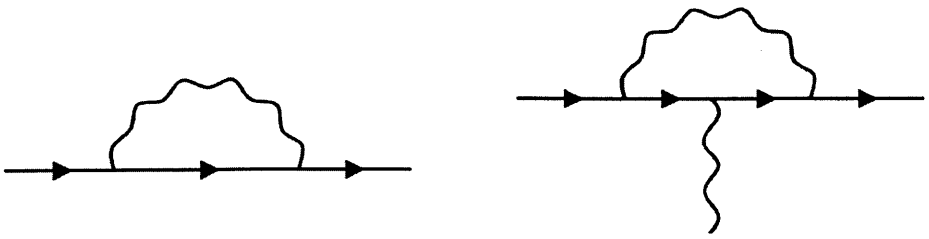

a) b)

Figure 4-1: Diagrammatic representation of self energy (a) and vertex correction (b) [Eqs.(4.14),(4.28)]. Straight lines with arrows represent fermion propagator, Eq.(4.13), wavy lines represent dynamically screened long range interaction, Eq.(4.5).

4.4 Self-consistent renormalization of the electron Green function

At first order in the interaction, the fermion Green function acquires a self energy Σ, represented diagrammatically (to leading order in the interaction) by Fig.4-1(a). A self-consistent expression for the change in the fermion propagator G is

$$\delta G(\omega, \mathbf{q}) = G_0(\omega, \mathbf{q})\Sigma(\omega, \mathbf{q})G_0(\omega, \mathbf{q}), \tag{4.12}$$

$$G_0(\omega, \mathbf{q}) = \frac{Z_0}{i\omega - H_0(\mathbf{q})}, \tag{4.13}$$

$$\Sigma(\omega, \mathbf{q}) = -\int \frac{d\varepsilon d^2p}{(2\pi)^3} \Gamma_0^2 U_{\varepsilon,\mathbf{p}} G_0(\varepsilon + \omega, \mathbf{p} + \mathbf{q}), \tag{4.14}$$

where Σ is a 2×2 matrix in sublattice space.

A number of general properties of the self energy can be established based on symmetry considerations. It follows from Eq.(4.14) that $\Sigma(0,0)$ vanishes, since the part of $G(\varepsilon, \mathbf{p})$ which is invariant under rotations of $\mathbf{p}$ is an odd function of frequency ε. Likewise, the expressions for diagonal entries $\Sigma_{AA}(0, \mathbf{q})$ and $\Sigma_{BB}(0, \mathbf{q})$, which involve an integral of an odd function of ε, vanish on integration over ε. For the same reason, the expressions for off diagonal entries $\Sigma_{AB}(\omega, 0)$ and $\Sigma_{BA}(\omega, 0)$ vanish upon integrating the momentum $\mathbf{p}$ over angles. Hence, nonvanishing contributions arise at lowest order when the right hand side of Eq.(4.14) is expanded to leading order in

small ω and $\mathbf{q}$. We obtain

$$\Sigma_{AA}(\omega,\mathbf{q}) = -i\omega\frac{i\partial\Sigma_{AA}(0,0)}{\partial\omega} + O(\omega^2,\omega q^2,q^4), \tag{4.15}$$

$$\Sigma_{AB}(\omega,\mathbf{q}) = \frac{\mathbf{q}_+^2}{2m}\frac{\partial\Sigma_{AB}(0,0)}{\partial(q_+^2/2m)} + O(\omega^2,\omega q^2,q^4), \tag{4.16}$$

where $\Sigma_{AA}=\Sigma_{BB}$ and $\Sigma_{AB}=\Sigma_{BA}^*$ by symmetry.

It was shown in Ref.[[9]] that $i\partial\Sigma_{AA}/\partial\omega$ and $\partial\Sigma_{AB}/\partial(q_+^2/2m)$ are both $\log^2$ divergent, and are equal to leading order (see below and Sec.4.8 for alternative derivation). Thus the self energy can be written, with $\log^2$ accuracy, as

$$\Sigma(\omega,\mathbf{q}) = -iZ_0\frac{\partial\Sigma}{\partial\omega}G_0^{-1}(\omega,\mathbf{q}) + O\left(\ln\frac{\Lambda}{\Lambda'}\right). \tag{4.17}$$

Here, it is understood that non-vanishing $\partial\Sigma/\partial\omega$ is due to the modes that have been integrated out, Eq.(4.10). Within the leading log approximation, the electron Green function, Eq.(4.13), retains its non-interacting form, whereby the self energy, upon substitution into Eq.(4.12), can be absorbed entirely into a redefinition of the quasiparticle residue, as

$$\delta G(\omega,\mathbf{q}) = \frac{1}{i\omega - H_0(\mathbf{q})}\delta Z, \qquad \delta Z = -i\frac{\partial\Sigma_{AA}}{\partial\omega}Z_0^2. \tag{4.18}$$

We emphasize that the lack of renormalization of the mass only holds at $\log^2$ order. The subleading single log renormalization of the mass will be analyzed in Sec.4.8.

The renormalization of the quasiparticle residue, Eq.(4.18), can be evaluated explicitly by calculating $i\partial\Sigma/\partial\omega$. Taking Σ from Eq.(4.14), we write

$$i\frac{\partial\Sigma}{\partial\omega}\Big|_{\omega=0} = -\int\frac{d\varepsilon d^2p}{(2\pi)^3}\frac{(\frac{p^2}{2m})^2-\varepsilon^2}{((\frac{p^2}{2m})^2+\varepsilon^2)^2}\frac{2\pi\Gamma_0^2Z_0e^2}{\kappa p - 2\pi e^2\Pi(\frac{2m\varepsilon}{p^2})}. \tag{4.19}$$

We express the momenta in polar coordinates $p_x = p\cos\alpha$, $p_y = p\sin\alpha$, and straightaway integrate over $-\pi<\alpha<\pi$. We further change to pseudopolar coordinates in the frequency-momentum space, $\varepsilon = r\cos\theta$, $p^2/2m = r\sin\theta$, with the "polar angle"

$0 < \theta < \pi$. Using the Rydberg energy E_0, Eq.(4.4), as units for r, we have

$$i\frac{\partial\Sigma}{\partial\omega} = -\int_{\Lambda'}^{\Lambda}\frac{dr}{r}\int_0^{\pi}\frac{d\theta}{2\pi}\frac{(\sin^2\theta-\cos^2\theta)\Gamma_0^2 Z_0}{\sqrt{2r\sin\theta}-\frac{2\pi}{m}\Pi(\theta)}, \tag{4.20}$$

where $\Pi(\theta)$ is the dimensionless polarization function, given by Eq.(4.6) with quasi-particle mass m suppressed and $2m\varepsilon/p^2 = \cot\theta$. We note that $\Pi(\theta)$ goes to zero when $\theta \to 0, \pi$, and these zeros of the polarization function dominate the integral and lead to the $\log^2$ divergence. Since $\Pi(\theta)$ is even about $\theta = \pi/2$, the $\log^2$ contribution can be evaluated by replacing $\Pi(\theta)$ in Eq.(4.20) by its asymptotic $\theta \ll \pi$ form,

$$\Pi(\theta) \approx \frac{Nm}{4}\tan\theta. \tag{4.21}$$

In the region $\theta \ll \pi$, we may approximate $\sin\theta \approx \theta$, $\tan\theta \approx \theta$ and $\cos\theta \approx 1$. Including a factor of 2 for the region $\theta \approx \pi$, which gives a contribution identical to that of the region $\theta \approx 0$, we can express the integral Eq.(4.20) with logarithmic accuracy as

$$i\frac{\partial\Sigma}{\partial\omega} = 2\int_{\Lambda'}^{\Lambda}\frac{dr}{r}\int_0^{\pi/2}\frac{d\theta}{2\pi}\frac{\Gamma_0^2 Z_0}{\sqrt{2r\theta}+\frac{N\pi}{2}\theta}. \tag{4.22}$$

Performing the integral over θ and assuming $r \ll N^2$ yields

$$i\frac{\partial\Sigma}{\partial\omega} = \frac{2\Gamma_0^2 Z_0}{N\pi^2}\int_{\Lambda'}^{\Lambda}\frac{dr}{r}\ln\frac{N^2\pi^2}{8r}. \tag{4.23}$$

Integrating over $\Lambda' < r < \Lambda$ (see Eq.(4.10)), we obtain

$$i\frac{\partial\Sigma}{\partial\omega} = \frac{2\Gamma_0^2 Z_0}{N\pi^2}\left(\ln\frac{N^2\pi^2 E_0}{8\Lambda'}\ln\frac{\Lambda}{\Lambda'} - \frac{1}{2}\ln^2\frac{\Lambda}{\Lambda'}\right). \tag{4.24}$$

We now consider an infinitesimal RG transformation. Defining an RG time

$$\xi = \ln\frac{\Lambda_0}{\Lambda}, \qquad \delta\xi = \ln\frac{\Lambda}{\Lambda'}, \tag{4.25}$$

we rewrite the recursion relation, Eq.(4.24), as

$$i\frac{\partial\Sigma}{\partial\omega} = \frac{2\Gamma_0^2 Z_0}{N\pi^2}(\xi + c)d\xi, \quad c = \ln\frac{N^2\pi^2 E_0}{8\Lambda_0}. \tag{4.26}$$

The constant term c describes corrections subleading in $\log^2$, and thus may seem to be irrelevant. However, we shall retain it in the RG equation since it will determine the form of renormalization near the UV cutoff (see discussion of TDOS in Sec.4.7).

In our derivation of Eq.(4.26) it was assumed that our initial UV cutoff $\Lambda_0 < N^2\pi^2 E_0/8$. Such choice of Λ_0 is certainly justified when N is large, which is the limit we worked in thus far. Better still, the condition remains entirely reasonable for the physical value $N = 4$, leading to $N^2\pi^2 E_0/8 = 24eV\kappa^{-2}$, which is much bigger than the bandwidth for BLG.

Substituting Eq.(4.26) into Eq.(4.18), we obtain a differential equation for the flow of the quasiparticle residue,

$$\frac{\partial Z}{\partial\xi} = -\frac{2\Gamma^2(\xi)Z^3(\xi)}{N\pi^2}(\xi + c). \tag{4.27}$$

This equation encapsulates a one loop RG flow for the residue Z, describing its renormalization within a $\log^2$ accuracy.

4.5 Self-consistent renormalization of the vertex function Γ

The screened Coulomb interaction renormalizes through the vertex correction, pictured in Fig.4-1(b). The RPA bubble diagrams, which have already been taken into account in moving from an unscreened to a screened interaction, Eq.(4.5), do not contribute to renormalization. It may be verified by an explicit calculation that the vertex correction in Fig.4-1(b) is given by

$$\delta\Gamma = -\int \frac{d\varepsilon d^2p}{(2\pi)^3}\frac{(\frac{p^2}{2m})^2 - \varepsilon^2}{((\frac{p^2}{2m})^2 + \varepsilon^2)^2}\frac{2\pi\Gamma_0^3 Z_0^2 e^2}{\kappa p - 2\pi e^2\Pi(\frac{2m\varepsilon}{p^2})}. \tag{4.28}$$

This is the same expression as for the residue renormalization [Eqs.(4.18),(4.19)], with Γ replacing Z, and a sign change. Hence, we obtain

$$\frac{\partial \Gamma}{\partial \xi} = \frac{2\Gamma^3(\xi)Z^2(\xi)}{N\pi^2}(\xi + c) \tag{4.29}$$

which is identical to the flow equation for Z, albeit with a reversed sign. Therefore, the product ΓZ does not renormalize at log square order, and we can write.

$$\Gamma(\xi)Z(\xi) = 1. \tag{4.30}$$

This result is not a coincidence, since the residue Z and the vertex function Γ are not independent quantities. The Hamiltonian, Eq.(4.2), is invariant under a gauge transformation of electron wavefunction $\psi' = \psi e^{i\chi}$, accompanied by energy and momentum shifts $\varepsilon' = \varepsilon - \partial_t \chi$, $\mathbf{p}' = \mathbf{p} + \nabla\chi$. This gauge invariance symmetry can be shown to lead to Eq.(4.30) through a Ward identity that relates the self-energy to the vertex function [[18, 10]].

4.6 Renormalization of the four point vertex Υ

The four point vertex Υ, introduced in Eq.(4.11), renormalizes through the diagrams presented in Fig.4-2(a,b), which represent the repeated scattering of two particles in the electron-electron and electron-hole channels respectively. We follow the naming conventions used in Ref.[[12]] in the context of the Luttinger liquid, and name these two diagrams, the BCS loop and the ZS' loop, pictured in Fig.4-2(a) and Fig.4-2(b), respectively. In the one dimensional Luttinger liquids, the two processes famously cancel[11], so that the four point vertex does not renormalize. In higher dimensions, such a cancellation is rare. However, the discrete nature of the Fermi surface in BLG results in a Luttinger liquid like cancellation of the processes Fig.4-2(a,b), as will be discussed below.

We argued in Sec.4.3 that the RG-relevant scattering processes allowed by symmetry must have sublattice structure $(A, A) \to (A, A)$, $(A, B) \to (A, B)$ or $(A, B) \to$

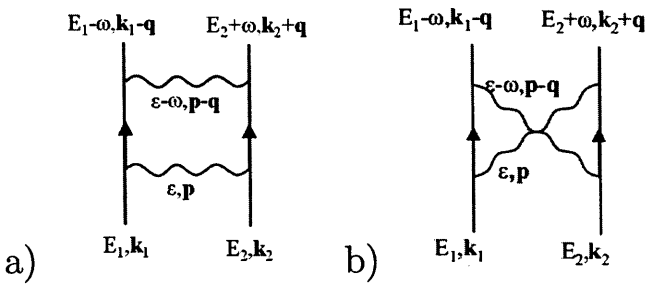

Figure 4-2: The renormalization of the four point vertex Υ proceeds through repeated scattering in the particle particle channel (a) and in the particle hole channel (b), known as the the BCS loop and the ZS' loop in the Luttinger liquid literature [12]. The RPA bubble diagrams (ZS loop in the language of Ref.[[12]]), which arise in the same order of perturbation theory, have already been taken into account in the screened interaction, Eq.(4.5).

(B, A). To see the mathematical origin of such selection, it is instructive to explicitly write out the form of the electron Green function. We have

$$G_{AA}(\varepsilon, \mathbf{p}) = \frac{-Zi\varepsilon}{\varepsilon^2 + (p^2/2m)^2} = G_{BB}(\varepsilon, \mathbf{p}), \tag{4.31}$$

$$G_{AB}(\varepsilon, \mathbf{p}) = \frac{-Zp_+^2/2m}{\varepsilon^2 + (p^2/2m)^2} = G^*_{BA}(\varepsilon, \mathbf{p}). \tag{4.32}$$

When the diagrams Fig.4-2(a,b) are evaluated in any channel other than these three channels, they vanish upon integration over inner momentum variables, due to the chiral structure of the sublattice changing Green functions, Eq.(4.32).

Similar reasoning leads to a conclusion that the $(A, B) \to (B, A)$ vertex cannot exhibit a $\log^2$ divergence. As we saw above, the $\log^2$ divergences arise because the effective interaction $U_{\varepsilon,\mathbf{p}}$ has a pole at $\mathbf{p} = 0$ and finite ε. However, the sublattice changing Green functions, Eq.(4.32), have zeros at small $\mathbf{p}$, which cancel the contribution of the pole in the interaction. Thus, the diagrams in Fig.4-2 can only be $\log^2$ divergent if all internal Green functions are sublattice preserving, given by Eq.(4.31). Since the process $(AB) \to (BA)$ involves two sublattice changing Green functions, it follows that the integrals associated with this processes cannot be $\log^2$ divergent, and hence this process does not contribute at leading $\log^2$ order.

Thus, at leading order, we need to consider only the processes $(AA) \to (AA)$ and

$(AB) \rightarrow (AB)$. Moreover, since the interaction (4.5) does not distinguish between sublattices, the ZS' and BCS contributions from Fig.4-2(a,b) in these channels are the same. Therefore, to demonstrate that Υ does not renormalize at leading order, it is sufficient to demonstrate that there are no $\log^2$ divergences in the $(AA) \rightarrow (AA)$ channel.

In evaluating the ZS' and BCS diagrams (Fig.4-2), it will prove important to keep track of external momenta. The vertex $\Upsilon(E_1, E_2, \omega, \mathbf{k}_1, \mathbf{k}_2, \mathbf{q})$ then represents the amplitude for the scattering process

$$\psi_{\sigma,A,E_1,\mathbf{k}_1}\psi_{\sigma',A,E_2,\mathbf{k}_2} \rightarrow \psi_{\sigma,A,E_1+\omega,\mathbf{k}_1+\mathbf{q}}\psi_{\sigma',A,E_2-\omega,\mathbf{k}_2-\mathbf{q}}.$$

Translating the ZS' and BCS diagrams in Fig.4-2 into integrals, we find the contributions

$$\begin{aligned}
\Upsilon^{\mathrm{ZS'}}_{AAAA} &= \Gamma^4 \int \frac{d\varepsilon d^2p}{(2\pi)^3} U_{\varepsilon,\mathbf{p}} U_{\varepsilon-\omega,\mathbf{p}-\mathbf{q}} G_{AA}(E_1+\varepsilon, \mathbf{k}_1+\mathbf{p}) \\
&\quad \times G_{AA}(E_2+\varepsilon-\omega, \mathbf{k}_2+\mathbf{p}-\mathbf{q}), \qquad (4.33) \\
\Upsilon^{\mathrm{BCS}}_{AAAA} &= \Gamma^4 \int \frac{d\varepsilon d^2p}{(2\pi)^3} U_{\varepsilon,\mathbf{p}} U_{\varepsilon-\omega,\mathbf{p}-\mathbf{q}} G_{AA}(E_1+\varepsilon, \mathbf{k}_1+\mathbf{p}) \\
&\quad \times G_{AA}(E_2-\varepsilon, \mathbf{k}_2-\mathbf{p}). \qquad (4.34)
\end{aligned}$$

Here, the interaction $U(\varepsilon, p)$ is defined by Eq.(4.5), the Green functions are defined by Eq.(4.31), and the integral goes over the shell defined by Eq.(4.10).

As always in a RG analysis, we assume that the external frequencies and momenta are small compared to the internal frequencies and momenta:

$$\max\left(\omega, \omega', \frac{\mathbf{q}^2}{2m}, \frac{\mathbf{q}'^2}{2m}\right) \ll \Lambda' < \sqrt{\varepsilon^2 + \left(\frac{\mathbf{p}^2}{2m}\right)^2} < \Lambda. \qquad (4.35)$$

In such a case, the standard approach to handling the integrals over ε and $\mathbf{p}$ involves setting the external frequency and momenta to zero at first, and restoring their finite values later to regulate the infrared (IR) divergences. However, a straightforward application of this recipe to the integrals in Eqs.(4.33),(4.34) proves impossible, because

these integrals are power law divergent when all external momenta are set to zero. The divergence arises from the region near $\mathbf{p} \approx 0$ (which lies within the shell defined by Eq.(4.10)), where the interaction is nearly unscreened. In this region, we have

$$U_{\varepsilon,\mathbf{p}} U_{\varepsilon-\omega,\mathbf{p}-\mathbf{q}} \sim \frac{1}{(|\mathbf{p}| + \alpha|\mathbf{p}|^2)\,(|\mathbf{p}-\mathbf{q}| + \alpha|\mathbf{p}-\mathbf{q}|^2)}, \tag{4.36}$$

with $\alpha = Ne^2/2\kappa\Lambda$. At finite $\mathbf{q}$, the poles in this expression are split apart, and thus the singular contribution of each pole, $\mathbf{p} = 0$ and $\mathbf{p} = \mathbf{q}$, is regularized by the integration measure d^2p so that the integrals in Eqs.(4.33),(4.34) remain well defined. However, when all external momenta are zero, the poles from the two interaction lines co-incide, and the expressions (4.33), (4.34) acquire a second order pole at $\mathbf{p} = 0$. When we integrate over this second order pole, we pick up a power law divergence.

Hence, if either of the ZS' or BCS diagrams existed in isolation, this power law divergence would indicate a strong (power law) instability, which would drive Υ into the strong coupling regime, where our $\log^2$ RG would cease to apply. However, as we will now show, the divergences in the contributions to Υ from the expressions (4.33), (4.34) in fact cancel out, so that Υ does not flow to $\log^2$ order. To analyse the cancellation between the ZS' and BCS diagrams, it is convenient to add the integrands of Eq.(4.33) and Eq.(4.34) together before doing the integral, while keeping external momenta finite. Preserving finite external momenta ensures that the integrals Eq.(4.33) and Eq.(4.34) are well defined. After combining the integrands, and denoting $\Upsilon^{ZS'}_{AAAA} + \Upsilon^{BCS}_{AAAA} = \tilde{\Upsilon}$, we obtain

$$\begin{aligned}\tilde{\Upsilon} = \Gamma^4 \int \frac{d\varepsilon d^2p}{(2\pi)^3} \quad & U_{\varepsilon,\mathbf{p}} U_{\varepsilon-\omega,\mathbf{p}-\mathbf{q}} G_{AA}(E_1+\varepsilon, \mathbf{k}_1+\mathbf{p}) \times \\ & \left[G_{AA}(E_2+\varepsilon-\omega, \mathbf{k}_2+\mathbf{p}-\mathbf{q}) + G_{AA}(E_2-\varepsilon, \mathbf{k}_2-\mathbf{p})\right].\end{aligned} \tag{4.37}$$

To simplify this expression we note that momentum $\mathbf{q}$ enters very differently in Eq.(4.38) as compared to other external frequencies and momenta E_1, E_2, ω , $\mathbf{k}_1$, $\mathbf{k}_2$. The momentum $\mathbf{q}$ is needed to split the poles coming from the two interaction terms

– if we take $\mathbf{q}$ to zero, the integral will acquire a second order pole at $\mathbf{p} = 0$, leading to a divergence. This divergence arises from within the shell that we are integrating out (Eq.(4.10)), and thus the RG will be ill defined. In contrast, sending the frequencies and momenta E_1, E_2, ω, $\mathbf{k}_1$, $\mathbf{k}_2$ to zero by applying Eq.(4.35) does not cause any concern. We thus have

$$\begin{aligned}\tilde{\Upsilon} &= \Gamma^4 \int \frac{d\varepsilon d^2p}{(2\pi)^3} U_{\varepsilon,\mathbf{p}} U_{\varepsilon,\mathbf{p}-\mathbf{q}} G_{AA}(\varepsilon,\mathbf{p}) \\ &\quad \times \left[G_{AA}(\varepsilon,\mathbf{p}-\mathbf{q}) + G_{AA}(-\varepsilon,-\mathbf{p})\right]. \end{aligned} \tag{4.38}$$

Interestingly, the expression in square brackets vanishes identically when $\mathbf{q} = 0$, since $G_{AA}(\varepsilon,\mathbf{p}) = -G_{AA}(-\varepsilon,-\mathbf{p})$. However, taking the limit $\mathbf{q} \to 0$ is potentially problematic because of the pole structure of $U_{\varepsilon,\mathbf{p}} U_{\varepsilon-\omega,\mathbf{p}-\mathbf{q}}$ discussed above. Instead, we proceed with caution, and evaluate Eq.(4.38) at finite $\mathbf{q}$, using the conditions (4.35) to simplify the analysis.

Given what we just said, it is now easy to see why there is no $\log^2$ divergence in $\tilde{\Upsilon}$. First, we note that the interaction (4.5) carries a soft UV cutoff, so the integral in Eq.(4.38) is UV convergent (this property of dynamically screened interaction in BLG is discussed e.g. in Ref.[[3]]). Hence, we can shift variables to $\mathbf{p}_\pm = \mathbf{p} \pm \mathbf{q}/2$ and rewrite the expression (4.38) as

$$\begin{aligned}\tilde{\Upsilon} &= -\Gamma^4 Z^2 \textstyle\int \frac{d\varepsilon d^2p}{(2\pi)^3} U_{\varepsilon,\mathbf{p}_+} U_{\varepsilon,\mathbf{p}_-} \varepsilon^2 \quad D(\varepsilon,\mathbf{p}_+)\left[D(\varepsilon,\mathbf{p}_-) - D(\varepsilon,\mathbf{p}_+)\right] \\ &= -\Gamma^4 Z^2 \textstyle\int \frac{d\varepsilon d^2p}{(2\pi)^3} U_{\varepsilon,\mathbf{p}_+} U_{\varepsilon,\mathbf{p}_-} \varepsilon^2 \quad \left[\frac{D(\varepsilon,\mathbf{p}_+) + D(\varepsilon,\mathbf{p}_-)}{2} + \frac{D(\varepsilon,\mathbf{p}_+) - D(\varepsilon,\mathbf{p}_-)}{2}\right] \times \\ &\qquad\qquad [D(\varepsilon,\mathbf{p}_-) - D(\varepsilon,\mathbf{p}_+)]\,, \end{aligned} \tag{4.39}$$

where we factored the Green functions as

$$G_{AA}(\varepsilon,p) = iZ\varepsilon D(\varepsilon,\mathbf{p}), \quad D(\varepsilon,\mathbf{p}) = \frac{1}{\varepsilon^2 + (\mathbf{p}^2/2m)^2}. \tag{4.40}$$

We note that because Υ should be even under $\mathbf{q} \to -\mathbf{q}$ the first term in the brackets

gives zero upon integration over $\mathbf{p}$. Hence, we can rewrite the result for $\tilde{\Upsilon}$, Eq.(39), as

$$\begin{aligned}\tilde{\Upsilon} &= \frac{\Gamma^4 Z^2}{2}\int \frac{d\varepsilon d^2p}{(2\pi)^3} U_{\varepsilon,\mathbf{p}_+} U_{\varepsilon,\mathbf{p}_-} \varepsilon^2 \left[D(\varepsilon,\mathbf{p}_-) - D(\varepsilon,\mathbf{p}_+)\right]^2 \\ &= \frac{\Gamma^4 Z^2}{2}\int \frac{d\varepsilon d^2p}{(2\pi)^3} U_{\varepsilon,\mathbf{p}_+} U_{\varepsilon,\mathbf{p}_-} \varepsilon^2 \left[\frac{z_+^2 - z_-^2}{(\varepsilon^2+z_+^2)(\varepsilon^2+z_-^2)}\right]^2,\end{aligned} \tag{4.41}$$

where $z_\pm = |\mathbf{p}_\pm|^2/2m$.

To extract the leading contribution at small $\mathbf{q}$, we approximate the effective interaction as

$$U(\varepsilon,\mathbf{p}) = -\frac{\Pi^{-1}(\varepsilon,\mathbf{p})}{1-\frac{\kappa|\mathbf{p}|}{2\pi e^2 \Pi(\varepsilon,\mathbf{p})}} \approx -\frac{1}{\Pi(\varepsilon,\mathbf{p})}. \tag{4.42}$$

From the definition of the polarization function, Eq.(4.6), we see that the approximation $U \approx -1/\Pi$ holds everywhere in the shell Eq.(4.10) except at $\mathbf{p} \approx 0$, since $\Pi(\mathbf{p}=0) = 0$. However, in the limit $\mathbf{p} \to 0$, the expression in brackets in Eq.4.41 tends to zero because of the expansion $z_+^2 - z_-^2 = (\mathbf{p}^2/m)(\mathbf{p}\cdot\mathbf{q}/2m) + O(\mathbf{p}^4)$, which ensures validity of the approximation (4.42).

Hence, using Eq.(4.6), we obtain

$$\begin{aligned}\tilde{\Upsilon} = \quad & \Gamma^4 Z^2 \int d\varepsilon d^2p \frac{\sqrt{(z_+^2+u\varepsilon^2)(z_-^2+u\varepsilon^2)}}{4\pi(Nm\ln 4)^2} \\ & \times \frac{\varepsilon^2}{z_+ z_-}\left[\frac{z_+^2 - z_-^2}{(\varepsilon^2+z_+^2)(\varepsilon^2+z_-^2)}\right]^2.\end{aligned} \tag{4.43}$$

Simple power counting shows that this integral is UV convergent, IR convergent, and is completely independent of q, which can be scaled out by defining new variables $p' = p/q$ and $\varepsilon' = 2m\varepsilon/q^2$. It follows that the the diagrams representing repeated scattering in the particle-particle and particle-hole channels do indeed cancel, so that $\Upsilon_{AAAA}Z^2$ does not renormalize.

Combining this with our argument demonstrating that $\Upsilon_{ABBA}Z^2$ does not renormalize at $\log^2$ order (see discussion below Eq.(32)), and recalling that $\Upsilon_{AAAA} =$

Υ_{AABB}, we conclude that we can set $\Upsilon = 0$ with $\log^2$ accuracy.

4.7 Solution of RG flow equations. Zero bias anomaly in bilayer graphene

Since the only quantities which renormalize at $\log^2$ order in a one loop RG are the quasiparticle residue Z and the interaction vertex function Γ, the problem of finding the RG flow of these quantities reduces to solving Eqs.(4.27),(4.29). All other quantities do not renormalize at log square order, and may thus be treated as constants with logarithmic accuracy.

Additional simplification arises due to the Ward identity $\Gamma Z = 1$, Eq.(4.30). Using it to decouple the RG equations for Z and Γ, we write the equation for Z as

$$\frac{\partial Z}{\partial \xi} = -\frac{2}{\pi^2 N}(\xi + c)\, Z, \tag{4.44}$$

where we retained a constant $c = \ln \frac{N^2\pi^2 E_0}{8\Lambda_0}$ corresponding to the first term in the self energy renormalization, Eq.(4.24).

Integrating the RG equation, and taking into account the boundary conditions $Z(0) = \Gamma(0) = 1$, we obtain

$$Z(\xi) = \exp\left(-\frac{2c\xi + \xi^2}{N\pi^2}\right) = \Gamma^{-1}(\xi), \quad \xi = \ln\frac{\Lambda_0}{\Lambda}. \tag{4.45}$$

We note that in the limit of small ξ^2/N, we reproduce the perturbative result[9] for the residue, Eq.(4.24). However, our result (4.45) applies for all ξ, both small and large. The fermion propagator at arbitrary energies and momenta is then given by

$$G(\omega, \mathbf{k}) = -Z(\xi)\frac{i\omega + H_0(\mathbf{k})}{\omega^2 + (\frac{\mathbf{k}^2}{2m})^2}. \tag{4.46}$$

At zero temperature, the infrared cutoff is supplied by the external frequency and momentum, such that $\xi = \ln\frac{\Lambda_0}{\Lambda}$ and $\Lambda = \sqrt{\omega^2 + (k^2/2m)^2}$

Thus, the quasiparticle residue in undoped BLG is suppressed to zero by electron-electron interactions, Eq.(4.46). This is reminiscent of the situation in disordered metals, where enhancement of interactions by disorder produces a renormalization of electron self energy of a $\log^2$ form [14], and analysis of an RG flow[15] yields a suppression of the quasiparticle residue similar in form to our Eq.(4.46). The suppression of the quasiparticle spectral weight at low energies, governed by the $Z(\xi)$ dependence, will manifest itself directly in the behavior of the tunneling density of states of BLG, similar to disordered metals.

We note parenthetically that, while keeping the constant term c in the RG equation (4.44) is formally beyond the $\log^2$ accuracy generally adopted in our analysis, it can be justified on the same grounds as in the discussion of the zero bias anomaly in disordered metals [16, 17]. Because of its fairly large value for $N = 4$, given by $c = \ln 2\pi^2 \approx 2.98$, this term may significantly alter predictions for the behavior of Z at intermediate energies $\varepsilon \lesssim \Lambda_0$.

To analyze the suppression of tunneling density of states (TDOS), we use its relation to the retarded Green function [14],

$$\rho(\omega) = -\frac{1}{\pi}\mathrm{Im}\left[\mathrm{Tr}G_R(\omega, \mathbf{k})\right], \tag{4.47}$$

where $G_R(\omega, \mathbf{k})$ is obtained from the Matsubara Green function analyzed above, Eq.(4.46), by the analytic continuation of frequency from imaginary to real values, $i\omega \to \omega + i\eta$.

It is convenient to take the trace before performing the analytic continuation. The trace may be most easily taken in a basis of free particle eigenstates (plane waves with appropriate spinor structure), which amounts to integrating Eq.(4.46) over all $\mathbf{k}$ values, $\mathrm{Tr}G = \int G(\omega, \mathbf{k})d^2k$. Noting that the term containing $H_0(\mathbf{k})$ vanishes upon integration due to the angular dependence, we write

$$\mathrm{Tr}G = \frac{2N_0}{\pi}\int_0^\infty Z(\xi)\frac{i\omega}{\omega^2 + z^2}dz, \tag{4.48}$$

where $z = \mathbf{k}^2/2m$ and N_0 is the density of electronic states in BLG in the absence of

interactions.

It can be seen that the integral over z is determined by $z \sim \omega$. It is therefore convenient to introduce a variable $\varphi = \sinh^{-1}(z/\omega)$ and write

$$\mathrm{Tr}G = i\frac{2N_0}{\pi}\int_0^\infty Z(\xi_\omega - \ln\cosh\varphi)\frac{d\varphi}{\cosh\varphi}, \tag{4.49}$$

where $\xi_\omega = \ln(\Lambda_0/\omega)$. Noting that this integral is dominated by $\varphi \sim 1$, we obtain an estimate of the spectral weight:

$$\rho(\omega) \approx N_0 Z(\xi_\omega) = N_0 \exp\left(-\frac{\xi_\omega^2 + 2c\xi_\omega}{N\pi^2}\right). \tag{4.50}$$

The form of this expression remains unchanged, to leading $\log^2$ order, upon analytic continuation to real frequencies.

The expression in Eq.(4.50) can be re-arranged by using Eq.(4.26) as

$$\rho(\omega) = N_0 \exp\left(-\frac{\ln^2\frac{N^2\pi^2E_0}{8\omega} - \ln^2\frac{N^2\pi^2E_0}{8\Lambda_0}}{N\pi^2}\right). \tag{4.51}$$

Thus, we see that the only effect of the UV cutoff Λ_0 is to rescale the prefactor for the TDOS without affecting the frequency dependence. Absorbing the dependence on Λ_0 in the prefactor, we have

$$\rho(\omega) = \tilde{N}_0 \exp\left(-\frac{1}{N\pi^2}\ln^2\frac{N^2\pi^2E_0}{8\omega}\right). \tag{4.52}$$

Tunneling measurements yield $\rho(\omega = eV)$, where V is the bias voltage. The interaction suppression of the TDOS, Eq.(4.50), will therefore manifest itself as a zero bias anomaly in tunneling experiments. The predicted behavior the TDOS is shown in Fig.4-3. Because of the exponential dependence in Eq.(4.52), the suppression rapidly becomes more pronounced at lower energies.

Closing our discussion of the zero bias anomaly in BLG, we note that the results described above apply only to the system at charge neutrality. Away from neutrality, with the Fermi surface size becoming finite, the effects of screening will grow stronger,

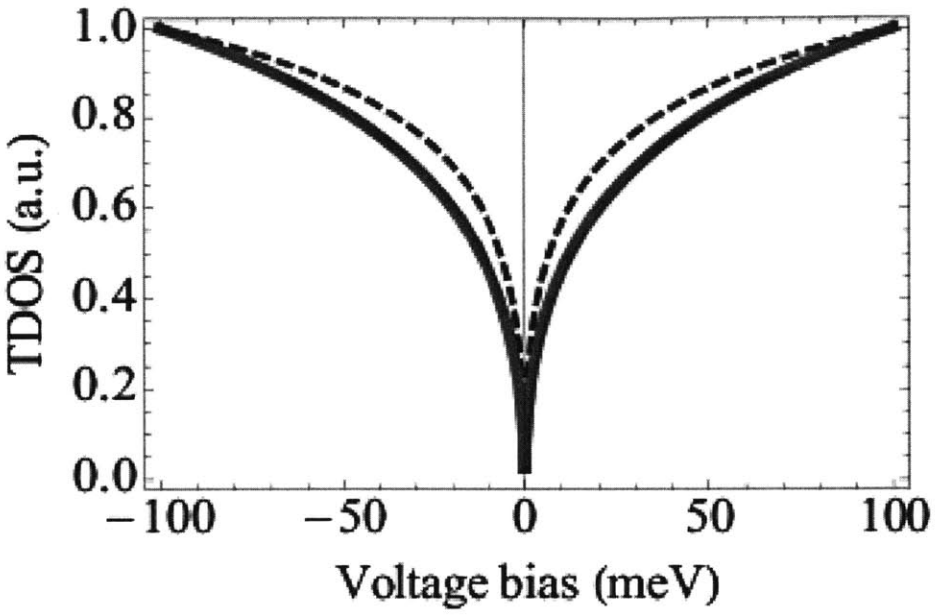

Figure 4-3: Tunneling density of states (TDOS) of BLG at charge neutrality, Eq.(4.52), is shown as a function of external bias $\omega = eV$. Predicted TDOS is shown for two different values of the dielectric constant in E_0, Eq.(4.4): $\kappa = 1$ (solid curve) and $\kappa = 2.5$ (dashed curve), describing free-standing BLG and BLG on SiO substrate, respectively. Plot is normalized so that $\rho = 1$ at an external bias of 100 meV.

resulting in a weaker effective interaction. Yet, even in this case, the tunneling density of states will be described by the suppression factor $\rho(\omega = eV)/N_0$ given by Eq.(4.50), provided that the bias voltage eV exceeds the Fermi energy measured from the neutrality point.

4.8 Single log renormalization of electron mass

Thus far we have concentrated on $\log^2$ flows. However, the analysis may be extended to obtain the subleading single log flows of the action. We illustrate this procedure by calculating the renormalization of the mass (which did not renormalize at $\log^2$ order in the RG). This calculation is interesting because it allows us to investigate the interaction renormalization of the compressibility–a directly measurable quantity, and also because it allows us to illustrate how much slower the single log flows are than the $\log^2$ flows.

In this section, we first analyze mass renormalization by extracting it directly from

the self energy. After that, in Sec.4.9 we consider electron compressibility of BLG and show that the log divergent correction to the compressibility matches exactly our prediction for mass renormalization obtained from the self energy.

In BLG, the self energy is a 2×2 matrix, given by Eq.(4.14)), which is related to the renormalized Green function by the Dyson equation,

$$G^{-1}(\omega, \mathbf{q}) = G_0^{-1}(\omega, \mathbf{q}) - \begin{pmatrix} \Sigma_{AA}(\omega, \mathbf{q}) & \Sigma_{AB}(\omega, \mathbf{q}) \\ \Sigma_{BA}(\omega, \mathbf{q}) & \Sigma_{BB}(\omega, \mathbf{q}) \end{pmatrix}. \tag{4.53}$$

As discussed in Sec.4.4, the leading $\log^2$ contribution to the self energy is proportional to G_0^{-1}, since $\partial\Sigma_{AB}/\partial(q_+^2/2m) = i\partial\Sigma_{AA}/\partial\omega$. This means that all renormalization can be attributed to the residue Z with mass remaining unchanged. However, as we now show, this equality is only true to leading logarithmic order.

Comparison of Eq.(4.53) with Eq.(4.15) and Eq.(4.16) indicates that the mass renormalization is given by

$$\frac{\delta m}{m} = Z_0 \left(i\frac{\partial\Sigma_{AA}}{\partial\omega} - \frac{\partial\Sigma_{AB}}{\partial(q_+^2/2m)} \right). \tag{4.54}$$

Here, $i\partial\Sigma_{AA}/\partial\omega$ is defined by Eq.(4.19). For the second term, we obtain the expression

$$\frac{\partial\Sigma_{AB}}{\partial(q_+^2/2m)} = \int \frac{d\varepsilon d^2p}{(2\pi)^3} \left(\frac{1}{\varepsilon^2 + (\frac{p^2}{2m})^2} - \frac{5(\frac{p^2}{2m})^2}{\left(\varepsilon^2 + (\frac{p^2}{2m})^2\right)^2} + \frac{4(\frac{p^2}{2m})^4}{\left(\varepsilon^2 + (\frac{p^2}{2m})^2\right)^3} \right) \Gamma^2 ZU(\varepsilon, \mathbf{p}), \tag{4.55}$$

where $U(\varepsilon, \mathbf{p})$ is given by Eq.(4.5). To evaluate the difference in Eq.(4.54), it is convenient to subtract the integrands of Eqs.((4.19,4.55)) before doing the integrals. Once again, we use the "polar" representation of the frequency and momentum variables,

$\omega = r\cos\theta$, $p^2/2m = r\sin\theta$, and obtain

$$\frac{\delta m}{m} = \int_{\Lambda'}^{\Lambda} \frac{dr}{r} \int_0^{\pi} \frac{d\theta}{2\pi} \frac{\Gamma_0^2 Z_0^2 (3\sin^2\theta - 4\sin^4\theta)}{\sqrt{2r\sin\theta} - \frac{2\pi}{m}\Pi(\theta)}, \tag{4.56}$$

where $\Pi(\theta)$ is the polarization function introduced in Eq.(4.6), and r is measured in units of E_0 as before. The integral over θ is now fully convergent, and the resulting expression is only single log divergent. Integrating analytically over r and then integrating numerically over θ, we find

$$\frac{\delta m}{m} = \frac{0.56}{2N\pi \ln 4} \Gamma_0^2 Z_0^2 \ln \frac{\Lambda}{\Lambda'}. \tag{4.57}$$

Converting this recursion relation into a differential equation, we obtain

$$\frac{d\ln m}{d\xi} = \frac{0.56}{2N\pi \ln 4} \Gamma^2 Z^2. \tag{4.58}$$

This equation cannot be solved for general ξ by applying the Ward identity Eq.(4.30), since the Ward identity only holds at leading $\log^2$ order, while the mass flows at subleading (single log) order in Eq.(4.58). In the perturbative limit $\frac{1}{N}\xi \ll 1$, when $Z \approx 1$ and $\Gamma \approx 1$, we obtain a logarithmic correction to the mass

$$m(\xi) = m(0)\left(1 + \frac{0.56}{2N\pi \ln 4}\xi\right). \tag{4.59}$$

We may relate this mass renormalization to a measurable quantity, by noting that the electronic compressibility K is proportional to the density of states which is proportional to the mass. Thus, the logarithmic renormalization of the mass in Eq.(4.59) should manifest itself in a logarithmic enhancement of the electronic compressibility. The relation between mass renormalization and compressibility will be further discussed in Sec.4.9.

4.9 Interaction correction to compressibility

Here we explicitly calculate the renormalization of the compressibility. By doing this we shall confirm that the compressibility does not renormalize at leading (log square) order, and also extract the single log renormalization of the compressibility. The interaction correction to the compressibility K is given by

$$\delta K = -\frac{\partial^2 F}{\partial \mu^2}, \tag{4.60}$$

where μ is the chemical potential, and F is the interaction energy. Within the RPA framework, the interaction energy is expressed as

$$F(\mu) = \int \frac{d\omega d^2p}{(2\pi)^3} \ln\left(1 - V(\mathbf{q})\Pi(\mu, \omega, \mathbf{q})\right). \tag{4.61}$$

Here, $\Pi(\mu, \omega, \mathbf{q})$ is the non-interacting polarization function evaluated at a chemical potential μ, and $V(q)$ is the unscreened Coulomb interaction $V(q) = 2\pi e^2/\kappa q$.

To evaluate the second derivative in (4.60), we consider the difference $\Delta F = F(\mu) - F(0)$. After rearranging logs under the integral, we rewrite this expression as

$$\Delta F = -\int \frac{d\omega d^2q}{(2\pi)^3} \ln\Big(1 - U_{\omega,q}(\Pi(\mu, \omega, q) - \Pi(0, \omega, q))\Big), \tag{4.62}$$

where now $U_{\omega,q}$ is the dynamically screened Coulomb interaction, Eq.(4.5). Since the compressibility is obtained from the free energy through $K = -\partial^2 F/\partial\mu^2$, the problem of calculating the interaction renormalization of the compressibility is reduced to that of calculating the polarization function at finite μ. This may be calculated through methods similar to those developed in Ref.[3]. We define $\varepsilon_\pm = \varepsilon \pm \omega/2$, $\mathbf{p}_\pm = \mathbf{p} \pm \mathbf{q}/2$ and $z_\pm = |\mathbf{p}_\pm|^2/2m$. The non-interacting polarization function at finite μ is given by

$$\begin{aligned}
&\Pi(\mu, \omega, q) = \mathrm{Tr} G(\mu, \varepsilon_+, \mathbf{p}_+) G(\mu, \varepsilon_-, \mathbf{p}_-) \\
&= \mathrm{Tr} \int \frac{d\varepsilon d^2p}{(2\pi)^3} \frac{1}{(i\varepsilon_+ - \mu - H_0(\mathbf{p}_+))(i\varepsilon_- - \mu - H_0(\mathbf{p}_-))} \\
&= 2N \int \frac{d\varepsilon d^2p}{(2\pi)^3 (\varepsilon_+ + i(\mu + z_+))(\varepsilon_+ + i(\mu - z_+))}
\end{aligned}$$

$$\times \frac{(i\varepsilon_+ - \mu)(i\varepsilon_- - \mu) + z_+ z_- \cos 2\theta_{pq}}{(\varepsilon_- + i(\mu + z_-))(\varepsilon_- + i(\mu - z_-))}, \tag{4.63}$$

where θ_{pq} is the angle between $\mathbf{p}_+$ and $\mathbf{p}_-$. We now perform the integral over ε by residues to obtain

$$\begin{aligned}\Pi(\mu,\omega,\mathbf{q}) &= N\int \frac{d^2p}{(2\pi)^2}\frac{(z_+ + i\omega + z_-\cos 2\theta_{pq})\Theta(z_+ - \mu)}{z_+^2 - z_-^2 - \omega^2 + 2i\omega z_+} \\ &\quad + (\omega, \mathbf{q} \to -\omega, -\mathbf{q}) \\ &= N\int_{z_+=0}^{z_+=\mu} \frac{d^2p_+}{(2\pi)^2}\left[\frac{1}{z_+ + i\omega - z_-} - \frac{2z_-\sin^2\theta_{pq}}{(z_+ + i\omega)^2 - z_-^2}\right] \\ &\quad + (\omega, \mathbf{q} \to -\omega, -\mathbf{q})\,. \end{aligned} \tag{4.64}$$

In the limit $\mu \to 0$, this reproduces the non-interacting polarization function from Ref.[[3]]. Now we expand Eq.(4.62) to leading order in small μ to obtain

$$\Delta F = -\frac{1}{2}\mu^2 \int \frac{d\omega d^2q}{(2\pi)^3} U(\omega, q)\frac{\partial^2\Pi(\mu,\omega,q)}{\partial\mu^2}. \tag{4.65}$$

The term linear in μ must vanish, by particle hole symmetry. Taking derivatives of Eq.(4.64) greatly simplifies the calculations, since it turns the two dimensional integral over momenta into a one dimensional integral over momentum angles, which is fully convergent, and may be evaluated numerically. We find

$$\frac{\partial^2\Pi}{\partial\mu^2} = \frac{Nm}{2\pi}\frac{3\omega^2 z_q^2 - z_q^4}{(\omega^2 + z_q^2)^2}, \qquad z_q = \frac{q^2}{2m}, \tag{4.66}$$

$$\Delta F = -\frac{\mu^2}{2}\int \frac{d\omega d^2q}{(2\pi)^3} U(\omega, \mathbf{q})\frac{\partial^2\Pi}{\partial\mu^2}. \tag{4.67}$$

We again change to the coordinates $\omega = r\cos\theta$, $z_q = r\sin\theta$, and measure r in units of E_0. Note that even though the interaction has a pole at $\theta \to 0, \pi$, this pole is canceled by $\partial^2\Pi/\partial\mu^2$ having a zero at $\theta \to 0, \pi$. As a result, the θ integral is fully convergent. Integrating numerically over θ and analytically over r, we find that the fractional change in the compressibility is

$$\frac{\delta K(\xi)}{K(0)} = \frac{0.56}{2N\pi \ln 4}\xi, \tag{4.68}$$

a result that agrees exactly with Eq.(4.59). We note that an enhancement of the compressibility due to interactions was also predicted in Ref.[[19]]. However, the effect described by Eq.(4.59) is much weaker than that predicted in Ref.[[19]], because we have worked with a screened interaction, whereas in Ref.[[19]] screening was not taken into account.

In summary, the compressibility does not renormalize at leading (log square) order, just as in the Luttinger liquids, and while there is a subleading logarithmic correction, the pre-factor is quite small ($0.56/(2N\pi \ln 4) \approx 0.016$). Thus, in contrast to the zero-bias anomaly in TDOS, experimental detection of the interaction correction to the compressibility is likely to be challenging. The difference arises because the single log flows are much weaker than the $\log^2$ flows, retrospectively justifying our earlier neglect of the single log flows in the RG. Hence, strong suppression of the tunneling density of states at energy scales where the compressibility is not significantly renormalized is a key signature of the marginal Fermi liquid physics in bilayer graphene.

4.10 Discussion and Conclusions

Here we briefly discuss the range of validity of our results. Our analysis was organized as a perturbation theory in $\Gamma^2 Z^2/N$. Since $\Gamma Z = 1$ at leading (log square) order, the perturbation theory remains well defined under the log square flows. However, our analysis neglected subleading single log flows. For $\xi \approx N\pi^2$, the subleading single log flows become important, and the analysis leading to the expression Eq.(4.45) no longer applies. A mean field theory of subleading single log effects [3] indicates that a gapped state develops at $\xi = \frac{3}{13} N\pi^2$, the scale which we tentatively identify as the limit of validity of our analysis.

How can the marginal Fermi liquid physics be distinguished from the formation of a gapped state? We note that at very low energies, once the gapped state has developed, the tunneling density of states will vanish anyway. However, in the gapped regime, the compressibility will vanish also. What we have shown, however, is that there is a large range of energies greater than the energy scale for gap formation, where

the tunneling density of states vanishes, while the compressibility remains essentially unchanged. Such behavior represents the key signature of the marginal Fermi liquid physics discussed above, which is analogous to the Luttinger liquid physics.

In our analysis, we neglected the short range interactions which are characterized by lattice scale, such as the interlayer density difference interaction $V_- = \frac{1}{2}(V_{AA} - V_{AB}) = \pi e^2 d$ and the Hubbard-type on-site repulsion. Short range interactions are non-dispersive, do not renormalize the Green function in the weak coupling limit, and hence do not alter our results. Short range interactions also produce only single log renormalization [4, 5] and therefore do not need to be included in our log square RG. Similarly, we justify our neglect of the trigonal warping effect [20] by noting that trigonal warping is significant only on energy scales smaller than the characteristic energy scale for onset of gapped states [3].

Finally, we note that our analysis made use of the fact that there were no un-canceled log square divergences at one loop order in the RG, except for the renormalization of the quasiparticle residue and the Coulomb vertex function, which were related by a Ward identity, Eq.(4.30). Technically, in order for our neglect of higher loop corrections to be justified, we also require that there are no un-canceled log square divergences beyond one loop order in the RG, except those that are constrained by Ward identities. We believe this to be the case, however, the proof requires a non-perturbative approach, which lies beyond the scope of the present work.

To conclude, we have examined the one-loop RG flow for bilayer graphene. We have demonstrated that the quasiparticle residue Z and the Coulomb vertex function Γ both flow as ξ^2, where ξ is the RG time. All other quantities flow only as ξ. The structure of the RG for Coulomb interacting BLG has strong similarities to the RG for the one dimensional Luttinger liquids. In particular, we predict a strong interaction suppression of the tunneling density of states for undoped BLG, even at energy scales where the electronic compressibility is essentially unchanged from its non-interacting value. These predictions may be readily tested by experiments.

Bibliography

[1] K. S. Novoselov et al, Nature Physics **2**, 177 (2006).

[2] H. Min, G. Borghi, M. Polini and A. H. MacDonald, Phys. Rev. B **77**, 041407(R) (2008).

[3] R. Nandkishore and L. Levitov. Phys. Rev. Lett. **104**, 156803 (2010).

[4] F. Zhang, H. Min, M. Polini and A. H. MacDonald, Phys. Rev. B **81**, 041402(R) (2010).

[5] O. Vafek and K. Yang, Phys. Rev. B **81**, 041401(R) (2010).

[6] K. Sun, H. Yao, E. Fradkin and S.A. Kivelson, Phys. Rev. Lett. **103**, 046811 (2009).

[7] R. Nandkishore and L. Levitov, Phys. Rev. B 82, 115124 (2010)

[8] E. McCann, Phys. Rev. B **74**, 161403(R) (2006).

[9] Y. Barlas and K. Yang, Phys. Rev. B **80**, 161408(R) (2009).

[10] J. Gonzalez, F. Guinea and M. A. H. Vozmediano, Phys. Rev. B **59**, 2474(R) (1999).

[11] I. E. Dzyaloshinskii and A. I. Larkin, Zh. Eksp. Teor. Fiz. **65**, 411 (1973) [JETP **38**, 202 (1974)].

[12] R. Shankar, Rev. Mod. Phys. **66**, 129 (1994).

[13] T. Giamarchi, *Quantum Physics in One Dimension*, Clarendon Press (2005).

[14] B. L. Altshuler, A. G. Aronov, and P. A. Lee, Phys. Rev. Lett. **44**, 1288 (1980).

[15] A. M. Finkelstein, Zh. Eksp. Teor. Fiz. **84**, 168 (1983) [Sov. Phys. JETP **57**, 97 (1983)].

[16] Yu. V. Nazarov, Zh. Eksp. Teor. Fiz. **96**, 975 (1989) [Sov. Phys. JETP **68**, 561 (1989)].

[17] L. S. Levitov and A. V. Shytov, Pisma v ZhETF **66**, 200 (1997) [JETP Lett. **66**, 214 (1997)].

[18] V. B. Berestetskii, E. M. Lifshitz and L. P. Pitaevskii, *Quantum Electrodynamics*, chapter 11. Butterworth-Heinemann, 1979 (Landau and Lifshitz, Course of Theoretical Physics, Vol 4).

[19] S.V. Kusminskiy, J. Nilsson, D. K Campbell and A.H. Castro Neto, Phys Rev Lett **100**, 106805 (2008).

[20] E. McCann and V.I. Falko, Phys. Rev. Lett. **96**, 086805 (2006).

[21] J. Nilsson, A. H. Castro Neto, N. M. R. Peres and F. Guinea, Phys. Rev. B **73**, 214418 (2006).

Chapter 5

Dynamical screening and spontaneous gap opening in bilayer graphene

Electron interactions in undoped bilayer graphene lead to instability of the gapless state, 'which-layer' symmetry breaking, and energy gap opening at the Dirac point. In contrast to single layer graphene, the bilayer system exhibits instability even for arbitrarily weak interaction. A controlled theory of this instability for realistic dynamically screened Coulomb interactions is developed, with full acount of dynamically generated ultraviolet cutoff. This leads to an energy gap that scales as a power law of the interaction strength, making the excitonic instability readily observable.

Graphene, due to its unique electronic structure of a two-dimensional semimetal, provides an entirely new setting for investigating many-body phenomena [1]. Since the conduction and valence band joined together in a semimetal mimic massless Dirac particles, electronic phenomena in graphene often have direct analogs in high energy physics[2]. In particular, several authors discussed the analogy between excitonic instability in a single-layer graphene and chiral symmetry breaking in $2+1$ Quantum Electrodynamics. While this instability is absent when interactions are weak[3], and the situation for realistic interaction strength is still debated, the instability can be "catalyzed" by a magnetic field[4, 5]. These predictions are in qualitative agreement

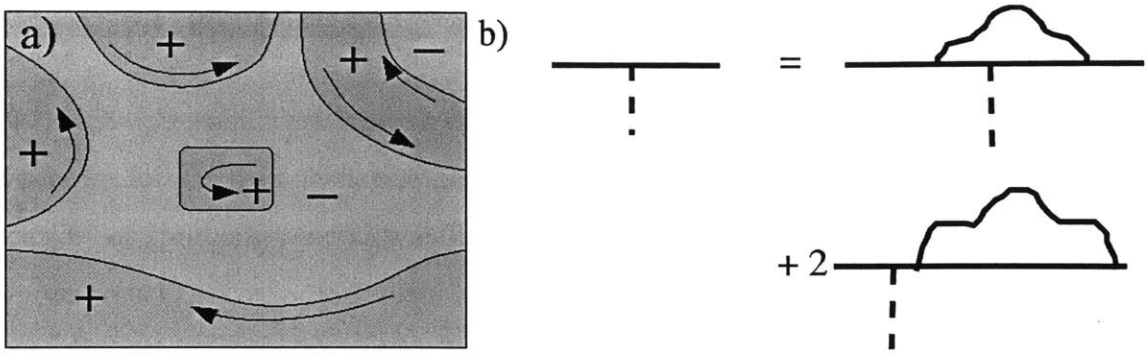

Figure 5-1: (a) Domains of opposite polarization in the ferroelectric state. Valley polarized chiral edge states propagate in opposite directions along domain boundaries. (b) Diagrammatic representation of gap equation. First term is vertex correction, second term is self energy correction. Both diagrams exhibit $\log^2$ divergence which cancels to leading order. Solid, wavy and dashed lines represent fermion propagators, the RPA interaction (5.4), and $\Delta\tau_3$ vertex, respectively.

with experiment[6].

The effect of interactions is drastically different for semimetals with linear (type I) and quadratic (type II) electron dispersion. This was recognised in an early work [7], where the difference in behavior was traced to the density of states at low energies, which is much lower in type I systems than in type II systems. Electronic properties of quadratically dispersing systems are governed by infrared divergences in Feynman diagrams, resulting in unconventional low energy states, such as the gapped excitonic states of a bilayer graphene (BLG) discussed in Ref.[21], whereas in linearly dispersing systems the free-particle description is robust.

In this Letter, we analyze excitonic instability in a BLG system with $1/r$ repulsion, focusing on a ferroelectric (FE) state that spontaneously breaks which-layer symmetry and polarizes the layers in charge. After accounting for dynamically generated ultraviolet cutoff, treated in the RPA screening approximation, we find a gap which in the weak coupling limit scales as a square of the interaction strength, $\Delta \propto (e^2/\kappa)^2$, with e the electron charge and κ the dielectric constant. This is in contrast to the exponential BCS-like behavior of the gap expected in single layers coupled via a dielectric spacer[8, 9, 10].

Interestingly, we find the behavior to be highly sensitive to the specifics of screening model: log divergent diagrams can become $\log^2$ divergent upon going from static

to dynamic screening (see Fig.5-1b). Thus for a reliable estimate of the gap it is necessary to properly treat dynamic screening. We evaluate the dynamical polarisation function for BLG and use it to estimate the gap value $\Delta \sim 10^{-3} m e^4 \kappa^{-2}$. For realistic parameters the predicted gap lies within the experimentally accessible range. The gap value found for the FE state coinsides with that for the anti-ferromagnetic (AF) states considered in [21], indicating that these states are near degenerate in energy.

The formation of a gapped state will manifest itself in strongly temperature dependent conductivity at $T \lesssim \Delta$. In the presence of long-range disorder, the gapped state will occur at the p-n boundaries separating electron and hole 'puddles', making these boundaries a bottleneck for transport. Hopping-like temperature dependence is indeed noted in all conductivity measurements near neutrality point in BLG but not in single-layer graphene [1].

Since the ferroelectric transition breaks a Z_2 symmetry, excitonic ordering will produce domains of opposite polarization (see Fig.5-1(a)). In the absence of disorder, the characteristic size of the domains L is determined by long-range attraction between polarization in neighboring domains, in analogy with "electronic microemulsion phases" discussed in Ref.[16], giving an estimate $8\rho^2 \ln(L/a_0) \approx \Delta/a_0$, where ρ is polarization density and a_0 is the correlation length, Eq.(5.3). As discussed in Ref.[18], the boundaries between regions with opposite polarization host valley polarized edge states. Since a two-dimensional system with two domain types should exhibit percolation of edge states, the FE state should be able to carry valley currents. This could be useful for valleytronics applications.

The low-energy Hamiltonian for BLG can be described in a 'two band' approximation, neglecting the higher bands that are separated from the Dirac point by an energy gap $W \sim 0.4$ eV [11]. The electron states are described by wavefunction taking values on the A and B sublattice of the upper and lower layer respectively. The non-interacting spectrum consists of quadratically dispersing quasiparticle bands $E_\pm = \pm p^2/2m$ with band mass $m \approx 0.054 m_e$. It is convenient to introduce the Pauli matrices τ_i that act on the sublattice space, and to define $\tau_\pm = \tau_1 \pm i\tau_2$ and $p_\pm = p_x \pm i\zeta p_y$ [11], where $\zeta = 1$ for the K valley and $\zeta = -1$ for the K' valley. The

Hamiltonian may then be written

$$\begin{aligned} H_0 &= \sum_{\mathbf{p},\alpha} \psi^\dagger_{\mathbf{p},\alpha} \left(\frac{p_+^2}{2m}\tau_+ + \frac{p_-^2}{2m}\tau_- \right) \psi_{\mathbf{p},\alpha} \\ H &= H_0 + \frac{e^2}{2\kappa} \sum_{\mathbf{x},\mathbf{x}'} \frac{n(\mathbf{x})n(\mathbf{x}')}{|\mathbf{x}-\mathbf{x}'|}, \quad n(\mathbf{x}) = \sum_\alpha \psi^\dagger_\alpha(\mathbf{x})\psi_\alpha(\mathbf{x}). \end{aligned} \tag{5.1}$$

The sum over α indicates summation over $N = 4$ spin and valley species, while the dielectric constant κ incorporates the effect of polarization of the substrate and of the higher bands of BLG. The interaction is invariant under $SU(N)$ rotations in spin/valley space. We also approximate by treating the interlayer and intra-layer interaction as equal, and defer discussing the effect of finite layer separation until after we present our main result.

We investigate stability of the gapless state by introducing a test gap-opening perturbation $\Delta\tau_3$ into the non-interacting Hamiltonian, where Δ must be real, but may take either sign. This test perturbation explicitly breaks the Z_2 layer symmetry of the Hamiltonian, and corresponds to a ferroelectric instability that polarises the layers by charge. We develop our analysis perturbatively in the interaction, and calculate the interaction renormalization of the $\Delta\tau_3$ vertex. At leading order in weak bare interactions, the vertex correction in Fig.5-1(b) takes the form $\delta\Gamma = \tau_3\delta\Delta$, where

$$\delta\Delta = -\int \frac{\Delta}{(iE + H_0)(iE - H_0)} U \tag{5.2}$$

Here H_0 is the Hamiltonian of the non-interacting system evaluated at $\Delta = 0$. The vertex correction is positive and preserves the form of the σ_3 vertex. Moreover, simple power counting shows that the vertex correction is divergent in the infrared for any form of interaction U, screened or unscreened. The infrared divergence indicates instability even for arbitrarily weak interactions (unlike monolayer graphene). The infrared divergence is power law when U is the unscreened Coulomb interaction, therefore it is important to include screening even at weak coupling, to moderate the infrared divergence.

We now introduce the interaction energy scale E_0 and the corresponding length-

scale a_0, defined as

$$E_0 = \frac{me^4}{\kappa^2} \approx \frac{1.47}{\kappa^2}\,\mathrm{eV}, \qquad a_0 = \frac{\kappa}{me^2} \approx \kappa \times 1.1\,\mathrm{nm} \tag{5.3}$$

For simplicity, we take the weak coupling limit $E_0 \lesssim W$, and neglect interaction-induced mixing of the low energy states with the higher bands [for discussion of mixing see Ref.[17]]. Moreover, when U is the unscreened or dynamically screened Coulomb interaction, the integral in Eq.(5.2) is convergent in the UV, without the need for any high energy cutoff. Thus E_0 emerges as the only energy scale in the problem. This then implies that the energy scale for the gap must scale as a power law in electric charge $\Delta \sim E_0 \sim e^4$.

As we shall see, it is necessary to properly treat dynamic screening to obtain a reliable estimate for the gap. We therefore take U in Eq.(5.2) to be the dynamically screened Coulomb interaction, defined as

$$\tilde{U}_{\omega,\mathbf{q}} = \frac{2\pi e^2}{\kappa q - 2\pi e^2 N \Pi_{\omega,\mathbf{q}}}. \tag{5.4}$$

Here we have introduced the single species polarisation function $\Pi_{\omega,\mathbf{q}} = -\int G(\mathbf{p}_+, \varepsilon_+) G(\mathbf{p}_-, \varepsilon_-) \frac{d\varepsilon d^2p}{(2\pi)^3}$, where we use the notation $\mathbf{p}_\pm = \mathbf{p} \pm \mathbf{q}/2$ and $\varepsilon_\pm = \varepsilon \pm \omega/2$, and define the imaginary frequency Green function in terms of the non-interacting Hamiltonian H_0 as $G^{-1}(E, \mathbf{p}, \Delta) = iE - H_0(\mathbf{p}, \Delta)$. Hence, we obtain

$$\Pi_{\omega,\mathbf{q},\Delta} = -2 \int \frac{dE d^2p}{(2\pi)^3} \frac{E_+E_- - p_+^2 p_-^2 \cos(2\theta_{pq}) - \Delta^2}{(E_+^2 + p_+^4 + \Delta^2)(E_-^2 + p_-^4 + \Delta^2)}. \tag{5.5}$$

Here, θ_{pq} is the angle between the vectors $\mathbf{p}_+$ and $\mathbf{p}_-$. To determine the dynamically screened interaction, it is sufficient to determine the polarisation function in the ungapped state. We therefore take $\Delta \to 0$ in Eq.(5.5), integrate over frequencies by residues, and scale out q. The integral then depends on a single dimensionless parameter $\tilde{\omega} = 2m\omega/q^2$, and may be evaluated analytically by integrating over momenta in polar co-ordinates (details in online supplement). This gives an exact expression for

the polarisation function $\Pi_{\omega,\mathbf{q},0} = -\frac{m}{2\pi} f(\tilde{\omega})$, where

$$f(\tilde{\omega}) = \frac{2\tan^{-1}\tilde{\omega} - \tan^{-1} 2\tilde{\omega}}{\tilde{\omega}} + \ln \frac{\tilde{\omega}^2 + 1}{\tilde{\omega}^2 + \frac{1}{4}} \approx \frac{\ln 4}{\sqrt{1 + u\tilde{\omega}^2}} \tag{5.6}$$

with $u = (2\ln 4\pi)^2$. The right hand side provides an approximate formula that reproduces $f(\tilde{\omega})$ exactly for $\tilde{\omega} \to 0$ and $\tilde{\omega} \to \infty$, interpolating accurately between the two limits. Result (5.6) agrees with the polarization function found in [12] continued to Matsubara frequencies.

The vertex correction Eq.(5.2), calculated with the dynamically screened interaction Eq.(5.4), is $\ln^2$ divergent in the infrared (see supplement). The enhanced divergence arises from the phase space region $\omega/q^2 \gg 1$, where the Coulomb interaction is not efficiently screened. However, it is also necessary to take account of the self-energy correction, so that the full gap equation is represented by Fig.5-1(b). In particular, the self energy undergoes a $\ln^2$ renormalisation [20], and this can be shown to cancel the vertex correction at $\ln^2$ order, leaving a residual logarithmic divergence.

Since demonstrating the cancellation of the self energy and vertex correction at leading $\ln^2$ order and extracting the subleading logarithmic divergence is fairly tedious, we employ an alternative scheme for solving the gap equation Fig.5-1(b). We note that calculating the free energy of BLG as a function of Δ, at leading non-vanishing order in Δ, simply produces the diagrams in Fig.5-2(a,b,c). Upon minimizing with respect to Δ, this yields the gap equation Fig.5-1(b), with correct combinatorial coefficients. Minimising the free energy of BLG with respect to Δ is therefore formally equivalent to solving the gap equation Fig.5-1(b), and is technically simpler. It may be verified that while Fig.5-2 (b) and (c) are individually $\ln^3$ divergent in the infrared, their sum is only $\ln^2$ divergent. This is the same leading order cancellation of divergences that is manifested by the gap equation.

We approximate by assuming that the gap function Δ is static and momentum independent, on the grounds that the screened interaction in the particle-hole channel depends only weakly on the transferred momentum. In this approximation, we evaluate the kinetic energy change δT represented by Fig.5-2(a) by including Δ in the

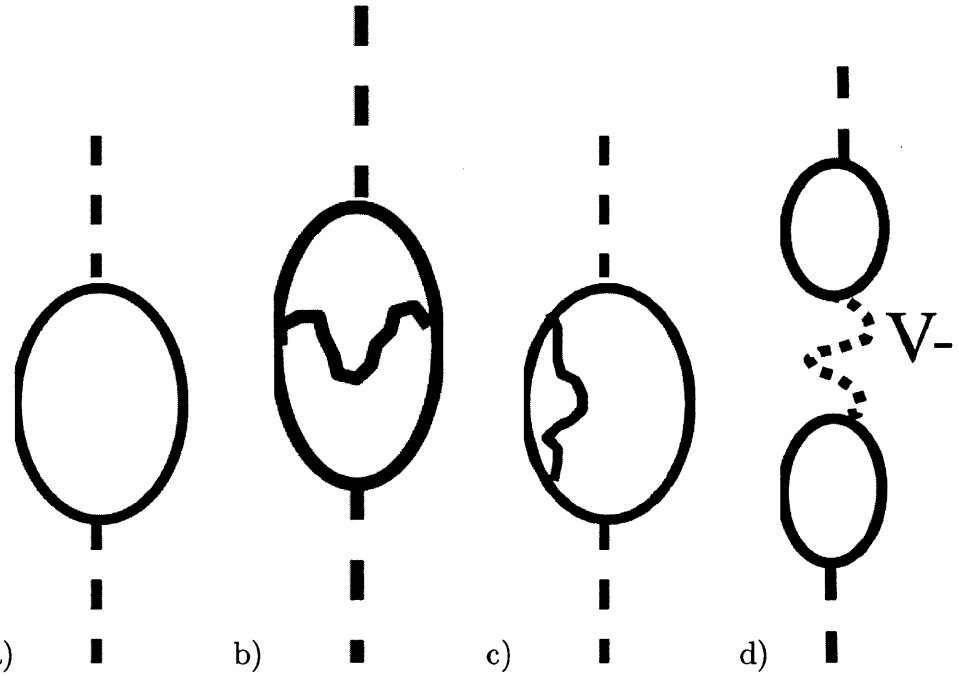

Figure 5-2: Free energy change from gap formation at leading order in Δ and in the interaction. V_- is the difference between interlayer and intra-layer interactions. While all these diagrams are nominally $O(\Delta^2)$, Δ also appears as a logarithmic infrared cutoff in each diagram Eq.(5.9). Physically, the diagrams may be interpreted as a) Kinetic energy cost from spontaneous gap opening. b, c) Interaction energy gain from gap opening. d) Hartree energy cost of layer polarisation - vanishes within the approximations of Eq.5.1

fermion Green function. We obtain, with logarithmic accuracy, $\delta T = \frac{m}{2\pi}\Delta^2 \ln(\Lambda/\Delta)$, where Λ is the maximum momentum scale up to which the gap persists.

To calculate the exchange energy gain, we note that the difference in interaction energy between the gapped and ungapped states, $\delta V = V(\Delta) - V(0)$ is given, within the RPA approach, by

$$\delta V = \int \frac{d\omega d^2p}{(2\pi)^3} \ln\left(1 - N\tilde{U}_{\omega,q}(\Pi_{\omega,q,\Delta} - \Pi_{\omega,q,0})\right). \tag{5.7}$$

Here, $\tilde{U}_{\omega,q}$ is the interaction Eq.(5.4) and $\Pi_{\omega,q,\Delta}$ is the single species polarisation function in the gapped state. The problem thus reduces to that of evaluating the polarisation function at finite Δ.

We calculate the quantity $\Pi_\Delta - \Pi_0$ by integrating Eq.(5.5) over frequencies by residues, Taylor expanding to leading order in small Δ^2, and analytically performing the integration over momenta, assuming as before that Δ is independent of momentum. After some algebra (available in the online supplement), we obtain

$$\Pi_\Delta - \Pi_0 = \frac{m\Delta^2}{2\pi r^2}\left(\ln\frac{r}{\Delta}\right)\left(-7\frac{q^4}{r^2} + 4\frac{q^8}{r^4}\right). \tag{5.8}$$

We are using the notation $r^2 = \omega^2 + q^4$.

We now evaluate the exchange energy gain from gap formation by substituting Eq.(5.8) into Eq.(5.7), and performing the integrals using polar co-ordinates, (see supplement for details). Combining this with the kinetic energy cost obtained earlier, we find that the free energy associated with gap opening is

$$F(\Delta) = \frac{m}{2\pi}\Delta^2 \ln(\Lambda/\Delta) - \frac{13m\Delta^2}{6\pi^3}\ln^2(N^2E_0/\Delta) \tag{5.9}$$

We note the expected emergence of a natural ultraviolet cutoff $\Lambda = N^2E_0$. Minimizing Eq.(5.9) with respect to Δ, we obtain, with logarithmic accuracy

$$\Delta = N^2E_0 \exp(-3\pi^2 N/13) \tag{5.10}$$

We emphasize that E_0 appears only outside the exponential, making Δ a power law function of interaction strength at weak coupling. However, Δ is exponentially small in N, where N is the number of fermion species participating in screening. If we had worked instead with static screening, we would have obtained $\Delta \sim N^2 E_0 \exp(-2N \ln 4)$, and would have underestimated the size of the gap by an order of magnitude.

For $N = 4$ Eq.(5.10) gives $\Delta \approx 10^{-3} E_0 \sim 1.5$ meV κ^{-2}, upto a numerical prefactor of order unity. Meanwhile, numerically evaluating the free energy integrals Eq.(5.7) and Fig.5-2(a) and minimising with respect to Δ gives $\Delta \approx 4$ meV κ^{-2}. This number lies within the experimentally accessible regime, although it can be reduced by screening in the substrate, by doping, or by disorder induced density inhomogeneity.

Thus far, we have neglected the effect of trigonal warping which leads to deviation of particle dispersion from a simple quadratic dependence, causing an overlap of the conduction and valence bands. Trigonal warping can provide an alternative IR cutoff and prevent formation of a gapped state, but only if the size of the trigonal warping effect exceeds the size of the estimated gap. Since the the upper estimate for trigonal warping, 1.5 meV [19], is less than the estimated gap value $\Delta = 4$ meV κ^{-2} the effect of trigonal warping on gap formation should be inessential, at least for suspended bilayers ($\kappa \approx 1$).

Our analysis can be easily generalized to any state that adds a term $\Delta \tau_3 \Omega$ to the Hamiltonian (5.1), where Ω is a 4×4 hermitian matrix in spin/valley space satisfying $\Omega^2 = 1$. The FE state considered above corresponds to $\Omega = 1$, wheras the AF states discussed in Ref.[21] are characterized by $\Omega = \sigma_3 \otimes 1$ or $\Omega = 1 \otimes \eta_3$, where σ_3 and η_3 are Pauli matrices in spin and valley space, respectively. All these inequivalent choices for Ω yield the same mean field free energy $F(\Delta)$, Eq.(5.9), and the same gap value as was obtained for the FE state. This mean field degeneracy occurs because the Hamiltonian is invariant under $SU(4)$ spin/valley rotations, within validity of Eq.(5.1), while the states corresponding to different choices of Ω differ only in their spin/valley structure.

We now examine the effect of finite layer separation $d \approx 3$Å, which differentiates

the interlayer and intra-layer interactions, giving an anisotropy $V_- = \frac{1}{2}(V_{AA} - V_{AB}) = \frac{1}{2}\frac{2\pi e^2}{q}(1 - e^{-qd}) = \pi e^2 d$. This anisotropy is small, because $d \ll a_0$. The leading order effect of finite layer separation is to introduce a Hartree energy Fig.5-2(d) for the states that polarise the layers in charge,

$$E_{Hartree} = \frac{Nm^2}{4\pi^2} V_- \Delta^2 \ln^2(\Lambda/\Delta). \tag{5.11}$$

Ref.[19] identified this Hartree energy, concluding that it prevents formation of the ferroelectric state. However, Ref.[19] neglected the exchange energy. We note that the Hartree energy is of the same functional form as the exchange energy Eq.(5.9) but is parametrically smaller by $d/a_0 \ll 1$, and so cannot prevent the instability.

Upon going beyond the weak coupling approximation, d/a_0 ceases to be a good control parameter, but our conclusions remain unchanged. This is because the V_- interaction is screened as $\tilde{V}_- = V_-/(1 - V_- \Pi_-)$, where $\Pi_- = \int \mathrm{Tr} G(\varepsilon_+, \mathrm{p}_+)\tau_3 G(\varepsilon_-, \mathrm{p}_-)\tau_3 \frac{\mathrm{d}\varepsilon \mathrm{d}^2\mathrm{p}}{(2\pi)^3} \sim \frac{\mathrm{m}}{2\pi} \ln(\Lambda/\Delta)$. Such logarithmic screening ensures that the Hartree energy remains smaller than the exchange energy Eq.(5.9) and so cannot prevent gap formation. However, when d/a_0 is not small, the Hartree energy may tip the balance from the FE state to one of the AF states, which do not polarise the layers by charge.

A ferromagnetic instability was predicted for unscreened interactions in [12]. However, the free energy gain from ferromagnetism was only cubic in the ferromagnetic order parameter. In contrast, the excitonic states all have a free energy gain of $O(\Delta^2)$, and should thus dominate for weak coupling.

After submitting this Letter we became aware of works [8] and [23]. Instabilities in BLG are analyzed in these papers within a renormalization group framework, with interactions modeled as being short range. It is found that different choices of short range interaction can result in different states, gapped [8] or gapless [23].

To conclude, we have demonstrated that electron-electron interactions drive BLG to a gapped state. Our analysis considers dynamically screened Coulomb interactions, and yields an estimate for the gap of $\Delta = 10^{-3} E_0$, where $E_0 = me^4/\hbar^2\kappa^2$. Manifestations of the energy gap opening in BLG include temperature dependent transport

at low temperatures, and also valley polarised edge states.

Bibliography

[1] A. K. Geim and K. S. Novoselov, Nature Mater. **6**, 183 (2007).

[2] J. Gonzales, F. Guinea, and M. A. H. Vozmediano, Nucl. Phys. B**424**, 595 (1994); Phys. Rev. B **59**, R2474 (1999).

[3] D. V. Khveshchenko, Phys. Rev. Lett. **87**, 246802 (2001).

[4] V. P. Gusynin, V. A. Miransky and I. A. Shovkovy, Phys. Rev. Lett. **73**, 3499 (1994).

[5] I. F. Herbut, Phys. Rev. Lett. 97, 146401 (2006) .

[6] J. G. Checkelsky, L. Li, and N. P. Ong, Phys. Rev. Lett. **100**, 206801 (2008).

[7] A. A. Abrikosov and S. D. Beneslavskii, Zh. Eksp. Teor. Fiz. **59**, 1280 (1970) [Sov. Phys. JETP **32**, 4 (1971)]; J. Low Temp. Phys. **5**, 2 (1971).

[8] H. Min, J. J. Su and A. H. MacDonald, Phys. Rev. B **78**, 121401(R)(2008).

[9] C. H. Zhang and Y. N. Joglekar, Phys. Rev. B **77**, 233405 (2008).

[10] M. Y. Kharitonov and K. B. Efetov, Phys. Rev. B **78**, 241401(R) (2008).

[11] E. McCann and V. Fal'ko, Phys. Rev. Lett. **96**, 086805 (2006); E. McCann, Phys. Rev. B **74**, 161403(R) (2006).

[12] J. Nilsson, A. H. Castro Neto, N. M. R. Peres and F. Guinea, Phys. Rev. B 73, 214418 (2006)

[13] S. V. Kusminskiy, J. Nilsson, D. K. Campbell, and A. H. Castro Neto, Phys. Rev. Lett. **100**, 106805 (2008).

[14] E. H. Hwang and S. Das Sarma, Phys. Rev. Lett. **101**, 156802 (2008).

[15] J. Alicea, M. Fisher, Phys. Rev. B 74, 075422 (2006) Discussion of symmetry is for single layer graphene, but applies equally to BLG.

[16] R. Jamei, S. Kivelson, and B. Spivak, Phys. Rev. Lett. **94**, 056805 (2005).

[17] D. S. L. Abergel and T. Chakraborty, Phys. Rev. Lett. 102, 056807 (2009).

[18] I. Martin, Y. M. Blanter and A. F. Morpurgo, Phys Rev Lett **100**, 036804 (2008).

[19] E. McCann, D. S. L. Abergel and V. Falko, Solid State Comm. **143**, 110 (2007).

[20] Y. Barlas and K. Yang, Phys. Rev. B 80, 161408(R) (2009).

[21] H. Min, G. Borghi, M. Polini and A. MacDonald, Phys Rev B 77, 041407(2008).

[22] F. Zhang, H. Min, M. Polini and A. H. MacDonald, Phys. Rev. B 81, 041402(R) (2010).

[23] O. Vafek and K. Yang, Phys. Rev. B 81, 041401(R) (2010).

Chapter 6

Spontaneously ordered states in Bilayer Graphene

We present a symmetry-based analysis of competition between different gapped states that have been proposed in bilayer graphene (BLG), which are all degenerate on a mean field level. We classify the states in terms of a hidden SU(4) symmetry, and distinguish symmetry protected degeneracies from accidental degeneracies. One of the states, which spontaneously breaks discrete time reversal symmetry but no continuous symmetry, is identified as a Quantum Anomalous Hall (QAH) state, which exhibits quantum Hall effect at zero magnetic field. We investigate the lifting of the accidental degeneracies by thermal and zero point fluctuations, taking account of the modes softened under a renormalisation group procedure (RG). Working in a 'saddle point plus quadratic fluctuations' approximation, we identify two types of RG-soft modes which have competing effects. Zero point fluctuations, dominated by 'transverse' modes which are unique to BLG, favor the QAH state. Thermal fluctuations, dominated by 'longitudinal' modes, favor a SU(4) symmetry breaking multiplet of states. We discuss the phenomenology and experimental signatures of the QAH state in BLG, and also propose a way to induce the QAH state using weak external magnetic fields.

6.1 Introduction

The Quantum Anomalous Hall (QAH) insulator is a state of matter where spontaneous breaking of time reversal symmetry produces (integer) quantum Hall effect in the absence of any external magnetic field. First predicted in 1988 [1], the QAH state has never yet been observed. In the recent literature on interaction driven topological insulators [2, 3], the elusiveness of the QAH state has been ascribed to fluctuations, which typically disfavor the QAH state with respect to a Quantum Spin Hall (QSH) state, which is degenerate with the QAH state on a mean field level. Here we point out that the fluctuations which govern the competition of different gapped phases proposed in bilayer graphene (BLG) [4, 5, 6] are dominated by the modes not present in the models [2, 3], leaving open the door to formation of a QAH state at zero field in BLG. Also, we will propose a mechanism for inducing the QAH state using external fields.

The theoretical literature on BLG predicts instabilities to numerous strongly correlated states, which are gapped [4, 5, 6] or gapless [7] depending on the way the electron-electron interaction is modeled. The numerous gapped states predicted in the literature are all degenerate at the level of mean field theory [4, 5], and have the same instability threshold under one loop RG [6]. The relation between these different states, and their experimental signatures, have not yet been understood.

Meanwhile, recent experiments indicate that the gapped state observed in charge neutral BLG in quantizing magnetic fields [8] persists down to low fields, crossing over to another gapped state at zero field [9]. However, the nature of the gapped state at zero field is unknown. Hence, clarifying the relation between different gapped states and understanding their physical properties is an interesting and timely task.

Here we present a unifying symmetry based analysis of strongly correlated states in BLG. The states predicted in Refs.[[4, 5, 6]] are classified according to a hidden SU(4) flavor symmetry into symmetry breaking multiplets and an SU(4) invariant singlet. The SU(4) singlet is a QAH state. The degeneracy of the multiplets and the singlet is an artefact of the approximations made in the analysis, and will be lifted

upon taking fluctuation effects into account.

Our analysis of fluctuations in BLG focuses on the effect of the modes softened under RG. Those include the 'longitudinal' fluctuation modes (L-modes) analogous to those discussed in Ref.[[2, 3]], and also 'transverse' fluctuation modes (T-modes) which are unique to BLG. We find that these two types of modes have competing effects: while the L-modes favor the symmetry breaking multiplets, the T-modes favor the SU(4) invariant QAH state. The zero-point fluctuations are dominated by the T-modes, and hence appear to favor a QAH state at zero temperature. Meanwhile, thermal fluctuations are dominated by the L-modes, and favor the symmetry breaking multiplets. We speculate that thermal fluctuations may drive a phase transition from the QAH state at low temperatures to a SU(4) symmetry breaking state at higher temperatures, and estimate the transition temperature. We also discuss the phenomenology of the QAH state, its possible experimental signatures, and propose a way to further stabilize it using external magnetic fields.

6.2 SU(4) symmetry

In this section we show that within the often-used approximation where the difference between interlayer and intra-layer interactions is neglected [4, 5, 6, 13, 14], the interacting Hamiltonian is invariant under rotations in a suitably defined four-dimensional flavor subspace. Specifically, we perform a unitary transformation by exchanging the sublattices A and B in one of the valleys, upon which the single particle Hamiltonian becomes identical for all spin and valley species, while the layer and sublattice blind interactions are left unchanged.

Before entering the discussion of the SU(4) invariance in BLG, we recall that electronic states in BLG at low energy are described by wave-functions on the A and B sublattices of the upper and lower layers [11], and are fourfold degenerate in spin and valley. To analyze the structure of the Hamiltonian, it will be convenient to combine the spin and valley components in a single eight-component wavefunction $\psi_{\alpha,s,v}(\mathbf{x})$, where α is the sublattice (layer) index. We shall use the Pauli matrices in

sublattice, spin and valley space, denoted below by τ_i, σ_i and η_i, respectively. The low energy non-interacting Hamiltonian may then be written as

$$H_0 = \frac{(p_x + ip_y\eta_3)^2}{2m}\tau_- + \frac{(p_x - ip_y\eta_3)^2}{2m}\tau_+, \tag{6.1}$$

where $\tau_\pm = \tau_1 \pm i\tau_2$. Here $m = 0.05m_e$ is the effective mass. Because of the presence of η_3 in Eq.(6.1), the single particle Hamiltonian is not invariant under rotations of valley components. To bring it to an SU(4) invariant form, we perform a unitary transformation on all operators

$$\tilde{O} = UOU^\dagger, \quad U = \frac{1+\eta_3}{2} + \frac{1-\eta_3}{2}\tau_1. \tag{6.2}$$

This transformation does not act on the spin space, however it mixes the layer and valley indices of the wavefunction $\psi_{\alpha,s,v}(\mathbf{x})$ by interchanging the τ pseudospin component (layer) in one of the valleys. As a result, τ_+ and τ_- are interchanged and τ_3 changes sign in the $\eta_3 = -1$ valley, after which the free-particle Hamiltonian, Eq.(6.1), becomes identical in both valleys.

Defining $p_\pm = p_x \pm ip_y$, the transformed non-interacting Hamiltonian takes the compact form

$$H_0 = \frac{p_+^2}{2m}\tilde{\tau}_- + \frac{p_-^2}{2m}\tilde{\tau}_+, \tag{6.3}$$

where $\tilde{\tau}_+$ and $\tilde{\tau}_-$ are obtained by transforming τ_+ and τ_- according to Eq.(6.2). This single particle Hamiltonian is manifestly invariant under $SU(4)$ rotations in the transformed spin/valley flavor space.

Meanwhile, electron interactions can be described by a many-body Hamiltonian written in terms of $\rho_\mathbf{q} = \sum_\mathbf{p} \psi_\mathbf{p}^\dagger \psi_{\mathbf{p}+\mathbf{q}}$ (the density summed over layers) and $\lambda_\mathbf{q} = \sum_\mathbf{p} \psi_\mathbf{p}^\dagger \tilde{\tau}_3 \tilde{\eta}_3 \psi_{\mathbf{p}+\mathbf{q}}$ (the density difference between layers). The interacting Hamiltonian, which incorporates a difference between interlayer and intralayer interaction [14], can be written as

$$H = \sum_\mathbf{p} \psi_\mathbf{p}^\dagger H_0 \psi_\mathbf{p} + \frac{1}{2}\sum_\mathbf{q} V_+(q)\rho_\mathbf{q}\rho_{-\mathbf{q}} + V_-\lambda_\mathbf{q}\lambda_{-\mathbf{q}}, \tag{6.4}$$

where $V_+(q) = 2\pi e^2/\kappa q$ is the Coulomb interaction, and $V_- = \pi e^2 d/\kappa$ accounts for the layer polarization energy (here $d = 3.5\mathring{A}$ is the BLG layer separation). The $\rho\rho$ term, which is isotropic in flavor space and thus is SU(4) invariant, dominates because d is small compared to

$$a_0 = \hbar^2\kappa/me^2 = 10\kappa\,\text{Å}, \tag{6.5}$$

the characteristic lengthscale set by interactions [5]. We therefore approximate by neglecting V_-, an approximation that becomes exact in the weak coupling limit, where $d/a_0 \to 0$. Under this approximation, the Hamiltonian is invariant under SU(4) flavor rotations, generated by the operators $\tilde{\eta}_i$ and $\tilde{\sigma}_i$. We will henceforth drop the $\sim$ symbols for notational convenience, and will refer to the operators $\tilde{\tau}$, $\tilde{\eta}$ and $\tilde{\sigma}$ as τ, η and σ respectively. All operators are assumed to be transformed operators unless specified otherwise.

6.3 Classification of states and topological properties

In the transformed basis, the mean field Hamiltonian for the gapped states described in [4, 5, 6] may be written as

$$H = \frac{p_+^2\tau_- + p_-^2\tau_+}{2m} + \Delta\tau_3 Q, \tag{6.6}$$

where $m = 0.05m_e$ is the effective mass. Here the Pauli matrices τ_i act on the transformed sublattice space, and Q is a 4×4 hermitian matrix in the transformed spin-valley space (flavor space), satisfying $Q^2 = 1$.

Since unitary hermitian matrices have eigenvalues ± 1, all gapped states can be classified as $(M_>, M_<)$, where $M_>$ and $M_<$ are the numbers of $+1$ and -1 eigenvalues of Q respectively. There are three general types of states: $(2,2)$, $(3,1)$, and $(4,0)$. There is an additional Z_2 symmetry associated with the overall sign of Q which is absorbed into the sign of Δ. Following Refs.[[1, 15]], the Hall conductance of a state

$(M_>, M_<)$ can be written as

$$\sigma_{xy} = (M_> - M_<)\frac{e^2}{h}, \tag{6.7}$$

where we took into account an additional factor of 2 due to the Berry phase 2π in BLG [11]. The (4,0) and (3,1) states, which have $M_> \neq M_<$, thus exhibit a quantized Hall conductance at zero magnetic field–the hallmark of a QAH state. Because these states have $\sigma_{xy} \neq 0$, they must spontaneously break time reversal symmetry. We will henceforth focus on comparing the (4,0) and (2,2) states, since the (3,1) states are intermediate between the two. We will refer to the (4,0) state as the QAH state, but it should be remembered that the (3,1) states are also QAH states. In contrast, the (2,2) states have $\sigma_{xy} = 0$, and preserve time reversal symmetry, but instead exhibit quantum flavor Hall effect. If we parameterize the flavor space by Pauli matrices η_i and σ_i in transformed valley and spin space respectively, then the $Q = \sigma_3$ state is a QSH state (Ref.[[16]]), while the $Q = \eta_3$ state is a Quantum Valley Hall (QVH) state (Ref.[[17]]).

These states are analogs of the 'topological Mott insulators' discussed in Refs.[[2, 3]], and as such host topologically protected edge states. The counter-propagating valley modes for the QVH state were worked out in Ref.[[17]], the co-propagating charge modes and the counter-propagating spin modes for the QAH and QSH states follow similarly. The protection of edge modes is strongest for the (4,0) state due to the unidirectional, chiral character of these modes. The counter-propagating spin currents in the QSH state are protected in the absence of spin-flip scattering, while the counter-propagating valley currents in the QVH state are protected in the absence of intervalley scattering (e.g. by short range disorder).

We note that the above classification of states superficially resembles that arising in an entirely different problem, namely the Quantum Hall Ferromagnet (QHF) in graphene in quantizing magnetic field[18]. In the latter case, however, the integers $M_>$ and $M_<$ are fixed by the electron density, i.e. by filling of the four-fold degenerate zeroth Landau level. In the QHF problem, spontaneous time-reversal symmetry

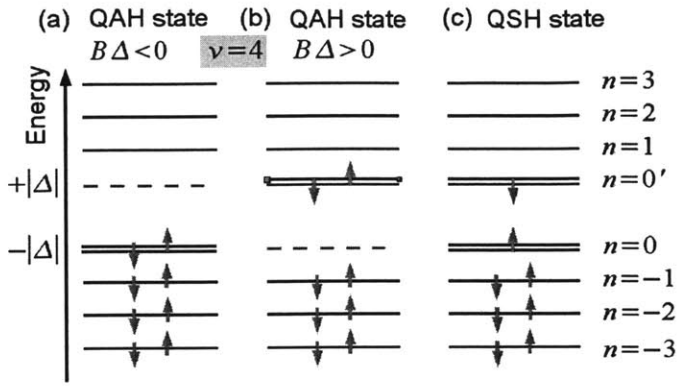

Figure 6-1: Landau level spectrum of the QAH and QSH states. Note an anomalous Landau level in the QAH state that has no particle-hole-symmetric counterpart. Occupation of this anomalous Landau level allows the QAH state (a) to lower its energy relative to the states (b,c) at filling factor $\nu = 4$.

breaking cannot occur: the analog of the (4,0) QAH state is a fully filled zeroth Landau level exhibiting quantized Hall conductance $2e^2/h$. Furthermore, in the QHF problem there is no competition between states with different $M_>$ and $M_<$ values, which is the main question of interest for us here.

6.4 Lifting accidental degeneracies using external fields

The SU(4) symmetry of the Hamiltonian guarantees the degeneracy of all states within a given manifold ($M_>$, $M_<$), even when the states involved have very different physical properties. For example, the QVH state is a ferroelectric state which polarizes the layers by charge, while the QSH state polarizes the layers by spin and valley. Nonetheless, the two states are related by SU(4) transformations, and are hence degenerate within the approximations leading to SU(4) symmetry.

In contrast, the degeneracy of the different manifolds ($M_>, M_<$) is purely accidental, and may be lifted in the presence of a weak SU(4) invariant perturbation. As an example, we consider application of a weak transverse magnetic field B. Incorporated in the Hamiltonian (6.6) through the replacement $\mathbf{p} \to \mathbf{p} - e\mathbf{A}$, it preserves the SU(4) symmetry, and causes the spectrum to split into Landau levels [19] with an energy

spacing of order $\hbar\omega_c$, where $\omega_c = eB/mc$. The Zeeman energy $2\mu_B B\sigma_3$ is not $SU(4)$ invariant, but may be neglected since $\hbar\omega_c \gg 2\mu_B B$. When $\Delta = 0$ and Zeeman terms are neglected, the Landau level spectrum is particle-hole symmetric and is fourfold degenerate in flavors.

Crucially, the T non-invariance of the mass term $\Delta\tau_3$ means that the Landau level spectrum for the (4,0) state is not invariant under $B \to -B$ and is not particle-hole symmetric [15]. In particular, the zeroth Landau level, which has an additional two-fold orbital degeneracy [19], forms at energy $\Delta \text{sign} B$ only, and has no counterpart at $-\Delta \text{sign} B$ (see Fig.6-1a,b). This breaking of particle hole symmetry can be exploited to induce the (4,0) state using magnetic fields.

We illsutrate this by comparing the energies of the $(4,0)$ QAH state and the $(2,2)$ QSH state in external magnetic field at filling factor $\nu = 4$. In a magnetic field, these states are no longer degenerate, because of the anomalous Landau level. It is clear from Fig.6-1 that the QAH state with the appropriate sign of Δ (such that $B\Delta < 0$) is favored over the QSH state:

$$F_{4,0} - F_{2,2} = \frac{4\Delta B}{\Phi_0} < 0, \tag{6.8}$$

where Φ_0 is the flux quantum and $F_{M_>,M_<}$ is the free energy per unit area for a state $(M_>, M_<)$. This mechanism for lifting the degeneracy between QAH and QSH states in favor of the QAH state applies to all systems where there is such a degeneracy, including the models studied in Refs.[[2, 3]]. Of course, at finite B, there is no time reversal symmetry, so the state realized is not a true QAH state, but rather is a state showing quantum Hall effect at anomalously low magnetic fields, which is smoothly connected to a QAH state at $B = 0$.

The analysis above is valid only for sufficiently small B, when BLG at $\nu = 4$ is not far from charge neutrality. This is because the excitonic instability that generates the gap Δ (Refs.[[4, 5, 6]]) is suppressed by detuning away from charge neutrality.

6.5 Saddle point analysis

We now investigate the energy splitting between the different manifolds at $B = 0$ by going beyond a mean field approximation, and including the effect of fluctuations. We consider BLG in the presence of screened Coulomb interactions between electrons. A static screening approximation, ignoring the effects of dynamical screening[5], is sufficient to understand the main features. In this approximation, the interaction is short range, and we can write the partition function as a functional field integral in Euclidean time,

$$Z = \int D\psi^\dagger D\psi \exp\left(-\int dx \mathcal{L}[\psi^\dagger(x), \psi(x)]\right), \tag{6.9}$$

where $x = (t, \mathbf{r})$, $dx = dtd^2r$, the ψ fields are fermionic fields, with the Lagrangian

$$\mathcal{L} = \psi^\dagger(\partial_t + H_0)\psi + \sum_{j,k=1\ldots8} \frac{\lambda}{2}\psi_j^\dagger\psi_k^\dagger\psi_k\psi_j. \tag{6.10}$$

Here j, k are combined sublattice and flavor indices, and H_0 is the non-interacting Hamiltonian (given by Eq.(6.6) at $\Delta = 0$). The coupling constant λ represents the statically screened Coulomb interaction, which in the RPA model takes value [20] $\lambda = 1/(4\nu_0 \ln 4)$, where $\nu_0 = m/2\pi$ is the non-interacting single species density of states.

We now decouple the four fermion interaction term via a Hubbard-Stratonovich transformation in the exchange channel, to obtain $Z = \int D\psi^\dagger D\psi Dh \exp[-\int dx \mathcal{L}(\psi^\dagger, \psi, h)]$, where

$$\mathcal{L} = \psi^\dagger[\partial_t + H_0 + h]\psi + \frac{1}{2\lambda}\mathrm{Tr}[hh^\dagger]. \tag{6.11}$$

Here, h is an 8×8 hermitian matrix, which we write as $h = M \otimes Q$, where M is a 2×2 hermitian matrix in sublattice space and Q is a 4×4 hermitian matrix in flavor space. The gapped states (Ref.[[4, 5, 6]]) correspond to taking $M = \Delta\tau_3$. Integrating

out the fermions yields $Z = \int D(Q)D(\Delta)\exp(-\int dx\mathcal{L}[\Delta(x), Q(x)]$, where

$$\mathcal{L}(\Delta, Q) = -\mathrm{Tr}\ln\left[\partial_t + H_0 + \Delta\tau_3 Q\right] + \frac{\Delta^2}{\lambda}\mathrm{Tr}[Q^2]. \tag{6.12}$$

The SU(4) flavor invariance manifests itself in an exact SU(4) flavor degeneracy of the many body states. Upon minimizing the action (6.12) in a saddle point approximation, we find $Q^2 = 1$, and $\Delta = \Lambda\exp(-2/\lambda\nu_0)$, where $\Lambda \approx 0.4\,\mathrm{eV}$ is the bandwidth for the two band Hamiltonian. This gives the mean field Hamiltonian, Eq.(6.6).

We note that instead of decoupling the interaction in the excitonic channel $h = \tau_3 \otimes Q$, we could have chosen the channel $h = \tau_{1,2} \otimes Q$. This choice would lead us to the nematic state of Ref.[7], which is gapless, but breaks lattice rotation symmetry. However, the nematic state is higher in energy than the gapped states at the saddle point level, so we will concentrate on the gapped states, and specifically on the lifting of the accidental degeneracies by thermal and zero-point fluctuations.

Our symmetry analysis, involving multiplets $(M_>, M_<)$ for different matrices Q, could also be applied to the nematic state [7]. However, the fluctuation analysis cannot be perfomed because the $\tau_3\delta Q$ mode has negative rigidity, i.e. the nematic mean field is unstable.

6.6 Lifting the degeneracy: zero-point fluctuations

We first analyze the case of zero temperature, when the degeneracy is lifted by zero point fluctuations. The most important fluctuation modes are those that are softened under RG. In BLG, this means the 'L' modes $\tau_3\delta Q$, which describe fluctuations longitudinal with respect to the order parameter in sublattice space, and also the 'T' modes $\tau_{1,2}\delta Q$, which describe fluctuations transverse to the order parameter in sublattice space. In that, δQ is an arbitrary 4×4 hermitian matrix.

We therefore expand the action in Eq.(6.12) to quadratic order in the fluctuation

modes $\tau_\alpha \otimes \delta Q^\alpha$, $\alpha = 1,2,3$, to obtain

$$\delta^2 S = \sum_{ijkl\alpha\beta} \sum_{\omega,\mathbf{q}} \delta Q^{\alpha}_{ij,\omega\mathbf{q}} K^{\alpha\beta}_{ijkl}(\omega,\mathbf{q}) \delta Q^{\beta}_{kl,-\omega,-\mathbf{q}}. \tag{6.13}$$

Here, Latin indices $i,j,k = 1...N$ refer to fermion flavor, whereas Greek indices $\alpha,\beta = 1,2,3$ refer to the Pauli matrices τ_α that parameterize the fluctuations in sublattice space. The matrix K is defined by

$$K^{\alpha\beta}_{ijkl}(\omega,\mathbf{k}) = \delta_{il}\delta_{jk}\left(\frac{\delta_{\alpha\beta}}{\lambda} + \Pi^{\alpha\beta}_{ij}(\omega,\mathbf{k})\right), \tag{6.14}$$

where we have introduced the polarization operator

$$\Pi^{\alpha\beta}_{ij}(\omega,\mathbf{q}) = \int \frac{d^2p d\varepsilon}{2(2\pi)^3} \mathrm{Tr}\left(\tau_\alpha G_i(p_+)\tau_\beta G_j(p_-)\right). \tag{6.15}$$

It is convenient to choose a diagonal background state $Q = \zeta_i \delta_{ij}$, where $\zeta_i = \pm 1$, so that the Greens function takes a form diagonal in the flavor space,

$$G_i(p_\pm) = \frac{1}{i(\varepsilon \pm \frac{1}{2}\omega) - H_0(\mathbf{p} \pm \frac{1}{2}\mathbf{q}) - \zeta_i \Delta \tau_3}. \tag{6.16}$$

The trace in Eq.(6.15) goes over sublattice indices, but not over flavors.

The matrix K is positive definite, so we may integrate out fluctuations to obtain an expression for the fluctuation contribution to the free energy,

$$F_{\text{fluct}} = \frac{1}{2}\sum_{\alpha ij}\sum_{\omega\mathbf{k}} \ln K^{\alpha\alpha}_{ijji}(\omega,\mathbf{k}), \tag{6.17}$$

where we took into account that the only contribution comes from the diagonal terms, $\alpha = \beta$, $i = l$, $j = k$. We now subtract the fluctuation energy of the $(4,0)$ QAH state from that of the $(2,2)$ state, to obtain

$$\delta F = F_{\text{fluct},(4,0)} - F_{\text{fluct},(2,2)} = 4\sum_{\alpha=1}^{3} \ln \frac{\frac{1}{\lambda} + \Pi^{\alpha\alpha}_{>>}}{\frac{1}{\lambda} + \Pi^{\alpha\alpha}_{><}}, \tag{6.18}$$

where $\Pi^{\alpha\alpha}_{>>}$ and $\Pi^{\alpha\alpha}_{><}$ are defined by Eq.(6.15), with $(\zeta_i, \zeta_j) = (1,1)$ and $(1,-1)$ respectively:

$$\Pi^{\alpha\beta}_{>>}(\omega, \mathbf{q}) = \int \frac{d^2p d\varepsilon}{(2\pi)^3} \frac{1}{2} \mathrm{Tr}\left(\tau_\alpha G_>(p_+) \tau_\alpha G_>(p_-)\right), \tag{6.19}$$

$$\Pi^{\alpha\beta}_{><}(\omega, \mathbf{q}) = \int \frac{d^2p d\varepsilon}{(2\pi)^3} \frac{1}{2} \mathrm{Tr}\left(\tau_\alpha G_>(p_+) \tau_\alpha G_<(p_-)\right), \tag{6.20}$$

$$G_{>(<)}(\varepsilon, \mathbf{p}) = \frac{1}{i\varepsilon - H_0(\mathbf{p}) \mp \Delta\tau_3},$$

where we used a shorthand notation $p_\pm = (\varepsilon \pm \frac{1}{2}\omega, \mathbf{p} \pm \frac{1}{2}\mathbf{q})$. To analyze the effect of competition of different modes in full detail, below we compare the fluctuation energy for the states of different type $(M_>, M_<)$.

To evaluate the difference of fluctuation energies, given by Eq.(6.18), it is convenient to rewrite it as

$$\delta F = 4 \sum_{\alpha=1}^{3} \ln\left(1 + \frac{\Pi^{\alpha\alpha}_{>>} - \Pi^{\alpha\alpha}_{><}}{\frac{1}{\lambda} + \Pi^{\alpha\alpha}_{><}}\right) \tag{6.21}$$

Below we evaluate the differences of polarization functions $\Pi^{\alpha\alpha}_{>>} - \Pi^{\alpha\alpha}_{><}$, and find that different modes, L and T, yield contributions of opposite sign.

In particular, we find that $\Pi^{33}_{>>} - \Pi^{33}_{><}$ is positive, i.e. the L-modes favor the (2,2) state. This effect of longitudinal modes is well known in the topological insulator literature [2]. In contrast, the differences $\Pi^{\alpha\alpha}_{>>} - \Pi^{\alpha\alpha}_{><}$ with $\alpha = 1, 2$ are negative. Thus, the T-modes, which are unique to BLG, favor the (4,0) state. We evaluate Eq.(6.18), and find that the T-modes dominate the free energy, favoring the QAH state.

To proceed with the analysis of the quantities $\Pi^{\alpha\alpha}_{>>} - \Pi^{\alpha\alpha}_{><}$, it is convenient to define $\varepsilon_\pm = \varepsilon \pm \omega/2$, and $z_\pm = |\mathbf{p} \pm \frac{1}{2}\mathbf{q}|^2/2m$. In this compact notation, we have

$$\begin{aligned} \Pi^{\alpha\alpha}_{>>} - \Pi^{\alpha\alpha}_{><} &= \int \frac{F_{\alpha\alpha}(\varepsilon, \mathbf{p})}{(\varepsilon_+^2 + z_+^2 + \Delta^2)(\varepsilon_-^2 + z_-^2 + \Delta^2)}, \\ F_{\alpha\alpha}(\varepsilon, \mathbf{p}) &= \Delta^2 \mathrm{Tr}(\tau_\alpha\tau_3\tau_\alpha\tau_3) + \Delta \mathrm{Tr}(\tau_\alpha\tau_\alpha\tau_3)(i\varepsilon_+) \\ &\quad + \Delta \mathrm{Tr}(\tau_\alpha H_0(\mathbf{p} + \frac{1}{2}\mathbf{q})\tau_\alpha\tau_3), \end{aligned} \tag{6.22}$$

where $\int ... = \int \frac{d^2p d\varepsilon}{(2\pi)^3} ....$ Terms in Eq.(6.22) linear in Δ must vanish, since the fluc-

tuation energy should be invariant under sign changing $\Delta \to -\Delta$. Technically, the vanishing of terms linear in Δ follows because $\mathrm{Tr}(\tau_\alpha \tau_3 \tau_\alpha) = 0$, and $\mathrm{Tr}(\tau_\alpha H_0 \tau_\alpha \tau_3) = 0$. As a result, the first term in $F_{\alpha\alpha}(\varepsilon, \mathbf{p})$ (at order Δ^2) is the only term that survives. We can substitute the expression in Eq.(6.22) into Eq.(6.18) and expand the logarithm in small Δ^2, to obtain

$$\begin{aligned}
\delta F &= 4\int \sum_\alpha \frac{\Delta^2 \mathrm{Tr}(\tau_\alpha \tau_3 \tau_\alpha \tau_3)}{D_{\alpha\alpha}(\omega, \mathbf{q})(\varepsilon_+^2 + z_+^2 + \Delta^2)(\varepsilon_-^2 + z_-^2 + \Delta^2)} \\
&= 4\int \left(-\frac{1}{D_{11}(\omega, \mathbf{q})} - \frac{1}{D_{22}(\omega, \mathbf{q})} \right. \qquad (6.23) \\
&\quad \left. + \frac{1}{D_{33}(\omega, \mathbf{q})} \right) \frac{2\Delta^2}{(\varepsilon_+^2 + z_+^2 + \Delta^2)(\varepsilon_-^2 + z_-^2 + \Delta^2)}, \qquad (6.24)
\end{aligned}$$

where $\int ... = \int \frac{d\varepsilon d\omega d^2p d^2q}{(2\pi)^6} ...$ and $D_{\alpha\alpha}(\omega, \mathbf{q}) = \frac{1}{\lambda} + \Pi_{><}^{\alpha\alpha}(\omega, \mathbf{q})$. The integral over ε may be performed exactly by the method of residues, to give

$$\begin{aligned}
\delta F &= 4\Delta^2 \int \frac{d\omega d^2q d^2p}{(2\pi)^5} \left(-\frac{1}{D_{11}(\omega, \mathbf{q})} - \frac{1}{D_{22}(\omega, \mathbf{q})} \right. \\
&\quad \left. + \frac{1}{D_{33}(\omega, \mathbf{q})} \right) \frac{\frac{1}{\xi_+} + \frac{1}{\xi_-}}{\omega^2 + (\xi_+ + \xi_-)^2},
\end{aligned}$$

where $\xi_\pm = \sqrt{z_\pm^2 + \Delta^2}$. The integral over p may now be performed with logarithmic accuracy. The dominant contributions come from $\xi_\pm \approx 0$, and may be evaluated as

$$\begin{aligned}
\delta F &= 8\Delta^2 \nu_0 \int \frac{d\omega d^2q}{(2\pi)^3} \left(-\frac{1}{D_{11}(\omega, \mathbf{q})} - \frac{1}{D_{22}(\omega, \mathbf{q})} \right. \\
&\quad \left. + \frac{1}{D_{33}(\omega, \mathbf{q})} \right) \frac{\ln(r/\Delta)}{r^2}, \qquad (6.25)
\end{aligned}$$

where we have used the pseudo-polar coordinates $r^2 = \omega^2 + (q^2/2m)^2$ and have assumed that $r \gg \Delta$.

We now have to calculate the various functions $D_{\alpha\alpha}$. We will calculate these quantities analytically with logarithmic accuracy. We begin with the definition $D_{\alpha\alpha} = \frac{1}{\lambda} + \Pi_{><}^{\alpha\alpha}$, where the polarization functions are defined in Eqs.(6.19),(6.20). We note that the polarization functions $\Pi_{ij}^{\alpha\alpha}$ are logarithmically divergent at small ω, small

$|\mathbf{q}|^2/2m$ and $\Delta = 0$. The coefficient of the logarithm can be extracted by setting $\omega, \mathbf{q}, \Delta = 0$ in the integral in Eqs.(6.19),(6.20), and introducing an IR cutoff r, where $r^2 = \omega^2 + (|\mathbf{q}|^2/2m)^2$, and we assume $r \gtrsim \Delta$. In this manner, we obtain

$$D_{11} = D_{22} = \frac{1}{\lambda} - \int_r^\Lambda \frac{d\varepsilon d^2p}{(2\pi)^3} \frac{\varepsilon^2 - z^2 e^{2i\theta_\mathbf{p}}}{(\varepsilon^2 + z^2)^2}, , \tag{6.26}$$

$$D_{33} = \frac{1}{\lambda} - \int_r^\Lambda \frac{d\varepsilon d^2p}{(2\pi)^3} \frac{\varepsilon^2 + z^2}{(\varepsilon^2 + z^2)^2}, \tag{6.27}$$

where we have introduced the notation $z = \frac{|\mathbf{p}|^2}{2m}$ and $|\mathbf{p}|e^{i\theta_\mathbf{p}} = p_x + ip_y$. The integrals may be straightforwardly performed by changing to the pseudopolar coordinates $(\rho, \varphi, \theta_p)$, where $\varepsilon = \rho\cos\varphi$, $z = \rho\sin\varphi$, and θ_p was defined above. The integral goes over $0 < \theta_p < 2\pi$, $0 < \varphi < \pi$ and $r < \rho < \Lambda$. Integrating in turn over θ_p, φ and ρ, we find

$$D_{11} = D_{22} = \frac{1}{\lambda} - \frac{\nu_0}{4}\ln\frac{\Lambda}{r}, \quad D_{33} = \frac{1}{\lambda} - \frac{\nu_0}{2}\ln\frac{\Lambda}{r}. \tag{6.28}$$

We now recall the relation $\lambda^{-1} = \frac{1}{2}\nu_0 \ln\Lambda/\Delta$ (the gap equation), and substitute it into Eq.(6.25), to obtain

$$\delta F = 8\Delta^2\nu_0 \int_\Delta^\Lambda \frac{dr}{r}\left(-\frac{4}{\ln\frac{\Lambda}{\Delta} + \ln\frac{r}{\Delta}} + \frac{1}{\ln\frac{r}{\Delta}}\right)\ln\frac{r}{\Delta}. \tag{6.29}$$

This integral can be evaluated using the substitution $x = \ln\frac{r}{\Delta}$, giving

$$\delta F = 8\Delta^2\nu_0 \int_0^{\ln(\Lambda/\Delta)} \frac{\ln(\Lambda/\Delta) - 3x}{\ln(\Lambda/\Delta) + x} dx. \tag{6.30}$$

Evaluating the integral, we obtain a negative value

$$\delta F = 8(-3 + 4\ln 2)\Delta^2\nu_0 \ln\frac{\Lambda}{\Delta} \approx -1.82\Delta^2\nu_0 \ln\frac{\Lambda}{\Delta}, \tag{6.31}$$

which favors the QAH state.

It should be noted that the difference in energies between the (4,0) and (2,2) manifolds is of the same order as the mean field energy, so the mean field plus fluctuations

analysis is ill controlled. However, it provides us with an intuition about the splitting between manifolds of different signatures, and we believe the qualitative details of the fluctuation splitting are reproduced correctly by this analysis.

We note that our fluctuation analysis included only those modes that correspond to weak coupling instability in BLG. We could also have included Stoner modes in our fluctuation analysis. These would produce an additional contribution

$$\delta F_{\text{Stoner}} = 8\Delta^2\nu_0 \int \frac{d\omega d^2q}{(2\pi)^3} \frac{1}{D_{00}(\omega,\mathbf{q})} \frac{\ln(r/\Delta)}{r^2}, \tag{6.32}$$

$$D_{00} = \frac{1}{\lambda} + \Pi^{00}_{><}, \tag{6.33}$$

where $\Pi^{00}_{><}$ is defined by Eq.(6.20) with $\alpha = \beta = 0$, i.e. with $\tau_\alpha = \tau_\beta = 1$. Now, since $\Pi^{00}_{><}$ is not log divergent, we can take $D_{00} = 1/\lambda$ with logarithmic accuracy. We then obtain a contribution $\delta F_{\text{Stoner}} = 4\Delta^2\nu_0 \ln \Lambda/\Delta$, which is sufficiently large to change the sign of the result Eq.(6.31). However, this calculation, which neglects correlation effects, is likely to strongly overestimate the effect of Stoner modes, and therefore we believe that Stoner modes should be left out of the fluctuation analysis.

6.7 Lifting the degeneracy: thermal fluctuations

Thermal fluctuations are dominated by gapless Goldstone modes, which are present only in the states that break SU(4) symmetry. In a state ($M_>$, $M_<$), there are $M_>M_<$ Goldstone modes. Thermal fluctuations due to Goldstone modes allow a state to gain entropy, and since the (2,2) states have the most Goldstone modes, they have the highest entropy. It may thus be expected that the (2,2) states dominate at sufficiently high temperature.

Below we present an analysis showing that this expectation is correct. Since gapless fluctuation modes appear only in the L-mode channel $\delta h \propto \tau_3 \delta Q$, it is sufficient to restrict our attention to the L-modes. The general expression for the fluctuation part of the free energy, taking into account L-modes only, is given by a sum over

Matsubara frequencies,

$$F_{\text{fluct}} = \frac{1}{2} T \sum_{\omega_n, \mathbf{k}} \sum_{i,j} \ln \left(\frac{1}{\lambda} + \Pi^{33}_{ij}(\omega_n, \mathbf{k}) \right), \tag{6.34}$$

where $\omega_n = 2\pi n T$.

We will perform a long wavelength expansion of $\Pi^{33}_{ij}(\omega, \mathbf{k})$. At zeroth order, we note that at ω, $\mathbf{k} = 0$ the values of $\Pi^{33}_{><}$ and $\Pi^{33}_{>>}$ are given by

$$\begin{aligned}
\Pi^{33}_{>>}(\omega, \mathbf{k} = 0) &= \frac{1}{2} \int \frac{d^2 p d\varepsilon}{(2\pi)^3} \text{tr} \ (\tau_3 G_> \tau_3 G_>) \\
&= - \int \frac{\varepsilon^2 + z^2 - \Delta^2}{(\varepsilon^2 + z^2 + \Delta^2)^2} \frac{d^2 p d\varepsilon}{(2\pi)^3}, \\
\Pi^{33}_{><}(\omega, \mathbf{k} = 0) &= \frac{1}{2} \int \frac{d^2 p d\varepsilon}{(2\pi)^3} \text{tr} \ (\tau_3 G_> \tau_3 G_<) \\
&= - \int \frac{\varepsilon^2 + z^2 + \Delta^2}{(\varepsilon^2 + z^2 + \Delta^2)^2} \frac{d^2 p d\varepsilon}{(2\pi)^3},
\end{aligned}$$

where $G_{>(<)} = 1/(i\varepsilon - H_0(\mathbf{p}) \mp \Delta\tau_3)$. To distinguish Goldstone modes from gapped modes, it is convenient to recall the gap equation

$$\frac{1}{\lambda} = \int \frac{1}{\varepsilon^2 + z^2 + \Delta^2} \frac{d^2 p d\varepsilon}{(2\pi)^3}. \tag{6.35}$$

Hence, we have $\frac{1}{\lambda} + \Pi^{33}_{><}(0) = 0$, which corresponds to a Goldstone mode, whereas in the case of $\Pi^{33}_{>>}$ we have

$$\frac{1}{\lambda} + \Pi^{33}_{>>}(0) = \int \frac{2\Delta^2}{(\varepsilon^2 + z^2 + \Delta^2)^2} \frac{d^2 p d\varepsilon}{(2\pi)^3}, \tag{6.36}$$

which is manifestly positive. Thus, Goldstone modes exist only in states $(M_>, M_<)$, where $M_> \neq 0$ and $M_< \neq 0$.

The free energy, Eq.(6.34), evaluated at leading order in a long wavelength expansion around $\omega, \mathbf{k} = 0$, is given by a sum

$$F_{\text{fluct}} = T \sum_{\omega_n, \mathbf{k}} M_> M_< \ln(a\omega_n^2 + b\mathbf{k}^2) \tag{6.37}$$

$$+\frac{1}{2}(M_>^2 + M_<^2)\ln(a'\omega_n^2 + b'\mathbf{k}^2 + c), \tag{6.38}$$

where the first term is the contribution of the gapless modes (originating from $\Pi^{33}_{><}$), while the second term is the contribution of the gapped modes (originating from $\Pi^{33}_{>>}$). The coefficients a, a', b, b' are obtained by Taylor expanding $\Pi^{33}_{ij}(\omega, \mathbf{k})$ in small ω and $\mathbf{k}$, while c is given by Eq.(6.36).

To simplify the sum over Matsubara frequencies, it is convenient to define the quantity $f(u) = T\sum_{\omega_n,\mathbf{k}} \ln(\omega_n^2 + u^2)$. We can evaluate $f(u)$ by first taking the derivative

$$\frac{df}{du} = T\sum_{\omega_n,\mathbf{k}} \frac{1}{i\omega_n + u} + \text{c.c.} = \coth\frac{u}{2T},$$

and then integrating it over u to obtain

$$f(u) = 2T\ln\sinh\frac{u}{2T} = 2T\ln\left(1 - e^{-u/T}\right) + u - (2\ln 2)T.$$

Plugging this identity into the sum (6.37), we see that the contribution of the gapped modes is exponentially small at low temperatures, $T \ll \sqrt{c/a'} \sim \Delta$, while the sum over gapless modes gives a negative contribution of a power law form,

$$F_{\text{fluct}} = \sum_{\mathbf{k}} 2M_>M_<T\ln\left(1 - e^{-v|\mathbf{q}|/T}\right), \tag{6.39}$$

where $v = b/a \sim \sqrt{\Delta/m}$. Evaluating the integral, we obtain an estimate

$$F_{\text{fluct}} \sim -M_>M_<(\nu_0/\Delta)T^3, \tag{6.40}$$

which describes the free energy gain due to thermal fluctuations of Goldstone modes.

We see that the gapless Goldstone modes dominate the finite-temperature fluctuation contribution to the free energy. These modes lower the free energy (by increasing entropy). Since the number of gapless modes $M_>M_<$ is maximal for the (2,2) states, these states are entropically favored by thermal fluctuations.

What is the outcome of competition between the zero-point fluctuations and ther-

mal fluctuations? In Sec.6.6 we found that at zero temperature the (0,4) QAH state is energetically favored by zero point fluctuations of the modes "softened" under RG. At the same time, the zero-point fluctuations of other modes, such as the Stoner modes, may have an opposite effect, favoring the (2,2) state. In the event the zero-point fluctuation energy is dominated by such non-soft modes, the (2,2) state will be realized in the entire temperature interval where the system is unstable to gap formation.

A more interesting situation may arise if the zero-point fluctuation energy is dominated by the RG-softened modes, favoring the QAH state at zero temperature. In this case, given the opposite effect of zero-point and thermal fluctuations, we have to consider the competition between the QAH and (2,2) states. Since the thermal fluctuation energy (6.40) vanishes at $T = 0$, we expect that zero point fluctuations will dominate below a certain temperature T_*, above which thermal fluctuations will dominate. If $T_* < T_c$, where $T_c \approx \Delta(T = 0)$ is the critical temperature for gap opening, then a QAH state will be realized at low temperatures $0 < T < T_*$, whereas a (2,2) gapped state will be realized in the interval $T_* < T < T_c$. In contrast, if $T_* > T_c$, then the QAH state will transition directly to an ungapped state at $T = T_c$ via a second order phase transition, and the (2,2) state will not be realized.

A rough estimate of the temperature T_* can be obtained by comparing the free energies (6.40) and (6.31),

$$\delta F_{\text{fluct},(2,2)} \sim -4\nu_0 \frac{T^3}{\Delta}, \quad \delta F_{\text{fluct},(0,4)} \sim -1.82\nu_0 \Delta^2 \ln \frac{\Lambda}{\Delta}, \tag{6.41}$$

indicating that the scale for T_* is comparable to the temperature T_c at which the gapped state forms. A more detailed analysis of temperature-driven transition between the QAH state and (2,2) state is beyond the scope of this work.

6.8 Experimental signatures of the QAH state

We now discuss experimental tests of the QAH state. The clearest experimental signature would be detection of the quantum Hall effect at zero external magnetic

field. However, detection of this effect requires four probe measurements performed on a sample of BLG that is sufficiently clean and at sufficiently low temperatures as to exhibit spontaneous gap opening [5]. Such measurements have not yet been performed. Moreover, detection of this effect could be complicated by the formation of domains with opposite signs of Δ. Different domains will have opposite σ_{xy}, so the Hall conductance of a macroscopic sample will average to a value near zero. However, if there is percolation of edges, there will be a non-vanishing two-terminal conductance of order e^2/h.

Alternative experimental tests of the QAH state may be performed by examining the electronic compressibility in weak magnetic fields. When the chemical potential sits near the missing Landau level in Fig.(6-1), there should be a gap that extrapolates to a non-zero value as $B \to 0$. This effect will be seen at either $\nu = 4$ or $\nu = -4$ if there is only one domain, and at $\nu = \pm 4$ if there are multiple domains.

The gap at $\nu = 4$ will be strengthened by the mechanism outlined around Eq.(6.8), however, a signal at $\nu = -4$ will be seen only if the QAH state is intrinsic, rather than field induced. An incompressible region at $\nu = -4$ combined with a gapped state at $B = 0$ can thus be taken as a diagnostic for a QAH state at $B = 0$. The filling factors $\nu = \pm 4$ are not equivalent because the QAH state breaks particle-hole symmetry in magnetic field.

Another experimental signature is a phase transition at filling factor $\nu = 0$ and finite B from a QAH state to the Quantum Hall Ferromagnet (QHF) states that are expected to form at large magnetic fields [13]. Such a phase transition would not be seen if the dominant state at small B was of (2,2) type, since the (2,2) states are smoothly connected to the QHF state.

An incompressible region at $\nu = \pm 4$ that occurs at anomalously low magnetic fields, such that the features in compressibility at other integer ν values are washed out, was found in recent experiments that employed a capacitance scanning probe to study suspended BLG samples [9]. In transport measurements [10] performed on the same system, a state with finite two-terminal conductance of order e^2/h was found at zero field, which at a finite B field undergoes a transition to an insulating state.

These measurements are all compatible with the QAH state, however, since there is as yet no four-terminal measurement, it is not possible to say for certain whether a QAH state has been observed.

In summary, our symmetry classification of the various gapped states proposed for BLG singles out the QAH state as the only gapped state not breaking any continuous symmetry. We have investigated the fluctuation-induced splitting of the gapped states, and concluded that at zero temperature and zero field, the leading instability is to the QAH state. We have discussed the phenomenology and experimental signatures of this state, and have shown that it can be stabilized by weak external magnetic field.

Bibliography

[1] F.D.M. Haldane, Phys. Rev. Lett. 61, 2015 (1988).

[2] S. Raghu, X.L. Qi, C. Honerkamp, S.C. Zhang, Phys. Rev. Lett. 100, 156401 (2008).

[3] K. Sun, H. Yao, E. Fradkin and S. Kivelson, Phys. Rev. Lett. 103, 046811 (2009).

[4] H. Min, G. Borghi, M. Polini and A.H. MacDonald, Phys. Rev. B 77, 041407(R) (2008).

[5] R. Nandkishore and L. Levitov. Phys. Rev. Lett. 104, 156803 (2010).

[6] F. Zhang, H. Min, M. Polini, and A. H. MacDonald Phys. Rev. B 81, 041402(R) (2010).

[7] O. Vafek and K. Yang, Phys. Rev. B 81, 041401(R) (2010).

[8] B. Feldman, J. Martin and A. Yacoby, Nature Physics 5, 889 (2009).

[9] J. Martin, B.E.Feldman, R.T.Weitz, M.T.Allen and A.Yacoby, Phys. Rev. Lett. 105, 256806 (2010)

[10] R.T.Weitz, M.T.Allen, B.E.Feldman, J. Martin and A. Yacoby, Science Vol. 330 no. 6005 pp. 812-816 (2010)

[11] K.S. Novoselov et al, Nature Physics 2, 177 (2006).

[12] I. Martin and C. D. Batista, Phys. Rev. Lett. 101, 156402 (2008).

[13] Y. Barlas, R. Cote, K. Nomura and A. H. MacDonald, Phys Rev Lett. 101 (2008).

[14] J. Nilsson, A.H.Castro Neto, N. Peres and F. Guinea, Phys. Rev. B 73, 214418 (2006).

[15] R. Jackiw, Phys. Rev. D 27, 2375 (1984).

[16] C. L. Kane and E. J. Mele, Phys. Rev. Lett. 95, 226801 (2005).

[17] I. Martin, Y. Blanter and A. Morpurgo, Phys. Rev. Lett. 100, 036804 (2008).

[18] K. Yang, S. Das Sarma, A. H. MacDonald, Phys. Rev. B 74, 075423 (2006).

[19] E. McCann and V. Fal'ko, Phys. Rev. Lett. 96, 086805 (2006).

[20] E. H. Hwang and S. Das Sarma, Phys. Rev. Lett. **101**, 156802 (2008).

[21] J. Jung, F. Zhang and A.H.MacDonald, Phys. Rev. B 83, 115408 (2011)

[22] R. Nandkishore and L. Levitov, Phys. Rev. B 82, 115124 (2010)

[24] Y. Lemonik, I.L.Aleiner, C.Toke and V.I.Fal'ko, Phys. Rev. B 82, 201408(R) (2010)

[25] O. Vafek, Phys. Rev. B 82, 205106 (2010)

Chapter 7

Electron interactions in bilayer graphene: phase diagram from ε expansion

We analyze the competition between various broken symmetry states in bilayer graphene (BLG) within a renormalization group formalism. This allows us to determine the leading instability, assuming that interactions are sufficiently weak. We take into account long range dynamically screened Coulomb interactions as well as short range lattice scale interactions. We restrict ourselves to a maximally symmetric set of interactions, in particular one that respects $SU(4)$ spin-valley symmetry. The leading divergences arising from the dynamically screened long range interaction are $\ln^2$ divergences, but these higher divergences cancel, leaving a residual flow of the interactions that is only logarithmic with RG scale. We extract the subleading logarithmic renormalizations by means of an ε expansion, and analyse the RG flow. There are two possible fixed points, which correspond to a gapped quantum anomalous Hall state and a gapless nematic state respectively. We determine the separatrix in parameter space which separates regions that flow to a QAH state from the regions that flow to a gapless nematic state. We conclude that for realistic parameter values, and without taking into account phonon mediated interactions, the system is likely to be in the basin of attraction of the nematic state.

The unusual electronic properties of bilayer graphene (BLG) have excited considerable experimental and theoretical interest. As a two dimensional gapless semiconductor with quadratic dispersion, BLG is a rich playground for realization of strongly correlated states. Theoretical work has proposed numerous gapped [2, 1, 3, 4, 5] and gapless [6, 9, 8] broken symmetry states. Intriguingly, these states are expected to arise even for weak interactions, owing to the presence of log divergences in perturbation theory. We presented a classification of the various possible states in [7], where we also surveyed methods of distinguishing between the various states experimentally.

Meanwhile, numerous experiments have confirmed that the ground state of suspended, double gated BLG is very different to what one would expect in the absence of interactions. The early experiments [11, 13, 12] appeared to be compatible with only two of the proposed strongly correlated states: either the gapped QAH state, which breaks time reversal symmetry, or the gapless nematic state, which breaks lattice rotation symmetry. However, the picture has grown more confusing as more experimental data has emerged. The experiments [15, 14] appear to argue definitively for a gapped state, whereas the experiments [16] appear to argue equally strongly for a gapless nematic state. We therefore turn our attention to the theoretical question of just how delicate is the balance between gapped and gapless states?

In this work, we address the nature of the weak coupling instability in BLG within the (unbiased) formalism of the perturbative renormalisation group (RG). In a previous work [10], we calculated the RG flow of BLG in the presence of dynamically screened long range interactions, and found that although long range interactions produced a $\log^2$ divergence in individual Feynman diagrams, the divergences all cancelled at leading order, so that BLG behaved as a marginal Fermi liquid with $\log^2$ accuracy. At next to leading order, however, there could still be (logarithmic) instabilities to strongly correlated states.

Meanwhile, in a recent work [8], Vafek examined the (logarithmic) RG flow of BLG in the presence of all possible symmetry allowed short range interactions for spinless and spinful fermions on the BLG lattice, neglecting long range interactions. For spinful fermions, it was found that the weak coupling RG led to either a nematic

state [6], which breaks rotational symmetry, or to a QAH state [4], that breaks time reversal symmetry, depending on the value of the microscopic couplings. For specific values of the initial couplings, the weak coupling RG can also flow to a non-interacting fixed point.

In this work, we combine the analysis of Ref.[8] for short range interactions with our earlier methodology for treating long range interactions [10] to obtain a complete description of the low energy physics of BLG. We find that the fixed point structure including long range interactions is the same as the fixed point structure in the presence of only short range interactions, except that the non-interacting fixed point disappears. It thus follows that when long range interactions are taken into account, then BLG must display an instability to a strongly correlated state at low energies. The strong correlation states accessible through weak coupling RG are the gapped QAH and gapless nematic states, which can both be realized, depending on the values of the microscopic interactions.

We calculate the surface in phase space which separates the basins of attraction of the gapped and gapless states. We find that the phase structure is controlled by whether, in the microscopic Hamiltonian, inter-sublattice repulsion is stronger or weaker than intra-sublattice repulsion (i.e. do two electrons on different sublattices repel more strongly or weakly than two electrons on the same sublattice?). If inter-sublattice repulsion dominates, then a gapped state results, whereas if intra-sublattice repulsion dominates, then a gapless state arises. It is not known to us which scenario is realized in practice. However, it seems plausible that inter-sublattice and intra-sublattce repulsions are of roughly equal strength, so that BLG is close to criticality. In this case, it is possible that different methods of sample preparation or suspension might slightly favor inter or intra sublattice repulsion,which might tip the balance towards either a gapped or a gapless state. This may explain the seemingly contradictory results obtained in different experiments.

7.1 Setting up the RG

We begin by writing the non-interacting Hamiltonian for BLG. We recall that electronic states in BLG at low energy are described by wave-functions on the A and B sublattices of the upper and lower layers [18], and are fourfold degenerate in spin and valley. To analyze the structure of the Hamiltonian, it will be convenient to combine the spin and valley components in a single eight-component wavefunction $\psi_{\alpha,s,v}(\mathbf{x})$, where α is the sublattice (layer) index. We shall use the Pauli matrices in sublattice, spin and valley space, denoted below by τ_i, σ_i and η_i, respectively. The low energy non-interacting Hamiltonian may then be written as

$$H_0 = \frac{(p_x + ip_y\eta_3)^2}{2m}\tau_- + \frac{(p_x - ip_y\eta_3)^2}{2m}\tau_+, \tag{7.1}$$

where $\tau_\pm = \tau_1 \pm i\tau_2$. Here $m = 0.05m_e$ is the effective mass. To bring it to an SU(4) invariant form, we perform a unitary transformation on all operators

$$\tilde{O} = UOU^\dagger, \quad U = \frac{1+\eta_3}{2} + \frac{1-\eta_3}{2}\tau_1. \tag{7.2}$$

This transformation mixes the layer and valley indices of the wavefunction $\psi_{\alpha,s,v}(\mathbf{x})$ by interchanging layers in one of the valleys. Defining $p_\pm = p_x \pm ip_y$, the transformed non-interacting Hamiltonian takes the compact form

$$H_0 = \frac{p_+^2}{2m}\tilde{\tau}_- + \frac{p_-^2}{2m}\tilde{\tau}_+. \tag{7.3}$$

Here $\tilde{\tau}_+$ and $\tilde{\tau}_-$ are obtained by transforming $\tau_\pm = \tau_1 \pm i\tau_2$ according to Eq.(7.2). This single particle Hamiltonian is manifestly invariant under $SU(4)$ rotations in the transformed spin/valley flavor space, generated by $\tilde{\eta}_\mu \otimes \tilde{\sigma}_\mu$, where $\mu = 0, 1, 2, 3$, $\tilde{\eta}_0 = 1 = \tilde{\sigma}_0$, and $\tilde{\eta}_{1,2,3}$ and $\tilde{\sigma}_{1,2,3}$ are the Pauli matrices in the transformed valley and spin space respectively.

To calculate the RG flow of the Hamiltonian, Eq.(7.1), in the weak coupling regime, we begin by writing the zero-temperature partition function Φ as an imaginary-

time functional field integral. We have

$$\Phi = \int D\psi^\dagger D\psi \exp\left(-S_0[\psi^\dagger,\psi] - S_1[\psi^\dagger,\psi]\right), \tag{7.4}$$

$$S_0 = \sum_\sigma \int \frac{d\omega d^2p}{(2\pi)^3} \psi^\dagger_{\sigma,\omega,\mathbf{p}} \left(\frac{-i\omega + H_0^\sigma(\mathbf{p})}{Z}\right) \psi_{\sigma,\omega,\mathbf{p}}, \tag{7.5}$$

$$S_1 = \frac{1}{2}\int \frac{d\omega d^2p}{(2\pi)^3} \Gamma^2 U(\omega,\mathbf{q}) n_{\omega,\mathbf{q}} n_{-\omega,-\mathbf{q}} + S_2. \tag{7.6}$$

Here the ψ fields are Grassman valued (fermionic) fields with flavour (spin-valley) index σ, while ω is a fermionic Matsubara frequency, Γ is a vertex renormalisation parameter, Z is the quasiparticle residue, and $n_{\omega,\mathbf{q}}$ is the Fourier transform of the electron density, summed over spins, valleys and sublattices. The effective interaction $U(\omega,\mathbf{q})$ is the dynamically screened long range Coulomb interaction, given by Eq.(7.7).

The term S_2 represents the short range (lattice scale) interactions in BLG. In principle, S_2 should contain all possible interactions that are allowed by the symmetries of the lattice. There are 18 such interactions. [8]. We simplify by imposing on S_2 not only the symmetries of the lattice, but also the symmetries of the low energy non-interacting Hamiltonian, which strongly constrains the possible terms S_2. The relevant symmetries are particle-hole symmetry, time reversal symmetry, SU(4) flavor symmetry, and the symmetry of the Hamiltonian under the transformation $e^{i\theta\tilde{\tau}_3}R(\theta)$, where $R(\theta)$ generates spatial rotations, $R(\theta)p_\pm = e^{\pm i\theta}p_\pm$.

The dynamically screened interaction may be calculated by summing over the RPA series of bubble diagrams, to obtain a screened interaction. The screened interaction in Fourier space takes the form

$$U(\omega,\mathbf{q}) = \frac{2\pi e^2}{\kappa q - 2\pi e^2 \Pi(\omega,q)} \tag{7.7}$$

Here $\Pi_{\omega,q}$ is the non-interacting polarisation function. The non-interacting polarisation function $\Pi_{\omega,q}$ was calculated analytically in [2]. It was shown that Π depends on

a single parameter $\chi = 2m\omega/q^2$, and is well described by the approximate form

$$\Pi_\chi = -\frac{Nm}{2\pi}\frac{\ln 4}{\sqrt{1+u\chi^2}} \tag{7.8}$$

where $u = (2\ln 4/\pi)^2$ and $N = 4$ is the number of fermion species. This approximate form reproduces Π_χ exactly in the limits $\chi \to 0$ and $\chi \to \infty$, and interpolates accurately between limits. Note that $\Pi_{q,\omega}$ vanishes when $q \to 0$, and so the dressed propagator Eq.7.7 retains some long range character. This will lead to unusually strong ($\ln^2$) divergences in Feynman diagrams. Nevertheless, the screened interaction Eq.7.7 is only marginal at tree level (in the RG sense) and therefore, it becomes possible to perform RG by working perturbatively in weak interactions.

The theory is defined with the initial UV cutoff Λ_0. Since the two band model, Eq.7.1, is only justified on energy scales less than the gap $W \approx 0.4eV$ to the higher bands in BLG, we conservatively identify $\Lambda_0 = W$. Our main results will be independent of Λ_0.

We will employ an RG scheme which treats frequency ω on the same footing as $p^2/2m$, in order to preserve the form of the free action Eq.(7.5) under RG. Thus, we integrate out the shell of highest energy fermion modes

$$\Lambda' < \sqrt{\omega^2 + (\mathbf{p}^2/2m)^2} < \Lambda. \tag{7.9}$$

and subsequently rescale $\omega \to \omega(\Lambda/\Lambda')$, $p \to p(\Lambda/\Lambda')^{1/z}$, where z is the dynamical critical exponent [17], which takes value $z = 2$ at tree level. Because the value $z = 2$ is not protected by any symmetry, it may acquire renormalization corrections. However, at one-loop level in the RG, we do not find any corrections to z. We therefore use $z = 2$ for the rest of the paper, which corresponds to scaling dimensions $[\omega] = 1$ and $[p^2] = 1$. Under such an RG transformation, the Lagrangian density in momentum space has scaling dimension $[\mathcal{L}] = 2$, and we have tree level scaling dimensions $[\psi] = 1/2$ and $[\Gamma] = [Z] = 0$ respectively.

Given these tree level scaling dimension values, it can be seen that all potentially

relevant terms arising as part of S_2 must involve four fermion fields. Indeed, any term involving more than four ψ fields will be irrelevant at tree level under RG, and may be neglected. The terms with odd numbers of ψ fields are forbidden by charge conservation, while the quadratic terms $\Delta_{ij}\psi_i^\dagger\psi_j$ cannot be generated under perturbative RG, since they break the symmetries of the Hamiltonian listed above[1].

Thus, the only potentially relevant terms that could arise under perturbative RG take the form of a four point interaction which may be written as

$$S_2 = \frac{1}{2}\int d^3x d^3x' \Upsilon^{\sigma\sigma'}_{ijkl}\psi^\dagger_{\sigma,i}(x)\psi_{\sigma,j}(x)\psi^\dagger_{\sigma',k}(x')\psi_{\sigma',l}(x'). \tag{7.10}$$

where $x = (\mathbf{r}, t)$, $x' = (\mathbf{r}', t')$, Here Υ is an effective four particle vertex, which is marginal at tree level, the indices σ, σ' refer to the flavour (spin-valley) of the interacting particles, and i, j, k, l are sublattice indices.

The symmetries of the Hamiltonian, Eq.(7.1), place strong constraints on the spin-valley-sublattice structure of the four point vertex Υ. Since the Coulomb interaction does not change fermion flavour (spin or valley), and the electron Green function is diagonal in flavour space, the vertex Υ cannot change fermion flavour. Moreover, the $SU(4)$ flavour symmetry of the Hamiltonian implies that Υ does not depend on the flavour index of the interacting particles, and we may therefore drop the indices σ, σ' in Eq.(7.10). Finally, the bare Hamiltonian (7.1) is invariant under combined pseudospin/spatial rotations through $e^{i\theta\tau_3}R(\theta)$. This symmetry further restricts the form of four point vertices in Eq.(7.10) to have sublattice structure Υ_{iijj} or Υ_{ijji} only [2]. That is, the allowed scattering processes are restricted to $(AA) \to (AA)$, $(AB) \to (AB)$ and $(AB) \to (BA)$. We note that the processes $(AB) \to (AB)$ and $(AB) \to (BA)$ are distinct, since the particles have flavour.

In this manner, we find that when we impose on the action all the symmetries of the non-interacting Hamiltonian (which are also respected by the Coulomb interaction), then there are only three symmetry allowed short range interactions, and we can write

[2]In that, we ignore vertices of the form $\Upsilon_{AAAB}\partial_+^2$, $\Upsilon_{AABA}\partial_-^2$, and other similar terms, which are allowed by symmetries, but are irrelevant in the RG sense.

$$S_2 = g_1(\psi^\dagger\psi)^2 + g_2(\psi^\dagger\tilde{\tau}_+\psi)(\psi^\dagger\tilde{\tau}_-\psi) + g_3(\psi^\dagger\tilde{\tau}_3\psi)^2 \tag{7.11}$$

These are the same three short range interactions that were considered in Ref.[6] if we make the identifications $g_1(\text{us}) = g_1(\text{Vafek} + \text{Yang})$, $g_2(\text{us}) = 2g_3(\text{Vafek} + \text{Yang})$ and $g_3(\text{us}) = g_2(\text{Vafek} + \text{Yang})$.

Under RG starting with the above three interactions, no other short range interactions are generated, thus it is sufficient to consider the above simplified set of interactions to calculate the RG flow. This maximally symmetric action will be sufficient to capture the competition between gapped and gapless phases.

7.1.1 Obtaining the beta functions

We obtain the RG flow for bilayer graphene, working in the manner of Ref.[[17]]. We consider the partition function, Eq.(7.4), where the interaction is given by Eq.(7.7). Starting from this action, supplied with ultraviolet (UV) cutoff Λ_0, we systematically integrate out the shell of highest energy fermion modes, Eq.(7.9). We perform the integrals perturbatively in the interactions, Eq.(7.7). This corresponds to a perturbation theory in small $\Gamma^2 Z^2/N$ and small g_1, g_2, g_3. We carry our calculations to one loop order, and examine the renormalisation of the various interactions Υ (Sec.4.6). At one loop order, all diagrams involve two interaction lines. However, they may involve two short range interactions, two long range interactions, or one short range interaction line and one long range interaction line.

The diagrams involving only short range interactions are log divergent in the infrared, and can be handled in the usual manner [17], where one performs RG up until some final infrared cutoff scale. The contributions to the beta functions from these diagrams were calculated in [6]. We agree with the beta functions presented in [6] for short range interactions only. However, we wish to supplement the calculations in [6] with the effects of long range interactions. Long range interactions contribute additional terms to the beta functions for the short range interactions, through the processes represented by the diagrams in Fig.7-1.

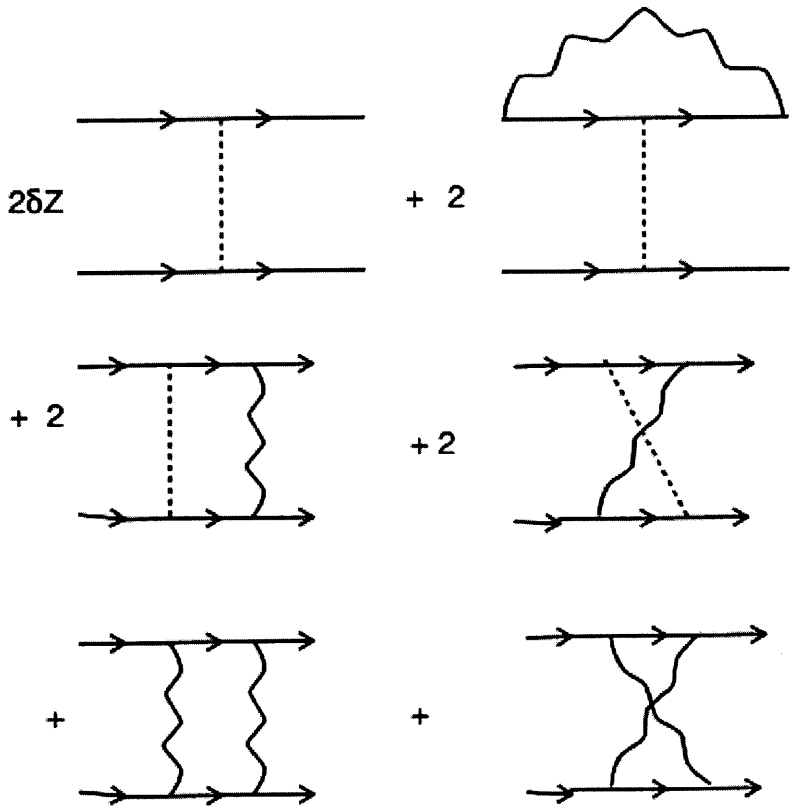

Figure 7-1: The long range interaction contributes to the beta functions of the short range interactions through the diagrams shown above. The wavy line represents the dynamically screened long range Coulomb interaction, the dashed lines represent short range interactions, and the solid lines with arrows represent fermion propagators.

We will now show how to calculate the contributions to the beta functions for the short range interactions arising from the diagrams in Fig.7-1. The calculation requires care, since the diagrams in Fig.7-1 all exhibit divergences that are more severe than logarithmic [10], and cannot be straightforwardly handled within the framework of the RG. However, when the diagrams are added together in pairs by row (in Fig.7-1), the leading order divergences all cancel out, such that the subleading un-cancelled pieces, which are log divergent, provide the desired contributions to the beta functions.

We begin by considering the final two diagrams, which involve two long range interaction lines. These diagrams involve particular care, as the usual RG procedure of setting all external momenta to zero cannot be performed. This is because when all external momenta are set to zero, the integrals exhibit power law singularities which arise inside the shell of energies and momenta that is being integrated out [10]. The problem arises because of the long range nature of the long range interaction, which forces us to perform the calculations keeping the external momenta finite. However, it was shown in [10] that when the two diagrams involving two long range interactions are added together, and are evaluated in the $(AA) \rightarrow (AA)$ or $(AB) \rightarrow (AB)$ channels, they cancel out at leading order, leaving an uncancelled piece which is constant (not even log divergent). Therefore, the diagrams with two long range interactions, when put together, make no contribution to the beta functions for the g_1 and g_3 interactions. In contrast, when the diagrams above are evaluated in the $(AB) \rightarrow (BA)$ channel (g_2 channel), they are individually only log divergent, and can be handled by standard techniques.

Next, we consider the diagrams in Fig.7-1 involving one short range interaction line and one long range interaction line. Again, the diagrams are individually log square divergent. However, it was shown in [10] that when the diagrams are grouped together by row as shown above, the leading order divergences cancel, such that the leading uncancelled divergence is only logarithmic, and may be handled by standard means. We illustrate the calculation by calculating the contribution to the beta function for the g_3 interaction arising from the first two diagrams in Fig.7-1 i.e. from the Green function renormalisation and the vertex correction respectively.

It is convenient to regularise the above diagrams by working in $2+\varepsilon$ dimensions, where ε is an infinitesimal positive number. Once the RG equations are obtained, we will take $\varepsilon \to 0$. In $2+\varepsilon$ dimensions, diagrams in the first row of Fig.7-1 are infrared convergent even when external momenta are taken to zero, hence we can safely set all external momenta to zero, greatly simplifying the calculations. The residue renormalisation, from [10], is given by

$$\delta Z = \int \frac{d\omega d^{2+\varepsilon}p}{(2\pi)^3} \frac{z^2-\omega^2}{(\omega^2+z^2)^2} V(\omega,p) \tag{7.12}$$

where $z = p^2/2m$ and $V(\omega,p)$ is the dynamically screened long range interaction Eq.7.7. This expression is log square divergent in the infrared at $\varepsilon = 0$, as shown in [10], but is convergent at finite ε.

Similarly, the vertex correction is given by

$$\delta g_3 = \int \frac{d\omega d^{2+\varepsilon}p}{(2\pi)^3} \frac{z^2+\omega^2}{(\omega^2+z^2)^2} V(\omega,p) \tag{7.13}$$

Since the expressions for the vertex correction and residue renormalisation are all convergent at finite ε, the integrands may be added together before doing the integral. In this manner, we find that the combination of the vertex correction and the residue renormalisation make a contribution to the beta function

$$\delta\beta(g_3) = 2\int \frac{d\omega d^{2+\varepsilon}p}{(2\pi)^3} \frac{2z^2}{(\omega^2+z^2)^2} V(\omega,p) \tag{7.14}$$

This residual expression is only log divergent in the infrared when $\varepsilon \to 0$, and may be calculated in standard ways, by changing to the co-ordinates $r^2 = \omega^2 + z^2$ and $\varphi = \arctan \omega/z$, and integrating in turn over $-\pi/2 < \psi < \pi/2$ and $\Lambda - d\Lambda < r < \Lambda$.

All the other diagrams involving only one interaction line may be calculated in the same way,. First, we change to $2+\varepsilon$ spatial dimensions (thus rendering the integrals convergent). Then, we add the integrands together pairwise (add the two diagrams in the top row of Fig.7-1 together, add the two diagrams in the second row together). This generates something that is only log divergent in the infrared when we take

$\varepsilon \to 0$. Thus, take $\varepsilon \to 0$ at this stage, and calculate the β function by standard means. In this way, we obtain the full beta functions for the short range interactions, taking into account the effect of long range interactions.

We define $\nu_0 = m/2\pi$, the single species density of states. We introduce $g_0 = 1/(N\nu_0 \ln 4)$, corresponding to the long range interaction (where $N = 4$ for spinful BLG). Hence, we obtain the RG equations

$$\begin{aligned}
\frac{dg_0}{dl} &= -\varepsilon g_0 \\
\frac{dg_1}{dl} &= -\varepsilon g_1 - g_2(g_1 + \frac{4g_0}{\pi})\nu_0 \\
\frac{dg_2}{dl} &= -\varepsilon g_2 + \frac{1}{2}\left(-2g_1^2 - (N+2)g_2^2 - 2g_3^2 + 2g_1g_2 + 2g_2g_3 + (2g_2 - 4g_1)\frac{4g_0}{\pi} - 4g_0^2\right)\nu_0 \\
\frac{dg_3}{dl} &= -\varepsilon g_3 + \frac{1}{2}\left(g_2^2 + 4g_1g_3 - 6g_2g_3 - 4(N-1)g_3^2 + \frac{16g_3g_0}{\pi}\right)\nu_0
\end{aligned} \tag{7.15}$$

These equations reduce to the β functions from Ref.[6] if we take the limit $\varepsilon \to 0$ and $g_0 \to 0$, and make the identifications $g_1 \to g_1$, $g_2 \to 2g_3$ and $g_3 \to g_2$. However, the mass (and hence the density of states) itself flows under RG, as a result of the renormalisation of the spectrum by the long range interactions. The flow of the density of states is given by [10]

$$\frac{d\nu_0}{dl} = 0.56 g_0 \nu_0^2(l) \tag{7.16}$$

If we set $\varepsilon = 0$, and define the dimensionless couplings $\tilde{g}_i = g\nu_0$, and straightaway drop the tildes, we obtain the modified RG equations

$$\begin{aligned}
\frac{dg_0}{dl} &= +0.56 g_0^2 \\
\frac{dg_1}{dl} &= -g_2(g_1 + \frac{4g_0}{\pi}) + 0.56 g_0 g_1 \\
\frac{dg_2}{dl} &= +\frac{1}{2}\left(-2g_1^2 - (N+2)g_2^2 - 2g_3^2 + 2g_1g_2 + 2g_2g_3 + (2g_2 - 4g_1)\frac{4g_0}{\pi} - 4g_0^2\right) + 0.56 g_0 g_2
\end{aligned} \tag{7.17}$$

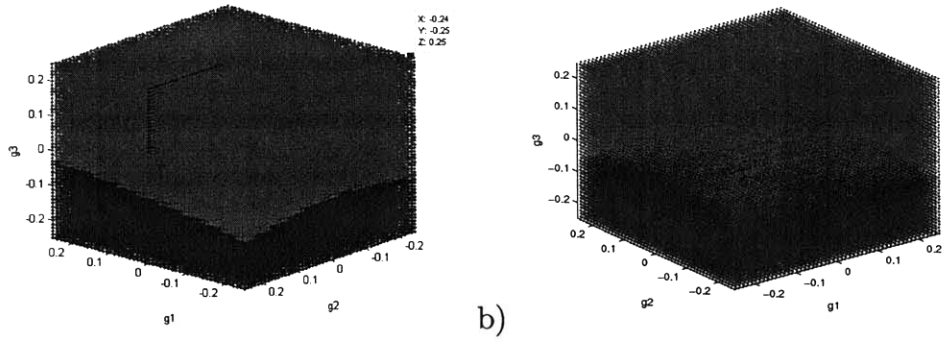

a) b)

Figure 7-2: Phase diagram of BLG, evaluated a) with $g_0 = 0$ and b) with $g_0 = 1/(4\ln 4)$. Blue region flows to QAH fixed point, red region flows to nematic fixed point

.

$$\frac{dg_3}{dl} = +\frac{1}{2}\left(g_2^2 + 4g_1g_3 - 6g_2g_3 - 4(N-1)g_3^2 + \frac{16g_3g_0}{\pi}\right) + 0.56g_0g_3 \tag{7.18}$$

The phase diagram may be obtained from this system of equations. Note that there are no stable fixed points at finite coupling, so the system must necessarily flow to strong coupling. When the couplings g_1, g_2, g_3 become strong, the screened long range interaction g_0 can be neglected, and the system of equations become homogenous. This homogenous system of equations was solved in [8], and was found to consist of only two stable fixed points - one corresponding to nematic order, and another to QAH order. Since the system of equations above asymtotes to that studied in [8] for long RG times, the fixed point structure must be the same. However, the position of the separatrix will be modified by the presence of g_0. The effect of g_0 on the separatrix will be particularly strong when the couplings g_1, g_2, g_3 are weak, which is likely the case for BLG.

We calculate the phase diagram in the 3 dimensional g_1, g_2, g_3 space numerically. We consider a grid of starting points. For each point, we integrate the RG equations, as we track whether it diverges along the nematic trajectory, or along the QAH trajectory. We perform this numerical evaluation for both $g_0 = 0$ (corresponding to the case of purely short range interactions studied in [8]) and for $g_0 = 1/4\ln 4$, corresponding to short range interactions plus RPA screened long range interactions. The resulting phase diagrams are plotted in Fig.7-2.

7.2 Discussion

We note from Fig.7-2 that the key determinant of whether we flow to the nematic or QAH phase is whether the initial value of g_3 is positive or negative. If we start with a sufficiently negative g_3, then we end up in the QAH phase, whereas otherwise we end up in the nematic phase. This general picture holds true also in the presence of long range interactions, although the long range interactions do shift the separatrix slightly.

What does it mean for g_3 to be positive or negative? We take it for granted that electrons repel. A positive g_3 means that the repulsion between two particles on the same sublattice is stronger than the repulsion between particles on different sublattices (i.e. dominant intra-sublattice repulsion). In contrast, a negative g_3 means that the repulsion between two particles on the same sublattice is weaker than the repulsion between particles on different sublattices (i.e. dominant inter-sublattice repulsion). Whether we end up in a gapped QAH phase or a gapless nematic phase is therefore controlled by whether intra sublattice repulsion is stronger, or inter sublattice repulsion.

We expect that the inter and intra sublattice repulsions are likely to be roughly similar in strength. However, the 'interlayer capacitance' effect (V_- in Chapter 1) should make the intra sublattice repulsion stronger than the inter sublattice repulsion. In this case, a nematic state would represent the leading instability for BLG. However, it remains possible that phonon mediated interactions could drive g_3 negative, in which case a QAH state could result.

We note also that the only gapped state arising within our analysis is the QAH gapped state. Other gapped states, exhibiting quantum spin hall effect, or Neel order, are also conceivable, but do not arise under RG starting with a maximally symmetric interaction. However, if we relax the symmetry constraints on the action, and allow all nine independent couplings allowed by the lattice symmetry, then additional fixed points may well become available, and other gapped states may result. The analysis of the 9+1 dimensional RG flow is beyond the scope of the present work.

Bibliography

[1] H. Min, G. Borghi, M. Polini and A.H. MacDonald, Phys. Rev. B 77, 041407(R) (2008).

[2] R. Nandkishore and L. Levitov. Phys. Rev. Lett. 104, 156803 (2010).

[3] F. Zhang, H. Min, M. Polini, and A. H. MacDonald Phys. Rev. B 81, 041402(R) (2010).

[4] R. Nandkishore and L. Levitov, Phys. Rev. B 82, 115124 (2010)

[5] J. Jung, F.Zhang and A.H.MacDonald, Phys. Rev. B 83, 115408 (2011)

[6] O. Vafek and K. Yang, Phys. Rev. B 81, 041401(R) (2010).

[7] R. Nandkishore and L. Levitov, Phys. Scr. T146, 014011 (2012)

[8] O. Vafek, Phys. Rev. B 84, 245417 (2011)

[9] Y. Lemonik, I.L Aleiner, C. Toke and V. I Falko, Phys. Rev. B 82, 201408 (2010)

[10] R. Nandkishore and L. Levitov, Phys. Rev. B 82, 115431 (2010)

[11] B. Feldman, J. Martin and A. Yacoby, Nature Physics 5, 889 (2009).

[12] J. Martin, B.E.Feldman, R.T.Weitz, M.T.Allen and A.Yacoby, Phys. Rev. Lett. 105, 256806 (2010)

[13] R.T.Weitz, M.T.Allen, B.E.Feldman, J. Martin and A. Yacoby, Science Vol. 330 no. 6005 pp. 812-816 (2010)

[14] J. Velasco et al, Nature Nanotechnology, 7, 156 (2012)

[15] F.Freitag et al, Phys. Rev. Lett. 108, 076602 (2012)

[16] A.S. Mayorov et al, Science 333(6044) pp. 860-863 (2011)

[17] R. Shankar, Rev. Mod. Phys. 66, 129-192 (1994)

[18] A. K. Geim and K. S. Novoselov, Nature Mater. **6**, 183 (2007).

Chapter 8

Spontaneously ordered states in bilayer graphene: experimental signatures, experiments, and the way forward

A very large number of different broken symmetry states compete to be the ground state of bilayer graphene. This chapter is devoted to classifying the various competing states, identifying their experimental signatures, reviewing the experimental evidence, and proposing a way forward for the field.

We begin by discussing the various interaction driven states that can arise in bilayer graphene near charge neutrality. Possible states are classified in terms of discrete and continuous symmetries. Differences in symmetry lead to differences in physical properties, which can be diagnostic of the state seen in experiments.

The unique sensitivity of optical response to different types of symmetry breaking can be used to detect and identify spontaneously ordered many-body states in bilayer graphene. We predict a strong response at optical frequencies, sensitive to electronic phenomena at low energies, which arises because of nonzero inter-band matrix elements of the electric current operator. In particular, the polar Kerr rotation and

reflection anisotropy provide fingerprints of the quantum anomalous Hall state and the nematic state, characterized by spontaneously broken time reversal symmetry and lattice rotation symmetry, respectively. These optical signatures, which undergo a resonant enhancement in the near-infrared regime, lie well within reach of existing experimental techniques.

We conclude by discussing existing experiments on BLG, and what ground state they appear to observe. As we will see, experiments are inconclusive (and not entirely consistent), and an unambiguous identification of the gapped state is not yet possible. We discuss the remaining challenges for both theory and experiment that must be addressed to advance the field.

Work reported in this chapter was published in [5, 66], and also in the review paper [47].

8.1 Broken symmetry states: a summary

We now list all the possible broken symmetry states that may arise, including gapless as well as gapped states, and review their properties. The simplest possibility is that interactions may cause a gap to open up between the conduction and valence bands. These states are referred to in the literature as 'pseudospin ferromagnets' [2, 6, 4], or as 'excitonic states' [3, 5], however, irrespective of the choice of nomenclature, the states being referred to are the same. The effective low energy Hamiltonian for these states may be written as

$$H = H_0 + \Delta \tau_3 Q, \tag{8.1}$$

where H_0 is the non-interacting Hamiltonian, and Q is a 4×4 unitary and hermitian matrix in spin-valley space. The gap Δ is real, and arises from interactions.

The gapped states where Δ takes the sign $+1$ in the K valley and -1 in the K' valley have nonzero Hall conductivity, and are commonly referred to as 'quantum anomalous Hall' (QAH) states. In fact, there is a more general set of states that display QAH effect, since any gapped state with $\mathrm{Tr}(Q\eta_3) \neq 0$ exhibits a non vanishing DC Hall conductivity. For example, the state where Δ takes sign $+1$ for three of the four spin/valley species, and takes sign -1 in the fourth species, also has $\sigma_{xy} \neq 0$, and should thus also be considered a QAH state.

Non-QAH gapped states have $\mathrm{Tr}(Q\eta_3) \neq 0$, and must necessarily break the approximate SU(4) spin-valley symmetry. The may (or may not) break time reversal symmetry and parity. The simplest possibility $Q = 1$ corresponds to a 'ferroelectric' or charge density wave state, which imbalances the two layers by charge [3]. Meanwhile, the possibility $Q = \sigma_i \eta_3$ corresponds to a Quantum Spin Hall (QSH) state, while $Q = \sigma_i$ corresponds to an 'antiferromagnet' state. The ferroelectric and QSH states break mirror reflection symmetry, and the ferroelectric state also breaks parity symmetry, but they both preserve time reversal symmetry, which the antiferromagnet state breaks.

The non-QAH gapped states all have edge states, but not all edge states are equal. The edge states of the QSH state are protected in the absence of spin flip

scattering, and should thus be robust, whereas the edge states of the other non-QAH gapped states are unprotected, and in realistic samples with disorder will most likely be gapped out, to yield a fully gapped state.

While spontaneous gap formation is one possibility in BLG, a second possibility is that interactions may cause the quadratic band crossing to split into two Dirac points. This corresponds to the nematic states of [9, 8, 7]. The Hamiltonian for the nematic state for one species (e.g. valley K and spin up) takes the form

$$H(\mathbf{p}, \Delta) = \left(\frac{p_+^2}{2m} + \Delta\right)\tau_+ + \left(\frac{p_-^2}{2m} + \Delta^*\right)\tau_- \tag{8.2}$$

where the nematic order parameter Δ can be complex.

What possible spin and valley structures can arise in the nematic state? The existing literature [7, 8, 9] on nematic states has focused only on the case when the full Hamiltonian $H = \mathrm{diag}(H_{K\uparrow}, H_{K,\downarrow}, H_{K',\uparrow}, H_{K',\downarrow})$ takes the form

$$H = \begin{bmatrix} H(\mathbf{p}, \Delta) & 0 & 0 & 0 \\ 0 & H(\mathbf{p}, \Delta) & 0 & 0 \\ 0 & 0 & (H(-\mathbf{p}, \Delta))^* & 0 \\ 0 & 0 & 0 & (H(-\mathbf{p}, \Delta))^* \end{bmatrix} \tag{8.3}$$

Such a state breaks both the approximate U(1) rotation symmetry, and also the exact C_3 lattice rotation symmetry. However, it preserves the symmetries of time reversal and parity inversion.

We point out that one can also construct more general states, which to our knowledge have not yet been discussed in the literature. These states would have a mean field Hamiltonian of the form Eq.8.2, where the order parameter Δ has a spin-valley

structure different to Eq.8.3. A simple example is a state with mean field Hamiltonian

$$H = \begin{bmatrix} H(\mathbf{p},\Delta) & 0 & 0 & 0 \\ 0 & H(\mathbf{p},\Delta) & 0 & 0 \\ 0 & 0 & (H(-\mathbf{p},\Delta^*))^* & 0 \\ 0 & 0 & 0 & H(-\mathbf{p},\Delta^*))^* \end{bmatrix} \tag{8.4}$$

This state breaks C_3 symmetry just like the standard nematic state, but in addition also breaks T, P and M symmetries, since under time reversal, parity inversion, or mirror reflection, $H(\Delta) \rightarrow H(\Delta^*)$. The SU(4) symmetry is also broken by such a state. However, this state has a low energy bandstructure which consists of eight Fermi points with linear dispersion, just like the standard nematic state, so it represents a 'generalised nematic state.'

A larger class of generalized nematic states can also be constructed, where the mean field Hamiltonian for a single species takes the form Eq.8.2, but the full Hamiltonian has some more complicated spin valley structure. These states will all break the C_3 symmetry, and will in general also break additional symmetries, like T, P, M and $SU(4)$. We note that whereas the spin-valley structure of the gapped states is characterized by four signs (the ± 1 eigenvalues of the matrix Q in Eq.8.1), the spin-valley structure of the generalised nematic states is characterized by four phases (the phases of the nematic order parameters for the four species).

Although we are not aware of any theoretical mechanism that leads to the generalised nematic states, these states are legitimate mean fields for BLG. Thus, it is possible that some hitherto unanticipated mechanism could drive BLG into one of these generalised nematic states. Fortunately, the fact that such states break C_3 and T symmetries means that the 'generalised nematic scenario' for BLG can be directly tested experimentally. In particular, since the generalised nematic states break time reversal symmetry, they can and should display a Hall conductance at zero field. However, in a gapless state the Hall conductance will not be quantised. The non-quantised Hall effect that can arise in such states can be thought of as an analog of the anomalous Hall effect that arises in a ferromagnet.

Table 8.1: Low energy bandstructure in various states: number of Fermi points and low energy dispersion.

State	Fermi points	Dispersion
Non-interacting	4	Quadratic
Gapped, Eq.(8.1)	0	Gapped
Nematic, Eq.(8.2)	8	Linear
Trigonal Warping, Eq.(7.1)	16	Linear

8.2 Experimental tests of the zero field ordered state

The three categories of possible state all have a different number of Fermi points, listed in Tab.8.1.. The BLG can open a spontaneous gap, the quadratic band crossing can split into two Dirac points, or the quadratic band crossing can split into four Dirac points. We now discuss how the number of Fermi points may be determined experimentally, using transport measurements.

8.2.1 Landau level degeneracy at weak fields

The number of Fermi points is linked with the Landau level degeneracy at weak magnetic field. Each Fermi point contributes one Landau level, except that for the zero energy Landau level only, each quadratic band crossing contributes two Landau levels [10]. In consequence, the low energy bandstructure can be inferred from the Landau level degeneracy. Landau level occupancy is labelled so that charge neutrality corresponds to filling factor $\nu = 0$.

In the absence of any gap, nematic splitting, or trigonal warping, the BLG Landau levels are fourfold degenerate, except for a zeroth Landau level that is eightfold degenerate, so that integer quantum Hall effect (IQHE) is observed at filling factors $\nu = \pm 4, \pm 8, \pm 12....$ However, the Landau level degeneracy is dramatically altered by all the possible non-trivial states.

Trigonal warping splits the four quadratic band crossing points into sixteen Dirac points. BLG in the trigonal warping regime thus exhibits a sixteenfold degeneracy of Landau levels, displaying IQHE at $\nu = \pm 8, \pm 24, ...$ Such a sixteenfold

degeneracy, if observed, would constitute direct evidence for trigonal warping.

The **nematic** mean field splits four quadratic band crossings of BLG into eight Dirac points, on an energy scale $\Delta_{nem} \approx 1\text{meV}$. In the limit $\hbar eB/mc < \Delta_{nem} \approx 1\text{meV}$, there is therefore an eightfold degeneracy of all Landau levels. The IQHE should thus be observed at the filling factors $\nu = \pm 4, \pm 12, \pm 20...$, but not at $\nu = \pm 8, \pm 16....$ Such a pattern of degenerate Landau levels would constitute direct evidence for the nematic states.

The **gapped states** can split the zeroth Landau level, producing low field IQHE at $\nu = \text{Tr}(Q\eta_3)$. However, they do not at all affect the fourfold degeneracy of the higher Landau levels. Thus, if a departure from non-interacting behavior is seen at zero magnetic field, but the weak field degeneracy of the higher Landau levels is unaltered, then this constitutes indirect evidence for the gapped states, since of the various possible candidate states, only the gapped states leave the degeneracy of the higher Landau levels untouched. Moreover, if a large zero field gap is observed at $\nu = 0, \pm 2$ or ± 4, then this will also determine what kind of gapped state we have, since in the presence of a magnetic field, the zero field gap turns into a gap at $\nu = \text{Tr}(Q\eta_3)$.

To see these effects, it is essential to work at magnetic fields such that the cyclotron frequency $\hbar\omega_c = \hbar eB/mc \approx 2.5\text{meV} \times B[\text{T}]$ is much less than the energy scale for the gap/nematic splitting (estimated [3] to be of order 1meV). Therefore, if is necessary to be able to resolve Landau level degeneracy at a transverse magnetic field $B \ll 0.5\text{T}$. This may be challenging experimentally.

8.2.2 Probing gapped states with AC conductivity

Here we discuss how the various states may be directly probed in optical experiments, by calculating the AC longitudinal and Hall conductivity. We assume that the frequency ω at which we measure the AC conductivity is much greater than $1/\tau$, where τ is the mean lifetime of quasiparticles in BLG.

The conductivity for a chiral system like BLG may be calculated using the for-

malism introduced in [24]. The conductance is given by

$$\sigma_{\mu\nu}(\omega) = \frac{1}{i\omega}K_{\mu\nu}(\omega) \tag{8.5}$$

$$K_{\mu\nu}(\omega) = \int \frac{d\varepsilon}{2\pi}\Big[\mathrm{Tr}\Big(G(\varepsilon+\frac{\omega}{2},\mathbf{p})j_\mu(\mathbf{p})G(\varepsilon-\frac{\omega}{2},\mathbf{p})j_\nu(\mathbf{p})\Big) - \mathrm{Tr}\Big(G(\varepsilon,\mathbf{p})j_\mu(\mathbf{p})G(\varepsilon,\mathbf{p})j_\nu(\mathbf{p})\Big)\Big] \tag{8.6}$$

Here the trace is taken over momenta $\mathbf{p}$, and over the sublattice, spin and valley degrees of freedom. The subtraction of the term at $\omega = 0$ is a convenient way to account for the contribution of the diamagnetic current. The current operator in Eq.(8.6) may be straightforwardly obtained by adding a vector potential to the Hamiltonian through the minimal coupling prescription $\mathbf{p} \to \mathbf{p} - e\mathbf{A}$, and defining $\mathbf{j} = \frac{\partial H}{\partial A}|_{A=0}$. In the K valley, this yields

$$j_x = \frac{1}{m}(p_+\tau_+ + p_-\tau_-); \qquad j_y = \frac{i}{m}(p_+\tau_+ - p_-\tau_-) \tag{8.7}$$

The current operators in the K' valley are obtained from those in the K valley by complex conjugation and by taking $\mathbf{p} \to -\mathbf{p}$. Meanwhile, the Green functions are in the imaginary time formalism, and take the form

$$G(i\varepsilon,\mathbf{p}) = \frac{i\varepsilon + H(\mathbf{p})}{\varepsilon^2 + H^2(p)} \tag{8.8}$$

where $H(p)$ is the effective low energy Hamiltonian for the state that we are looking at, and $H^2(p)$ has no matrix structure (is proportional to the identity in spin-valley-sublattice space). The calculations are all done in the imaginary time formalism, before finally continuing to real frequencies. Details of the calculations are presented in the appendix. Here we simply quote the results.

For **non-interacting BLG**, we obtain

$$\sigma_{xx}(\omega) = \frac{N\pi e^2}{4h} = \sigma_{yy}(\omega) \tag{8.9}$$

$$\sigma_{xy}(\omega) = 0 = \sigma_{yx}(\omega) \tag{8.10}$$

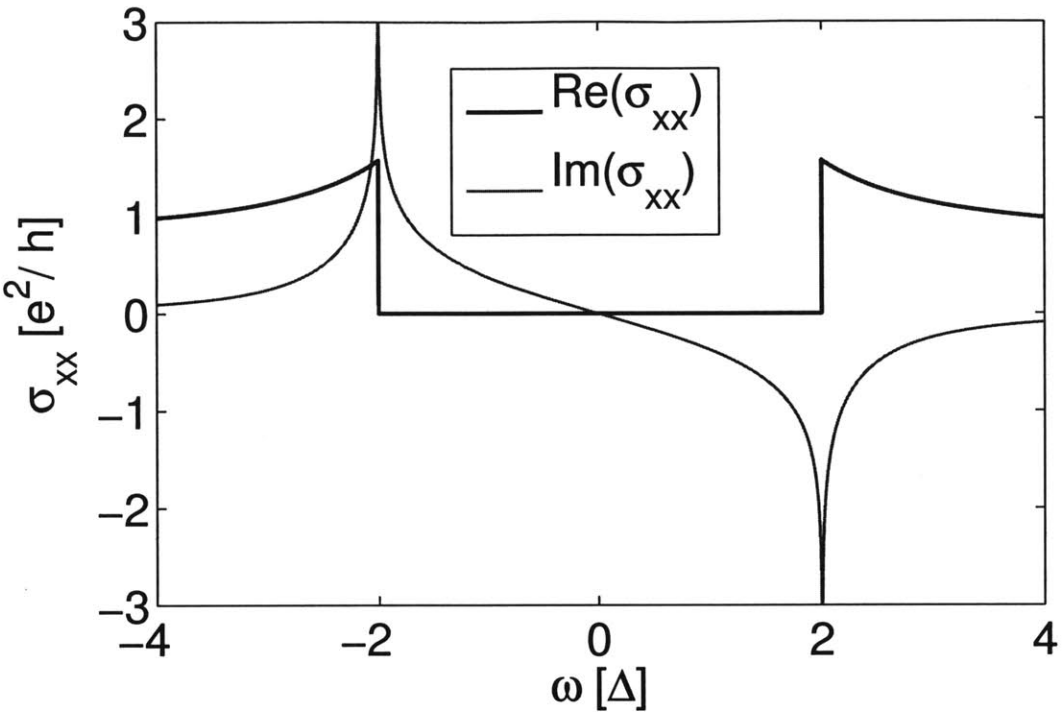

Figure 8-1: Real and imaginary part of the single species longitudinal conductivity in the gapped state.

where $N = 4$ is the number of fermion species in BLG. Note that there is a frequency independent AC conductivity for non-interacting BLG [25, 26].

For **the gapped states** (Eq.8.1), we obtain

$$\sigma_{xx}(\omega) = \frac{e^2}{h}\Big[\frac{i|\Delta|}{\omega} - (\frac{\Delta^2}{\omega^2} + \frac{1}{4})i\ln\Big(\frac{2|\Delta|+\omega}{2|\Delta|-\omega}\Big)\Big] = \sigma_{yy}(\omega) \tag{8.11}$$

The real and imaginary parts are plotted in Fig.8-1. Note that the real part of the conductivity vanishes inside the gap. Note too the singularity at $\omega = \pm 2\Delta$, which is a clear signature of the gapped state. If a gapped state is seen in the longitudinal conductivity, then the spin-valley structure may be established by looking at the Hall conductivity. The Hall conductivity of the gapped states takes the form

$$\sigma_{xy}(\omega) = \frac{e^2}{h}\frac{\Delta}{\omega}\ln\Big(\frac{2|\Delta|+\omega}{2|\Delta|-\omega}\Big)\mathrm{Tr}(Q\eta_3) \tag{8.12}$$

The real and imaginary parts of the conductivity are plotted in Fig.8-2. In the limit

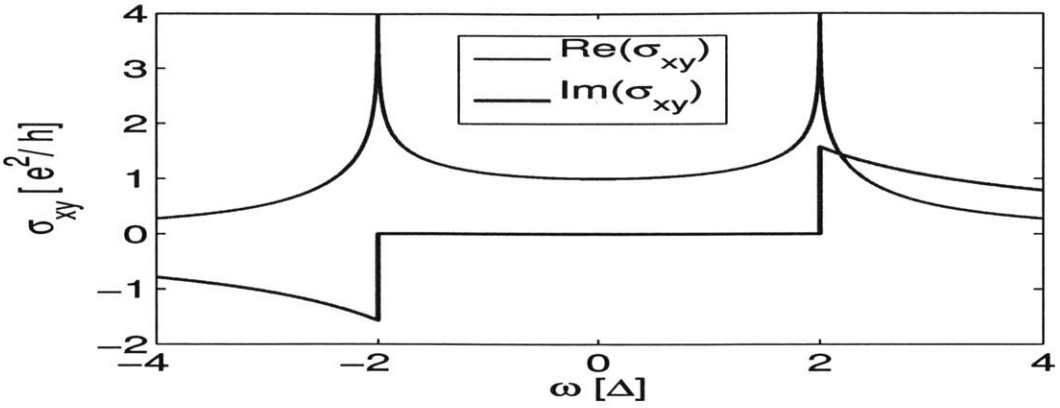

Figure 8-2: Real and imaginary part of single species Hall conductivity in the gapped state. The total Hall conductivity is obtained by summing over spin and valley species, which multiplies the above result by a factor of $\mathrm{Tr}(Q\eta_3)$. In time reversal symmetry preserving gapped states, $\mathrm{Tr}(Q\eta_3) = 0$ and the Hall conductivity vanishes.

$\omega \to 0$, we obtain the result

$$\sigma_{xy}(\omega \to 0) = (e^2/h)\mathrm{sign}(\Delta)\mathrm{Tr}(Q\eta_3) \tag{8.13}$$

that is expected from [27, 11], with an additional factor of 2 that comes from the 2π Berry phase of BLG. Thus, from the DC Hall conductivity, we can extract $\mathrm{Tr}(Q\eta_3)$. Note that a non-zero Hall conductivity appears only in the QAH gapped states with $\mathrm{Tr}(Q\eta_3) \neq 0$, when time reversal symmetry is broken. A non-vanishing, quantised DC Hall conductance is a clear signature of the QAH state, just as a longitudinal conductivity that vanishes inside the gap, accompanied by a singular conductivity at $\omega = \pm 2\Delta$ is a clear signature of the gapped states.

The nematic states (Eq.8.2) are gapless states, so the conductivity does not vanish in the small ω limit. However, the nematic states break rotational symmetry - both the approximate continuous rotation symmetry of the low energy Hamiltonian, and the exact C_3 symmetry of the lattice. This manifests itself in an anisotropic conductivity, which is a clear signature of the nematic states. We calculate, for spin-

valley species j that

$$\sigma_j(\theta) = \sigma(\Delta = 0) - \delta\sigma_j \cos\left(2\theta - \chi \arg \Delta_j\right) \tag{8.14}$$

where $\sigma(\theta)$ is the longitudinal conductivity at an angle θ to the x axis and χ takes the value $+1(-1)$ in the K valley (K' valley). The anisotropy is non-zero and non-singular at all frequencies, and in the high frequency limit takes the form

$$\delta\sigma_j = \frac{e^2}{\omega}\Big(\pi + i \ln \frac{\omega^2}{|\Delta|^2}\Big)|\Delta_j|. \tag{8.15}$$

The total conductivity is obtained by summing over spin-valley species j.

We can also calculate the Hall conductivity for the nematic states. In the standard nematic state [9, 7, 8], the DC Hall conductivity must be zero, since time reversal symmetry is preserved. However, in the generalised nematic states, time reversal symmetry is broken, and a DC Hall conductance can develop. However, because the nematic states are gapless, this Hall conductance will not be quantised. In the high frequency limit, the Hall conductance takes the form

$$\sigma_{xy}(\omega) = \frac{e^2}{\omega}\Big(\pi + i \ln \frac{\omega^2}{|\Delta|^2}\Big) \sum_j |\Delta_j| \sin\left(\arg \Delta_j\right) \tag{8.16}$$

This will be useful for our discussion of optical effects. The above expression assumed $\omega \gg \Delta$. An integral expression valid for arbitrary frequencies is provided in the appendix.

The **trigonal warping** effect also generates an anisotropic conductivity. However, trigonal warping preserves all the symmetries of the lattice. Thus, the trigonal warping effect cannot produce a DC Hall conductivity, since this would break TRS. Moreover, the anisotropic longitudinal conductivity produced by trigonal warping will exhibit the threefold rotation symmetry of the lattice, unlike the nematic state where the conductivity displays only a two-fold rotation symmetry.

8.2.3 Optical tests of broken symmetry

A number of the states discussed above break **time reversal symmetry**. Time reversal symmetry breaking can be probed directly through optical measurements [28, 29, 53, 32, 51]. The key signature is the 'polar Kerr effect', whereby linearly polarised light incident normally on a material is reflected as elliptically polarised light, with the major axis rotated relative to the incident polarisation by the Kerr angle θ_K. Such optical rotation occurs because the left and right circularly polarised light is reflected with different amplitudes and phases, but crucially, this optical rotation in reflection only occurs if the sample breaks time reversal symmetry [28, 29]. Thus, by looking for optical rotation of reflected light, we can directly probe the breaking of time reversal symmetry in the sample.

The Kerr effect should be easily detectable for both the Quantum Anomalous Hall gapped states, and also for the time reversal symmetry breaking generalised nematic states. The calculation of the Kerr angle is provided in the appendix. Here we simply quote the result. For BLG on a substrate of dielectric constant n, the reflection and transmission coefficients are

$$t^{\pm} = \frac{2}{1+n+\frac{4\pi}{c}\sigma_{\pm}(\omega)}, \quad r^{\pm} = \frac{1-n-\frac{4\pi}{c}\sigma_{\pm}(\omega)}{1+n+\frac{4\pi}{c}\sigma_{\pm}(\omega)}$$

where $\sigma_{\pm} = \sigma_{xx} \pm i\sigma_{xy}$ and $t_{\pm}, r_{\pm}$ are the transmission and reflection coefficients respectively for right (+) and left (-) circularly polarised light. To find the Kerr angle, we consider an incoming wave that is linearly polarised along the x axis, $\mathbf{E}_{in} = E_0\hat{x}$. The outgoing wave is

$$\mathbf{E}_{out} = \frac{r^+ + r^-}{2}E_0\hat{\mathbf{x}} + \frac{r^+ - r^-}{2i}E_0\hat{\mathbf{y}}. \tag{8.17}$$

This describes linear polarization if $\arg(r^+ - r^-)/(r^+ + r^-) = \pi/2$, otherwise the polarization is elliptic. The Kerr angle, which describes rotation of the major polar-

ization axis of the reflected wave relative to that of the incident wave, is

$$\begin{aligned}\theta_K &= \mathrm{Im}\,\frac{r^+ - r^-}{r^+ + r^-} \approx -\frac{4\pi}{c}\,\mathrm{Im}\, i\sigma_{xy}(\omega)\left(\frac{1}{1-n}+\frac{1}{1+n}\right) \\ &= \frac{8\pi}{c(n^2-1)}\,\mathrm{Re}\,\sigma_{xy}(\omega) \end{aligned} \tag{8.18}$$

where we approximated $r^{\pm}$ taking into account that σ_{xx} and σ_{xy} are small compared to c at all frequencies. This follows because the conductivity is of order $e^2/\hbar$, and $e^2/\hbar c = 1/137$. The above expression is appropriate for BLG on substrate, $n \neq 1$. For suspended BLG, where $n = 1$, the Kerr angle is equal to the Hall angle.

In the microwave limit $\hbar\omega \ll \Delta$, we have $\sigma_{xy} = e^2/h$. The expression Eq.(8.18) then predicts a fairly large optical rotation for the QAH states

$$\theta_K = \frac{2}{137(n^2-1)}\mathrm{sign}(\Delta) \sim 10^{-2}\mathrm{sign}(\Delta) \tag{8.19}$$

This is well within the measurable range for optical experiments, which are sensitive enough to detect Kerr angles as small as 10^{-8} [[53]]. For higher frequencies $\hbar\omega > \Delta$, we have

$$\theta_K = \frac{2}{137(n^2-1)}\frac{\Delta^2}{\omega^2}\mathrm{sign}(\Delta) \sim 10^{-2}\frac{\Delta^2}{\omega^2}\mathrm{sign}(\Delta) \tag{8.20}$$

This expression is valid for $\hbar\omega \ll \Lambda$, where $\Lambda \approx 0.4eV$ is the bandgap to the higher BLG bands. For experiments at $\hbar\omega \gtrsim \Lambda$, the two band model is not sufficient, and a four band model must be used. This will be discussed in the latter half of this chapter. For the moment, we simply note that optical rotation in reflection is an unambiguous signal of time reversal symmetry breaking, and would thus be an extremely useful measurement to perform on BLG.

We note that gapped states which break discrete symmetries, such as the QAH state, can form domains, with different domains having a Kerr angle of opposite sign. Domain structure can be directly imaged in optical experiments, unlike transport experiments where only the net effect of all domains can be observed.

We note that symmetry considerations permit optical rotation in reflection even from the antiferromagnetic gapped state, which also breaks time reversal symmetry,

even though it has a vanishing Hall conductance. The optical activity here arises because this state has a spin dipole moment, which interacts with the optical field through the Zeeman coupling. The optical rotation from such a state was analysed in Ref.[29]. It is suppressed by the small parameter d/λ, where $d \approx 3\mathring{A}$ is the interlayer spacing and λ is the wavelength of the light used. We note that the Kerr angle arising from such a mechanism is many orders of magnitude smaller than the large Kerr angle obtained above (Eq.(8.18)), particularly in the microwave regime. Nevertheless, it may be within the reach of optical experiments, which can detect Kerr angles as small as 10^{-8} [[53]].

Broken inversion symmetry Additional information may be obtained by considering optical rotation in transmission. Optical rotation in transmission requires breaking of either time reversal symmetry or parity (space inversion) symmetry. Therefore, if optical rotation is observed in transmission but not in reflection, then this definitively indicates that parity symmetry is broken, but time reversal symmetry is not, which implies a quantum valley hall effect (i.e. ferroelectric) state.

Broken rotational symmetry The nematic states exhibit an anisotropic conductivity. This will manifest itself in anisotropic transmission, with light polarised linearly along the $\hat{x}$ axis having a different transmission coefficient to light polarised linearly along the $\hat{y}$ axis. This is demonstrated by explicit calculation in the appendix. It is found that the ratio of the transmission amplitudes for the two linear polarizations is

$$\frac{t_x}{t_y} = \frac{n+1+\frac{4\pi}{c}\sigma_{xx}}{n+1+\frac{4\pi}{c}\sigma_{yy}} \tag{8.21}$$

$$\approx 1+\frac{8\pi}{c}\delta\sigma \tag{8.22}$$

Where $\delta\sigma$ is the anisotropy in conductivity, Eq.(8.14, 8.15). For the nematic state, the anisotropy is of order

$$\frac{t_x - t_y}{t_y} \approx 10^{-2}\frac{\Delta_{nem}}{\omega}$$

for $\omega > \Delta$. This anisotropic transmission allows us to directly probe the broken

rotational symmetry.

Trigonal warping will also produce an anisotropic conductivity, however the anisotropy will respect the exact threefold rotation symmetry of the lattice. In contrast, the anisotropic conductivity in the nematic state will exhibit only a twofold rotation symmetry Eq.8.14, and this difference in symmetry is a diagnostic for the nematic states.

8.3 Kerr effect as a probe of broken time reversal symmetry: four band calculations

Optical experiments have been successfully used to probe diverse electronic phenomena in graphene [38]. For bilayer graphene (BLG), physical properties such as the gate tunable bandgap [39, 40] and the electron phonon coupling [41, 42] were investigated with the help of infrared and optical spectroscopy. These techniques have also been used to probe interaction effects such as band renormalization [43, 32] and exciton formation [45, 46]. However, there has not yet been any effort to apply optical methods to the investigation of strongly correlated states, which are expected to form in BLG at low energies [2, 4, 7, 9, 3, 5, 6, 8, 47]. This can be partly due to the low characteristic energy scales for these symmetry breaking states, estimated to be of order 1 meV [3], which lie far outside the range of characteristic energies probed in optical experiments. In this Letter, we point out that the problem of energy scales is offset by the unique sensitivity of optical response to broken symmetries, making these methods ideally suited to the investigation of the interacting ground state of BLG.

A large number of possible interacting phases have been proposed for BLG [2, 4, 7, 9, 3, 5, 6, 8, 47]. Recent compressibility and transport experiments on charge neutral, suspended, double gated bilayer graphene [14, 15, 16] appear to confirm the prediction of a non-trivial interacting ground state. The experimental data was argued [16] to be consistent with only two of the proposed phases: the Quantum Anomalous Hall

phase (QAH) predicted in [5, 6], and the nematic phase predicted in [7, 8, 9]. Both these phases are uniquely interesting phases. The QAH phase spontaneously breaks time reversal symmetry (TRS) and exhibits quantum Hall effect at zero magnetic field, while the nematic state involves a distortion of the Dirac bandstructure that spontaneously breaks the exact rotational symmetry of the lattice. If either of these phases is confirmed in BLG, it would fulfill a long quest for an experimental realization of a QAH instability [11] (QAH phase) or a Pomeranchuk instability [12, 49] (nematic phase).

The possible broken symmetries are expected to manifest themselves through characteristic transport properties such as a non-zero Hall response or anisotropy in longitudinal conductance [2, 4, 7, 9, 3, 5, 6, 8, 47]. Detecting these effects in transport experiments requires fabrication of samples of BLG with at least four contacts, which proves challenging in suspended BLG currently used in these experiments. However, optical experiments allow us to measure the AC conductivity in a contact-free manner. As we discuss below, the AC conductivity shows distinctive signatures of broken symmetry just like the DC conductivity.

The polar Kerr effect, wherein linearly polarized light has its polarization axis rotated upon reflection, is a well known optical probe of the Hall conductivity. It has been used to probe quantum Hall states [58], and more recently has been applied to topological insulator thin films in the vicinity of a ferromagnet [51, 52], and to $p+ip$ superconductors [53]. It is closely related to the Faraday effect, which has been measured for graphene in the Quantum Hall regime [54]. A similar experimental setup should suffice for measurement of the Kerr effect. However, unlike the Faraday effect, which requires breaking of either TRS or inversion symmetry, the polar Kerr effect can arise *only* if TRS is broken [28], hence offering a direct test of the QAH scenario for BLG.

Our analysis of optical response reveals that the QAH state exhibits an AC Hall conductivity that undergoes a resonant enhancement in the optical and near infrared regime (see Fig.8-3). This resonant enhancement occurs because the microscopic current operator has inter-band matrix elements (Fig.8-3 inset) corresponding to transi-

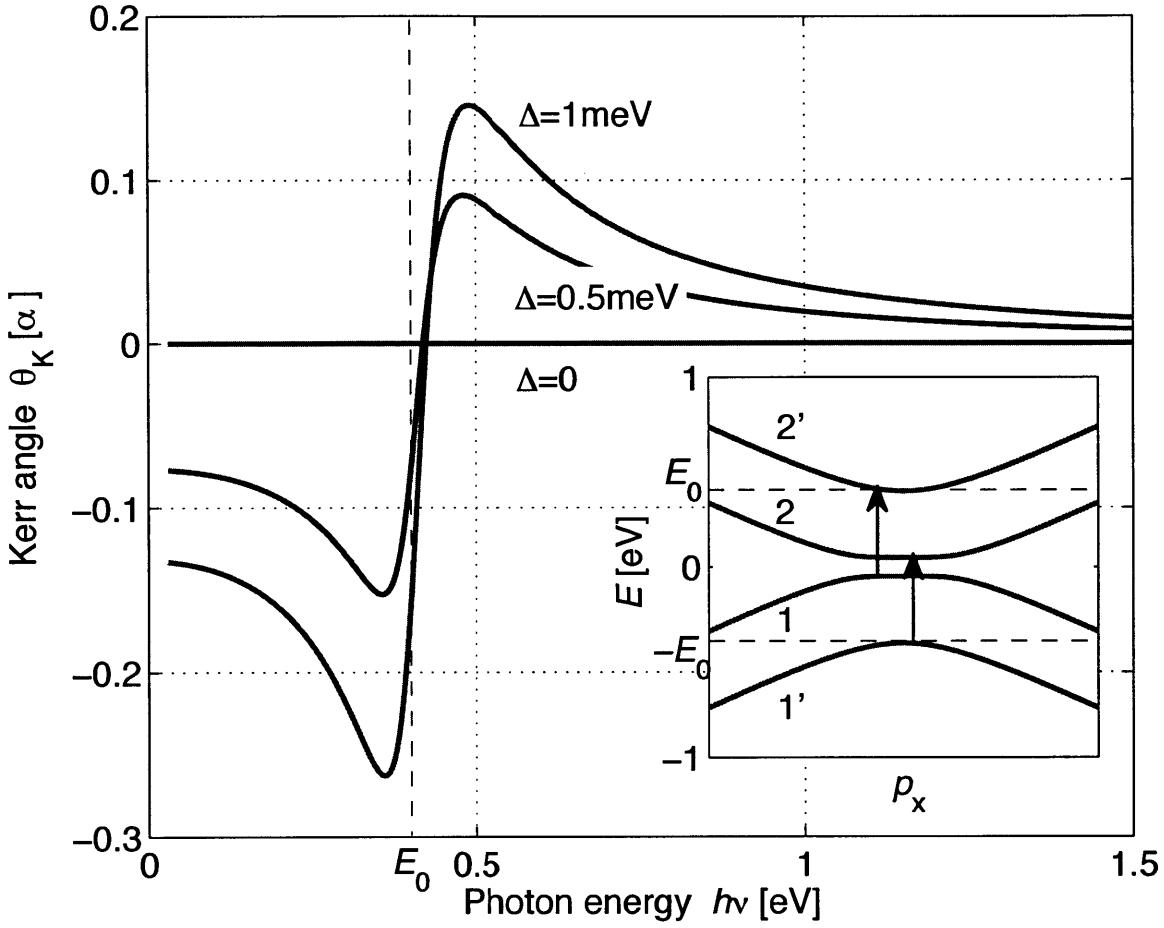

Figure 8-3: Kerr angle (in units of fine structure constant $\alpha = e^2/\hbar c$) as a function of photon energy for BLG in the QAH phase. Note the resonant enhancement near $E_0 = 0.4\,\mathrm{eV}$, arising from direct transitions to the higher BLG bands, Eq.(8.34). Inset: Schematic band structure of BLG near the K point, for the QAH phase. The Kerr response arises from transitions $1' \to 2$ and $1 \to 2'$, involving states in the bands 1 and 2 which are affected by broken TRS.

tions from the low energy bands $1, 2$ to the high energy bands $1', 2'$. As a result, the Kerr rotation (plotted in Fig.8-3) is many orders of magnitude larger than that observed in p-wave superconducting materials [53], and lies well within reach of existing experimental techniques.

Optical methods can be used to probe domain formation expected to occur in the TRS breaking QAH phase. Since different domains will produce a Kerr rotation of opposite sign, the spatial domain structure can be directly imaged in optical experiments – a significant advantage over transport experiments, which can only measure the net effect of all domains. For a non-focused optical experiment, the effect of random domains will be to reduce the total Kerr angle by a factor $\sqrt{N_D}$, where N_D is the number of domains.

While the Kerr rotation allows to test for TRS breaking, anisotropy in reflection allows to test for rotation symmetry breaking. As we discuss below, this leads to a characteristic dependence of the reflection amplitude on the polarization angle of incident light which offers a way to test the nematic scenario for BLG [7, 8].

Finally, we note that spontaneous symmetry breaking is only expected to occur below a critical temperature, estimated to be of order $1 - 10\,\mathrm{K}$ [3, 16]. The optical signatures of interacting states will thus show a strong temperature dependence, and will vanish entirely above a critical temperature. This provides a way to distinguish spontaneously broken symmetries from explicitly symmetry breaking effects (e.g. magnetic impurities), which will not show any comparable temperature dependence.

Electron properties of a clean BLG are governed by a four-band Hamiltonian written for the four component wavefunction $\psi = (\psi_1, \psi_2, \psi_3, \psi_4)$, describing electron wavefunction on the sublattices A, B and A', B' on the two layers:

$$H(\mathbf{p}) = \begin{bmatrix} 0 & t_{\mathbf{p}} & 0 & 0 \\ t^*_{\mathbf{p}} & 0 & E_0 & 0 \\ 0 & E_0 & 0 & t_{\mathbf{p}} \\ 0 & 0 & t^*_{\mathbf{p}} & 0 \end{bmatrix}, \quad E_0 \approx 0.4\,\mathrm{eV}, \tag{8.23}$$

with $t_{\mathbf{p}} = t_0(1 + e^{-i\mathbf{p}\mathbf{e}_1} + e^{-i\mathbf{p}\mathbf{e}_2})$, where $t_0 \approx 3.1\,\mathrm{eV}$ is the hopping amplitude, and E_0 is bandgap parameter for the upper and lower bands. The quantity $t_{\mathbf{p}}$ vanishes at the K and K' points, behaving as vp_+ near point K and as $-vp_-$ near point K', where $p_\pm = p_x \pm ip_y$.

The Hamiltonian (8.23) features four bands with energies

$$\varepsilon^2(\mathbf{p}) = |t_{\mathbf{p}}|^2 + \frac{1}{2}E_0^2 \pm \frac{1}{2}E_0^2\sqrt{1 + 4|t_{\mathbf{p}}|^2/E_0^2}. \tag{8.24}$$

Near the points K and K', this gives two massless Dirac bands $\varepsilon_{1,2}(\mathbf{p})$ that cross quadratically at zero energy, and two high-energy bands $\varepsilon_{1',2'}(\mathbf{p}) \approx \pm E_0$. The dispersion near K and K' can be obtained by expanding in small $t_{\mathbf{p}}/E_0$, giving $\varepsilon_{1,2} = \pm|t_{\mathbf{p}}|^2/E_0 = \pm v^2p^2/E_0$, $\varepsilon_{1',2'} = \pm\,(E_0 + v^2p^2/E_0)$.

We now consider the effect of interactions. Interactions can open a bulk bandgap between bands 1 and 2 [5, 3, 6, 2, 4], resulting in a bandstructure of the form Fig.8-3(inset). One particularly interesting gapped state is the QAH state, [5, 6], the mean field Hamiltonian of which we present below. To exhibit more clearly the block structure we reorder basis vectors by interchanging the components ψ_2 and ψ_4. In this representation, we obtain

$$H_K(\mathbf{p}, \Delta) = \begin{bmatrix} \Delta & 0 & vp_+ & 0 \\ 0 & -\Delta & 0 & vp_- \\ vp_- & 0 & 0 & E_0 \\ 0 & vp_+ & E_0 & 0 \end{bmatrix} = H^*_{K'}(-\mathbf{p}, -\Delta) \tag{8.25}$$

where Δ is the order parameter describing gap opening at the K and K' points. The other possible gapped states [2, 4, 3] have a similar mean field Hamiltonian, but the sign of Δ is distributed differently among the spins and valleys. We note that under time reversal, $H_K(\Delta) \oplus H_{K'}(-\Delta) \to H_{K'}(\Delta) \oplus H_K(-\Delta)$, so this phase breaks TRS. In consequence, the QAH state can exhibit a non-vanishing Hall conductance at zero magnetic field. However, the gap preserves the isotropy of the bandstructure. Thus, the QAH state must exhibit isotropic longitudinal conductivity.

Next, we discuss the relation between the Hall response in the QAH phase and the Kerr rotation. We consider an experimental setup where light is incident normally on a BLG sheet that is placed on a substrate. If the BLG sheet has a non-vanishing Hall conductance, then incident linearly polarized light will be reflected as elliptically polarized light, with the major axis of the ellipse rotated with respect to the incident polarization by the Kerr angle θ_K. The standard formula relating the Kerr angle to the Hall conductance is $\theta_K \sim \mathrm{Im}\,(\sigma_{yx})$ [28]. However, this formula is derived for light incident on a conducting half space, whereas we are considering a BLG sheet that is much thinner than the optical wavelength. For this case, the relationship between Hall conductivity and Kerr angle must be calculated afresh. This was accomplished using topological field theoretic methods in [52, 51]. More straightforwardly, the relationship may be obtained by solving the Maxwell equations on two sides of the BLG sheet and matching solutions at the boundary [55]. This leads to an expression in agreement with [51, 52], which takes the form

$$\theta_K = \mathrm{Re}\,\frac{-(8\pi/c)\,\sigma_{yx}}{1-(n+\frac{4\pi}{c}(\sigma_{xx}+i\sigma_{xy}))^2} \approx \frac{8\pi\,\mathrm{Re}\,\sigma_{yx}}{c(n^2-1)}. \tag{8.26}$$

where n is the refractive index of the substrate, which is taken to be real (complex case considered in [55]).

We now calculate the magnitude of the Kerr rotation, by evaluating the conductivity. The AC conductivity can be written using the Kubo formula as

$$\sigma_{xy} = \frac{e^2}{i\omega}\sum_{i,j,\mathbf{p}} \frac{\langle i,\mathbf{p}|V_x|j,\mathbf{p}\rangle\langle j,\mathbf{p}|V_y|i,\mathbf{p}\rangle}{\omega-(\varepsilon_{j,\mathbf{p}}-\varepsilon_{i,\mathbf{p}})+i\gamma}(n_{i,\mathbf{p}}-n_{j,\mathbf{p}}), \tag{8.27}$$

where i and j are band indices, $n_{i,\mathbf{p}} = n(\varepsilon_{i,\mathbf{p}})$ is a Fermi function, and the sum over momenta $\mathbf{p}$ stands for an integral. The velocity operators V_α are defined as $V_\alpha = \partial H(\mathbf{p})/\partial p_\alpha$, and γ describes the excited state lifetime.

We focus on the contributions which correspond to optical interband transitions between the massless low energy bands (i=1,2), and the high energy bands (i=1',2'), which are separated from the low energy bands by the energy E_0. We focus on these

transitions because they are of resonant character at a frequency close to the band separation energy E_0, and hence dominate the optical response. We now note that $\langle i,\mathbf{p}|V_\alpha|j,\mathbf{p}\rangle\langle j,\mathbf{p}|V_\beta|i,\mathbf{p}\rangle = \mathrm{Tr}(V_\alpha \Pi_{i,\mathbf{p}} V_\beta \Pi_{j,\mathbf{p}})$, where $\Pi_{i,\mathbf{p}}$ projects onto the state in band i with momentum $\mathbf{p}$. Assuming we are at a temperature $T \ll E_0/k_B = 4000K$, we obtain

$$\begin{aligned}\sigma_{xy}(\omega) = \quad & \frac{e^2}{i\omega}\int \frac{d^2p}{(2\pi)^2}\frac{\mathrm{Tr}\left(V_x\Pi_{1'}V_y\Pi_2 + V_x\Pi_1 V_y\Pi_{2'}\right)}{\omega+\varepsilon_{1'}(\mathbf{p})-\varepsilon_2(\mathbf{p})+i\gamma} \\ & -\frac{\mathrm{Tr}\left(V_x\Pi_2 V_y\Pi_{1'} + V_x\Pi_{2'}V_y\Pi_1\right)}{\omega-\varepsilon_{1'}(\mathbf{p})+\varepsilon_2(\mathbf{p})+i\gamma},\end{aligned} \tag{8.28}$$

where we used the relation $\varepsilon_{2'}-\varepsilon_1 = \varepsilon_2-\varepsilon_{1'}$ that follows from particle/hole symmetry of the Hamiltonian (8.25).

We evaluate the expression (8.28) for $\mathbf{p}$ near point K with the help of the projectors

$$\Pi_{1,2} = \frac{1}{2}\left(1 \pm \frac{h(\mathbf{p})}{||h(\mathbf{p})||}\right), \quad \Pi_{1',2'} = \frac{1\pm\tilde{\sigma}_x}{2} \tag{8.29}$$

Here $\tilde{\sigma}_x$ acts on the $B1$ and $A2$ sublattices (lower right corner of the Hamiltonian in (8.25)) and $\Pi_{1',2'}$ projects on this subspace. Meanwhile, $\Pi_{1,2}$ project on the $A1$ and $B2$ sublattices (upper left corner of Eq.(8.25)), and $h(\mathbf{p})$ is the effective two band Hamiltonian for the massless Dirac states, which has eigenvalues $E(\mathbf{p}) = \pm||h(\mathbf{p})||$. The trace over projectors takes the form

$$\begin{aligned} g^{1'2}_{\alpha\beta} &= \mathrm{Tr}\left(V_\alpha\Pi_{1'}V_\beta\Pi_2\right) = \langle 1'|V_\beta\Pi_2 V_\alpha|1'\rangle \\ &= \frac{1}{4}\begin{bmatrix}\nabla_\beta t^*(\mathbf{p}) \\ \nabla_\beta t(\mathbf{p})\end{bmatrix}^{\mathrm{T}}\left(1-\frac{h(\mathbf{p})}{||h(\mathbf{p})||}\right)\begin{bmatrix}\nabla_\alpha t(\mathbf{p}) \\ \nabla_\alpha t^*(\mathbf{p})\end{bmatrix} \\ g^{12'}_{\alpha\beta} &= \mathrm{Tr}\left(V_\alpha\Pi_1 V_\beta\Pi_{2'}\right) = \langle 2'|V_\alpha\Pi_1 V_\beta|2'\rangle \\ &= \frac{1}{4}\begin{bmatrix}\nabla_\alpha t^*(\mathbf{p}) \\ -\nabla_\alpha t(\mathbf{p})\end{bmatrix}^{\mathrm{T}}\left(1+\frac{h(\mathbf{p})}{||h(\mathbf{p})||}\right)\begin{bmatrix}\nabla_\beta t(\mathbf{p}) \\ -\nabla_\beta t^*(\mathbf{p})\end{bmatrix}. \end{aligned} \tag{8.30}$$

Here ∇_α denotes $\partial/\partial p_\alpha$. We now compute $h(\mathbf{p})$ by using second order perturbation

theory in vp/E_0, and obtain

$$h_K(\mathbf{p}) = \begin{bmatrix} \Delta & v^2p_+^2/E_0 \\ v^2p_-^2/E_0 & -\Delta \end{bmatrix}, \quad h_{K'}(\Delta) = h_K^*(-\Delta). \tag{8.31}$$

This result agrees with [10]. We substitute this two band Hamiltonian into Eq.(8.30) and obtain

$$\begin{aligned} g_{xy}^{1'2} = g_{xy}^{12'} &= \frac{1}{4}\left(1 - \frac{\Delta}{||h(\mathbf{p})||}\right)\nabla_y t^*(\mathbf{p})\nabla_x t(\mathbf{p}) \\ &+\frac{1}{4}\left(1 + \frac{\Delta}{||h(\mathbf{p})||}\right)\nabla_y t(\mathbf{p})\nabla_x t^*(\mathbf{p}), \end{aligned} \tag{8.32}$$

where we suppressed the terms arising from off-diagonal parts of $h(\mathbf{p})$ — these terms give zero upon integration over d^2p. Hence, we find $g_{xy}^{12'} = -g_{xy}^{2'1} = \frac{1}{2}iv^2\frac{\Delta}{||h(\mathbf{p})||}$. We substitute these results into Eqs.(8.28),(8.30), to obtain

$$\sigma_{xy}(\omega) = \frac{Ne^2v^2\Delta}{(2\pi)^2\omega}\int \frac{d^2p}{||h(\mathbf{p})||}\left[\frac{1}{\omega + i\gamma - \Omega_\mathbf{p}} + (\Omega_\mathbf{p} \to -\Omega_\mathbf{p})\right] \tag{8.33}$$

where $N = 4$ is the number of spin/valley flavors, and $\Omega_\mathbf{p} = \varepsilon_2(\mathbf{p}) - \varepsilon_{1'}(\mathbf{p})$.

We now specialize to optical frequencies $\omega \gg \Delta$, and also assume $\gamma \gg \Delta$. We approximate by taking $||h(\mathbf{p})|| \approx v^2p^2/E_0$ and $\Omega_p \approx E_0 + 2v^2p^2/E_0$, and perform the momentum integral in polar co-ordinates. The log divergence near $p^2 = 0$ is cut by $|\Delta|$, but there is no need for any high energy cutoff. In this manner, we obtain the Hall conductivity

$$\begin{aligned} \sigma_{xy}(\omega) &= \frac{Ne^2}{h}\frac{\Delta}{2\omega}\Big[\frac{E_0}{\omega + E_0 + i\gamma}\ln\left(\frac{E_0 + \omega + i\gamma}{2|\Delta|}\right) \\ &+ \frac{E_0}{\omega - E_0 + i\gamma}\ln\left(\frac{E_0 - \omega - i\gamma}{2|\Delta|}\right)\Big]. \end{aligned} \tag{8.34}$$

There is also a contribution from $1 \to 2$ transitions, which may be evaluated in the two band model [47, 56]. This contribution, extrapolated to optical frequencies $\omega \sim E_0 \gg \Delta$ is of order $(\Delta|\Delta|/\omega^2)e^2/h$. This is smaller than the contribution (8.34)

by a large factor

$$\frac{E_0}{\Delta}\ln\frac{E_0}{\Delta} \gg 1. \tag{8.35}$$

Thus, the Hall conductivity at optical frequencies is dominated by transitions to the higher bands, necessitating our four band analysis.

From the result Eq.(8.34) and the expression Eq.(8.26) we can extract the Kerr angle θ_K. We take $n = 1.5$, which describes SiO_2 substrate, and take $\Delta \approx 10^{-3}$ eV [3]. To estimate γ, we use the electron lifetime $\tau \approx 0.1ps$ from [57], which corresponds to $\gamma \sim 0.01eV$. We take $\gamma = 0.05$ eV to be conservative, and plot the resulting Kerr angle as a function of frequency in Fig.8-3. In optical experiments on cuprate materials, Kerr angles as small as 10^{-9} radians have been measured [53]. The six orders of magnitude larger Kerr rotation in the QAH phase should thus be comfortably within reach of experiments.

The nematic state [7, 8, 9] is another interesting ordered state proposed to explain the experiments [16, 15]. This state is time-reversal invariant, featuring no Kerr rotation. Instead, it breaks rotation symmetry of graphene crystal lattice. The Hamiltonian for this state is

$$H_K(\mathbf{p},\Delta) = \begin{bmatrix} 0 & \Delta & vp_+ & 0 \\ \Delta^* & 0 & 0 & vp_- \\ vp_- & 0 & 0 & E_0 \\ 0 & vp_+ & E_0 & 0 \end{bmatrix} = H_K^*(-\mathbf{p},\Delta). \tag{8.36}$$

After reduction to the two low-energy bands, it becomes

$$h_K(\mathbf{p},\Delta) = \begin{bmatrix} 0 & \frac{v^2p_+^2}{E_0} + \Delta \\ \frac{v^2p_-^2}{E_0} + \Delta^* & 0 \end{bmatrix} = h_K^*(-\mathbf{p},\Delta). \tag{8.37}$$

This Hamiltonian describes splitting of the quadratic band crossing into two linear band crossings. The argument of the nematic order parameter Δ specifies the orientation of the nematic axis, which is defined as the line joining the two linear band crossings. The nematic axis makes an angle $\varphi = -\pi/2 + \arg(\Delta)/2$ with respect to the

p_x axis. The nematic state manifestly breaks the approximate rotation invariance of the low energy band-structure, which manifests itself in an anisotropic longitudinal conductivity. Writing $\sigma(\theta) = \sigma_0 + \delta\sigma(\theta)$, where θ is the angle with respect to the x axis, we obtain an expression for the reflection amplitude $r(\theta)$,

$$r(\theta) \approx \frac{1-n}{n+1} - \frac{8\pi}{c(n+1)^2}\delta\sigma(\theta). \tag{8.38}$$

For high frequencies $\omega \gg \Delta$, we calculate using the formalism introduced above that

$$\delta\sigma(\theta) \sim \frac{ie^2}{\hbar}\frac{|\Delta|}{\omega}\ln\frac{E_0 - \omega - i\gamma}{\Delta}\cos(2(\theta-\varphi)) \tag{8.39}$$

Again, this exceeds the anisotropy calculated in the two band model [47] by the large factor Eq.(8.35). We note that trigonal warping of the BLG bandstructure arising from higher neighbor hopping can also lead to a reflection anisotropy. However, these effects respect the threefold rotation symmetry of the lattice. In contrast, the anisotropy resulting from formation of a nematic state exhibits a twofold rotation symmetry. The breaking of the exact lattice rotation symmetry can serve as diagnostic of the nematic state.

To conclude, optical experiments can be used to probe broken symmetries in BLG by measuring the conductivity in a contact free manner. The polar Kerr effect, by providing a means for measuring Hall conductivity, can be used to detect the QAH phase. TRS breaking gapped states that do not display a Hall conductance [6] can also be probed using the Kerr effect, although for these states the Kerr angle will be smaller than that for the QAH state by the small parameter d/λ, where $d = 3\mathring{A}$ is the BLG interlayer spacing and λ is the wavelength of the light used in the experiment [29]. Nevertheless, this much weaker Kerr rotation will still be much larger than that measured in [53], and will be within reach of experiments. Meanwhile, the nematic scenario for BLG may be probed by looking for an angle dependence of the reflection amplitude, which provides a direct test of broken rotational symmetry.

8.4 Summary and outlook for bilayer graphene

8.4.1 Theoretical methods

Which broken symmetry state do we expect to be realized in BLG, given realistic interactions? Within the weak coupling framework that has been widely adopted, the method of choice is the weak coupling renormalization group. The weak coupling RG provides an unbiased and controlled way to sum up all diagrams in perturbation theory. High energy states are successively integrated out, and their effect is absorbed into a renormalization of the interaction matrix elements (or couplings), which flow with energy scale. When the RG procedure is applied to BLG, the RG flow leads to strong couplings at low energy scales, indicating a break down of the perturbation theory at low energies. Tracking the susceptibilities to the various ordered states as one flows to strong coupling allows one to identify the leading weak coupling instability - it is the instability with the largest susceptibility.

We note that for a problem which flows to strong coupling (such as BLG), the leading weak coupling instability may not be the same as the state that eventually forms at low energies. This is because the perturbative RG procedure itself breaks down at low energies, and following the perturbative RG flow into the strong coupling region itself represents an unjustifiable approximation. In practice, the leading weak instability represents an unbiased 'best guess' as to the likely strongly ordered state, but the ultimate test of whether this guess is correct is whether the predictions thereby obtained agree with experiment.

Numerous weak coupling RG studies have been performed on BLG. The first studies [4, 7] assumed SU(4) symmetric, purely short range interactions. The work [4] identified that the RG flows to strong coupling, but did not determine the weak coupling instability, rather assuming that the flow to strong coupling represented formation of a gapped state. The work [7] determined that, depending on the bare interactions, the leading weak coupling instability is either the gapless nematic state, or the gapped QAH state, with the QAH state forming only if the bare repulsion between electrons on different layers was stronger than that between electrons in the

same layer. Since the bare repulsion between different layer electrons is expected to be weaker than that between same layer electrons, [7] concluded that the nematic state represented the leading weak coupling instability for BLG. Similar results were obtained in an extensive calculation [9] that considered all possible interactions (not just the SU(4) invariant subset), but assumed all the interactions were short range.

A further layer of complexity is added when the long range nature of the interactions is taken into account. This leads to an enhanced $\ln^2$ divergence in individual Feynman diagrams, with the $\ln^2$ divergences canceling when all diagrams are added together [60]. Some of these cancellations follow from charge conservation, whereas others are decidedly non-trivial, and arise because the diagrams with enhanced ($\ln^2$) divergences also conserve $n_{AK} - n_{BK} - n_{AK'} + n_{BK'}$, where n_{AK} represents the density of electrons on sublattice A with valley K, and the other labels follow similarly [60]. A possible consequence is that even when the $\ln^2$ divergences cancel, there may be a residual ln divergent contribution, which could alter the RG flow and the nature of the weak coupling instability. In the work [8], the RG flow with long range interactions was computed, assuming that no residual ln contributions are produced when the $\ln^2$ divergent diagrams cancel. This assumption has not been justified, as far as we are aware, but if this assumption is made then the calculation also leads to a nematic state as the leading weak coupling instability for BLG.

8.4.2 What about experiments?

The experimental situation in BLG is somewhat muddled. The system of interest is charge neutral BLG, however, it is essential that there be no transverse electric field, because a transverse electric field explicitly breaks inversion symmetry and opens a gap. Thus, it is necessary to be able to independently control density and transverse electric field. This requires double gated samples. Moreover, the strongly ordered states are only observed in suspended samples.

The first experiments with suspended, double gated BLG were [15, 16]. In the experiments [15], a locally incompressible state was observed, with a characteristic energy scale of a few meV. However, all the candidate states are incompressible:

the gapped states are gapped, and the gapless states have a vanishing density of states at low energy. In two probe transport measurements [16], this incompressible state was observed to have a non-zero minimum conductivity, an observation which again could be interpreted either in terms of a gapless nematic state, or a gapped state with protected edge states. However, in compressibility measurements [15], it was also observed that when a weak transverse magnetic field was applied, an incompressible state at zero field was smoothly connected to an incompressible state at filling factor ± 4. Only the QAH state and nematic state are expected to display such behavior, hence the experiments [15, 16] were tentatively interpreted in terms of either a QAH or a nematic state.

Two probe transport measurements can distinguish nematic and QAH states. The nematic state should also give rise to strong incompressibility at weak fields at filling factors $\nu = \pm 12, 20, 28...$, whereas the QAH state should not. No such signatures were observed in experiments, which was argued [5] to suggest a QAH state may be forming. However, the lack of any signature at $\nu = \pm 12, 20...$ could simply have been due to limited experimental resolution. Meanwhile, in experiments from the Manchester group [65], a similar behavior was observed. However, various other features of this experiment, such as the broadening and amplitude of the conductivity minimum as a function of temperature, were argued to be more consistent with a nematic state than a QAH state. Thus, the experiment was argued [65] to indicate formation of a nematic state in BLG.

It should be noted that two probe transport measurements (as performed in [16, 65]) cannot unambiguously identify the ground state of BLG, because they are not directly sensitive to the broken symmetry. A direct identification of the broken symmetry requires either four probe measurements, or optical experiments. However, two probe transport measurements can determine whether the state is conducting or insulating, and the first experiments [16, 65] seemed to indicate that the ground state of BLG is conducting.

More recently, however, there have appeared a new set of experiments [64, 59, 17], which all see insulating behavior in two probe transport measurements, with gaps on

the scale of a few meV. The observed insulating behavior cannot be reconciled with either a gapless nematic state or a QAH state. However, the theoretical calculations appeared to indicate that the nematic state should be the ground state [9, 7, 8], and that if a gapped state does form, it should be a QAH state [5]. What went wrong?

One possibility is that the long range interactions were not properly treated. In [9], an extensive numerical weak coupling RG has been constructed, taking into account all possible interactions, and also the long range nature of Coulomb interactions. An extremely complicated phase diagram in the space of interactions has been obtained where the nematic and antiferromagnetic states are the most likely winners, with the antiferromagnet state resulting for short screening lengths, and a nematic state resulting for long screening lengths. Similar results were later obtained through a similar calculation by [61]. The discrepancy in the experiments is then explained as resulting from a difference in the screening length (which depends on the distance to the gates). However, we believe this is unlikely to be the correct explanation, since the distance to the gates in all the experiments [64, 59, 17] is significantly greater than the correlation length of the ordered state. The correlation length may be straighforwardly estimated as $l_\Delta = 2\pi\hbar(2m\Delta)^{-1/2}$, where $\Delta \approx 4meV$ is the characteristic energy scale for the ordered state, and it seems unlikely that gates which are much farther away than the correlation length could materially alter the physics.

Another possibility, which has not yet been addressed in the literature, is that the electron phonon coupling might be important for understanding the phase structure of BLG. The nature of the coupling between electrons and phonons, especially flexural phonons, is not well understood, and it is not known how the electron phonon coupling might alter the nature of the low energy phase. A theoretical analysis of the electron phonon coupling is thus an important next step for bilayer graphene.

Finally, the most exciting possibility is that the strongly ordered state is not the same as the leading weak coupling instability. This would be the case if the state in [64, 59, 17] was not an antiferromagnet, or if the state in [65, 16] was not a nematic. If this turns out to be the case, then it will imply that the low energy physics of BLG is controlled by a non trivial *strong coupling* fixed point. Experiments on BLG

could then shed light on one of the longest standing and most interesting questions in many body theory - namely how to follow an RG flow to strong coupling, and how to determine what happens when interactions can no longer be treated perturbatively. Answering this question will require development of new theoretical techniques, and experiments on BLG could provide valuable signposts on a road that could lead to dramatic new progress in many body theory.

We now entertain the possibility that some of the commonly made assumptions that underlie the existing literature could actually be incorrect. One possibility, advanced in [62], is that the experiments do not see a strongly correlated broken symmetry state at all, but rather see something that results from a combination of trigonal warping and strain. This can lead to a nematic-like state which does not break any of the symmetries of the strained BLG. This can in principle explain the experiments [16, 65], but whether it is the correct explanation cannot be determined until the symmetry structure of these states is determined. However, this theory cannot explain the experiments [64, 59, 17], and thus cannot be the full story for BLG.

An alternative explanation, advanced in [63], is that the weak coupling approach itself is flawed, and that interactions are really strong, and necessitate a four band treatment. The apparent success of the non-interacting model for BLG at all but the lowest energy scales would appear to argue against this concern, but the possibility of four band physics should be considered. In [63] it was proposed that the experiments [64, 59, 17] are explained by a 'magneto-electric' state that has opposing current loops in the two layers. This state breaks time reversal symmetry and parity, although it preserves the combination of time reversal and parity. Such a state is predicted to have a hard gap at charge neutrality, and is also predicted to display a non-quantized anomalous Hall effect in the presence of a (parity breaking) weak *electric* field. Pending four probe experiments, it is not yet possible to rule this scenario either in or out.

Bibliography

[1] K.S. Novoselov et al, Nature Physics 2, 177 (2006).

[2] H. Min, G. Borghi, M. Polini and A.H. MacDonald, Phys. Rev. B 77, 041407(R) (2008).

[3] R. Nandkishore and L. Levitov. Phys. Rev. Lett. 104, 156803 (2010).

[4] F. Zhang, H. Min, M. Polini, and A. H. MacDonald Phys. Rev. B 81, 041402(R) (2010).

[5] R. Nandkishore and L. Levitov, Phys. Rev. B 82, 115124 (2010)

[6] J. Jung, F. Zhang and A.H.MacDonald, Phys. Rev. B 83, 115408 (2011)

[7] O. Vafek and K. Yang, Phys. Rev. B 81, 041401(R) (2010).

[8] Y. Lemonik, I.L.Aleiner, C.Toke and V.I.Fal'ko, Phys. Rev. B 82, 201408(R) (2010)

[9] O. Vafek, Phys. Rev. B 82, 205106 (2010)

[10] E. McCann and V. Fal'ko, Phys. Rev. Lett. 96, 086805 (2006); E. McCann and V. Fal'ko, AIP Conf Proceedings - April 10, 2007 – Volume 893, pp. 617-618;

[11] F.D.M. Haldane, Phys. Rev. Lett. 61, 2015 (1988).

[12] Pomeranchuk II. 1958. Sov. Phys. JETP 8:36

[13] E. Fradkin, S.A.Kivelson, M.J.Lawler, J.P.Eisenstein and A.P.Mackenzie, Annual Review of Condensed Matter Physics, Vol1: 153-178 (2010)

[14] B. Feldman, J. Martin and A. Yacoby, Nature Physics 5, 889 (2009).

[15] J. Martin, B.E.Feldman, R.T.Weitz, M.T.Allen and A.Yacoby, Phys. Rev. Lett. 105, 256806 (2010)

[16] R.T.Weitz, M.T.Allen, B.E.Feldman, J. Martin and A. Yacoby, Science Vol. 330 no. 6005 pp. 812-816 (2010)

[17] F. Freitag, J. Trbovic and C. Shonenberger, Rev. Lett. 108, 076602 (2012)

[18] J. Alicea and M. Fisher, Phys Rev B 74, 075422 (2006)

[19] Y. Barlas, R. Cote, K. Nomura and A. H. MacDonald, Phys Rev Lett. 101 (2008).

[20] Y. Zhang, T.T.Tang, C. Girit, Z. Hao, M.C.Martin, A. Zetti, M.F.Crommie, Y.R.Shen and F. Wang Nature, 459, 820-823 (2009)

[21] E. McCann, Phys. Rev. B 74, 161403(R) (2006)

[22] J. Nilsson, A.H.Castro Neto, N. Peres and F. Guinea, Phys. Rev. B 73, 214418 (2006).

[23] E. McCann, D. S. L. Abergel, and V. Falko, Solid State Commun. 143, 110 (2007).

[24] A.W.W.Ludwig, M.P.A.Fisher, R.Shankar and G.Grinstein, Phys. Rev. B 50, 7526-7552 (1994)

[25] R.R.Nair, et al, Science, 320, 1308 (2008)

[26] A. Hill, A. Sinner and K. Ziegler, cond-mat: 1005.3211v1 (2010)

[27] R. Jackiw, Phys. Rev. D 27, 2375 (1984).

[28] R.M. White and T.H.Geballe, *Long Range Order in Solids*, Academic Press (1979). p 317, 321.

[29] I. Dzyaloshinskii and V. Papamichail, Phys. Rev. Lett. 75, 3004-3007 (1995)

[30] J. Xia, Y. Maeno, P.T.Beyersdorf, M.M.Fejer and A. Kapitulnik, Phys. Rev. Lett. 97, 167002 (2006)

[31] W.Tse and A.H.MacDonald, Phys. Rev. Lett. 105, 057401 (2010)

[32] W. Tse and A.H.MacDonald, Phys. Rev. B 82, 161104(R) (2010)

[33] L.D.Landau, E.M.Lifshitz and L.P Pitaevskii, *Electrodynamics of Continuous Media*, 2nd Edition, Section 101. Butterworth-Heinemann (2008).

[34] K. Shizuya, Phys. Rev. B 79, 165402 (2009).

[35] E. H. Hwang and S. Das Sarma, Phys. Rev. Lett. **101**, 156802 (2008).

[36] R. Laughlin, Phys. Rev. Lett. 50, 1395-1398 (1983)

[37] E.V.Gorbar, V.P Gusynin, V.A.Miransky, Phys. Rev. B 81, 155451 (2010)

[38] N. M. R. Peres, Rev. Mod. Phys. **82**, 2673 (2010).

[39] Y. Zhang *et al* Nature, **459**, 820 (2009).

[40] K. F. Mak *et al*,Phys. Rev. Lett. **102**, 256405 (2009).

[41] J. Yan *et al*, Phys. Rev. Lett. **101**, 136804 (2008).

[42] S. Berciaud *et al*, Phys. Rev. Lett. **104**, 227401 (2010).

[43] D. S. L. Abergel and T. Chakraborty, Nanotechnology **22**, 015203 (2011).

[44] W.K. Tse and A. H. MacDonald, Phys. Rev. B **80**, 195418 (2009).

[45] L. Yang *et al*, Phys. Rev. Lett. **103**, 186802 (2009).

[46] P. E. Trevisanutto *et al*, Phys. Rev. B. **81**, 121405(R) (2010).

[47] R. Nandkishore and L. Levitov, Phys. Scr. T146, 014011 (2012)

[48] I. J. Pomeranchuk, Sov. Phys. JETP **8**, 361, (1958).

[49] E. Fradkin *et al*, Annu. Rev. Condens. Matter Phys., **1**, 153 (2010).

[50] R. Lang *et al*, Phys. Rev. B **72**, 024430 (2005).

[51] W.K.Tse and A. H. MacDonald, Phys. Rev. Lett. **105**, 057401 (2010).

[52] W.K. Tse and A. H. MacDonald, Phys. Rev. B **82**, 161104(R) (2010)

[53] J. Xia *et al*, Phys. Rev. Lett. **97**, 167002 (2006).

[54] I. Crassee *et al*, Nat. Phys. **7**, 48-51 (2011)

[55] See appendix E

[56] A. Hill, A. Sinner and K. Ziegler, New J. Phys. **13**, 035023 (2011)

[57] E.H.Hwang, B.Y.K. Hu and S.DasSarma, Phys. Rev. B 76, 115434 (2007)

[58] R. Lang *et al*, Phys. Rev. B **72**, 024430 (2005).

[59] W. Bao et al, ArXiv: 1202.3212 (2012)

[60] R. Nandkishore and L. Levitov, Phys. Rev. B 82, 115431 (2010)

[61] Y. Lemonik, I.L.Aleiner, C. Toke and V.I. Falko, Phys. Rev. B 85, 245451 (2012)

[62] Marcin Mucha-Kruczynski, Igor L. Aleiner, Vladimir I. Fal'ko, Physical Review B 84, 041404 (2011)

[63] Lijun Zhu, Vivek Aji, Chandra M. Varma, arXiv:1202.0821 (2012)

[64] J. Velasco et al, Nature Nanotechnology, 7, 156 (2012)

[65] A.S.Mayorov et al, Science 333(6044) pp. 860-863 (2011)

[66] R. Nandkishore and L. Levitov, Phys. Rev. Lett. 107, 097402 (2011)

Chapter 9

Bilayer graphene in the quantum Hall regime: quantum Hall ferromagnetism and topological defects

We discuss the nature of the quantum Hall ferromagnet (QHF) state in BLG. We explain how screening effects cause the QHF gaps to scale as $\sim B$, rather than the $\sqrt{B}$ scaling that is naively expected. We also explain how application of a transverse electric field can be used to trigger phase transitions between different QHF states.

We interpret recent experiments on bilayer graphene (BLG) using the theory of the quantum Hall ferromagnet (QHF) state. We explain several puzzling experimental observations, and interpret the observed high conductance region that is seen at filling factor $\nu = 2$ as a signature of charge $2e$ topological defects known as skyrmions. We propose that BLG could be used to detect deconfined merons (fractionalized skyrmions), a form of topological defect that has not yet been observed experimentally. Finally, we generalize our analysis to chiral n layer graphenes, and show that they host skyrmions with charge ne.

9.1 Phase diagram in external fields

Thus far we have concentrated on BLG in the absence of any external applied fields. In this limit, there is a rich variety of possible interacting states, which may be distinguished experimentally in the manner discussed in the previous chapter. We now present the phase diagram in external electric and magnetic fields. It turns out that the phase diagram in not-too small external fields is simple, and can be straightforwardly written down.

First, we consider applying a transverse electric field to BLG, which imbalances the potentials on the two layers. This breaks the approximate SU(4) symmetry of the Hamiltonian down to $SU(2)_{\text{spin}} \otimes U(1)_{\text{valley}}$. We note that electric field favors polarizing the layers by charge. This corresponds to a gapped state with $Q = 1$. Thus, the mean field Hamiltonian in large transverse electric field has the form Eq.(8.1) with $Q = 1$. We note that this state has the same symmetries as the Hamiltonian (at non-zero electric field). Thus the state that is expected to form at large transverse electric field is not a broken symmetry state - it is the same gapped state that arises through the electric field effect in non-interacting bilayer graphene, with the gap enhanced by exchange.

We note that such a state, which polarises the layers by charge, is not expected to form at zero electric field. We estimate the critical electric field for formation of a trivial insulating state, E_0 by equating eE_0d/κ to Δ, the order parameter in the zero field ordered state. Here κ is the dielectric constant of the substrate. Using the value $\Delta \approx 1.5\text{meV}\kappa^{-2}$ from [5], we obtain an order of magnitude estimate of $E_0 \lesssim 2.6\kappa^{-1}\text{meV/Å}$.

9.1.1 Quantum Hall Ferromagnet state

We now consider BLG in a magnetic field at $E = 0$. The main effect of magnetic field is on the orbital physics, through the replacement $\mathbf{p} \to \mathbf{p} - e\mathbf{A}$ in the Hamiltonian Eq.(7.1). This preserves the SU(4) symmetry, but causes the spectrum to split into Landau levels [14] with an energy spacing of order $\hbar\omega_c$, where $\omega_c = eB/mc$. A

magnetic field also provides a Zeeman energy $2\mu_B B\tilde{\sigma}_3$, which is not $SU(4)$ invariant. However, since $\hbar\omega_c \gg 2\mu_B B$, we begin by neglecting the Zeeman field, and restore it only later on in our analysis.

The ground state in a sufficiently large magnetic field is a quantum Hall ferromagnetic (QHF) state [10], which spontaneously breaks SU(4) symmetry. The QHF state in high magnetic field is smoothly connected to a SU(4) symmetry breaking gapped state at zero field. If the zero field ground state is not a SU(4) symmetry breaking gapped state, then there must be a phase transition to a QHF state at a critical magnetic field B_0. An order of magnitude estimate for the critical magnetic field B_0 may be estimated by equating the energy of the QHF state Eq.(9.4) to Δ, the zero field order parameter. If we take $\Delta \approx 1.5$meV from [5], we obtain $B_0 \approx 0.5T$.

We now review some basic properties of the QHF state, taking full account of screening [10].

9.1.2 Exchange interaction and energetics of QHF state

The zeroth Landau level of BLG is eightfold degenerate, exhibiting an orbital $n = 0, 1$ degeneracy in addition to the spin and valley degeneracies. Exchange energy favors a spontaneous ferromagnetic polarisation of the zeroth Landau level. At $\nu = 0$, the system can choose whether to polarise in the spin, valley or orbital spaces. Spin and valley polarisation are degenerate by SU(4) spin-valley symmetry, but the orbital polarisation has a different energy. It turns out that spin or valley polarisation is preferred energetically to orbital polarisation [10]. Intuitively, this is because electrons with different spin or valley have no mutual exchange interaction, whereas electrons with different orbital index have a partial exchange interaction. Therefore, a greater amount of exchange energy is gained by polarising in the spin-valley space than by polarising in the orbital space.

When evaluating the energy gain from QHF, it is essential to take into account screening arising from inter-Landau level transitions. This is because the characteristic energy scale for interactions within the zeroth Landau level $e^2/\kappa l_B$ greatly exceeds the Landau level spacing $\hbar\omega_c$ for all experimentally relevant magnetic fields, where

we have introduced the magnetic length $l_B = \sqrt{\hbar c/eB}$. We therefore introduce the screened Coulomb interaction $\tilde{V}_+(q)$. We shall show that we only need to evaluate $\tilde{V}_+$ in the long wavelength limit $ql_B \lesssim 1$. The screened interaction in this limit was computed in [15], and was found to take the form

$$\tilde{V}_+(ql_B < 1) = \frac{2\pi e^2/\kappa}{q + Nq^2 l_B^2 a_0^{-1}\lambda} \approx \frac{2\pi\hbar^2}{Nmq^2 l_B^2 \lambda} \tag{9.1}$$

where $\lambda = 0.88$ is a purely numerical pre-factor. The right hand side provides an approximate form of the potential which is valid for the large range of momentum scales $1 > ql_B > Nl_B a_0^{-1}$. Upon inverse Fourier transforming to real space, we note that the potential $\tilde{V}_+(r)$ is *logarithmic*. We interpret this as a magnetic field induced unscreening of the short range screened potential from [8]. This 'unscreening' will be manifested by any state that opens a dipole active gap at the Fermi level.

There exists a simple intuitive argument that allows us to obtain the screened potential Eq.(9.1) without any reference to Landau levels. We take the *dynamical* polarization function from [5], at $B = 0$ and in the absence of any gap, and evaluate it at frequency $\omega = \omega_c$. In the limit $ql_B < 1$, this intuitive argument yields the screened interaction Eq.(9.1), with $\lambda = 1$.

Having obtained the screened potential $\tilde{V}_+$, we may then calculate the QHF exchange energy per electron $J(B)$ in a 'jellium model' [16] as

$$J(B) = \frac{N}{2}\int \frac{d^2p}{(2\pi)^2}\,(g(p) - 1)\,\tilde{V}_+(p). \tag{9.2}$$

Here, $N = 4$ reflects the number of occupied states in the zeroth Landau level, and $g(p)$ is the Fourier transform of the exchange hole $g(r)$ [16], defined as $g(r) = \langle\rho_0(r)\rho_0(0)\rangle/\langle\rho_0(0)\rangle^2$, where ρ_0 is the electron density in the zeroth Landau level, and the average is taken with respect to the many body wavefunction $|\Psi\rangle$ of the system ($\langle A\rangle = \langle\Psi|A|\Psi\rangle$).

It is sufficient to consider a state $|\Psi\rangle$ that is polarised in spin, and to use it to calculate $g(r)$. Valley polarised states have the same exchange hole, by SU(4) symmetry. The exchange hole for a spin polarised state may be calculated by working

in Landau gauge, and remembering that single particle states with different flavor are orthogonal, whereas single particle states with different orbital index or guiding center coordinate are not orthogonal. After some algebra, we obtain

$$g(r) = 1 - \frac{1}{32} e^{-R^2/2} \left(R^2 - 4\right)^2, \quad R = \frac{r}{l_B}. \tag{9.3}$$

We note from Eq.(9.2) and Eq.(9.3) that the exchange energy comes predominantly from wavevectors $ql_B < 1$, as expected, so we only need the screened interaction $\tilde{V}_+$ in the long wavelength limit, Eq.(9.1).

The energy gain due to QHF ordering can be found by substituting the screened interaction, Eq.(9.1), and the exchange hole profile, Eq.(9.3), into Eq.(9.2). We obtain, with logarithmic accuracy,

$$J(B) = -\frac{2\pi}{8} \frac{e^2 a_0 \ln\left(1 + N\frac{l_B}{a_0}\right)}{\kappa\lambda l_b^2} \approx -\frac{\pi\hbar\omega_c}{8\lambda} \ln\frac{B_0}{B}, \tag{9.4}$$

where B_0 is given by the condition $N l_{B_0} a_0^{-1} = 1$. This differs strongly from the $E \sim \sqrt{B}$ prediction from [10]. The difference arises because we have taken account of screening. The same result as (9.4) was obtained in [18], where screening was also taken into account.

Our above analysis of the QHF state can be compared with recent experiments [6], where a resistive state was observed at $\nu = 0$ for $B > 0.1$ T. This resistive state was identified with QHF order. The resistance was observed to increase exponentially with magnetic field, where the exponent scaled linearly with B/k_BT. Both predictions are consistent with our analysis above, if we identify the critical field for the onset of QHF as B_c, and assume that transport in the QHF state is controlled by thermal activation across the gap $J(B)$

9.1.3 Phase transition between QHF state and the layer-polarized gapped state

We can now analyse how the QHF state is affected by electric field. This is conveniently accomplished through the development of a 'sigma-model' framework, where the sigma model field is the SU(4) symmetry breaking order parameter, and SU(4) symmetry breaking perturbations like the external electric field, the 'capacitance energy', and the Zeeman term are treated as perturbation fields.

The ground state manifold in the charge neutral QHF state consists of all possible spin or valley polarised SU(4) symmetry breaking states. States that are polarised in the orbital index have a higher energy, and may be neglected. We therefore suppress the orbital index, and characterise the structure of the QHF state by a 4×4 matrix Q' acting in the spin-valley space. The matrix Q' is defined as $Q' = -1+2P_{oc}$, where P_{oc} projects onto the occupied spin and valley species in the spin-valley polarised zeroth Landau level. We note that in the zeroth Landau level, different valleys are localized on different layers, and so the valley and layer indices are interchangeable. We further define the matrices $M_E = \eta_3 \otimes 1$ and $\mathbf{M}_s = (M_x, M_y, M_z) = (1\otimes\sigma_1, 1\otimes\sigma_2, 1\otimes\sigma_3)$ and we recognise $m_E = \mathrm{Tr}Q'M_E$, and $\mathbf{m_s} = \mathrm{Tr}Q'\mathbf{M}_s$ to be the charge and spin dipole moments respectively. We denote the flux quantum by Φ_0. The free energy per electron is then given by a functional $F = \int d^2r F[Q'(\mathbf{r})]$, where

$$\begin{aligned} F &= J(B_\perp)\mathrm{Tr}|\nabla Q'|^2 + \frac{2\pi e^2 d B_\perp}{\Phi_0 \kappa_- \kappa}(\frac{1}{4}\mathrm{Tr}Q'M_E)^2 \\ &+ \mu_B\Big(\frac{1}{4}\mathrm{Tr}(Q'(\mathbf{B}\cdot\mathbf{M_s}))\Big) + \frac{1}{2}\frac{eEd}{\kappa\kappa_-}(\frac{1}{4}\mathrm{Tr}Q'M_E). \end{aligned} \tag{9.5}$$

Here, $J'(B)$ equals $J(B)$, Eq.(9.4), up to numerical prefactors of order unity. The first term is the gradient energy cost of deformations of the order parameter, the second term is the 'capacitor' energy cost of polarising the layers by charge, the third term is the coupling to the Zeeman field, and the fourth term is the charge dipole coupling to the external electric field. The 'capacitor energy' term is proportional to B because the density of electrons in the zeroth Landau level is proportional to B. We

now note that the Zeeman term is parametrically smaller than the capacitor energy by $m/m_e \ll 1$, where m_e is the free electron mass, and can therefore be neglected. The capacitance term, meanwhile is parametrically smaller than J(B) by d/a_0. The perturbative treatment of SU(4) anisotropies is therefore valid provided the electric field is not too large, so that the perturbation fields are all small compared to the stiffness J(B).

The sigma model Eq.(9.11) has symmetry group $SU(2)_{\text{spin}} \otimes U(1)_{\text{valley}}$, when we neglect the Zeeman coupling, which is the weakest of the SU(4) anisotropies. The QHF state breaks this symmetry for any choice of Q other than $Q = \eta_3 \otimes 1$. In the limit $E \to \infty$ the sigma model Eq.(9.11) predicts $Q = \eta_3 \otimes 1$ - which is a layer polarized gapped state that does not break any symmetries. However, for small electric fields, such a state is disfavoured by the capacitor energy cost of polarising the layers by charge. Thus, the symmetry preserving state is only realised for $E > E_c$, where E_c may be calculated precisely from Eq.(9.11). We write $Q' = \cos\theta M_E + \sin\theta \tilde{Q}$, where $\tilde{Q}$ is a SU(4) symmetry breaking matrix that is orthogonal to M_E, $\text{Tr}(\tilde{Q}M_E) = 0$. We now solve Eq.(9.11) for the critical electric field when $\theta \to 0$. This yields the universal and sample independent answer

$$\frac{E_c}{B_\perp} = 4\alpha; \qquad \frac{eE_c d}{B_\perp} \approx 2.5\text{meV/T}.. \tag{9.6}$$

Here $\alpha = 1/137$ is the fine structure constant, and the first expression is in Gaussian units, whereas the second expression is in SI. We stress that this critical electric field is independent of screening in the substrate, and the same critical electric field applies to suspended samples and to samples on a dielectric substrate.

This critical electric field marks a second order phase transition involving the spontaneous breaking of either spin SU(2) or valley U(1) symmetry. We note that at E_c the electric field energy is less than J(B) by d/a_0, hence the phase transition occurs within the realm of validity of the sigma model. Since for $E > E_c$ the system is already layer polarised by charge, we expect no further phase transitions as we raise E beyond E_c.

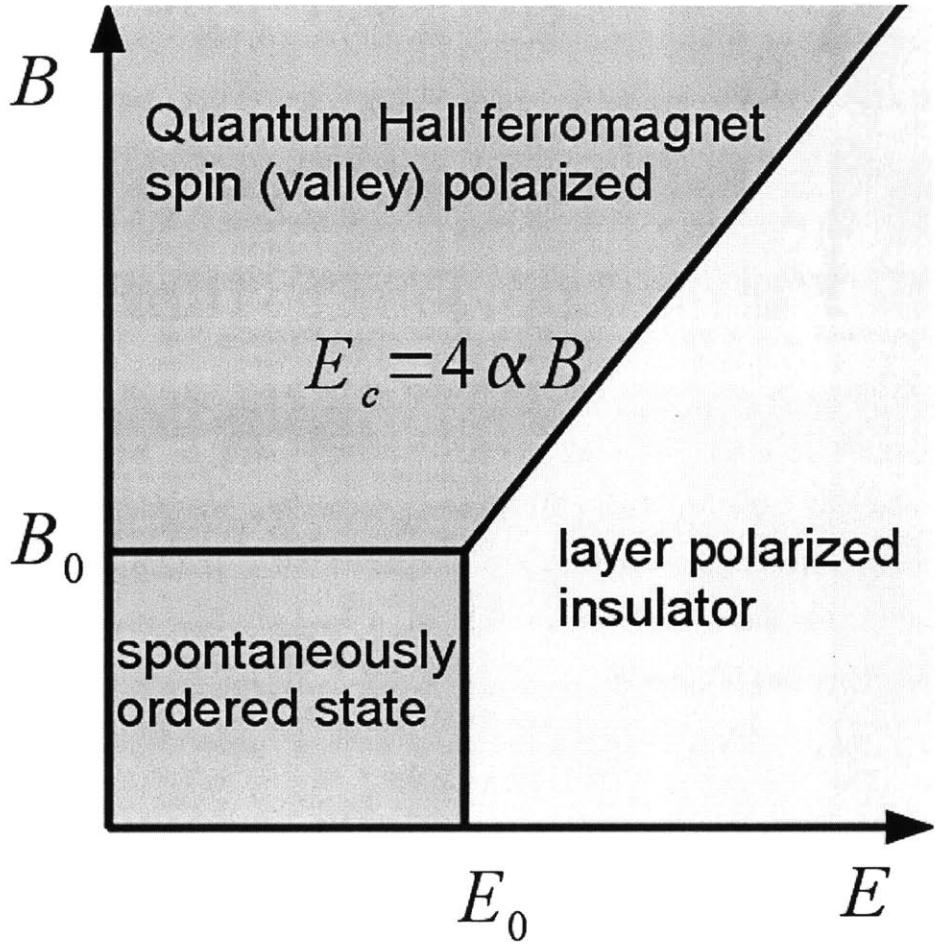

Figure 9-1: Phase diagram for BLG at charge neutrality (schematic). A layer polarized state is obtained at high E and a quantum Hall ferromagnet state at high B. The transition between the two occurs at a critical field $E_c = 4\alpha B$ (Eq.(9.13)). In the zero field limit, there is a rich variety of possible strongly interacting states. How to distinguish which of these states is realised in experiment was the subject of Sec.8.2.

Thus, the phase diagram for BLG in external electric and magnetic fields has the form shown in Fig.9-1. At large electric fields, the system is in a layer polarized gapped state. At large magnetic fields, it is in a QHF state. The transition between the QHF state and the layer polarized gapped state happens at a critical field given by Eq.(9.13). Meanwhile, in the zero field limit there is a rich variety of possible ground states that can arise. Identifying the experimental signatures of the candidate states has been one of the main purposes of this paper.

9.2 Topological defects and their signatures

A recent series of experiments on dual gated bilayer graphene (BLG) [6, 8, 7] unveils a cornucopia of interaction effects in the quantum Hall regime. Compressibility and transport measurements performed on suspended, dual gated BLG reveal an incompressible state at filling factors corresponding to a partially filled zeroth Landau level, an observation which has been explained in terms of an interaction driven ferromagnetic polarisation of the ground state [10]. However, tuning experimental knobs such as the transverse electric field and the parallel magnetic field also reveals a complex pattern of high conductance regimes (Fig.9-2), which require explanation.

We note in particular that the $\nu = \pm 2$ quantum Hall state, unlike the $\nu = 0$ state, displays a high conductance region at zero bias (Fig.9-2), whereas in compressibility measurements [6, 8], the $\nu = 0$ and $\nu = \pm 2$ states are both incompressible. How can the sample be simultaneously conducting and incompressible? Moreover, why does the sample cease to be conducting once we move away from zero bias?

We argue that at the experimental temperature, the $\nu = 2$ region near zero bias is everywhere gapped, but nonetheless contains deconfined topological defects (skyrmions), which carry electric charge. A system with a local gap but mobile skyrmions can be simultaneously incompressible and conducting. An applied voltage bias increases the skyrmion mass, and confines the skyrmions, explaining the suppression of conductivity by applied bias. This interpretation is not without problems. The experimental temperature is much lower than the calculated temperature for

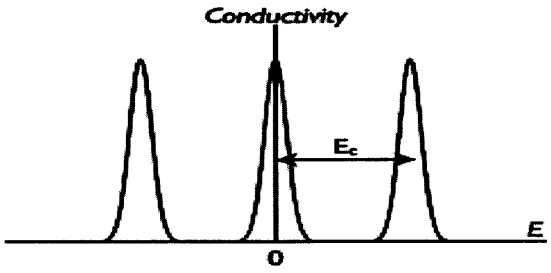

Figure 9-2: Schematic representation of experimental measurements in eightfold degenerate zeroth Landau level of BLG [14]. Blue line corresponds to filling factor $\nu = 0$ whereas red line corresponds to filling factor $\nu = \pm 2$. Full (empty) zeroth LL corresponds to $\nu = 4(\nu = -4)$. We attribute the peak at $\nu = \pm 2$ and $E = 0$ to skyrmions, whereas the peak at $\nu = 0$ and $E = \pm E_c$ is attributed to gap collapse.

skyrmion deconfinement, and a certain amount of fine tuning of parameters is necessary to explain the zero bias peak in terms of skyrmions. Nevertheless, this is the only reasonable explanation we could conceive for the experimental results - and this interpretation can be readily tested by measuring the charge of the current carriers in the zero bias peak, since the skyrmions are predicted to have charge $2e$.

We also consider whether there may be other interesting physics associated with topological defects that may be uncovered in BLG. In particular, we point out that in a particular region of parameter space, the skyrmions should unbind into merons - exotic topological defects with continuously tunable charge which have a long history in the theory literature [1, 2], but have not yet been conclusively observed experimentally. Although there is no signature of merons in the experiments [8, 7], the detection of merons seems a interesting direction for future work on BLG. We conclude by generalizing the theory of topological defects to chiral n layer graphenes, of which BLG is the simplest example.

The physics of BLG in the quantum hall regime is analagous to semiconductor double well systems [3, 4], with the added advantage that the doping level and interlayer bias are independently controllable by gating. We may thus analyze BLG using the theoretical framework developed for semiconductor double wells [1, 2], even though the parameter regime that describes BLG is very different to that relevant for double well systems.

We begin our analysis by projecting on the zeroth Landau level. Wavefunctions in the zeroth Landau level are represented by eight component spinors $\psi_{s,v,n}(\mathbf{r})$, where s and v refer to spin and valley index, and $n = 0, 1$ refers to the orbital index [14]. Different valleys are localised on different layers. The projected Hamiltonian is dominated by exchange interactions between electrons, which are invariant under SU(4) rotations in the spin-valley space, but are not invariant in the orbital space.

At all integer filling factors, exchange interactions trigger an instability to a QHF state [10], whereby the zeroth Landau level spontaneously polarizes and opens a gap at the chemical potential. Polarisation can occur in spin, valley or orbital (n=0,1) space. However, particles of different spin-valley have no mutual exchange interaction, whereas particles with different orbital index have a partial exchange interaction, so spin and valley polarisation is preferable to orbital polarisation. Hence, theory predicts [10] that the ground state at $\nu = 0$ is spin or valley polarised, the ground state at $\nu = \pm 2$ is spin and valley polarised, and orbital polarisation only occurs at $\nu = 1, 3$. For understanding the behavior at $\nu = 0, 2$, it is therefore sufficient to suppress the orbital index, and to study the spontaneous breaking of the SU(4) spin-valley symmetry.

We now introduce the effective low energy theory of the QHF states at $\nu = 0, \pm 2$. We characterise the broken SU(4) spin-valley symmetry by the 4×4 order paramater matrix $Q = 1 - 2P$, where P projects on the occupied spin-valley states. The QHF states at $\nu = 0, \pm 2$ are then described by matrices

$$Q_0(\mathbf{r}) = U^\dagger(\mathbf{r})\Lambda_0 U(\mathbf{r}); \Lambda_0 = \mathrm{diag}(+1, +1, -1, -1) \tag{9.7}$$

$$Q_2(\mathbf{r}) = U^\dagger(\mathbf{r})\Lambda_2 U(\mathbf{r}); \Lambda_2 = \mathrm{diag}(+1, +1, +1, -1) \tag{9.8}$$

where $U(\mathbf{r})$ is an SU(4) rotation matrix, and $Q_{-2} = -Q_2$.

We now discuss topological defects in the QHF state. Formation of the QHF state at $\nu = 0$ (Eq.9.7) reduces the symmetry of the Hamiltonian from SU(4) to $SU(2) \otimes SU(2) \otimes U(1)$[9]. The manifold of the $\nu = 0$ QHF states is thus given by the eight dimensional coset space $SU(4)/(SU(2) \otimes SU(2) \otimes U(1))$. Similarly, formation of a

$\nu = \pm 2$ QHF state (Eq.9.8) lowers the symmetry to $SU(3) \otimes U(1)$, so the the manifold of the $\nu = \pm 2$ states is the six dimensional coset space $SU(4)/(SU(3) \otimes U(1)) = CP_3$. These coset spaces supports topological defects, because

$$\pi_2 \left(\frac{SU(4)}{SU(2) \otimes SU(2) \otimes U(1)} \right) = Z; \quad \pi_2(CP_3) = Z \tag{9.9}$$

Here π_n denotes the n^{th} homotopy group, and we have made use of the identity [19] $\pi_2(G/H) = \pi_1(H)$, for simply connected groups G and H. The CP_3 skyrmions at $\nu = 2$ are standard [20, 22], whereas the SU(4) skyrmions at $\nu = 0$ are more exotic, and have not (to our knowledge) been seen experimentally. The topological defects are charged, because flavor and charge are entangled when one projects on the lowest Landau level (LLL) [2].

Skyrmions are massive excitations, that can form in a system that is everywhere gapped [1]. Thus, the QHF state has no gapless charged excitations, and will be observed to be incompressible in local compressibility measurements. However, the absence of gapless charged excitations at zero temperature does *not* imply that the system must be insulating at finite temperature.

At finite temperature in two dimensions, there is no spontaneous breaking of SU(4) symmetry. Therefore, in the absence of SU(4) anisotropies, there will be proliferation of skyrmions, which are charged and can carry current. Thus, thermal fluctuations at any non-zero temperature will establish a non-zero conductance, even in a locally incompressible state.

The low temperature transport properties are altered significantly even by weak SU(4) anisotropies, such as the Zeeman splitting, the finite layer separation, and the external electric field. We will treat these anisotropies perturbatively. We introduce $\rho_s(B)$, the stiffness of fluctuations in the QHF order parameter. We also introduce the matrices $M_E = \eta_3 \otimes 1$ and $(M_x, M_y, M_z) = (1 \otimes \sigma_1, 1 \otimes \sigma_2, 1 \otimes \sigma_3)$, where η_i and σ_i are Pauli matrices in layer and spin space respectively. The free energy per electron

is then given by a functional $F = \int d^2r F[Q(\mathbf{r})]$, where

$$\begin{aligned} F &= \frac{\rho_s}{8}\mathrm{Tr}|\nabla Q|^2 + \frac{2\pi e^2 d B_\perp}{\Phi_0 \kappa_- \kappa}(\frac{1}{4}\mathrm{Tr}QM_E)^2 \\ &+ \mu_B\Big(\frac{1}{4}\mathrm{Tr}(Q(\mathbf{B}\cdot\mathbf{M_s}))\Big) + \frac{1}{2}\frac{eEd}{\kappa\kappa_-}(\frac{1}{4}\mathrm{Tr}QM_E). \end{aligned} \tag{9.10}$$

Here, Φ_0 is the flux quantum, and we have assumed that the $n = 0, 1$ orbital degrees of freedom are slaved together, and exhibit the same spatial pattern of spin-valley polarisation. We justify this assumption by noting that any misalignment of spin-valley polarisations for the $n = 0, 1$ orbitals carries a large exchange energy cost [22].

The stiffness ρ_s can be extracted from the local compressibility measurements [8]. These measure the cost of introducing charge into the system. Charge can be introduced in the form of charge e electrons, or charge $(4 - \nu)$ skyrmions [1]. At $\nu = 0, \pm 2$, individual electrons are the cheapest way to introduce charge, carrying energy cost $2\Delta = \frac{128\pi}{25}\rho_s$ [22]. From the compressibility experiments, which measure a discontinuity of the chemical potential of magnitude

$$\frac{2\Delta(\nu = 0)}{B_\perp} = 1.7\mathrm{meV/T}, \quad \frac{2\Delta(\nu = 2)}{B_\perp} = 1.2\mathrm{meV/T}. \tag{9.11}$$

we conclude that

$$\rho_s(\nu = 0) = 0.1meV/T; \qquad \rho_s(\nu = 2) = 0.07meV/T \tag{9.12}$$

While compressibility experiments probe electron excitations, low temperature transport experiments should be controlled by skyrmion excitations. This is because the energetic cost of $(4 - \nu)$ electrons is higher than the energetic cost of a single charge $(4-\nu)e$ skyrmion, at $\nu = 0, \pm 2$ [22]. Therefore, provided we are at low enough temperatures for energetic considerations to dominate over entropic ones, electrons should spontaneously bind into skyrmions, which should dominate transport. As we show below, the transport signatures of skyrmions are heavily influenced by the SU(4)

anisotropies in 9.11.

We now discuss the behavior of BLG in the presence of anisotropies, using Eq.9.11. We first consider $\nu = 0$, when there is a competition between spin and valley polarisation. At $E = 0$, the Zeeman field uniquely selects a spin polarised ground state. The $E \neq 0$ case will be discussed later. Long range order survives up to a critical temperature $T_* = 4\pi\rho_s/((N_0 - 1)\ln(\Delta/2\mu_B B))$ [25], where $N_0 = 8$ is the dimension of the $\nu = 0$ target space. This result can be understood by noting that the disordering effect of thermal fluctuations (which is logarithmically divergent in two dimensions) gets cutoff by the Zeeman energy. For $T < T_*$, there is long range order, and the system is insulating, whereas for $T > T_*$, long range order is destroyed, SU(4) skyrmions proliferate, and the system becomes conducting, even though the system may be locally ferromagnetically polarised and incompressible. Substituting in the experimentally extracted value for $\rho_s(\nu = 0)$ (9.12), we obtain a critical temperature of $T_* = 700mK * B_\perp/T$. At the experimental [7] magnetic field of $0.78T$, the critical temperature $T_* = 550mK$ is much greater than the experimental temperature of $60mK$, suggesting that the system should be in the long range ordered, insulating state. This agrees with experimental observation.

At $\nu = \pm 2$, there is no competition between spin and valley polarisation, since the system must polarise in spin *and* valley. At $E = 0$ the ground state is spin polarised along the Zeeman field and valley polarised in the XY plane, spontaneously breaking valley symmetry. The order persists up-to a temperature of order $T'_* = 2\pi\rho_s/((N_2 - 1)\ln(\Delta/\min(2\mu_B B, E_{cap})))$, where E_{cap} is the capacitor energy and $N_2 = 6$ is the dimension of the target space. Taking ρ_s from compressibility measurements (9.12), we obtain the critical temperature $T'_* = 350mK * B_\perp/T$. The critical temperature is lower at $\nu = 2$ than at $\nu = 0$ firstly because the bare stiffness is lower, and secondly because skyrmions at $\nu = 2$ carry only half the charge of skyrmions at $\nu = 0$, and hence have only half the mass.

At the experimental magnetic field of $0.78T$, the critical temperature of $270mK$ is still larger than the experimental temperature of $60mK$. However, the two temperature scales are much closer together than at $\nu = 0$, and it seems plausible that

disorder could suppress T_*' sufficiently to cause skyrmions to proliferate, explaining the high conductance peak at zero bias (Fig.9-2).

Attributing the high conductance peak to skyrmions also allows us to naturally explain why the conductance drops when electric field is applied. The low energy excitations above the $\nu = 2$ incompressible state are CP_3 skyrmions, which evolve smoothly from valley skyrmions in the limit $E \to 0$ to spin skyrmions in the limit $E \to \infty$ [20]. The mass of the CP_3 skyrmions is minimal at the charge balanced point, increasing with E field as $\mathcal{E}_{act} \approx 1.4\Delta(1 + 3E^2/(2\alpha^2 B_\perp^2) + O(E^4))$ [20, 21]. Increasing the skyrmion mass raises the critical temperature required for skyrmions to proliferate, and thus causes the system to revert to an insulating state.

Our proposal that the high conductance peak is due to skyrmions can be readily tested. Firstly, the critical temperature increases rapidly with applied magnetic field, so if our proposal is correct, then the high conductance feature at $\nu = 2$ should get rapidly weaker as the applied magnetic field is increased. Secondly, the CP_3 skyrmions carry charge $2e$, where the factor of 2 reflects the fact that the $n = 0, 1$ orbital states have their valley polarizations locked together by mutual exchange interactions [22]. The charge of the current carriers may be tested using shot noise experiments.

Experiments also observe a high conductance regime at $\nu = 0$ and finite bias E_c (Fig.9-2). However, this feature has been attributed to gap collapse as the system transitions from spin polarisation to layer polarisation [23, 18, 11]. A theoretical calculation starting from Eq.9.11 [11] leads to the universal, sample independent critical bias of

$$\frac{E_c}{B_\perp} = 4\alpha; \qquad \frac{eE_c d}{B_\perp} \approx 2.5\text{meV/T}. \tag{9.13}$$

where $\alpha = 1/137$ is the fine structure constant, $d \approx 3\mathring{A}$ is the interlayer spacing and we are working in Gaussian units. This result is in good agreement with the experimental measurements

$$\frac{eE_c d}{B_\perp} = 1.45\text{meV/T} \tag{9.14}$$

We now turn to other exotic physics connected with topological defects that may

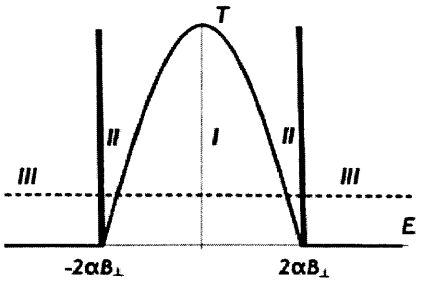

Figure 9-3: Phase diagram at $\nu = 2$, in the limit of strong in plane magnetic field. The spins are frozen out and the system behaves as an easy plane valley ferromagnet in an axial field. The regions I break valley U(1) symmetry. In the regions III the valley polarisation vector is aligned along the z axis. In the regions II, the valley polarisation vector has an in-plane component, which is not ordered. The II regions support de-confined merons. The meron deconfinement transition occurs at $T \approx \pi J(1 - E^2/4\alpha^2 B_\perp^2)$.The dashed line indicates the temperature for the proposed experiment to detect merons.

be accessed using BLG. An interesting behaviour may be realised if we tune the Zeeman splitting (by applying in plane magnetic field) until it is much larger than the capacitor energy and interlayer bias, so the spin degrees of freedom are frozen out. The CP_3 skyrmions then approximate to SU(2) valley skyrmions. In this limit, at intermediate bias and finite temperature (region II of Fig.9-3), the skyrmions unbind into merons - vortex like configurations in the valley XY ordering, where the valley pseudospin rotates out of the plane in the vortex core [1, 17]. Merons have non-quantised charge, and in particular the charge of the low energy merons tends to zero as $|E| \to 2\alpha B$ [26]. The presence of deconfined merons should thus manifest itself not just in a high conductance regime at $\nu = 2$ and finite bias, but also in a sharp increase in the signal to noise ratio as we tune electric field through the meron deconfinement transition, proceeding along the dashed line in Fig.9-3.

Although merons have a long history in the theory literature [1, 2], they have never been observed experimentally. The elusiveness of merons in experiments on quantum double wells was attributed to interlayer tunneling, which confines the merons into skyrmions. However, in chiral graphenes, the states on different layers lie in different valleys, and so interlayer tunneling is largely blocked. For this reason, we believe BLG (and chiral n layer graphene) are promising candidate materials for observation

of deconfined merons.

We now generalize the above results to $n > 2$ layer, ABC stacked multilayer graphene. With this stacking order, each lattice site in the bulk is either directly above or directly below another lattice site. Interlayer hopping causes all the bulk sites to dimerize, opening up a bulk gap of size γ at the charge neutrality point. However, on the top and bottom surfaces, there are undimersized lattice sites, which give rise to gapless surface states. The low energy single particle Hamiltonian for the surface states takes the form [27]

$$H(\mathbf{p}) = \frac{v^n}{\gamma^{n-1}} \begin{pmatrix} 0 & p_+^n \\ p_-^n & 0 \end{pmatrix}; \quad p_\pm = p_x \pm i p_y \tag{9.15}$$

written in a basis such that $(1,0)$ is a Bloch state in the A sublattice of the top layer, and $(0,1)$ is a Bloch state in the B sublattice of the bottom layer. Here v is the Fermi velocity for single layer graphene.

A perpendicular magnetic field may be introduced into the above Hamiltonian by minimal substitution $\mathbf{p} \to \hat{\pi} = \mathbf{p} - e\mathbf{A}$, where $\mathbf{A}$ is the vector potential. Choosing to work in Landau gauge $\mathbf{A} = (0, eB_\perp x)$, we recognize that $\hat{\pi}_+ = \frac{\sqrt{2}}{l_B} a^\dagger$, where $a^\dagger$ is the Harmonic oscillator raising operator and $l_B = \sqrt{\hbar c/eB_\perp}$ is the magnetic length. The spectrum may then be obtained by squaring the Hamiltonian, and takes the form of an infinite tower of Landau levels indexed by an integer m, with energy

$$E_m = \mathrm{sign}(m) \frac{2v^n}{l_B^n \gamma^{n-1}} \sqrt{\prod_{l=0}^{n-1} (|m| - l)}. \tag{9.16}$$

The zeroth Landau level has an n-fold orbital degeneracy supplementing the spin and valley degeneracies.

In the QHF regime, the spin and valley degeneracies will be lifted before the orbital degeneracy, for the same reason as for bilayer graphene [11, 10]. At filling factors $\nu = 0, \pm n$, the effective theory for the n layer chiral graphene ferromagnet will be Eq.9.11, with the interlayer capacitance and external bias terms multiplied

by a factor of $n-1$. This is because the K and K' valleys are localized on the top and bottom surfaces respectively, and the separation between the two surfaces is $(n-1)d$. The topological defects will have the same spin and valley structure, except they will now be n fold degenerate in the orbital index, and will thus carry charge ne and will have statistical angle $n\pi$. Thus, chiral n layer graphene allows us to realize topological defects with arbitrary integer charge and statistical angle. The charge ne may be readily measured by doing shot noise experiments at a temperature that is sufficiently high for the skyrmions to be deconfined.

Thus, we have performed a detailed analysis of the experiments [7, 8] within the framework of the theory of quantum Hall bilayers. Our analysis illuminates the interaction driven origins of various features observed in experiments. We explain the observed high conductance peak at zero bias in the $\nu = 2$ incompressible quantum Hall state as a signature of skyrmions, which carry charge $2e$. We propose that BLG may allow detection of merons, a type of topological defect which has not yet been observed experimentally. We generalized the BLG results to chiral n layer graphenes, where the skyrmions have charge ne.

We thank B. Feldman, J. Martin, T. Weitz and A. Yacoby for sharing unpublished experimental data with us, and we acknowledge useful conversations with A. Young, P. Kim and K. Yang.

Bibliography

[1] S.M.Girvin and A.H.MacDonald, in S.DasSarma and A.Pinczuk (Eds), *Perspectives in Quantum Hall Effects*, Wiley (1997).

[2] K. Moon, H. Mori, Kun Yang, S.M.girvin, A.H.Mac-Donald, L. Zheng, D. Yoshioka and S.C.Zhang, Phys.Rev.B 51, 5138 (1995)

[3] J.P Eisenstein, in S.DasSarma and A.Pinczuk (Eds), *Perspectives in Quantum Hall Effects*, Wiley (1997).

[4] A. Sawada et al, Phys. Rev. Lett. 80, 45344537 (1998)

[5] R. Nandkishore and L. Levitov. Phys. Rev. Lett. 104, 156803 (2010)

[6] B. Feldman, J. Martin and A. Yacoby, Nature Physics 5, 889 - 893 (2009)

[7] R.T. Weitz, M.T.Allen, B.E.Feldman, J. Martin and A. Yacoby, Science Vol. 330 no. 6005 pp. 812-816 (2010)

[8] J. Martin, B.E.Feldman, R.T.Weitz, M.T.Allen and A. Yacoby, Phys. Rev. Lett. 105, 256806 (2010)

[9] K. Yang, S. Das Sarma, and A. H. MacDonald, Phys. Rev. B 74, 075423 (2006).

[10] Y. Barlas, R. Cote, K. Nomura and A.H.MacDonald, Phys Rev Lett. 101 (2008)

[11] R. Nandkishore and L. Levitov, Phys. Scr. T 146, 014011 (2012).

[12] K.S. Novoselov et al, Nature Physics 2, 177-180 (2006)

[13] E. McCann, D. S. L. Abergel, and V. I. Falko, Solid State Commun. 143, 110 (2007)

[14] E. McCann and V. Fal'ko, AIP Conf Proceedings - April 10, 2007 – Volume 893, pp. 617-618; Phys. Rev. Lett. 96, 086805 (2006).

[15] K. Shizuya, Phys. Rev. B 79, 165402 (2009).

[16] R. Laughlin, Phys. Rev. Lett. 50, 1395-1398 (1983)

[17] K. Yang, Phys Rev B 60, 15578-15581 (1999)

[18] E.V.Gorbar, V.P.Gusynin, V.A.Miransky, Phys. Rev. B 81, 155451 (2010)

[19] N.D.Mermin, Rev. Mod. Phys. 51, 591 (1979)

[20] Ezawa, Phys. Rev. Lett. 82, 3512?3515 (1999)

[21] S. Ghosh and R. Rajaraman, Phys. Rev. B 63, 035304 (2000)

[22] D.A. Abanin, S. A.Parameswaran and S.L. Sondhi, Phys. Rev. Lett. 103, 076802 (2009).

[23] C. Toke and V. Falko, Phys. Rev. B 83, 115455 (2011)

[24] R. Cote, J. Lambert, Y. Barlas and A.H.MacDonald, Phys. Rev. B82, 035445 (2010)

[25] S.B.Khokhalachev, Zh. Eksp. Teor. Fiz. 71, 812, (1976)

[26] E. Demler, E.H.Kim and S. Das Sarma, Phys. Rev. B 61, R10567-R10570 (2000)

[27] F. Zhang, B. Sahu, H. Min and A.H.MacDonald, Phys. Rev. B, 82, 035409 (2010)

Chapter 10

Summary and outlook

This thesis has focused on many body physics in graphene. We have studied three distinct graphene based systems where there are significant departures from single particle behavior: doped single layer graphene, bilayer graphene, and graphene in the quantum Hall regime. We now review the essential results and the outlook for these systems.

10.1 Single layer graphene doped to the Van Hove point

We showed that when graphene is doped to a Van Hove singularity in the density of states (which occurs at a doping level of either 3 or 5 electrons for every four carbon atoms), there is a strong likelihood of realizing non-trivial correlated states. The most likely correlated state is a d-wave superconductor, which forms even though the bare interactions are repulsive. Moreover, the superconducting state is chiral, and provides a realization of chiral, topological superconductivity. Meanwhile, the only competing instability is a spin density wave, which also has unusual features, such as having gapless charged excitations in one spin branch only.

Further development of this subfield largely depends on experiments. In order to see the non-trivial many body physics described in this thesis, it is necessary to dope

graphene without introducing enormous amounts of disorder, since disorder destroys both d-wave superconductivity and spin density waves. One promising experimental technique for doping graphene without introducing enormous disorder is ionic liquid gating. Experimental efforts to dope graphene to the Van Hove point using ionic liquid gating are currently underway and may soon be able to test the predictions made in this thesis.

10.2 Bilayer graphene

We also showed that the quadratic band crossing in bilayer graphene is unstable to arbitrarily weak interactions. There are a large number of possible phases which can arise, both gapped and gapless, and we classified these phases, as well as indicating the key experimental signatures.

The principal outstanding experimental problem is to directly probe the nature of the broken symmetry in the strongly ordered states. This requires either four probe transport measurements, or else use of optical techniques. Optical signatures such as Kerr rotation (broken time reversal) and anisotropy in reflection (broken rotation symmetry) in particular provide a direct test of the nature of the broken symmetry state.

There are several major outstanding theoretical challenge. One challenge, for the ab initio community, is to determine the 'microscopic' coupling constants that should be input into the RG procedure. This would allow to identify a specific phase as the leading weak coupling instability, rather than just constructing phase diagrams in the space of unknown couplings. The second challenge is to understand the nature of the electron phonon coupling, and to determine how it affects the phase structure - a challenge which has thus far been ignored. The final challenge for the many body theory community is to develop techniques that are capable of following the RG flow into the strong coupling regime, to determine the nature of the strongly ordered phase (which may not be the same as the weak coupling instability). A rigorous treatment of the dynamically screened long range interactions also needs to be done, taking

into account the possibility that cencelling $\ln^2$ divergences may lead to residual ln divergences, which could alter the RG flow.

10.3 Graphene in the quantum Hall regime

A third set of exotic many body phenomena arise when a magnetic field is applied to graphene. Quantum Hall phenomena were not the central focus of this thesis, but in Chapter 9 we did present some calculations regarding the quantum Hall ferromagnet state in graphene, and the unusual topological defects that may be found in this state.

There are a number of promising future directions for graphene in the quantum Hall regime. One potential direction for experiments is to look for the unusual topological defects that arise in the quantum Hall ferromagnet state. Another interesting direction, for both theory and experiments, is to study fractional quantum Hall physics in single and bilayer graphene. Abelian fractional quantum Hall states have been observed in experiment, but non-Abelian quantum Hall states have not yet been observed in graphene. Whether there are any unusual non-Abelian quantum Hall states that can arise in graphene is a worthwhile topic for future investigation.

10.4 Future Directions

There are a number of additional promising future directions for research in many body physics in graphene. One promising line of research involves chiral multilayers (i.e. graphene layers stacked in an ABC arrangement, where each successive layer is rotated by $2\pi/3$ with respect to the previous one). Chiral multilayers have a divergent density of states even at charge neutrality, and may well also realize exotic strongly correlated states. Another interesting line of research may involve studying dynamical many body effects, instead of just ground state properties. Time will tell what surprises graphene still has in store for us, but it seems likely that there will be many.

Appendix A

Supplementary material for 'Chiral superconductivity from repulsive interactions in doped graphene'

A.0.1 Calculating Tc

We start by noting the tight binding dispersion

$$E = \pm t\sqrt{1 + 4\cos(\pi k_x a)(\cos(\pi k_x a) + \cos(\sqrt{3}\pi k_y a))} \tag{A.1}$$

where $t = 3eV$ is the nearest neighbor hopping for graphene and $a \approx 1\mathring{A}$ is the lattice constant. This defines a bandwidth $W \approx 9ev$. The linearization of the dispersion about the M point is valid for $\pi ka \ll 1$, which corresponds to an energy window of width $\Lambda_0 \approx t$. In this energy window, the density of states takes the form

$$\nu(E) \approx \nu_0 \ln \Lambda_0/E \tag{A.2}$$

with $\nu_0 \sim 1/(2\pi t)$.

The RG is performed starting from some UV scale Λ. Since the RG is performed with the linearized dispersion, it is essential that $\Lambda \leq \Lambda_0$. The natural choice would be to take $\Lambda = \Lambda_0 = t$. For technical reasons, however, it will prove convenient to

take Λ to be close to but slightly smaller than Λ_0. For the present, we simply treat Λ as a free parameter.

Now, we start with the Coulomb interaction $V(q) = 2\pi e^2/(qa^2)$ (we keep track of the lattice scale, so that the Coulomb interaction in momentum space continues to have dimensions of energy). Let us integrate out all states between the bandwidth W and the UV cutoff Λ. We will take into account the effect of these states in the RPA. The RPA can be formally justified by appealing to the large number of fermion flavors present in the problem, N=6 (3 patches and 2 spins). The effect of the high energy states in the RPA is to screen the Coulomb interaction

$$V(q,\omega) = \frac{\frac{2\pi e^2}{qa^2}}{1 + \frac{2\pi e^2}{qa^2} N \Pi_\Lambda(q,\omega)} \tag{A.3}$$

where $N = 6$ is the number of fermion flavors participating in screening and Π_Λ is the single species polarisation function obtained by integrating out states with energies greater than Λ. The interactions g_1 and g_4 do not alter the patch label of electrons - treat these as having momentum transfer $q = q_\Lambda \approx 1/(\pi a)$, where $tq_\Lambda^2 a^2 \approx \Lambda$. Meanwhile, the interactions g_2 and g_3 transfer momentum $Q = 1/a$, equal to the nesting vector connecting in-equivalent patches. Neglecting any frequency dependence of the interaction,

$$g_1(0) \approx g_4(0) \approx V(q_\Lambda, 0); \tag{A.4}$$

$$g_2(0) \approx g_3(0) \approx V(Q,0) \tag{A.5}$$

Now, Π_Λ should be like the polarisation function for an insulator with bandgap Λ. In particular, for large momentum transfer $q \geq q_\Lambda$, there should be metallic type screening, with $\Pi_\Lambda(q \geq q_\Lambda) \approx \nu(\Lambda) = \nu_0 \ln(\Lambda_0/\Lambda)$. Thus, we get

$$g_1\nu_0 = g_4\nu_0 = \frac{\pi e^2/(at)}{1 + N\pi \ln(\Lambda_0/\Lambda) e^2/(at)} \tag{A.6}$$

$$g_1\nu_0 = g_4\nu_0 = \frac{e^2/(at)}{1 + N \ln(\Lambda_0/\Lambda) e^2/(at)} \tag{A.7}$$

where we have taken $\nu_0 = 1/2\pi t$. Now $e^2/(at) \approx 5$ for $a = 1\mathring{A}$ and $t = 3eV$, so we are close to unitarity. In this limit, we have

$$g_1\nu_0 \approx g_2\nu_0 \approx g_3\nu_0 \approx g_4\nu_0 \approx g_0\nu_0 = \frac{1}{N\ln(\Lambda_0/\Lambda)} \tag{A.8}$$

Let us take $\ln \Lambda_0/\Lambda = 1$, i.e. $\Lambda = 1eV$. There is admittedly an arbitrariness in this choice. However, this arbitrariness reflects itself only in an O(1) uncertainty in the prefactor for our eventual expression for T_c. Calculation of this prefactor is beyond the scope of RG, which can only calculate the exponent in the expression for T_c (logarithmic accuracy). Thus, with logarithmic accuracy, we have $g_i = g_0 = 1/6$. We take these to be the bare couplings at the UV scale $\Lambda = 1eV$, and henceforth do RG. Substituting into the results obtained by integrating the $\ln^2$ RG equations, we obtain the result

$$T_c = \Lambda \exp(-1.5/\sqrt{g_0\nu_0}) \approx 200K \tag{A.9}$$

(up to pre-factors of order unity). If true, this would be a remarkable result, exceeding the critical temperature of all other known superconductors. However, we have made some strong approximations in obtaining this result. For example, we have completely neglected single log terms in the RG equations. While such single log terms are formally subleading in the limit of weak coupling, they may well affect T_c. Moreover, since T_c is exponentially sensitive to g_0, our approximate calculation of g_0 carries an exponentially large uncertainty in the value of T_c.

A.0.2 The fixed point trajectory

Here, we address the question of how large is the basin of attraction for the fixed point investigated in the main text. We show that the basin of attraction for the fixed trajectory includes the entire parameter space of weak repulsive interactions. We recall the RG equations

$$\frac{dg_1}{dy} = 2d_1 g_1(g_2 - g_1), \qquad \frac{dg_2}{dy} = d_1(g_2^2 + g_3^2),$$

$$\frac{dg_3}{dy} = -(n-2)g_3^2 - 2g_3g_4 + 2d_1g_3(2g_2 - g_1), \qquad \frac{dg_4}{dy} = -(n-1)g_3^2 - g_4^2 \tag{A.10}$$

We note that the equations (A.10) are homogenous, and the β function for g_2 is positive definite. If we assume that the initial g_2 interaction is positive (repulsive), then g_2 is monotonically increasing under RG, and can be treated as a proxy for the RG time, following [1]. Making the substitutions $g_1 = x_1g_2$, $g_3 = x_3g_2$ and $g_4 = x_4g_2$, we can rewrite (A.10) for $n = 3$ as

$$\begin{aligned} \frac{dx_1}{d\ln g_2} &= -x_1 + \frac{2x_1(1-x_1)}{1+x_3^2}, \quad \frac{dx_3}{d\ln g_2} = -x_3 + \frac{2d_1x_3(2-x_1) - x_3^2 - 2x_3x_4}{d_1(1+x_3^2)}, \\ \frac{dx_4}{d\ln g_2} &= -x_4 - \frac{2x_3^2 + x_4^2}{d_1(1+x_3^2)} \end{aligned} \tag{A.11}$$

The fixed points of (A.11) (e.g., solutions with constant x_1, x_3, and x_4) correspond to fixed trajectories of the RG flow. When solving (A.11) with $dx_i/d\ln g_2 = 0$, d_1 should be interpreted as $d_1(y_c)$, and we should restrict ourselves to solutions with real values of x_1, x_3 and x_4, with $x_1 > 0$ and $x_3 > 0$. The latter constraint follows because the β functions for g_1 and g_3 (A.10) vanish when the respective couplings go to zero, and so g_1 and g_3 cannot become negative if they start out positive.

The set of non-linear algebraic equations for x_i reduces to 7th order equation on. say, x_1, hence in general there are 7 different fixed trajectory. However, three of them correspond to negative values of either x_1 or x_3, and three fixed trajectories are unstable, as we verified by solving the set (A.11) near the fixed trajectory. This leaves the fixed trajectory discussed in the main text as the only stable fixed point of (A.11) that is compatible with the above constraints. Thus, any choice of weak repulsive interactions leads to the same fixed trajectory.

The solutions for x_i along the fixed trajectory can be obtained analytically if we assume that the bare value of the exchange coupling g_1 is zero, in which case $g_1 = 0$ holds during RG flow, and $x_1 = 0$. The set of two algebraic equations for x_3 and x_4 at the fixed point then reduces to 4th order polynomial algebraic equation, which can be solved exactly. Out of 4 soltions, two correspond to imaginary x_3 and one to a

negative g_3. This leaves only one fixed trajectory, consistent with intial conditions.

A.0.3 Ordering in $O(\ln)$ divergent channels

Here we consider the possibility of ordering in an $O(\ln)$ divergent channel, and show that it cannot compete with superconductivity. First, we recall the scaling form of the superconducting susceptibility,

$$\frac{\tilde{\Delta}_{a,b}(y)}{\tilde{\Delta}_{a,b}(0)} = \chi_{SCd}(y) \sim (y_c - y)^{2(G_4 - G_3)} \sim \left(\frac{-g_0}{g_4(y)}\right)^{2(G_4-G_3)}, \tag{A.12}$$

We wish to contrast this with the susceptibility in an $O(\ln)$ divergent channel. We therefore introduce a vertex corresponding to particle-hole pairing on the same patch, and examine how it renormalizes under RG. We find a scaling solution for the susceptibility, generic for any ordering in a $O(\ln)$ divergent channel, which takes the form

$$\chi \sim (y_c - y)^{\alpha/\sqrt{y_c}} \sim (g_0/g_4(y))^{\alpha\sqrt{g_0}}, \tag{A.13}$$

where α is some linear combination of the G_i with $O(1)$ coefficients. Naively, such susceptibilities will also diverge as $y \to y_c$ if $\alpha < 0$, although the exponent will be parametrically smaller than (A.12) by $\sqrt{g_0}$. However, we argue that not only is the exponent for these divergences parametrically small, but in fact such divergences lie outside the range of justifiable applicability of the RG. To understand why, it is essential to remember that the one loop RG only applies upto an energy scale y_1 when the couplings become of order one. (The limiting scale y_1 may actually be even smaller once we take into account self energy $\Sigma(\omega, k_F) \propto g^2\omega \log^2 \Lambda/|\omega|$ (Ref.[2])).

At the scale y_1, (A.13) gives $\chi(y_1) = \exp(\alpha\sqrt{g_0}\ln g_0)$.In the weak coupling limit, $g_0 \to 0$ and $\chi(y_1) \approx 1$. Therefore, the susceptibility in a $\ln^1$ divergent channel is not significantly enhanced within the region of applicability of the one loop RG. In contrast, for $\ln^2$ divergent channels like SCd, (A.12) gives $\chi_{SCd}(y_1) \sim g_0^{\alpha_{SCd}}$, which goes to infinity as $g_0 \to 0$. Therefore, only susceptibilities in $\ln^2$ divergent channels are strongly enhanced in the regime of justifiable applicability of weak coupling RG.

A.0.4 Hubbard-Stratanovich treatment of superconductivity

Here, we provide details of the Hubbard Stratanovich treatment used to investigate the superconducting phase at temperatures lower than T_c. We begin by writing the partition function in the path integral formalism as $Z = \int D[\bar{\psi}, \psi] \exp(-\int \mathcal{L}[\bar{\psi}, \psi])$, where

$$\mathcal{L} = \sum_{\alpha} \psi_{\alpha}^{\dagger}(\partial_{\tau} - \varepsilon_{\mathbf{k}} + \mu)\psi_{\alpha} - \frac{1}{2}\left[\begin{array}{ccc} \psi_1^{\dagger}\psi_1^{\dagger} & \psi_2^{\dagger}\psi_2^{\dagger} & \psi_3^{\dagger}\psi_3^{\dagger} \end{array}\right] \left[\begin{array}{ccc} g_4 & g_3 & g_3 \\ g_3 & g_4 & g_3 \\ g_3 & g_3 & g_4 \end{array}\right] \left[\begin{array}{c} \psi_1\psi_1 \\ \psi_2\psi_2 \\ \psi_3\psi_3 \end{array}\right] \tag{A.14}$$

Here α is a patch index and the momentum, frequency and spin indices have been suppressed for clarity. We have included only the 'pair hopping' interactions g_3 and g_4 since these are the only interactions that contribute to d-wave superconductivity.

We demonstrated earlier that under the 3-patch RG, g_3 and g_4 flow such that

$$g_3 - g_4 = \lambda > 0. \tag{A.15}$$

When this is the case, then the interaction matrix in Eq.A.14 has two eigenvectors with degenerate negative eigenvalues. These reflect the two possible d-wave superconducting phases, which have identical instability threshold. We introduce two 3×3 matrices in patch space, d_1 and d_2, where

$$d_a = \frac{1}{\sqrt{2}}\mathrm{diag}(0, 1, -1); \quad d_b = \sqrt{\frac{2}{3}}\mathrm{diag}(1, -\frac{1}{2}, -\frac{1}{2}) \tag{A.16}$$

These matrices obey $\mathrm{Tr}(d_a^2) = 1$, $\mathrm{Tr}(d_b^2) = 1$ and $\mathrm{Tr}(d_a d_b) = 0$, where the trace goes over the patch space. Using these matrices, we can define the order parameters of the two d-wave instabilities as $\Delta_a = 2\lambda\langle\psi d_a \psi\rangle$ and $\Delta_b = 2\lambda\langle\psi d_b \psi\rangle$. We can now decouple the quartic interaction in Eq.A.14 using a Hubbard Stratonovich transformation, and can hence rewrite the partition function as $Z = \int D[\bar{\psi}, \psi, \Delta_{a,b}, \Delta_{a,b}^*] \exp(-\int \mathcal{L}'[\bar{\psi}, \psi, \Delta_1, \Delta_1^*, \Delta_2, \Delta_2^*]$

where

$$\mathcal{L}' = \begin{bmatrix} \bar{\psi}_\alpha & \psi_\beta \end{bmatrix} \begin{bmatrix} G_+^{-1} & \Delta_a d_a + \Delta_b d_b \\ \Delta_a^* d_a + \Delta_b^* d_b & G_-^{-1} \end{bmatrix} \begin{bmatrix} \psi_\alpha \\ \bar{\psi}_\beta \end{bmatrix} + \frac{|\Delta_a|^2 + |\Delta_b|^2}{4\lambda} \quad \text{(A.17)}$$

We have written the action in a Nambu spinor form, and we have introduced the particle and hole Green functions G_+ and G_- These Green functions are diagonal in Fourier space, and have the form $G_\pm^{-1}(\omega, \mathbf{k}) = i\omega \mp (\varepsilon_\mathbf{k} - \mu)$ where ω is a Matsubara frequency, $\varepsilon_\mathbf{k}$ is the energy of a state with momentum $\mathbf{k}$ and μ is the chemical potential. We now integrate out the fermions in Eq.A.17 to obtain an exact action in terms of the order parameter fields alone. This action $\mathcal{L}''(\Delta_a, \Delta_a^*, \Delta_b, \Delta_b^*)$ takes the form

$$\mathcal{L}'' = \mathrm{Tr}\ln \begin{pmatrix} G_+^{-1} & \Delta_a d_a + \Delta_b d_b \\ \Delta_a^* d_a + \Delta_b^* d_b & G_-^{-1} \end{pmatrix} + \frac{|\Delta_a|^2 + |\Delta_b|^2}{4\lambda} \quad \text{(A.18)}$$

The trace goes over patch space and over the Nambu spinor space. We expand this action in small $\Delta_{a,b}$ to order Δ^4, exploiting the fact that the Green functions commute with the order parameter matrices, and the trace over patch space vanishes for any expression with an odd number of d_a or d_b matrices. We make use of the identities $\mathrm{Tr}(d_a^2) = \mathrm{Tr}(d_b^2) = 1$, $\mathrm{Tr}(d_a^4) = \mathrm{Tr}(d_b^4) = 1/2$, $\mathrm{Tr}(d_a^2 d_b^2) = \mathrm{Tr}(d_a d_b d_a d_b) = 1/6$, transform from partition function to free energy and obtain, up to an overall factor,

$$F = (|\Delta_a|^2 + |\Delta_b|^2)\left(\frac{1}{4\lambda} + \mathrm{Tr}(G_+ G_-)\right) + K\left(|\Delta_a|^4 + |\Delta_b|^4 + \frac{4}{3}|\Delta_a|^2|\Delta_b|^2 + \frac{\bar{\Delta}_a^2\Delta_b^2 + \bar{\Delta}_b^2\Delta_a^2}{3}\right), \quad \text{(A.19)}$$

where $K = \mathrm{Tr}(G_+ G_- G_+ G_-) > 0$.

Superconductivity sets in when the coefficient of the quadratic terms first becomes negative, which leads to

$$T_c \sim \Lambda' \exp(-1/\sqrt{\lambda}). \quad \text{(A.20)}$$

The nature of the superconducting phase below T_c is controlled by the anisotropic quartic term. Since $K > 0$, minimization of the quartic term leads to $|\Delta_a| = |\Delta_b|$

and $\mathrm{Arg}(\Delta_a/\Delta_b) = \pi/2$. The full superconducting order parameter is thus

$$\Delta_a \pm i\Delta_b = \Delta\Big(\sqrt{\frac{2}{3}}, \pm\frac{i}{\sqrt{2}} - \frac{1}{\sqrt{6}}, \mp\frac{i}{\sqrt{2}} - \frac{1}{\sqrt{6}}\Big). \tag{A.21}$$

Bibliography

[1] Vafek, O. and Yang, K. Many-body instability of Coulomb interacting bilayer graphene. *Phys. Rev. B* **81**, 041401(R) (2010)

[2] see e.g., Katanin, A.A., Kampf, A.P. and Irkhin, V.Y. Anomalous self-energy and Fermi surface quasisplitting in the vicinity of a ferromagnetic instability. *Phys. Rev. B* **71**, 085105 (2005) and references therein.

Appendix B

Attraction in d-wave channel from perturbation theory for doped graphene

We recently demonstrated using a renormalization group (RG) method that graphene doped to the M point of the Brillouin zone displays an instability to chiral d-wave superconductivity, even when the bare interactions between electrons are repulsive. An attraction in the d-wave channel is generated spontaneously by the RG. In this Letter, we point out that the source of the attraction can be understood already within second order perturbation theory, without invoking the full machinery of the RG. We hope this will assist readers in developing an intuition for our results.

Non-interacting problem Let us first ignore interactions and focus on the tight-binding dispersion for the honeycomb lattice. This takes the form

$$E = \pm t\sqrt{1 + 4\cos(\pi k_x a)(\cos(\pi k_x a) + \cos(\sqrt{3}\pi k_y a))} \tag{B.1}$$

where $t = 3eV$ is the nearest neighbor hopping for graphene and $a \approx 1\mathring{A}$ is the lattice constant. This defines a bandwidth $W \approx 9ev$. Near the energy $E \approx \pm t$, the fermi surface (FS) takes the form of a perfect hexagon, displaying perfect nesting when third and higher neighbor hoppings are neglected. Moreover, the corners of the hexagonal

FS are saddle points of the dispersion. The tight binding dispersion, expanded about the saddle point $M1$, takes the form

$$\varepsilon(\mathbf{k}) = \frac{3t(\pi a)^2}{2}(q_x^2 - \sqrt{3}q_x q_y) + O((\pi q a)^4) \tag{B.2}$$

where ε is the energy relative to the saddle point, and $\mathbf{q}$ is the momentum relative to the saddle point. The expansion is valid for $\pi ka \ll 1$, which corresponds to an energy window of width $\Lambda_0 \approx t$. A similar expansion is obtained about the other two inequivalent saddle points. The existence of saddle points is a topological property associated with a change from a two-piece to a one-piece Fermi surface, and thus is robust against all small perturbations. It leads to a logarithmic divergence in the density of states, such that the density of states for energies $\varepsilon < \Lambda_0$ takes the form

$$\nu(E) \approx \nu_0 \ln \Lambda_0/E \tag{B.3}$$

with $\nu_0 \sim 1/(2\pi t)$.

Interactions: We introduce Coulomb interactions into the Hamiltonian, which may be written (in second quantized notation) as

$$H = \sum_{\mathbf{k},\sigma} E_{\mathbf{k}} c^\dagger_{\mathbf{k},\sigma} c_{\mathbf{k},\sigma} + \sum_{\mathbf{k_1},\mathbf{k_2},\mathbf{k_3},\mathbf{k_4}\sigma,\sigma'} \frac{2\pi e^2}{|\mathbf{k_1} - \mathbf{k_4}|} c^\dagger_{\mathbf{k_1},\sigma} c^\dagger_{\mathbf{k_2},\sigma} c_{\mathbf{k_3},\sigma} c_{\mathbf{k_4}} \delta(\mathbf{k_1}+\mathbf{k_2}-\mathbf{k_3}-\mathbf{k_4}-\{\mathbf{K}_i\}) \tag{B.4}$$

where $\mathbf{k}_{1,2,3,4}$ are momenta, σ, σ' are spin labels, $\{\mathbf{K}_i\}$ denotes the set of reciprocal lattice vectors and the δ function enforces conservation of crystal momentum.

From this Hamiltonian, we can obtain a set of matrix elements $\{g\}$ (loosely termed 'interactions'), defined as

$$g^{\sigma,\sigma'}_{\mathbf{k_1},\mathbf{k_2},\mathbf{k_3},\mathbf{k_4}} = \langle(\mathbf{k}_1,\sigma),(\mathbf{k}_2,\sigma')|\frac{e^{-\beta H}}{Z}|(\mathbf{k}_3,\sigma'),(\mathbf{k}_4,\sigma)\rangle \tag{B.5}$$

where β is the inverse temperature.

We wish to study the scattering matrix elements $\{g\}$ at low energy. The effective

matrix elements at an energy scale E are obtained by tracing out all states with energies $E' > E$. We follow a two-fold procedure for tracing out high energy states. We integrate out states displaced from the M point by energies greater than $\Lambda \approx \Lambda_0$ within the Random Phase Approximation (RPA). For technical reasons, it is convenient to take Λ to be close to but slightly smaller than Λ_0. This defines for us an RPA screened Coulomb interaction at the scale Λ, of the form

$$V(q,\omega) = \frac{\frac{2\pi e^2}{qa^2}}{1 + \frac{2\pi e^2}{qa^2} N \Pi_\Lambda(q,\omega)} \tag{B.6}$$

where q is the momentum transferred, N is the number of fermion flavors participating in screening and Π_Λ is the single species polarisation function obtained by integrating out states with energies greater than Λ.

We then calculate the perturbative corrections to the RPA screened Coulomb interaction, arising from states with energy $E < \Lambda$. For these states, we do not use just the RPA, but instead take into account all processes at second order in perturbation theory. We show that the full second order perturbation theory already generates an attraction in the d-wave channel. The attraction has two distinct sources: an overscreening effect (Kohn Luttinger mechanism), and an attraction mediated by spin fluctuation exchange, with spin fluctuation exchange being the dominant mechanism for generating attraction.

Perturbation theory The effective interaction at the energy scale Λ is given by

$$g^{\sigma,\sigma'}_{\mathbf{k_1},\mathbf{k_2},\mathbf{k_3},\mathbf{k_4}}(\Lambda) = V(\mathbf{k_1} - \mathbf{k_4}, \Lambda) \tag{B.7}$$

where $V(\mathbf{q},\omega)$ is defined by (B.6). However, we want to know the effective interaction at energy scales $E \ll \Lambda$. We calculate this in perturbation theory. When we do this, we note that we can make a great simplification. Namely, the matrix elements where $\mathbf{k}_{1,2,3,4}$ lie near the saddle points of the dispersion will acquire much stronger perturbative corrections ($\ln^2 \Lambda/E$) than all other matrix elements ($\ln^1 \Lambda/E$). This is because the density of states is logarithmically enhanced near the saddle points,

and thus the phase space for interactions is logarithmically enhanced near the saddle points also. With logarithmic accuracy, we can thus restrict ourselves to only those matrix elements where $\mathbf{k_{1,2,3,4}}$ all lie near a saddle point. We further approximate by assuming that the Hamiltonian has no spin structure, which should be a safe assumption given the weakness of the spin orbit coupling in graphene.

There are only four interactions that satisfy the above conditions. These are illustrated in Fig.2-2, where we introduce also the shorthand labelling $g_{1,2,3,4}$. In terms of these interactions, the effective Hamiltonian at the energy scale Λ takes the form

$$\begin{aligned} H^{\Lambda}_{eff} &= \sum_{\alpha=1}^{3} \psi^{\dagger}_{\alpha}\varepsilon_{\mathbf{k}}\psi_{\alpha} + \frac{1}{2}g^{\Lambda}_{4}\psi^{\dagger}_{\alpha}\psi^{\dagger}_{\alpha}\psi_{\alpha}\psi_{\alpha} && \text{(B.8)} \\ &+ \sum_{\alpha\neq\beta} \frac{1}{2}[g^{\Lambda}_{1}\psi^{\dagger}_{\alpha}\psi^{\dagger}_{\beta}\psi_{\alpha}\psi_{\beta} + g^{\Lambda}_{2}\psi^{\dagger}_{\alpha}\psi^{\dagger}_{\beta}\psi_{\beta}\psi_{\alpha} && \text{(B.9)} \\ &+ g^{\Lambda}_{3}\psi^{\dagger}_{\alpha}\psi^{\dagger}_{\alpha}\psi_{\beta}\psi_{\beta}], \end{aligned}$$

Here $\alpha, \beta = 1, 2, 3$ label the three inequivalent saddle points. Meanwhile, the bare couplings g^{Λ} are defined at an energy scale Λ which is equal to the UV cutoff of the theory. The interactions g_1 and g_4 do not alter the patch label of electrons - treat these as having momentum transfer $q = q_{\Lambda} \approx 1/(\pi a)$, where $tq^2_{\Lambda}a^2 \approx \Lambda$. Meanwhile, the interactions g_2 and g_3 transfer momentum $Q = 1/a$, equal to the nesting vector connecting in-equivalent patches. Neglecting any frequency dependence of the interaction,

$$g_1(0) \approx g_4(0) \approx V(q_{\Lambda}, 0); \quad \text{(B.10)}$$

$$g_2(0) \approx g_3(0) \approx V(Q, 0) \quad \text{(B.11)}$$

where $V(q, \omega)$ is given by Eq.B.6.

Now, Π_{Λ} in (B.6) should be like the polarisation function for an insulator with bandgap Λ. In particular, for large momentum transfer $q \geq q_{\Lambda}$, there should be

metallic type screening, with $\Pi_\Lambda(q \geq q_\Lambda) \approx \nu(\Lambda) = \nu_0 \ln(\Lambda_0/\Lambda)$. Thus, we get

$$g_1\nu_0 = g_4\nu_0 = \frac{\pi e^2/(at)}{1 + N\pi \ln(\Lambda_0/\Lambda) e^2/(at)} \tag{B.12}$$

$$g_1\nu_0 = g_4\nu_0 = \frac{e^2/(at)}{1 + N \ln(\Lambda_0/\Lambda) e^2/(at)} \tag{B.13}$$

where we have taken $\nu_0 = 1/2\pi t$. Now $e^2/(at) \approx 5$ for $a = 1\mathring{A}$ and $t = 3eV$, so we are close to unitarity. Taking $N = 6$ to reflect the presence of three inequivalent saddle points and two spin species per saddle point, we obtain

$$g_2^\Lambda \nu_0 = g_4^\Lambda \nu_0 \approx 0.16, \qquad g_1^\Lambda \nu_0 = g_3^\Lambda \nu_0 \approx 0.15 \tag{B.14}$$

We have taken $\ln \Lambda_0/\Lambda = 1$, i.e. $\Lambda = 1eV$. There is admittedly an arbitrariness in this choice. However, since the parameter Λ sits inside the logarithm, we believe this arbitrariness is inessential.

All four interactions in (B.8) are marginal at tree level, but acquire logarithmic corrections in perturbation theory. The building blocks of the perturbation theory are the susceptibilities in the particle-particle and particle-hole channels, Π_{pp} and Π_{ph}, evaluated at momentum transfer zero and at momentum transfer $Q_{\alpha\beta}$ (Fig.2-1). Similarly to [21], we have

$$\begin{aligned} \Pi_{pp}(0) &= \frac{\nu_0}{4} \ln \frac{\Lambda}{\max(T,\mu)} \ln \frac{\Lambda}{T}, \\ \Pi_{ph}(Q_i) &= \frac{\nu_0}{4} \ln \frac{\Lambda}{\max(T,\mu)} \ln \frac{\Lambda}{\max(T,\mu,t_3)}, \end{aligned} \tag{B.15}$$

and $\Pi_{ph}(0), \Pi_{pp}(Q_i) = \nu_0 \ln \frac{\Lambda}{\max(T,\mu)}$, where Λ is the maximum scale up to which higher order terms in the dispersion can be neglected, (Fig.2-1) and T is the temperature. One log factor reflects the divergent density of states (and is present only for the interactions where all states are near the saddle points). The additional ln factor in $\Pi_{pp}(0)$ (Cooper channel) arises because $\varepsilon_{\mathbf{k}} = \varepsilon_{-\mathbf{k}}$, generic for any system with time reversal or inversion symmetry. In contrast, the additional ln factor in $\Pi_{ph}(Q_i)$ requires nesting of the FS, and is cut by any term that spoils the nesting, such as

third neighbor hopping t_3 or doping μ.

Using the above building blocks, we can readily write down the interactions, including corrections to second order in perturbation theory. The perturbation theory generates corrections of the form $g \ln^2 \Lambda/E$ and $g \ln \Lambda/E$, where $g \approx 0.15$ is one of the interactions. The limits of justifiable applicability of the perturbation theory are set by the condition $g \ln^2 \sim O(1)$. At this scale, the single log corrections are $g \ln \sim O(\sqrt{g}) \ll 1$, where for the last inequality we have assumed we are in the weak coupling limit. Therefore we can neglect all single log corrections and retain just $\ln^2$ corrections at second order in perturbation theory. The small parameter justifying this approximation is $\sqrt{g}$. For the RPA screened interaction (B.6), $\sqrt{g} \approx 0.38$. This same parameter controls the patch approximation, whereby we take into account only those interactions where all incoming and outgoing states lie near a saddle point. Within this leading log approximation, we find that at the scale E, the various interactions are

$$\begin{aligned} g_1^E &= g_1^\Lambda + 2\Pi_{ph}(Q_i) g_1 (g_2 - g_1) \\ g_2^E &= g_2^\Lambda + \Pi_{ph}(Q_i)(g_2^2 + g_3^2) \\ g_3^E &= g_3^\Lambda - (n-2)\Pi_{pp}(0) g_3^2 - 2\Pi_{pp}(0) g_3 g_4 + 2\Pi_{ph}(Q_i) g_3 (2g_2 - g_1), \\ g_4^\Lambda &= g_4^\Lambda - (n-1)\Pi_{pp}(0) g_3^2 - \Pi_{pp}(0) g_4^2. \end{aligned} \tag{B.16}$$

where $n = 3$ is the number of inequivalent saddle points and the susceptibilities are defined by (B.15). The limit of applicability of the perturbation theory is set by the scale at which the corrections to these interactions become of order the bare interaction i.e. $g^\Lambda \frac{\nu_0}{4} \ln^2 \Lambda/E \approx 1$. This happens when $\frac{\nu_0}{4} \ln^2 \Lambda/E \approx 1/g^\Lambda \approx 6.7$.

It is now useful to make a basis transformation, and to define

$$g_{SCd} = g_4 - g_3 \quad g_{sdw} = g_3 + g_2 \quad g_{KL} = g_2 - g_4 \tag{B.17}$$

where g_{SCd} is the coupling in the d-wave pairing channel, g_{sdw} is the coupling to spin

fluctuation at momentum equal to half a reciprocal lattice vector, and g_{KL} reflects the fact that screening in the presence of a fermi surface may depend on the relative positions of the scattered states, and not just on the momentum transferred. At the energy scale Λ, we obtain from (B.13) the bare couplings

$$g_{SCd}\nu_0 = 0.01 \quad g_{sdw}\nu_0 = 0.31 \quad g_{KL}\nu_0 = 0 \tag{B.18}$$

Note that g_{SCd} is positive, indicating the presence of a bare repulsion in the d-wave channel. However, the size of this repulsion is much less than the size of the bare repulsive interactions, $g_{SCd}\nu_0 = 0.01 \ll g_{1,2,3,4}\nu_0 \approx 0.15$. This difference in scales will allow us to generate an attraction in the d-wave channel within the limits of applicability of the second order perturbation theory. Note also that although $g^{\Lambda}_{KL} = 0$ within RPA, a non-zero g_{KL} will be generated in perturbation theory.

The perturbative correction in the d-wave pairing channel takes the form

$$\delta g^{E}_{SCd} = g^{E}_{SCd} - g^{\Lambda}_{SCd} = -\frac{1}{2}\Big[(g^{\Lambda}_{sdw})^2 + g^{\Lambda}_{sdw}g^{\Lambda}_{SCd} - 3g^{\Lambda}_{sdw}g^{\Lambda}_{KL} + (g^{\Lambda}_{KL})^2\Big]\frac{\nu_0}{4}\ln^2\frac{\Lambda}{E} \tag{B.19}$$

Firstly, note that the correction to g_{SCd} is negative i.e. perturbation theory introduces an attractive correction. Secondly, note that there are two distinct routes to generating attraction. If the screened interaction depends on the relative position of the scattered states, and not just on the transferred momentum ($g_{KL} \neq 0$) then this generates an attractive correction. This is just the Kohn Luttinger mechanism. The Kohn Luttinger effect is generic to any Fermi liquid - however, it is also a weak effect. If we start from the RPA screened Coulomb interaction and work in the patch model, then $g^{\Lambda}_{KL} = 0$. A nonzero g_{KL} will be generated at second order in perturbation theory, but this will feed back to produce an attraction in the d-wave channel only at fourth order in perturbation theory. In contrast, spin fluctuation exchange can already generate an attraction at second order in perturbation theory.

Attraction due to spin fluctuation exchange is represented by the first term in (B.19). This term arises only in the presence of a nested Fermi surface, and moreover

it requires that the nesting vector connecting inequivalent saddle points must be half of a reciprocal lattice vector (so that pair hopping is allowed). However, if these conditions are met (as they are in graphene at the M point), then it allows to generate an attrraction already at second order in perturbation theory. At the limit of applicability of the perturbation theory, when $\frac{\nu_0}{4}\ln^2\Lambda/E \approx 6.7$, we have

$$\delta g_{SCd}\nu_0 = -\frac{1}{2}\Big[0.31^2 + 0.31 * 0.01 - 0 + 0\Big]6.7 = -0.31 \tag{B.20}$$

Adding this to the bare coupling, $g^{\Lambda}_{SCd} = 0.01$, we find that

$$g^{E}_{SCd}\nu_0 = 0.01 - 0.31 = -0.3 \tag{B.21}$$

Note that this is negative i.e. there is an attraction in the d-wave pairing channel. This attraction is generated already at second order in perturbation theory. It arises largely due to spin fluctuation exchange (with the Kohn Luttinger contribution kicking in only at fourth order in perturbation theory). Once an attraction is generated, the standard BCS mechanism indicates that there will be an instability to superconductivity.

Of course, there are also other competing instabilities in other ordering channels, so the generation of an attraction does not estabish that superconductivity will arise. Nor is it clear from the perturbation analysis how universal our results are. However, it may be shown using RG methods that in fact out results apply for any choice of weak repulsive interactions at the scale Λ, and moreover that superconductivity dominates over all competing instabilities at weak coupling. We hope that exhibiting the mechanism for generating attraction within second order perturbation theory will make clearer the origin of our results.

Appendix C

Uniaxial antiferromagnetic half-metal on the hexagonal lattice: Supplementary material

C.1 Coupling of interactions to spin density waves

The minimal low energy model for graphene doped to the vicinity of the Van Hove point was presented in [1]. This model contains four interactions – density-density, exchange, pair-hopping and forward scattering, labeled g_1, g_2, g_3, g_4, respectively. In our calculations, we used only the interactions g_2 and g_3, reasoning that g_1 and g_4 do not couple to spin density waves. We now justify this statement.

Firstly, the interaction g_4 describes the process $|\mathbf{k}, \mathbf{k}\rangle \rightarrow |\mathbf{k}, \mathbf{k}\rangle$. It is a forward scattering interaction between two states at the same momentum. This interaction cannot couple to density waves, which involve states at momenta separated by a nesting vector $\mathbf{Q}$.

Secondly, the interaction g_1 describes the process $|\mathbf{k}, \mathbf{k}+\mathbf{Q}\rangle \rightarrow |\mathbf{k}+\mathbf{Q}, \mathbf{k}\rangle$. This interaction does couple to charge density waves – it connects one particle-hole bubble with momentum $\mathbf{Q}$ to the other bubble with the same momentum. However, this interaction does not couple to the spin density wave vertex because of the property

of spin σ matrices: $\sum_{i,j} \sigma^i_{i,j} = 0$ (Ref. [2]).

Thus, to study SDW physics, it is sufficient to study the $g_2 - g_3$ sector of the low energy model from [1]. We emphasize that this does not introduce any approximations.

C.2 Calculation of expansion co-efficients

In this supplement we present the calculations that were quoted in the main text. We present analytic calculations, but we also did evaluate these integrals exactly numerically and confirmed the analytic results.

C.2.1 Calculation of Z_1

We wish to evaluate

$$Z_1 = T\sum_{\omega_n} \int \frac{d^2k}{(2\pi)^2} G^2(\mathbf{k}, \omega_n) G^2(\mathbf{k} + \mathbf{Q}_3, \omega_n) \tag{C.1}$$

The integral over the Brillouin zone is dominated by those values of $\mathbf{k}$ where both Green functions correspond to states near a saddle point. Expanding the energy about the saddle points, we rewrite the integral as

$$Z_1 \approx T\sum_{\omega_n} \int \frac{d^2k}{(2\pi)^2} \frac{1}{(i\omega_n - \frac{3t_1}{4}(3k_x^2 - k_y^2))^2 (i\omega_n - \frac{3t_1}{4} 2k_y(k_y - \sqrt{3}k_x))^2} \tag{C.2}$$

Where the integral is understood to have a UV cutoff for $\mathbf{k}$ of order 1. We now define $a = \sqrt{3t_1/4}(k_y - \sqrt{3}k_x)$ and $b = \sqrt{3t_1/4}(k_y + \sqrt{3}k_x)$, and rewrite the above integral as

$$Z_1 = T\sum_{\omega_n} \frac{2}{3\sqrt{3}t_1} \int_{-\sqrt{t_1}}^{\sqrt{t_1}} \frac{dadb}{(2\pi)^2} \frac{1}{(i\omega_n + ab)^2 (i\omega_n - a(a+b))^2} \tag{C.3}$$

We now define $x = ab$ and rewrite the integral as

$$Z_1 = T\sum_{\omega_n} \frac{2}{3\sqrt{3}t_1} \int_{-\sqrt{t_1}}^{\sqrt{t_1}} \frac{da}{2\pi} \frac{1}{|a|} \int_{-\sqrt{t_1}a}^{\sqrt{t_1}a} \frac{dx}{2\pi} \frac{1}{(i\omega_n + x)^2 (i\omega_n - a^2 - x)^2} \tag{C.4}$$

We now assume $T_N \ll t_1$ (which should certainly be the case for weak/moderate coupling). In this limit, we can perform the integral over x approximately, using the Cauchy integral formula, to get

$$Z_1 = T\sum_{\omega_n} \frac{2}{3\sqrt{3}t_1}\int_{-\sqrt{t_1}}^{\sqrt{t_1}} \frac{da}{2\pi}\frac{1}{|a|}\frac{2i\text{sign}\omega_n}{(a^2-2i\omega_n)^3} = T\sum_{\omega_n}\frac{4}{3\sqrt{3}t_1}\int_{-\sqrt{t_1}}^{\sqrt{t_1}}\frac{da}{2\pi}\frac{1}{|a|}\frac{i\text{sign}\omega_n(a^2+2i\omega_n)^3}{(a^4+4\omega_n^2)^3} \tag{C.5}$$

The imaginary part of the above integral is odd in ω and hence vanishes upon performing the Matsubara sum to leave an integral that is purely real

$$Z_1 = T\sum_{\omega_n}\frac{8|\omega_n|}{3\sqrt{3}t_1}\int_{-\sqrt{t_1}}^{\sqrt{t_1}}\frac{da}{2\pi}\frac{1}{|a|}\frac{4\omega_n^2-3a^4}{(a^4+4\omega_n^2)^3} \approx T\sum_{\omega_n}\frac{8|\omega_n|}{3\sqrt{3}t_1}\int_{-\sqrt{t_1}}^{\sqrt{t_1}}\frac{da}{2\pi}\frac{1}{|a|}\frac{4\omega_n^2}{(a^4+4\omega_n^2)^3} \tag{C.6}$$

with logarithmic accuracy. Performing the integral over a (again with logarithmic accuracy) gives

$$Z_1 \approx T\sum_{\omega_n}\frac{1}{12\pi\sqrt{3}t_1}\frac{1}{|\omega_n|^3}\ln\frac{t_1}{\omega_n} = \frac{1}{48\pi^4\sqrt{3}T_N^2 t_1}(16.8\ln\frac{t_1}{2\pi T}+10.5) \approx \frac{16.8\ln\frac{t_1}{T_N}}{48\pi^4\sqrt{3}T_N^2 t_1} \tag{C.7}$$

Where we take $\omega_n = 2\pi(n+1/2)T_N$, $T = T_N$ and perform the discrete sum on mathematica.

C.2.2 Calculation of Z_2

This time we want to evaluate

$$Z_2 = T\sum_{\omega_n}\int\frac{d^2k}{(2\pi)^2}G^2(\mathbf{k},\omega_n)G(\mathbf{k}+\mathbf{Q}_3,\omega_n)G(\mathbf{k}+\mathbf{Q}_1,\omega_n) \tag{C.8}$$

Again, we anticipate this integral will be dominated by regions of the Brillouin zone where all three Green functions correspond to states near saddle points. Expanding

the dispersion about the saddle points, we obtain

$$Z_2 \approx T\sum_{\omega_n}\int \frac{d^2k}{(2\pi)^2}\frac{1}{(i\omega_n - \frac{3t_1}{4}(3k_x^2-k_y^2))^2(i\omega_n - \frac{3t_1}{4}2k_y(k_y-\sqrt{3}k_x))(i\omega_n - \frac{3t_1}{4}2k_y(k_y+\sqrt{3}k_x))} \tag{C.9}$$

Making the same coordinate substitutions as in the preceding section, we recast this as

$$Z_2 = T\sum_{\omega_n}\frac{2}{3\sqrt{3}t_1}\int_{-\sqrt{t_1}}^{\sqrt{t_1}}\frac{dadb}{(2\pi)^2}\frac{1}{(i\omega_n+ab)^2(i\omega_n - a(a+b))(i\omega_n - b(a+b))} \tag{C.10}$$

After scaling out ω_m, we can rewrite it as

$$Z_2 = T\sum_{\omega_n}\frac{2}{3\sqrt{3}t_1|\omega_n|^3}\int_{-\sqrt{t_1}}^{\sqrt{t_1}}\frac{dadb}{(2\pi)^2}\frac{1}{(i+ab)^2(i - a(a+b))(i - b(a+b))} = T\sum_{\omega_n}\frac{2}{12\pi^2\sqrt{3}t_1|\omega_n|^3} \tag{C.11}$$

Where the rescaled integral is fully convergent, and can be done numerically on mathematica. The sum over Matsubara frequencies can also be done on Mathematica, and yields the answer

$$Z_2 = T\sum_{\omega_n}\frac{2.9\times 16.8}{48\pi^4\sqrt{3}t_1T_N^2} \tag{C.12}$$

Comparing with the previous expression for Z_1, we see that $Z_2 \approx Z_1 \times 2.9/\ln(T/t_1)$. Thus, $Z_2 \ll Z_1$ provided the log is large. (If the log is not large then the evaluation of Z_1 with logarithmic accuracy does not suffice, and sub-logarithmic contributions to Z_1 must also be taken into account.)

C.2.3 Calculation of Z_3

We want to evaluate

$$Z_3 = T\sum_{\omega_n}\int \frac{d^2k}{(2\pi)^2}G(\mathbf{k},\omega_n)G(\mathbf{k}+\mathbf{Q}_3,\omega_n)G(\mathbf{k}+\mathbf{Q}_1,\omega_n)G(\mathbf{k}+\mathbf{Q}_1+\mathbf{Q}_3,\omega_n) \tag{C.13}$$

This time it is not possible to place all the Green functions at the saddle points. In fact, we cannot even place all the Green functions at the Fermi surface - the best that can be done is to place three of the Green functions near a saddle point, but the fourth has to be off Fermi surface. Thus, we obtain,

$$Z_3 \approx T\sum_{\omega_n}\int \frac{d^2k}{(2\pi)^2}\frac{1}{(i\omega_n - \frac{3t_1}{4}(3k_x^2-k_y^2))(i\omega_n - \frac{3t_1}{4}2k_y(k_y-\sqrt{3}k_x))(i\omega_n - \frac{3t_1}{4}2k_y(k_y+\sqrt{3}k_x))(i\omega - 2} \tag{C.14}$$

Making the usual substitutions, and assuming $t_1 \gg T_N$, we obtain

$$Z_3 \approx \sum_{\omega_n}\frac{T_N}{12\sqrt{3}\pi^2 t_1^2\omega_n^2}\int_{-t_1}^{t_1}\frac{dadb}{(i\omega_n+ab)(i\omega_n-a(a+b))(i\omega_n-b(a+b))} \tag{C.15}$$

$$\approx \sum_{\omega_n}\frac{T_N}{12\sqrt{3}\pi^2 t_1^2\omega_n^2}\int_{-t_1/\omega_n}^{t_1/\omega_n}\frac{dadb}{(i+ab)(i-a(a+b))(i-b(a+b))} \tag{C.16}$$

The integral is convergent. As usual, the imaginary part is odd in ω and vanishes and we care only about the real part. Performing the integral on mathematica and taking the real part, we obtain

$$Z_3 \approx \sum_{\omega_n}\frac{6.5T_N}{12\sqrt{3}\pi^2 t_1^2\omega_n^2} \approx \frac{6.5}{48\sqrt{3}\pi^2 t_1^2 T_N} \tag{C.17}$$

Which is parametrically smaller than Z_1 and Z_2 by T_N/t_1.

C.2.4 Calculation of Z_4

We now calculate the coefficient of the sixth order chirality sensitive term in the free energy, $v(\mathbf{\Delta}_1\cdot(\mathbf{\Delta}_2\times\mathbf{\Delta}_3))^2$. After some analysis of diagrams we find that,

$$Z_4 = T\sum_{\omega_n}\int\frac{d^2k}{(2\pi)^2}G^2(\mathbf{k},\omega_n)G^2(\mathbf{k}+\mathbf{Q}_3,\omega_n)G^2(\mathbf{k}+\mathbf{Q}_1,\omega_n) \tag{C.18}$$

We can now place all the Green functions on the near a saddle point. Making the usual substitutions, we obtain

$$Z_4 = \sum_{\omega_n} \frac{T_N}{12\sqrt{3}\pi^2 t_1 |\omega_n|^5} \int_{-t_1/\omega_n}^{t_1/\omega_n} \frac{dadb}{(i+ab)^2(i-a(a+b))^2(i-b(a+b)^2)} \quad \text{(C.19)}$$

$$= \sum_{\omega_n} \frac{T_N}{12\sqrt{3}\pi^2 t_1 |\omega_n|^5} \int_{-t_1/T_N}^{t_1/T_N} \frac{dadb}{(i+ab)^2(i-a(a+b))^2(i-b(a+b)^2)} \quad \text{(C.20)}$$

where in the second line we have assumed that the Matsubara sum is controlled by the first few Matsubara frequencies. The integral can be done numerically, and it is negative for small T_N/t_1. It then follows that at weak/moderate coupling $Z_4 < 0$, so that the Free energy at sixth order also disfavors chirality.

C.2.5 Scaling functions

The above calculations were performed at weak/moderate coupling, assuming $T_N/t_1 \ll 1$. However, the integrals can be evaluated at arbitrary T_N/t_1. To this end, it is useful to define the scaling functions $f_i(T_N/t_1) = Z_i(T_N/t_1)/Z_i(0)$. These scaling functions are evaluated numerically and shown in Fig.C-1. At small T_N/t_1 we found perfect agreement with analytical results: all $f_i(x)$ tend to 1 if we use our analytical results for $Z_i(0)$.

C.3 Phase diagram at strong coupling

At strong coupling, when $g_{2,3} \geq t_1$ and $T_N \sim t_1$, our analysis based on Ginzburg-Landau expansion is less accurate because fermions can no longer be approximated as free particles (the self-energy corrections to fermionic lines and vertex corrections to square and hexagonal diagrams are generally of order one). Nevertheless, if we apply our analysis to $T_N \sim t_1$, we find that Z_3, Z_4 and $Z_2 - Z_1 - Z_3$ all change signs at some T_N/t_1 (see Fig. C-1).

The first sign change occurs in the sixth order chirality sensitive term Z_4, which becomes positive for $T_N/t > 0.1$. When Z_4 is positive, the chiral SDW state [3] is

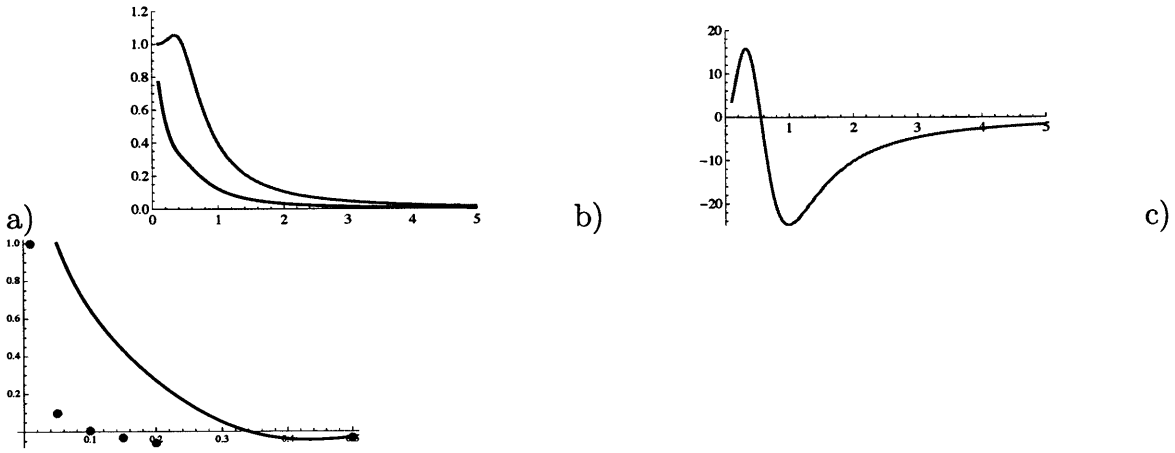

Figure C-1: (Color online) The behavior of scaling functions $f_i(x) = f_i\left(\frac{T_N}{t_1}\right)$. a) The scaling functions f_1 (black) and f_2 (blue). b) The scaling function f_3. c) The scaling function f_5 corresponding to the term $Z_2 - Z_1 - Z_3$ (solid line). Superimposed on this is a discrete plot of f_4 (points). Note that the scaling functions $f_3(x)$, $f_4(x)$ and $f_5(x)$ change sign between small T_N/t_1 (weak/moderate coupling) and $T_N \sim t_1$ (strong coupling).

energetically favored, provided we are sufficiently far below T_N for the sixth order term to dominate over the quartic term Z_3. Thus, at large T_N/t_1, the uniaxial SDW phase has a much narrower region of stability, and the transition into the chiral SDW phase happens quite close to T_N.

The term $Z_1 - Z_2 - Z_3$ is next to change sign, becoming negative for $T_N/T > 0.35$. Once this term becomes negative, the system prefers instead a $1Q$ collinear state, of the form discussed in [3], wherein SDW order develops only at a single nesting vector. The subsequent sign change of Z_3 at $T_N/t \approx 0.55$ has no physical consequences.

The $1Q$ collinear SDW state that forms at $T_N/t > 0.35$ is a (full) metal because the entire FS is not gapped out. The competition between a metallic collinear state and non-coplanar insulating state has been detected numerically in the mean-field analysis at strong coupling [4], and our results for the strong coupling case are in line with this earlier study. Our strong coupling results are also consistent with the studies that found a non-coplanar, chiral SDW order in the models of spins of the same fixed length at every lattice site [3, 4]. However, in the weak/moderate coupling limit, our results indicate that the preferred state is a uniaxial $3Q$ state of a sort not considered before, which can only be realized in a model starting from itinerant

fermions.

We also analyzed the evolution of Z_i with T_N/t_1 for fermions on a triangular lattice. We found similar trends, e.g., sign change of Z_4. However, for a triangular lattice, the first sign change (in Z_4) occurs at a much larger $T_N/t_1 \sim 0.5$, when the itinerant approach is very questionable.

Bibliography

[1] R. Nandkishore, L. Levitov and A. Chubukov, Nature Physics 8, 158-163 (2012)

[2] N. Furukawa, T. M. Rice, and M. Salmhofer, Phys. Rev. Lett. 81, 3195 (1998)

[3] T. Li, arXiv: 1001.0620 (2010)

[4] I. Martin and C. D. Batista, Phys. Rev. Lett. **101**, 156402 (2008)

[5] T. Li, cond-mat: 1103.2420 (2011)

Appendix D

Ferroelectric-type Excitonic Instability in Bilayer Graphene - Supplement

D.0.1 Calculating polarisation function

Throughout this supplement, we use a shorthand whereby p^2 represents $p^2/2m$, unless otherwise specified. We wish to evaluate the polarisation function at non-zero Δ. This was defined as

$$\Pi_{\omega,\mathbf{q},\Delta} = -2\int \frac{dEd^2p}{(2\pi)^3}\frac{E_+E_- - p_+^2p_-^2\cos(2\theta_{pq}) - \Delta^2}{(E_+^2 + p_+^4 + \Delta^2)(E_-^2 + p_-^4 + \Delta^2)}, \tag{D.1}$$

where $E_\pm = E \pm \omega/2$, $\mathbf{p}_\pm = \mathbf{p} \pm \mathbf{q}/2$ and θ_{pq} is the angle between $\mathbf{p}_+$ and $\mathbf{p}_-$. We begin by integrating by residues over frequencies, to obtain

$$\begin{aligned}\Pi_{\omega,q,\Delta} &= -\int \frac{d^2p}{(2\pi)^2}\frac{\xi_+ + \xi_-}{\tilde{\omega}^2 + (\xi_+ + \xi_-)^2}\Big(2\sin(\theta_{pq})^2 - \frac{\tilde{\Delta}^2}{\xi_+\xi_-} \\ &+ \cos(2\theta_{pq})(1 - \frac{\tilde{p}_+^2\tilde{p}_-^2}{\xi_+\xi_-})\Big).\end{aligned} \tag{D.2}$$

We are using the notation $\xi_\pm^2 = p_\pm^4 + \Delta^2$. Upon setting $\Delta = 0$, we obtain the polarisation function in the ungapped state. We take q to lie along the x axis without loss of generality, change to polar coordinates $p_x = p\cos\varphi$, $p_y = p\sin\varphi$ and scale out q. The integral then depends on a single dimensionless parameter $\tilde{\omega} = \omega/q^2$, and may be evaluated analytically by integrating in turn over φ and p/q. This gives an exact expression for the polarisation function $\Pi_{\omega,\mathbf{q},0} = -\frac{m}{2\pi} f(\tilde{\omega})$, where

$$f(\tilde{\omega}) = \frac{2\tan^{-1}\tilde{\omega} - \tan^{-1} 2\tilde{\omega}}{\tilde{\omega}} + \ln\frac{\tilde{\omega}^2+1}{\tilde{\omega}^2+\frac{1}{4}} \approx \frac{\ln 4}{\sqrt{1+u\tilde{\omega}^2}} \tag{D.3}$$

with $u = (2\ln 4/\pi)^2$. We note that the polarisation function vanishes for $q^2 \ll \omega$, so that in this regime of parameter space, the interaction is not efficiently screened.

We now calculate $\Pi_\Delta - \Pi_0$ by Taylor expanding Π_Δ to leading order in small Δ^2 to obtain

$$\Pi_\Delta - \Pi_0 = \Delta^2 \int \frac{d^2p}{(2\pi)^2} \quad \frac{p_+^2+p_-^2}{\omega^2+(p_+^2+p_-^2)^2}\left(\frac{1}{p_+^2p_-^2} - \frac{1}{2}(\frac{1}{p_+^4}+\frac{1}{p_-^4})\cos 2\theta_{pq}\right) + \frac{\sin^2\theta_{pq}\left(\frac{p_+^6+p_-^6}{p_+^2p_-^2} + 3(p_+^2+p_-^2) - \frac{\omega^2(p_+^2+p_-^2)}{p_+^2p_-^2}\right)}{(\omega^2+(p_+^2+p_-^2)^2)^2} \tag{D.4}$$

We note that the integral has singularities at $p_\pm = 0$, which must be regularised by introducing an IR cutoff Δ. The singularities at p_+ and p_- contribute equally, so we evaluate just the contribution from the singularities at $p_- = 0$, and multiply by two. We change variables to $\mathbf{p}_- \to p$, and $\mathbf{p}_+ \to \mathbf{p}+\mathbf{q}$ and work in polar coordinates, taking q to lie along the x axis. Again, we scale out q and keep only the singular terms, to obtain

$$\delta\Pi_\Delta = 2\tilde{\Delta}^2 \int \frac{pdpd\varphi}{(2\pi)^2}\frac{1}{\omega^2+1}\frac{1}{p^2} + \frac{\sin^2\theta_{pq}\left(\frac{1}{p^2}-\frac{\omega^2}{p^2}\right)}{(\omega^2+1)^2} - \frac{1}{2}F(p) \tag{D.5}$$

Here, we have measured all variables in units of q, have defined φ to be the angle between $\mathbf{p}$ and $\mathbf{q}$, and have defined

$$F(p) = \frac{1 + 2p^2 + 2p\cos\varphi}{\omega^2 + (2p^2 + 2p\cos\varphi + 1)^2} \frac{1 - 2\sin^2\theta_{pq}}{p^4} \tag{D.6}$$

We can readily determine that in this basis, $\sin^2\theta_{pq} = \sin^2\varphi/(p^2 + 2p\cos\varphi + 1)$. We can then expand $F(p)$ as a power series in small p. We note that the terms at $O(p^{-4})$ and $O(p^{-3})$ vanish upon angular integration, so that the leading term comes at $O(p^{-2})$. After integration over angles φ, and after making the substitution $z = p^2/2m$ we obtain

$$\delta\Pi_\Delta = \frac{m\tilde{\Delta}^2}{2\pi}\left(\frac{-7}{(\omega^2+1)^2} + \frac{4}{(\omega^2+1^4)^3}\right)\int\frac{dz}{z} \tag{D.7}$$

After restoring q, we obtain

$$\delta\Pi_\Delta = \frac{m\Delta^2}{2\pi}\ln(\frac{\sqrt{\omega^2+q^4}}{\Delta})\left(\frac{-7q^4}{(\omega^2+q^4)^2} + \frac{4q^8}{(\omega^2+q^4)^3}\right). \tag{D.8}$$

D.0.2 Calculating exchange energy

In the main text, we derived

$$\delta V = \int\frac{d\omega d^2p}{(2\pi)^3}\ln\left(1 - N\tilde{U}_{\omega,q}(\Pi_{\omega,q,\Delta} - \Pi_{\omega,q,0})\right). \tag{D.9}$$

Substituting our expression Eqn.D.8 into this, and expanding the logarithm to leading order in small Δ^2, we obtain

$$E_{exchange} = -\int\frac{d\omega d^2q}{(2\pi)^3} \quad \frac{m\Delta^2}{2\pi}\ln(\frac{\sqrt{\omega^2+q^4}}{\Delta})\left(\frac{-7q^4}{(\omega^2+q^4)^2} + \frac{4q^8}{(\omega^2+q^4)^3}\right) \times \frac{2\pi}{q + Nq^2\ln 4/\sqrt{q^4 + (2\ln 4/\pi)^2\omega^2}} \tag{D.10}$$

We have used the approximate form for the interaction, and have measured everything in units of E_0 and a_0. We note that $|\Pi_\Delta - \Pi_0|$ vanishes in the limit $q^2/\omega \ll 1$, when the Coulomb interaction is not efficiently screened. This is the region of phase

space that is responsible for the vertex correction having an enhanced $\ln^2$ infrared divergence (see next section). The vanishing of $\Pi_\Delta - \Pi_0$ in the region of phase space where the Coulomb interaction is strongest is responsible for the weakened divergence, and is another way of understanding the leading order cancellation between the vertex correction and the self energy. To formally calculate the exchange energy, we approximate the interaction by taking

$$\frac{1}{q + Nq^2 \ln 4/\sqrt{q^4 + (2\ln 4/\pi)^2\omega^2}} \rightarrow \frac{2\theta(N-q)}{N\pi q^2/\omega} \tag{D.11}$$

where $\theta(x)$ represents the Heaviside step function. We take the $q^2 > \omega$ limit of the interaction, because this is where the interaction is strongest. We now substitute into Eq.D-10, change to polar co-ordinates $\omega = rcos\theta$, $q^2 = r\sin\theta$, and integrate in turn over θ and r to obtain the result quoted in the main text

$$E_{exchange} = -\frac{13m\Delta^2}{6\pi^3}\ln^2(N^2E_0/\Delta) \tag{D.12}$$

D.0.3 $\ln^2$ divergence of vertex correction

We analyse the vertex correction $\delta\Delta$ with the dynamically screened effective interaction. After including Δ in the fermion green functions, we obtain

$$\delta\Delta_{\omega,q} = \int \frac{d\varepsilon dz d\theta}{(2\pi)^3} \frac{\varepsilon^2 + z^2 - \Delta_{\varepsilon,p}^2}{(\varepsilon^2 + z^2 + \Delta_{\varepsilon,p}^2)^2} \frac{2\pi e^2 \Delta_{\varepsilon,p}}{\kappa|\mathbf{p}-\mathbf{q}| + me^2Nf(\tilde{\omega})} \tag{D.13}$$

We use the notation $z = p^2$ and $\tilde{\omega} = \omega/|\mathbf{p}-\mathbf{q}|^2$. We now measure energies and wavevectors in the units E_0 and $1/a_0$ respectively, to recast the vertex correction in the dimensionless form

$$\delta\Delta_{\omega,q} = \int \frac{d\varepsilon dz d\theta}{(2\pi)^3} \frac{\varepsilon^2 + z^2 - \Delta_{\varepsilon,p}^2}{(\varepsilon^2 + z^2 + \Delta_{\varepsilon,p}^2)^2} \frac{2\pi\Delta_{\varepsilon,p}}{\sqrt{2z'} + Nf(\xi)}, \tag{D.14}$$

where $z' = (\mathbf{p}-\mathbf{q})^2$ and $\xi = (\varepsilon - \omega)/z'$. We note that integration over z can be extended to infinity without running into a UV divergence.

We approximate by treating the gap function Δ as a constant. Using the approx-

imate form of $f(\tilde{\omega}) \approx \ln 4/\sqrt{1+u\tilde{\omega}^2}$, with $u = (2\ln 4/\pi)^2$, and changing to polar coordinates $\varepsilon = \rho\sin\varphi$, $z = \rho\cos\varphi$, we integrate in turn over ρ and φ. Working to leading order in small $\Delta/(N^2E_0)$, we obtain

$$\delta\Delta = \Delta\frac{1}{\pi^2 N}\ln^2\left(aN^2E_0/\Delta\right). \tag{D.15}$$

One logarithm comes from the integration over 'angles' φ, and reflects the singularity of the dynamically screened interaction in the region $q^2/\omega \ll 1$, whereas the second logarithm comes form the integration over ρ, and reflects the non-vanishing density of states at low energies in BLG. This second logarithm would be present even if we worked with short range (delta function) interations.

The self energy is also $\ln^2$ divergent, for the same reasons, and cancels the logarithmic divergence that comes from the singularity of the interaction as $q \to 0$. This manifests itself in the free energy calculation through $\Pi_\Delta - \Pi_0$ vanishing as $\sim q^4$ in the limit $q \to 0$. However, we note that the cancellation between vertex correction and self energy exists only to leading order. At subleading, logarithmic order, there remains an instability, as was made evident through the free energy approach.

Appendix E

Conductivity of bilayer graphene: supplement

Here we derive a relationship between the AC Hall conductance of a 2D sheet and the Kerr rotation in reflection θ_K. The standard formula $\theta_K \sim \mathrm{Im}\,\sigma_{xy}$ [1] cannot be used for BLG, because the standard formula is derived for reflection from a half-space, whereas we are considering a BLG sheet that is much thinner than the optical wavelength. As we will show, in this limit, the relationship between AC Hall conductance and Kerr rotation is modified to $\theta_K \sim \mathrm{Re}\,\sigma_{xy}$.

We consider light incident normally on a BLG sheet placed on a substrate with refractive index $n = n' + in''$. Incident and transmitted waves propagate in the $+z$ direction, while the reflected wave propagates in the $-z$ direction. The BLG sheet is taken to be in the $z = 0$ plane, whereas the substrate occupies the halfspace $z > 0$. We calculate the reflection amplitudes for incident light that is linearly polarised along the x axis. The reflected wave, $E_r = r_{xx}\hat{\mathbf{x}} + r_{yx}\hat{\mathbf{y}}$, is linearly polarised if $\mathrm{Im}\,(r_{yx}/r_{xx}) = 0$, and elliptically polarised otherwise. The major axis of the polarisation is rotated with respect to the x axis by the Kerr angle $\theta_K = \mathrm{Re}\,(r_{yx}/r_{xx})$.

We start with rewriting Maxwell's equations $\mathbf{k} \times \mathbf{H} = -\frac{\omega}{c}\mathbf{D}$, $\mathbf{k} \times \mathbf{E} = \frac{\omega}{c}\mathbf{H}$ as

$$\begin{aligned} kH_x &= -\frac{\omega}{c}n^2 E_y \qquad kH_y = \frac{\omega}{c}n^2 E_x \\ kE_x &= \frac{\omega}{c}H_y \qquad kE_y = -\frac{\omega}{c}H_x \end{aligned} \tag{E.1}$$

Similar relations hold in the vacuum region with n replaced by 1. At the interface $z = 0$ we must match EM field amplitudes on both sides using continuity of the E field $E_< = E_>$ and the Ampère's law for the H field:

$$(H_> - H_<)_x = \frac{4\pi}{c}(\sigma E)_y \qquad (H_> - H_<)_y = -\frac{4\pi}{c}(\sigma E)_x.$$

For an incident wave polarised along the x axis, $E_{\text{in}} = \hat{\mathbf{x}}$, we have $E_> = t_{xx}\hat{\mathbf{x}} + t_{yx}\hat{\mathbf{y}}$, $E_< = (1 + r_{xx})\hat{\mathbf{x}} + r_{yx}\hat{\mathbf{y}}$, $H_> = n(t_{xx}\hat{\mathbf{y}} - t_{yx}\hat{\mathbf{x}})$, $H_< = (1 - r_{xx})\hat{\mathbf{y}} + r_{yx}\hat{\mathbf{x}}$. Applying Ampère's law to the magnetic field leads to the continuity relations

$$\begin{aligned} nt_{xx} - 1 + r_{xx} &= -\frac{4\pi}{c}(\sigma_{xx}t_{xx} + \sigma_{xy}t_{yx}) \\ nt_{yx} + r_{yx} &= -\frac{4\pi}{c}(\sigma_{yx}t_{xx} + \sigma_{yy}t_{yx}) \end{aligned} \tag{E.2}$$

Eliminating t using the continuity relations for electric field, $E_< = E_>$, we obtain the single matrix equation

$$\begin{bmatrix} n + 1 + \frac{4\pi}{c}\sigma_{xx} & \frac{4\pi}{c}\sigma_{xy} \\ \frac{4\pi}{c}\sigma_{yx} & n + 1 + \frac{4\pi}{c}\sigma_{yy} \end{bmatrix} \begin{bmatrix} r_{xx} \\ r_{yx} \end{bmatrix} = \begin{bmatrix} 1 - n - \frac{4\pi}{c}\sigma_{xx} \\ -\frac{4\pi}{c}\sigma_{yx} \end{bmatrix} \tag{E.3}$$

This equation can be solved to obtain

$$\begin{bmatrix} r_{xx} \\ r_{yx} \end{bmatrix} = \frac{1}{D}\begin{bmatrix} 1 - (n + \frac{4\pi}{c}\sigma_{xx})^2 + (\frac{4\pi}{c})^2\sigma_{xy}\sigma_{yx} \\ -\frac{8\pi}{c}\sigma_{yx} \end{bmatrix}; \tag{E.4}$$

We have denoted $D = (n + 1 + \frac{4\pi}{c}\sigma_{xx})^2 - |\frac{4\pi}{c}\sigma_{xy}|^2 \approx (n + 1)^2$, and have assumed isotropy, so that $\sigma_{xx} = \sigma_{yy}$. The Kerr angle is given by $\text{Re}\,(r_{yx}/r_{xx})$, and thus takes the form

$$\begin{aligned} \theta_K &= \text{Re}\left[\frac{-\frac{8\pi}{c}\sigma_{yx}}{1 - (n + \frac{4\pi}{c}\sigma_{xx})^2 + (\frac{4\pi}{c}|\sigma_{xy}|)^2}\right] \\ &\approx \text{Re}\left(\frac{8\pi}{c(n^2 - 1)}(\sigma_{yx})\right) \end{aligned}$$

$$= \frac{8\pi[(n'^2 - n''^2 - 1)\mathrm{Re}\,(\sigma_{xy}) - 2n'n''\mathrm{Im}\,(\sigma_{xy})]}{c[(n'^2 - n''^2 - 1)^2 + 4n'^2n''^2]}$$

where in the last line we have taken $n = n' + in''$ with n' and n'' real. Now if we assume $n = n'$ and $n'' = 0$, we obtain the formula quoted in the main text

$$\theta_K = \frac{8\pi}{c(n^2 - 1)}\mathrm{Re}\,\sigma_{xy} \tag{E.5}$$

E.1 2 band model calculations

E.1.1 Conductivity calculations

The conductivity for a chiral system like BLG may be calculated using the formalism introduced in [2]. The conductance is given in the Matsubara (imaginary frequency) representation by

$$\sigma_{\mu\nu}(i\omega) = \frac{1}{\omega}\int_{-\infty}^{\infty}\frac{d\varepsilon}{2\pi}K_{\mu\nu}(\varepsilon,\omega) \tag{E.6}$$

$$K_{\mu\nu}(\omega) = \Big[\mathrm{Tr}\Big(G(\varepsilon+\frac{\omega}{2},\mathbf{p})j_\mu(\mathbf{p})G(\varepsilon-\frac{\omega}{2},\mathbf{p})j_\nu(\mathbf{p})\Big) - \mathrm{Tr}\Big(G(\varepsilon,\mathbf{p})j_\mu(\mathbf{p})G(\varepsilon,\mathbf{p})j_\nu(\mathbf{p})\Big)\Big] \tag{E.7}$$

Here the trace is taken over momenta $\mathbf{p}$, and over the sublattice, spin and valley degrees of freedom. The subtraction of the term at $\omega = 0$ is a convenient way to account for the contribution of the diamagnetic current. The Green functions are in the imaginary time formalism, and take the form

$$G(i\varepsilon,\mathbf{p}) = \frac{i\varepsilon + H(\mathbf{p})}{\varepsilon^2 + H^2(p)} \tag{E.8}$$

where $H(p)$ is the effective low energy Hamiltonian for the state that we are looking at, and $H^2(p)$ has no matrix structure (is proportional to the identity in spin-valley-sublattice space).

The current operator in Eq.(E.7) may be straightforwardly obtained by adding a vector potential to the Hamiltonian through the minimal coupling prescription

$\mathbf{p} \to \mathbf{p} - e\mathbf{A}$, and defining $\mathbf{j} = \frac{\partial H}{\partial A}|_{A=0}$. This yields

$$j_x = \frac{1}{m}(p_x\tau_1 + p_y\tau_2) \quad j_y = \frac{1}{m}(p_x\tau_2 - p_y\tau_1) \tag{E.9}$$

The conductivity in any given state can be obtained by substituting Eq.(E.9) and Eq.(E.8) into Eq.(E.7), and taking the Hamiltonian to be the appropriate low energy Hamiltonian for the state. This will give the conductivity in the Matsubara frequency representation. The conductivity in terms of real frequencies may then be obtained by making the analytic continuation

$$i\omega \to \omega + i\delta \tag{E.10}$$

where δ is a positive infinitesimal. To obtain the retarded correlation function (and hence the conductivity), we must take the analytic continuation from the positive imaginary ω axis to the real axis.

First, we analyze the Hamiltonian to be that of the **non-interacting bilayer**,

$$H_0 = \frac{p_+^2}{2m}\tau_+ + \frac{p_-^2}{2m}\tau_-. \tag{E.11}$$

This Hamiltonian is appropriate for calculating conductivity in the **Fermi liquid** state. Substituting this Hamiltonian in Eq.(E.7), we find that the Hall conductivity is zero. The longitudinal conductivity for a single species takes the form

$$\begin{aligned} \sigma_{xx}(i\omega) &= \frac{4e^2}{2m\omega}\Big(\int_{\varepsilon,\mathbf{p}} \frac{2z(\varepsilon_+\varepsilon_-)}{(\varepsilon_+^2 + z^2)(\varepsilon_-^2 + z^2)} \\ &- \int_{\varepsilon,\mathbf{p}} \frac{2z\varepsilon^2}{(\varepsilon^2 + z^2)^2}\Big) \end{aligned} \tag{E.12}$$

where we have used the notation $z = p^2/2m$ and $\varepsilon_\pm = \varepsilon \pm \omega/2$. We integrate over ε by the method of residues to obtain

$$\sigma_{xx}(i\omega) = e^2\omega \int_0^\Lambda \frac{dz}{2\pi} \int_0^{2\pi} \frac{d\varphi}{2\pi} \frac{1}{\omega^2 + 4z^2} \tag{E.13}$$

where we have used $d^2p = mdzd\varphi$, we are working in units where $\hbar = 1$, and Λ is the UV cutoff for the two band model ($\Lambda \approx 0.4eV$). It is necessary to keep Λ finite, since it sets the only energy scale in the problem. The integration over angles is trivial, and the integration over z may also be performed straightforwardly. Restoring $\hbar$, we obtain

$$\sigma_{xx}(i\omega) = \frac{e^2}{2h} \arctan\left(\frac{2\Lambda}{\omega}\right) \tag{E.14}$$

This must now be continued to real frequencies. It is useful to first rewrite the arctan function in terms of logarithms, as

$$\sigma_{xx}(i\omega) = \frac{e^2}{2h}\frac{i}{2} \ln\left(\frac{i\omega + 2\Lambda}{i\omega - 2\Lambda}\right) \tag{E.15}$$

The analytic continuation Eq.(E.10) may now be performed, and yields

$$\sigma_{xx}(\omega) = \frac{e^2}{4h} i \ln\left(\frac{\omega + 2\Lambda}{\omega - 2\Lambda}\right) \approx \frac{\pi e^2}{4h} + O(\omega/\Lambda) \tag{E.16}$$

Note that Λ sets the only energy scale in the problem. For $\omega \ll \Lambda$, we are in the DC limit, and the conductivity is real, and of order the conductance quantum.

Next, we consider **gapped states** described by the low energy Hamiltonian

$$H = \frac{p_+^2}{2m}\tau_+ + \frac{p_-^2}{2m}\tau_- + \Delta\tau_3 \tag{E.17}$$

Substituting in Eq.(E.7), we can straightforwardly obtain the Hall conductivity (for a single species). It takes the form

$$\sigma_{xy}(i\omega) = \frac{8e^2\Delta}{2m} \int \frac{d\varepsilon d^2p}{(2\pi)^3} \frac{z}{(\varepsilon_+^2 + z^2 + \Delta^2)(\varepsilon_-^2 + z^2 + \Delta^2)} \tag{E.18}$$

using the same notation $z = p^2/2m$ and $\varepsilon_\pm = \varepsilon \pm \omega/2$ that was introduced earlier. Integrating over ε by residues, using $d^2p = mdzd\varphi$, and performing the trivial integration over angles φ, we obtain

$$\sigma_{xy}(i\omega) = 4e^2\Delta \int_0^\infty \frac{dz}{2\pi} \frac{z}{\sqrt{z^2 + \Delta^2}(\omega^2 + 4z^2 + 4\Delta^2)} \tag{E.19}$$

The frequency ω is assumed to be positive, since the analytic continuation will be taken from the positive imaginary axis. We have taken $\Lambda \to \infty$, since the gap Δ now introduces an energy scale to which we can compare ω. The integral over z may be done exactly, to obtain (restoring $\hbar$)

$$\sigma_{xy}(i\omega) = \frac{e^2}{h}\frac{2\Delta}{\omega}\arccos\left(\frac{2|\Delta|}{\sqrt{\omega^2+4\Delta^2}}\right) \tag{E.20}$$

The arccos function is on the branch giving values from 0 to π. To simplify the analytic continuation, we re-write the arccos function in terms of logarithms as

$$\sigma_{xy}(i\omega) = \frac{e^2}{h}\frac{2\Delta}{i\omega}\frac{1}{2}\ln\left(\frac{2|\Delta|+i\omega}{2|\Delta|-i\omega}\right) \tag{E.21}$$

where the branch cut of the ln function is taken along the negative real axis. The analytic continuation is now straightforward, and yields

$$\sigma_{xy}(\omega) = \frac{e^2}{h}\frac{\Delta}{\omega}\ln\left(\frac{2|\Delta|+\omega}{2|\Delta|-\omega}\right) \tag{E.22}$$

The branch cut of the ln function is taken along the negative real axis. The real and imaginary parts of the conductivity are plotted in Fig.8-2. Note that the real part of the conductivity is even in ω and the imaginary part is odd in ω, which satisfies the Kramers Kronig relations. In the limit $\omega \to 0$, we obtain the result $\sigma_{xy} = (e^2/h)\text{sign}(\Delta)$ that is expected from [4], with an additional factor of 2 that comes from the 2π Berry phase of BLG. Note too that in the conditional limit when we first take $\omega \to 0$ and then take $\Delta \to 0$, there is a non-zero quantised Hall conductance. Thus, the DC Hall conductivity in the limit $\Delta \to 0$ is not the same as the DC Hall conductivity at $\Delta = 0$. This difference is a sign of the chiral anomaly that underlies the QAH effect [3, 4].

Thus far, we have calculated the Hall conductivity in a single species. Summing over spin and valley species multiplies the above result by $\text{Tr}(Q\eta_3)$ [[34]]. Thus, the Hall conductivity is non-vanishing for the QAH states, with $\text{Tr}(Q\eta_3) \neq 0$, and is identically zero for the non-QAH gapped states with $\text{Tr}(Q\eta_3) = 0$.

The longitudinal conductivity may also be calculated through Eq.(E.7). For the gapped states, we obtain (for a single species) the expression

$$\begin{aligned}\sigma_{xx}(i\omega) &= \frac{4e^2}{2m\omega}\Big(\int_{\varepsilon,\mathbf{p}} \frac{2z(\varepsilon_+\varepsilon_- + \Delta^2)}{(\varepsilon_+^2 + z^2 + \Delta^2)(\varepsilon_-^2 + z^2 + \Delta^2)} \\ &- \int_{\varepsilon,\mathbf{p}} \frac{2z(\varepsilon^2 + \Delta^2)}{(\varepsilon^2 + z^2 + \Delta^2)^2}\Big)\end{aligned}$$

Integrating over ε by residues, rewriting $d^2p = mdzd\varphi$, and performing the trivial integral over angles, we obtain

$$\sigma_{xx}(i\omega) = e^2\omega \int_0^\Lambda \frac{dz}{2\pi} \frac{z(z^2 + 2\Delta^2)}{(\omega^2 + 4z^2 + 4\Delta^2)(z^2 + \Delta^2)^{3/2}} \tag{E.23}$$

The integral over z may be performed exactly, and yields

$$\sigma_{xx}(i\omega) = \frac{e^2}{h}\Big[-\pi\frac{\Delta^2}{\omega^2}\mathrm{sign}(\omega) + \frac{|\Delta|}{\omega} + \frac{\pi}{4}\mathrm{sign}(\omega) + (\frac{2\Delta^2}{\omega^2} - \frac{1}{2})\mathrm{sign}(\omega)\arcsin\Big(\frac{2|\Delta|}{\sqrt{4\Delta^2 + \omega^2}}\Big)\Big] \tag{E.24}$$

where the arcsin is on the branch returning values from $-\pi/2$ to $\pi/2$. Note that in the limit $\Delta \to 0$, we recover the result obtained for non-interacting BLG, with $\Lambda \to \infty$.

The analytic continuation will be taken from the positive imaginary axis to the real axis. For the purposes of the analytic continuation, it is convenient to rewrite the arcsin in terms of logarithms to obtain

$$\sigma_{xx} = \frac{e^2}{h}\Big[\frac{|\Delta|}{\omega} + (\frac{\Delta^2}{\omega^2} - \frac{1}{4})i\ln\Big(\frac{2|\Delta| + i\omega}{2|\Delta| - i\omega}\Big)\Big] \tag{E.25}$$

Note that this expression vanishes identically as $\omega \to 0$. The analytic continuation is now straightforward, and yields

$$\sigma_{xx}(\omega) = \frac{e^2}{h}\Big[\frac{i|\Delta|}{\omega} - (\frac{\Delta^2}{\omega^2} + \frac{1}{4})i\ln\Big(\frac{2|\Delta| + \omega}{2|\Delta| - \omega}\Big)\Big] \tag{E.26}$$

The real and imaginary parts are plotted in Fig.8-1. Note that the real part of the

conductivity vanishes inside the gap. Note too the singularity at $\omega = \pm 2\Delta$, which is a signature of the gapped state.

We can apply the same procedure to **the nematic states**. Now the Hamiltonian is

$$H = \Big(\frac{p_+^2}{2m} + \Delta\Big)\tau_+ + \Big(\frac{p_-^2}{2m} + \Delta^*\Big)\tau_-. \tag{E.27}$$

Note that Δ is now a complex number. The eigen-energies are $E(\mathbf{p}) = \pm\xi(\mathbf{p})$, where

$$\xi(\mathbf{p}) = |\mathbf{z} + \Delta| = \sqrt{(\mathbf{z} + \Delta)(\mathbf{z}^* + \Delta^*)}; \qquad \mathbf{z} = \frac{p_+^2}{2m} \tag{E.28}$$

We have $|\mathbf{z}| = z = p^2/2m$. Substituting in Eq.(E.7), we obtain

$$\begin{aligned} \sigma_{xx} &= \frac{4e^2}{2m\omega}\int \frac{d\varepsilon d^2p}{(2\pi)^3}\Big[\frac{2\varepsilon_+\varepsilon_- z - ((z^2\mathbf{z} + \Delta^2\mathbf{z}^* + 2\Delta z^2) + c.c)}{(\varepsilon_+^2 + \xi^2)(\varepsilon_-^2 + \xi^2)} \\ &- \frac{2\varepsilon^2 z - ((z^2\mathbf{z} + \Delta^2\mathbf{z}^* + 2\Delta z^2) + c.c)}{(\varepsilon^2 + \xi^2)^2}\Big] \end{aligned} \tag{E.29}$$

We can integrate over ε by the method of residues, and hence we obtain

$$\begin{aligned} \sigma_{xx} &= \frac{4e^2}{2m\omega}\int \frac{d^2p}{(2\pi)^2}\Big[\frac{((z^2\mathbf{z} + \Delta^2\mathbf{z}^* + 2\Delta z^2) + c.c) - 2\xi^2 z}{\xi} \\ &\times \Big(\frac{1}{4\xi^2 + \omega^2} - \frac{1}{4\xi^2}\Big)\Big] \\ &= \frac{4e^2\omega}{2m}\int \frac{d^2p}{(2\pi)^2}\Big[\frac{((z^2\mathbf{z} + \Delta^2\mathbf{z}^* + 2\Delta z^2) + c.c) - 2\xi^2 z}{\xi^3(4\xi^2 + \omega^2)} \end{aligned} \tag{E.30}$$

We now write $d^2p = \frac{m}{2i}\frac{d\mathbf{z}d\mathbf{z}^*}{z}$, and hence re-write the above as

$$\sigma_{xx} = ie^2\omega\int \frac{d\mathbf{z}d\mathbf{z}^*}{(2\pi)^2}\frac{((z^2\mathbf{z} + \Delta^2\mathbf{z}^* + 2\Delta z^2) + c.c) - 2|\mathbf{z} + \Delta|^2 z}{z|\mathbf{z} + \Delta|^3(4|\mathbf{z} + \Delta|^2 + \omega^2)}$$

It is now convenient to shift variables, defining $\mathbf{z}' = \mathbf{z} + \Delta$. Straightaway dropping the primes, we obtain.

$$\sigma_{xx} = e^2 i\omega\int \frac{d\mathbf{z}d\mathbf{z}^*}{(2\pi)^2}\frac{|\mathbf{z} - \Delta|^2(\mathbf{z} + \mathbf{z}^* + \Delta + \Delta^*) + \Delta^2(\mathbf{z}^* - \Delta^*) + (\Delta^*)^2(\mathbf{z} - \Delta)}{|\mathbf{z} - \Delta|z^3(4z^2 + \omega^2)} - \frac{2}{z(\omega^2 + 4z^2)}$$

$$= e^2 i\omega \int \frac{dzdz^*}{(2\pi)^2} \frac{(\mathbf{z}-\Delta)\mathbf{z}^{*2} + (\mathbf{z}^*-\Delta^*)\mathbf{z}^2}{|\mathbf{z}-\Delta| z^3(4z^2+\omega^2)} - \frac{2}{z(\omega^2+4z^2)} \tag{E.31}$$

We note that the integral is convergent. It is convenient to perform the integral over the complex plane in polar coordinates, changing to $\mathbf{z} = r\exp(i\varphi)$, where $0 < r < \infty$ and $0 < \varphi < 4\pi$. The integral goes over the complex plane twice, because of the way z is defined. We also write $\Delta = |\Delta|e^{i\theta}$ and. In polar coordinates, we then have

$$\sigma_{xx} = -4e^2\omega \int_0^\infty \frac{dr}{2\pi} \int_0^{4\pi} \frac{d\varphi}{2\pi} \frac{r\cos\varphi + |\Delta|\cos(\theta-2\varphi)}{\sqrt{r^2+|\Delta|^2-2r|\Delta|\cos(\theta-\varphi)}(\omega^2+4r^2)} - \frac{1}{(\omega^2+4r^2)} \tag{E.32}$$

The first term vanishes (by integration over angles) when $|\Delta| \to 0$, whereas the second term reproduces the non-interacting result. Thus we have

$$\delta\sigma_{xx} = -8e^2\omega \int_0^\infty \frac{drd\varphi}{(2\pi)^2} \int_0^{4\pi} \frac{r\cos\varphi + |\Delta|\cos(\theta-2\varphi)}{\sqrt{r^2+|\Delta|^2-2r|\Delta|\cos(\theta-\varphi)}(\omega^2+4r^2)} \tag{E.33}$$

where the integral now goes over $0 < \varphi < 2\pi$. We have not been able to find a closed form solution for this integral, however, in the limit $\omega \gg \Delta$, we can Taylor expand in small Δ to obtain the leading contribution to the change in the conductivity. To this end, we scale out ω, redefining $r \to r/\omega$ and $\tilde{\Delta} = |\Delta|/\omega$, and Taylor expand in small $\tilde{\Delta}$, to find

$$\delta\sigma_{xx} = -\frac{8e^2}{\omega} \int_{\tilde{\Delta}}^\infty \frac{dr}{2\pi} \int_0^{2\pi} \frac{d\varphi}{2\pi} \frac{(r\cos\varphi + \tilde{\Delta}\cos(\theta-2\varphi))(1+(\tilde{\Delta}/r)\cos(\theta-\varphi))}{r(1+4r^2)} + O(\tilde{\Delta}^2) \tag{E.34}$$

These integrals may now be performed. We find that the change in the conduc-

tivity as a result of nematic state formation is

$$\delta\sigma_{xx} = -\frac{e^2|\Delta|\cos\theta}{\omega}\ln\frac{\omega^2}{|\Delta|^2} + O(\Delta^2/\omega^2) \tag{E.35}$$

Note that the change to the conductivity depends on the phase of $\Delta = |\Delta|e^{-\theta}$. Therefore, there is an anisotropic conductivity. Analytic continuation is now straightforward, and we obtain

$$\delta\sigma_{xx} = \frac{e^2|\Delta|\cos\theta}{\omega}\Big(\pi + i\ln\frac{\omega^2}{|\Delta|^2}\Big) \tag{E.36}$$

Now we note that a nematic order parameter Δ leads to the quadratic band crossing splitting into two Dirac points. The line joining these two Dirac points is the nematic axis, which makes angle $\varphi = -\pi/2 + \arg(\Delta)/2$ with the p_x axis. Invoking the overall rotational symmetry of the BLG Hamiltonian (which is spontaneously broken by the nematic order parameter), we find a general expression for the longitudinal conductivity $\sigma(\varphi)$

$$\sigma(\varphi,\Delta) = \sigma(\Delta=0) + \delta\sigma\cos(2\varphi - \arg\Delta) \tag{E.37}$$

$$\delta\sigma = \frac{e^2|\Delta|}{\omega}\Big(\pi + i\ln\frac{\omega^2}{|\Delta|^2}\Big) \tag{E.38}$$

Here φ is the angle with respect to the x axis. The expression above is the result for a single species. The total longitudinal conductivity is obtained by summing over spins and valleys

We can also evaluate the **Hall conductivity** in the nematic state. We have

$$\sigma_{xy}(\Delta) = \frac{ie^2}{2m\omega}\int\frac{d\varepsilon d^2p}{(2\pi)^3}\Big[\frac{\mathbf{z}(\mathbf{z}^*+\Delta^*)^2 - \mathbf{z}^*(\mathbf{z}+\Delta)^2}{(\varepsilon_+^2 + |\mathbf{z}+\Delta|^2)(\varepsilon_-^2 + |\mathbf{z}+\Delta|^2)} - \frac{\mathbf{z}(\mathbf{z}^*+\Delta^*)^2 - \mathbf{z}^*(\mathbf{z}+\Delta)^2}{(\varepsilon^2 + |\mathbf{z}+\Delta|^2)^2}\Big] \tag{E.39}$$

performing the integral over frequencies, we obtain

$$\sigma_{xy}(\Delta) = \frac{e^2 i\omega}{2m} \int \frac{d^2p}{(2\pi)^2} \frac{\mathbf{z}(\mathbf{z}^* + \Delta^*)^2 - \mathbf{z}^*(\mathbf{z} + \Delta)^2}{|\mathbf{z} + \Delta|^3(\omega^2 + 4|\mathbf{z} + \Delta|^2)} \tag{E.40}$$

Again, this is a convergent integral that can be done by similar methods to those employed for evaluating $\delta\sigma_{xx}$. We obtain

$$\sigma_{xy} = \frac{e^2|\Delta|\sin(\arg\Delta)}{\omega} \ln\frac{\omega^2}{|\Delta|^2} + O(\Delta^2/\omega^2) \tag{E.41}$$

Analytic continuation then leads to

$$\sigma_{xy}(\omega) = \frac{e^2|\Delta|\sin(\arg\Delta)}{\omega}\left(i\pi + \ln\frac{\omega^2}{|\Delta|^2}\right) = \sigma^*_{yx}(\omega) \tag{E.42}$$

This result is for a single spin valley species. The total Hall conductivity is obtained by summing over different spin and valley species.

E.1.2 Transmission, reflection and Kerr rotation

We analyze transmission of EM waves through graphene placed on a substrate with dielectric constant n. Incident and transmitted waves propagate in the $+z$ direction, reflected wave propagates in the $-z$ direction. The graphene sheet is taken to be in the $z = 0$ plane, the substrate occupies the halfspace $z > 0$.

We start with rewriting Maxwell's equations $\mathbf{k} \times \mathbf{H} = -\frac{\omega}{c}\mathbf{D}$, $\mathbf{k} \times \mathbf{E} = \frac{\omega}{c}\mathbf{H}$ in terms of the complex amplitudes $E^{\pm} = E_x \pm iE_y$, $H^{\pm} = H_x \pm iH_y$ describing circular polarized waves. In the dielectric region we find the relations

$$\pm ikH^{\pm} = -\frac{\omega}{c}n^2E^{\pm}, \quad \pm ikE^{\pm} = \frac{\omega}{c}H^{\pm}.$$

Similar relations hold in the vacuum region with n replaced by 1. At the interface $z = 0$ we must match EM field amplitudes on both sides using continuity of the E

field and the Ampère's law for the H field:

$$\begin{aligned} E_<^\pm &= E_>^\pm, \qquad H_<^\pm = H_>^\pm + i\frac{4\pi}{c}\sigma_\pm(\omega)E_>^\pm, \\ \sigma_\pm(\omega) &= \sigma_{xx}(\omega) \pm i\sigma_{xy}(\omega) \end{aligned} \tag{E.43}$$

where $\sigma_{xx}(\omega)$, $\sigma_{xy}(\omega)$ is the longitudinal and Hall parts of the AC conductivity of graphene. Expressing the fields in terms of the incident wave amplitude E_0 (and suppressing the circular polarization superscripts $\pm$ for brevity), we have $E_> = tE_0$, $E_< = E_0 + rE_0$, $H_> = inE_>$, $H_< = iE_0 - irE_0$, where t and r are the transmission and reflection coefficients. Eliminating $E_<$, $H_<$, $E_>$, $H_>$, we find equations for t and r:

$$1 + r = t, \quad 1 - r = \left(n + \frac{4\pi}{c}\sigma(\omega)\right) t$$

Solving these equations, and restoring the circular polarization notation, we find

$$t^\pm = \frac{2}{1 + n + \frac{4\pi}{c}\sigma_\pm(\omega)}, \quad r^\pm = \frac{1 - n - \frac{4\pi}{c}\sigma_\pm(\omega)}{1 + n + \frac{4\pi}{c}\sigma_\pm(\omega)}$$

To find the Kerr angle, we consider polarization rotation of the reflected wave. The field

$$\mathbf{E} = \frac{\hat{\mathbf{x}} - i\hat{\mathbf{y}}}{2}E^+ + \frac{\hat{\mathbf{x}} + i\hat{\mathbf{y}}}{2}E^- = \frac{r^+ + r^-}{2}E_0\hat{\mathbf{x}} + \frac{r^+ - r^-}{2i}E_0\hat{\mathbf{y}} \tag{E.44}$$

describes linear polarization if $\arg(r^+ - r^-)/(r^+ + r^-) = 0$, otherwise the polarization is elliptic. The Kerr angle, which describes rotation of the major polarization axes of the reflected wave relative to that of the incident wave, is

$$\begin{aligned} \tan\theta_K \approx \theta_K &= \operatorname{Im}\frac{r^+ - r^-}{r^+ + r^-} \\ &\approx -\frac{4\pi}{c}\operatorname{Im} i\sigma_{xy}(\omega)\left(\frac{1}{1-n} + \frac{1}{1+n}\right) \\ &= \frac{8\pi}{c(n^2-1)}\operatorname{Re}\sigma_{xy}(\omega) \end{aligned} \tag{E.45}$$

where we approximated $r^\pm$ taking into account that σ_{xx} and σ_{xy} are small compared to c at all frequencies. The above expression is appropriate for BLG on substrate,

$n \neq 1$. For suspended BLG, where $n = 1$, the Kerr angle is equal to the Hall angle.

In the microwave limit $\hbar\omega \ll \Delta$, we have $\sigma_{xy} = e^2/h$. The expression Eq.(E.45) then predicts a fairly large optical rotation

$$\theta_K = \frac{2}{137(n^2-1)}\text{sign}(\Delta) \sim 10^{-2}\text{sign}(\Delta) \tag{E.46}$$

For higher frequencies $\hbar\omega > \Delta$, we have

$$\theta_K = \frac{2}{137(n^2-1)}\frac{\Delta^2}{\omega^2}\text{sign}(\Delta) \sim 10^{-2}\frac{\Delta^2}{\omega^2}\text{sign}(\Delta) \tag{E.47}$$

This expression is valid for $\hbar\omega \ll \Lambda$, where $\Lambda \approx 0.4eV$ is the bandgap to the higher BLG bands. For experiments at $\hbar\omega \gtrsim \Lambda$, the two band model is not sufficient, and a four band model must be used.

E.1.3 Anisotropic transmission in nematic state

We now demonstrate that the broken rotational symmetry in the nematic states manifests itself in an anisotropic transmission coefficient for linearly polarised light. We consider an incident wave that is linearly polarised along the x axis, and calculate the transmission coefficient through a BLG sample that is in the nematic state. We then repeat for a wave that is linearly polarised along the y axis, and compare the two transmission coefficients. For maximum simplicity, we consider the standard nematic state, which preserves time reversal symmetry and has $\sigma_{xy} = 0$. This is sufficient to demonstrate the anisotropy in transmission.

We consider the same geometry that was used to study the Kerr angle. We consider first a wave polarised such that $\mathbf{E} = E\hat{x}$, $\mathbf{H} = H\hat{y}$. Maxwell's equations $\mathbf{k} \times \mathbf{H} = -\frac{\omega}{c}\mathbf{D}$, $\mathbf{k} \times \mathbf{E} = \frac{\omega}{c}\mathbf{H}$ with $\mathbf{k} = k\hat{z}$ now read

$$kH = \frac{\omega}{c}n^2 E \qquad kE = \frac{\omega}{c}H$$

Similar relations hold in the vacuum region with $n = 1$. At the interface, we must

match EM field amplitudes using the continuity equations

$$E_< = E_>, \qquad H_< = H_> + \frac{4\pi}{c}\sigma_{xx}E_>$$

Now we have $E_> = tE_0$, $E_< = E_0 + rE_0$, $H_> = nE_>$, $H_< = E_0 - rE_0$. Eliminating $E_<, H_<, E_>, H_>$, we find equations for t and r

$$1 + r = t, \qquad 1 - r = \left(n + \frac{4\pi}{c}\sigma_{xx}\right)t$$

Solving these equations, we obtain

$$t_x = \frac{2}{1 + n + \frac{4\pi}{c}\sigma_{xx}(\omega)}$$

Similarly, we obtain

$$t_y = \frac{2}{1 + n + \frac{4\pi}{c}\sigma_{yy}(\omega)}$$

This leads to the expressions quoted in the main text.

Bibliography

[1] R. M. White and T. H. Geballe, *Long Range Order in Solids*, p 317, 321 [Academic Press (1979)].

[2] A.W.W.Ludwig, M.P.A.Fisher, R.Shankar and G.Grinstein, Phys. Rev. B 50, 7526-7552 (1994)

[3] F.D.M. Haldane, Phys. Rev. Lett. 61, 2015 (1988).

[4] R. Jackiw, Phys. Rev. D 27, 2375 (1984).